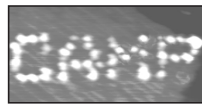

Scanning Tunneling Microscopy
Studies of Organic Molecules
on Metal Surfaces

Michael Schunack

Institute of Physics and Astronomy
Center for Atomic-scale Materials Physics
University of Aarhus, Denmark

PhD thesis
January 2002

This thesis is submitted to the Faculty of Science at the University of Aarhus, Denmark, in order to fulfill the requirements for obtaining the PhD degree in physics. The studies have been carried out under the supervision of Flemming Besenbacher in the scanning tunneling microscopy laboratory at the Institute of Physics and Astronomy from November 1998 to January 2002.



Contents

List of Publications	vii
Abbreviations	ix
1 Introduction	1
1.1 Motivation	1
1.2 Outline	5
1.3 Other studies	6
2 Experimental methods	9
2.1 Introduction	10
2.2 Scanning tunneling microscopy	11
2.2.1 Basic principles	11
2.2.2 Aarhus STM	12
2.2.3 Theory of STM	15
2.2.4 Imaging of adsorbates	18
2.2.5 General remarks	20
2.3 Low- and variable-temperature STM	21
2.3.1 General set-up	22
2.3.2 Cryostat sample holder connection	26
2.3.3 Performance	30
2.4 Molecular evaporator	35
2.4.1 General design	35
2.4.2 Uniformity of the deposited layer	37
3 Bonding of molecules to surfaces	39
3.1 Introduction	40
3.2 A chemist's view	41
3.3 A physicist's view	43
3.4 van-der-Waals bonding	46

4	HtBDC on Cu(110)	49
4.1	Introduction	50
4.2	HtBDC molecule	51
4.3	Restructuring of the surface	53
4.3.1	Double row structure	53
4.3.2	STM manipulation experiments	58
4.3.3	Driving force for the restructuring	62
4.4	Chirality of the restructuring	66
4.5	Conclusion	71
5	DC on Cu(110)	73
5.1	Introduction	74
5.2	DC molecule	74
5.3	Low coverages	74
5.4	High coverages	77
5.5	Conclusions	82
6	Lander molecules on Cu(110)	83
6.1	Introduction	84
6.2	Lander molecule	84
6.3	Adsorption geometries	86
6.4	Restructuring processes	90
6.5	Conclusions	95
7	Surface diffusion of large molecules	97
7.1	Introduction	98
7.2	Data acquisition	101
7.2.1	Tip influence	103
7.3	Theoretical background	105
7.3.1	General relations	105
7.3.2	Rate theories and multiple jumps	107
7.4	Data analysis	110
7.4.1	Extraction of the hopping rate	111
7.4.2	Kinetic Monte Carlo simulations	115
7.5	Results and discussion	121
7.5.1	Arrhenius parameters	122
7.5.2	RMS jump lengths	127
7.6	Conclusions	132
8	Summary	135
A	Stereochemical principles	139
A.1	General definitions	139
A.2	Cahn-Ingold-Prelog convention	140
A.3	Fischer convention	141

B Random walk theory	143
B.1 Poisson process	143
B.2 Displacement distributions	144
C Nucleation and growth of a new CAMP member	147
Bibliography	151
Acknowledgements	169

List of Publications

Publications related to thesis

- [I] A fast-scanning, low- and variable-temperature scanning tunneling microscope
L. Petersen, M. Schunack, B. Schaefer, T. R. Linderoth, P. B. Rasmussen, P. T. Sprunger, E. Lægsgaard, I. Stensgaard, and F. Besenbacher,
Rev. Sci. Instrum. **72**, 1438–1444 (2001).
- [II] Anchoring of organic molecules to a metal surface: HtBDC on Cu(110)
M. Schunack, L. Petersen, A. Kühnle, E. Lægsgaard, I. Stensgaard, I. Johannsen, and F. Besenbacher,
Phys. Rev. Lett. **86**, 456–459 (2001).
- [III] A chiral metal surface
M. Schunack, E. Lægsgaard, I. Stensgaard, I. Johannsen, and F. Besenbacher,
Angew. Chem. **113**, 2693–2696 (2001)
Angew. Chem. Int. Ed. **40**, 2623–2626 (2001).
- [IV] Long jumps in the surface diffusion of large molecules
M. Schunack, T. R. Linderoth, F. Rosei, E. Lægsgaard, I. Stensgaard, and F. Besenbacher,
submitted to *Phys. Rev. Lett.* .
- [V] Lander molecules acting as nanomolds on metal surfaces
F. Rosei, M. Schunack, P. Jiang, A. Gourdon, E. Lægsgaard, I. Stensgaard,
C. Joachim and F. Besenbacher,
submitted to *Science*.
- [VI] Lander molecules on clean and oxygen covered Cu(110): a way of preparing ordered molecular domains
Y. Naitoh, F. Rosei, M. Schunack, E. Lægsgaard, I. Stensgaard, and F. Besenbacher,
in preparation.

- [VII] Bonding and mobility of related aromatic molecules on Cu(110)
M. Schunack, T. R. Linderoth, E. Lægsgaard, I. Stensgaard, and F. Besenb-
bacher,
to be published.

Other publications

- [VIII] Chiral modifier: cinchona alkaloids on Pt(111)
M. Schunack, E. Lægsgaard, I. Stensgaard, and F. Besenbacher,
to be published.
- [IX] Cysteine on Au(111)
M. Schunack, A. Kühnle, T. R. Linderoth, and F. Besenbacher,
in preparation.
- [X] Nucleation and growth of a new German CAMP member
J. Schunack, M. Schunack, and *not* F. Besenbacher,
Single-paper handout publishing company Schunack LTD 1, 1 (2000).

Abbreviations

AES	Auger electron spectroscopy
AFM	atomic force microscopy
CD	compact disk
CIP	Cahn-Ingold-Prelog
DC	decacyclene
DOS	density of states
EMT	effective medium theory
ESQC	electron scattering quantum chemistry
FCC	face centered cubic
FIM	field ion microscopy
GLE	generalized Langevin equation
GS	ground state
HOMO	highest occupied molecular orbital
HtBDC	hexa-(<i>tert</i> -butyl)decacyclene
IC	integrated circuit
KMC	kinetic Monte Carlo
LDOS	local density of states
LED	light emitting diode
LEED	low energy electron diffraction
LITD	laser induced thermal desorption
LUMO	lowest unoccupied molecular orbital
MD	molecular dynamics
ML	monolayer
MS	mass spectrometry
NN	nearest neighbor
NNN	next-nearest neighbor
OFHC	oxygen-free high conductivity
OMBD	organic molecular beam deposition
PC	personal computer
PID	proportional integral differential

PVBA	4-Trans-2-(pyridy-4-yl-vinyl)benzoic acid
RMS	root mean-squared
ROM	read only memory
RT	room temperature
SPM	scanning probe microscope
STM	scanning tunneling microscope
TMR	transfer and mobility of researchers
TPD	temperature programmed desorption
TS	transition state
TST	transition state theory
UHV	ultrahigh vacuum

CHAPTER 1

Introduction

1.1 Motivation

Nanotechnology is the blanket term used to describe the precision manufacture of materials and structures where the characteristic dimensions are less than about 100 nm. [1]. The long-term goals of nanotechnology are to design materials with specific, advanced properties by controlling processes at the ultimate length scale of atoms and molecules [2]. In order to reach this goal, fundamental problems have to be tackled in areas as diverse as molecular biology, lithography, catalysis, and molecular-scale machines [3], as will be exemplified in the following.

A primary motivation for nanotechnology stems from the desire to find alternatives to the traditional “top-down” approach in semiconductor industries that uses lithography techniques for the fabrication of smaller and smaller electronic components onto silicon wafers. In 1965 Moore, co-founder of the Intel company, predicted that the number of transistors per integrated circuit (IC) would double every 18 months [4].¹ The scaling down of the (optical) lithographic process (with 130 nm feature size being state of the art today [5]) is a matter not only of fabrication costs, but also of reaching fundamental physical limits [6].² New ways have to be explored if the miniaturization of electronic devices is to be continued.

¹Note that Moore predicted this only four years after the invention of the first planar integrated circuit. At that time the number of transistors per IC was well below 100 — one of the latest processors manufactured by Intel comprises 55 million transistors.

²Such fundamental limits are, e.g. connected with the minimum thickness at which a gate silicon oxide film (the narrowest feature of silicon devices) is still electrically insulating (four atomic layers [7, 8]). This border will be reached in about 10 years, if Moore’s law continues.

One idea is the so-called “bottom-up” approach that is based on the formation of functional devices out of prefabricated molecular building blocks with intrinsic basic electronic properties. Molecules can be considered as the ultimate limit of electronic devices with sizes in the order of magnitude of 1 nm. The density of transistors on computer chips can hence in principle be improved by a factor of 10^5 compared to present standards. According to Moore’s law this would roughly take another 40 years via the top-down approach.

Without doubt, the bottom-up approach is aiming very high and major problems have to be tackled to reach the final goal. Even though many visions may sound far-fetched, we must keep in mind that the technological standard of today was widely imagined impossible 20 years ago; predicting the development of (nano)technology is basically impossible. The first demonstrations of functional networks built out of carbon nanotubes is a proof of possibilities and a reason for optimistic perspectives [9–12]; these achievements have been voted as “breakthrough of the year 2001” by the journal *Science* [13].

The fundamental difficulties within the bottom-up-approach can be divided into two groups. One problem is the development of functional molecular devices later to be used as the building blocks. The field of molecular electronics is quite old, considering that the first molecular device, a molecular rectifier, has been proposed as early as 1974 [14], and is one of the areas of nanotechnology that attracts a lot of interest [15]. The experimental determination of fundamental properties like the electrical conductance through single molecules are far from straightforward [16–18], but basic electronic principles like diode [19], transistor [20, 21] and switch behavior [22] have meanwhile been proven possible. For use as molecular wire interconnects carbon nanotubes are studied quite intensively [23–25].³

The difficulties in this area are a result of the tiny molecule size which, in turn, is also the reason for the enormous perspectives within the field! The small size is also connected with the second group of problems: the difficulty of how to gather the gigantic amounts of molecules (about $10^{14}/\text{cm}^2$) into ordered devices. Two strategies can be envisioned.

The first strategy is enabled by the development of scanning probe microscopes (SPM) that opened up the possibility of not only imaging and studying matter at the atomic scale, but actually interacting with it. It was demonstrated that single atoms/molecules can be positioned at will one at a time [26–32], just as in Feynman’s more than 40 years old vision to “arrange the atoms the way we want” [33]. Although fundamentally interesting model systems could be built in this way, this serial approach is technologically less attractive because of its extreme slowness, even though probe arrays have been developed by now [34].

The second strategy is the so-called (molecular) self-assembly approach. Self-assembly has been defined by Whitesides as the spontaneous organization of molecules or objects into stable, well-defined (supramolecular) structures by non-covalent forces [35]. This is a parallel and therefore very promising route. One

³The electrical connection not only between molecules, but also between single molecules and the outer world are a basically unsolved problem which will not be discussed in further detail here. Related to this is the problems of investigating single molecules.

hopes to gain control over the involved processes in such detail that desired arrangements and structures can be built from specifically designed molecules.⁴

Not only because of the potential application in the bottom-up approach, self-assembly processes of large molecules are currently the subject of widespread research projects [35–40]. Self-assembled monolayers of thiol molecules (R-SH) on, e.g. gold surfaces are widely investigated and are actually used for nanostructuring of surfaces (dip-pen nanolithography [41], soft-lithography [42]).

From a technological point of view self-assembled monolayers or thin organic films in general are of high interest and already today numerous applications exist, where organic thin films are involved in one way or another [36]. A potential field of use is within the area of organic optoelectronics in, e.g. electroluminescent devices [43], photovoltaics [44], and inexpensive, large-area organic field effect transistors [45]. As coatings, thin organic films are used in computer hard disks to provide a corrosion resistance and a low friction environment [46, 47]: the disk flying height (some 10 nm) is crucial for the data storage density, a low surface roughness is strongly demanded.⁵

Applications of organic thin films in the field of (bio)chemistry are found in sensors [49], heterogeneous catalysis [40], and biomaterials interfaces in medical implants [50]. The assembly and growth of molecules on surfaces may also be of considerable technological significance for pharmaceutical industries. Polymorphism, the ability of a molecule to adopt different crystal forms, is very difficult to control in standard growth procedures and determines important physical properties of drugs like solubility and bioavailability. It was demonstrated recently how the epitaxial growth of crystals onto organic single crystal substrates can influence the morphology [51], which may be exploited for controlling the crystal morphology through specific surfaces.

In all these areas the molecular arrangement on the surface influences their growth and hence the final properties of the organic films, e.g. their electronic coupling, adhesion or porosity. The sensitivity of crystal nucleation and growth to the substrate surface structure reflects the delicate balance of forces responsible for guiding the molecular organization. A proper atomic-level understanding of the underlying mechanisms is a primary scientific motivation for investigating molecular assembly. The development of realistic models of such processes may enable us to gain full control over the assembly processes and by that get closer to the dream of nanotechnology to construct materials of specific properties with atomic precision.

So far, different aspects have been investigated like single-molecule adsorption [52–54], monolayer structures [55–58] and thin film growth [59, 60]. Within

⁴Self-assembly processes moreover may open up a third dimension for fabricating ICs. This would additionally extend the possibilities of molecular devices compared to a lithographic approach which is restricted to two dimensions.

⁵Organic films have also been used directly as storage environment in a device of a million-fold larger storage density compared to the CD-ROM technology used nowadays [48]. For achieving this high density, however, the STM had to be used for reading/writing the data, which in a real device yields only a slow data throughput.

these studies the STM proved over the years to be especially useful. Its atomic-scale, direct space view of surfaces is of crucial importance in growth processes when a long-range ordering is not yet developed and integral probe techniques that rely on scattering processes at large symmetric domains can not be applied. The study of organic molecules on surfaces started quite soon after the invention of the STM about 20 years ago [61–64], and recently extended to quite large and complex molecules, because of prospective applications in nano-electronics and nano-mechanical devices as discussed above [17, 18, 65–69]. Important insight into the bonding and ordering of such molecules on metal and semiconductor surfaces could be gained.

These studies are mainly concerned with static effects, i.e. the structures that form as a result of the growth processes [70–76]. The adsorbates can form complicated structures if directional, non-covalent bonding via hydrogen bonds [77, 78] or electrostatic interactions [79, 80] is possible between molecules. These intermolecular forces are often considered as entirely governing the molecular assembly into ordered structures [77, 78, 81, 82]. The metal surface is then considered only as a static substrate that simply enables (weak) bonding to the molecules.⁶

The assembly of molecules on surfaces is, however, ruled by a delicate balance between the molecule-molecule and the molecule-substrate interactions. The latter not only enables the adhesion of molecules on surfaces in general, but also controls the epitaxial growth. Moreover, the molecule-substrate bonding governs another important property: the surface mobility of adsorbates. This becomes very important during the structure formation since the diffusion determines the probability of meeting other adsorbates.

The diffusion of individual atoms and molecules across solid surfaces and their aggregation into complex structures are among the most fundamental interactions in surface science. The detailed understanding of such dynamical processes has again been influenced tremendously by the STM, where the time evolution of single atoms and molecules can be followed.⁷ Microscopic mechanisms like the diffusion barriers of atoms migrating across perfect crystal planes [85, 86], mutual adatom interactions [87, 88] and the participation of jumps other than to nearest neighbor sites on the substrate [89–91] have been investigated in detail for metal-on-metal systems. This knowledge is, however, rudimentary for such processes as soon as molecules instead of atoms are involved; such studies have just started to emerge [92–94].

The STM studies in this thesis focus on the molecule-substrate interactions and their consequences for the static *and* the dynamical behavior of adsorbates on a single-crystal Cu(110) surface. For this purpose three molecules (HtBDC, DC and Lander) were investigated which are designed such that intermolecular interactions were reduced to a minimum (van-der-Waals forces), i.e. directional

⁶This view seems to be confirmed for cases of simple van-der-Waals bonding between molecules, where simple close-packed adsorbate layers are often observed [82, 83].

⁷Even though such atomic-scale investigations have been performed with the field ion microscope (FIM) long before one imagined the STM, the FIM has limitations due to high electric fields, restricting experiments to refractory metals [84].

bonding effects can be neglected.

The molecules all possess an aromatic π system as a key structure thought to be important in building blocks for possible future molecular electronics devices (conducting backbone) and can hence be viewed as model systems within this field. Due to their extended aromatic units, the molecules are also technologically interesting. The property to adsorb light in the visible range provides the molecules with beautiful colors [95] and makes them interesting candidates as dyes in optoelectronic applications. Again, the understanding of the growth and crystallization is strongly desired to tailor devices with specific properties.

It is investigated how a modulation in the interaction strength of the molecules to the substrate affects their bonding, ordering and mobility on the surface. This modulation is achieved by spacer groups that surround the molecules and provide a separation of the (generally strong bonding) aromatic center from the substrate. It will be shown that molecule-substrate interactions can in fact become a dominating effect that leads to self-assembly phenomena of molecules on surfaces. A detailed study of the dynamical behavior of the related HtBDC and DC molecules elucidates important, fundamental aspects of the surface mobility which have not been addressed before. This study demonstrates furthermore, how delicate variations in the chemical structure of the molecules influence the microscopic diffusion mechanisms. Such a microscopic understanding in the investigated model systems is valuable for eventually extending this understanding to more applied systems.

1.2 Outline

The thesis starts in Chap. 2 with a description of the experimental equipment and methods which focus on the STM. Its basic operation principle is described along with the design of the STM used in our group. Different theoretical concepts of electron tunneling and the imaging of surface and adsorbate structures are presented. A major part of this chapter summarizes the design optimization of a low- and variable-temperature STM based on a He flow-cryostat. Finally, the evaporator developed for dosing well-controlled amounts of molecules is presented.

In Chap. 3 general principles of the molecule bonding to surfaces are discussed. The bonding is described in two different approaches: from a chemist's view, stimulated by complex chemistry, and from a physicist's view, influenced by concepts from solid state physics — the similarity of both approaches is emphasized. Physisorption is discussed in terms of weak van-der-Waals bonding.

The following three chapters describe structural aspects of the HtBDC, DC, and Lander molecules on a Cu(110) surface. The self-assembly of HtBDC molecules into double rows along specific directions of the substrate is reported in Chap. 4. It is shown that this row assembly of molecules is associated with a restructuring of the substrate surface underneath. Effective medium theory (EMT) calculations are presented that attempt to explain different aspects of the structure formation. The unexpected chirality of the restructured substrate surface is

finally discussed in detail, since the phenomenon of chirality at metal surfaces is not widespread. It is described how extended, ordered chiral metal surfaces can be formed at high coverages which comprise large, enantiomorphous domains.

The adsorption of DC molecules is discussed in Chap. 5. The molecule lacks the surrounding spacer groups of HtBDC and is hence well suited as a reference to results obtained in the previous chapter. No restructuring of the surface is found in the case of DC. This difference to HtBDC leads to a low tendency to order into domains. The structures found at very high coverages are analyzed.

Chap. 6 accounts for the structural aspects of the adsorption of Lander molecules. The chemical similarity to HtBDC is expressed in a likewise restructuring of the substrate surface upon adsorption which is, however, restricted to step edges. This is with the help of electron scattering quantum chemistry (ESQC) calculations discussed in terms of the subtle differences in the Lander spacer groups compared to the HtBDC spacer groups.

Chap. 7 deals with dynamical aspects, the one-dimensional diffusive motion of HtBDC and DC molecules on a Cu(110) surface. The diffusion has been investigated from STM movies, following the displacements of individual molecules. First, a broad theoretical background on surface diffusion is provided. Second, the data analysis describes in detail how the mean-squared displacements and the hopping rate have been extracted from the STM movies. It is outlined how this can be used to extract root mean-squared (RMS) jump lengths in a new approach; its accuracy is assessed by Kinetic Monte Carlo (KMC) simulations. Finally, the results for the Arrhenius parameters and the RMS jump length are summarized and discussed.

The thesis is concluded by a summary in Chap. 8 which emphasizes the most important results. Three appendices include supplementary information. Fundamental principles of stereochemistry and common terminology are collected in App. A. App. B provides details of the random walk theory and describes useful background information with respect to the analysis of the adsorbate diffusion. Finally, App. C reports on experiments which are maybe not of public (scientific) importance, but mean very much to me.

1.3 Other studies

During my time as a PhD student I studied also the adsorption of naturally occurring chiral molecules, namely cysteine molecules on Au(111) surfaces and of cinchona alkaloids on Pt(111) surfaces. The first project was performed in collaboration with Line Kühnle and Trolle Linderöth and was motivated by the general interest in self-assembly processes of thiol molecules on gold surfaces. Cysteine is a natural amino acid which can be viewed as a model system for the interaction of biomaterials with inorganic interfaces.

The cinchona project was motivated by asymmetric heterogeneous catalysis. Chemical asymmetric syntheses with high selectivity are dominated by soluble catalysts, but for industrial applications heterogeneous systems are preferable due

to their easier handling and reduced loss of catalyst material.⁸ Compared to the nowadays very advanced homogeneous catalytic systems, progress in heterogeneous asymmetric catalysis is lagging far behind. Nevertheless, the cinchona-platinum system is successfully used for the hydrogenation of α -keto esters with high selectivity (enantiomeric excess > 90%) [96, 97]. On a molecular level, however, the system is not well understood, and conflicting reaction mechanisms are reported [97, 98].

These two projects are not presented for two reasons. Firstly, the studies especially on the cinchona alkaloids, turned out to be quite complex and are far from complete. Demonstrating that the cinchona molecules are immobile in the temperature range used under reactions conditions (around RT) is, however, in itself an interesting result with respect to the conflicting reaction mechanism. Secondly, including these studies in the present thesis would certainly extend it to a hardly tolerable length.

⁸The importance of asymmetric synthesis in general is emphasized by the 2001 Nobel Prize in chemistry which was awarded to Knowles, Noyori and Sharpless for their fundamental studies on homogeneous asymmetric hydrogenation and oxidation reaction.

CHAPTER 2

Experimental methods

The experimental methods described in this chapter focus on the scanning tunneling microscope (STM) which is the main tool employed for experimental studies in this thesis. The first part describes the general operation principle of the STM, and, briefly, the design of the Aarhus STM. Theories of the tunneling current (i.e. the imaging contrast mechanism) are presented. The second part summarizes the development and build-up of a low- and variable-temperature STM based on a He flow-cryostat that was published in paper [I]; we concentrate on the thermal connection of the cryostat to the sample and theoretical and practical aspects of the performance. Finally, an evaporator developed for dosing well-controlled amounts of molecules is presented.

2.1 Introduction

All experiments in this thesis were performed in ultrahigh vacuum (UHV) chambers with a base pressure below 1×10^{-10} mbar. The chambers were equipped with an ion (Ar/Ne) gun for sputter-cleaning of the samples and facilities to dose well-controlled amounts of gases and molecules. Moreover, a variety of analytical surface science tools for scanning tunneling microscopy (STM), Auger electron spectroscopy (AES), low-energy electron diffraction (LEED), and mass spectrometry (MS), with the possibility of temperature-programmed desorption (TPD), were available.

The key instrument used in this thesis is certainly the STM which over the years has proved to be a powerful tool for investigating static and dynamical effects of (conducting) surfaces (mainly of metals and semiconductors) and adsorbate layers with atomic resolution in real space. Since its invention in 1982 [99], a variety of STMs have emerged which are operative in different environments (from ultrahigh vacuum [100] up to high pressures [101] and even liquids [102]), and over a wide range of temperatures (from around 700 K [103] down to room temperature (RT) [104], 4 K [105] and even below 1 K [106]).

Opposite to numerous STMs that allow operation at a fixed temperature there are only rather few STMs which are operative over a whole temperature range down to very low temperatures [107–110]. The construction of a variable- and low-temperature STM is, however, highly desirable, since temperature is a very important experimental parameter for, e.g. diffusion studies. The option of low temperatures opens up new possibilities such as atomic/molecular manipulations, single-molecule vibrational spectroscopy [111, 112] and diffusion studies of weakly bound adsorbates, where the hopping rate must be reduced to the time-scale of the STM (typically 10 s).

The general principle of the STM is explained in Sec. 2.2 along with the set-up realized in our group: the so-called Aarhus STM. The most important theoretical aspects of the tunneling current and the STM imaging in general are summarized. This helps to understand the results presented later in the thesis.

A significant part of my PhD project was spent building up a low- and variable-temperature STM capable of operating at 25–400 K, a project which was founded in the PhD work of Petersen [113]. This will be treated separately in Sec. 2.3. Apart from the general design, the key features modified to overcome experimental limitations are presented and the achieved performance is discussed.

Finally, the construction of a molecular evaporator is described in Sec. 2.4. The evaporator permits the dosing of well-controlled amounts of molecules onto a surface under UHV conditions. Aspects of the homogeneity of the deposited layer are briefly discussed.

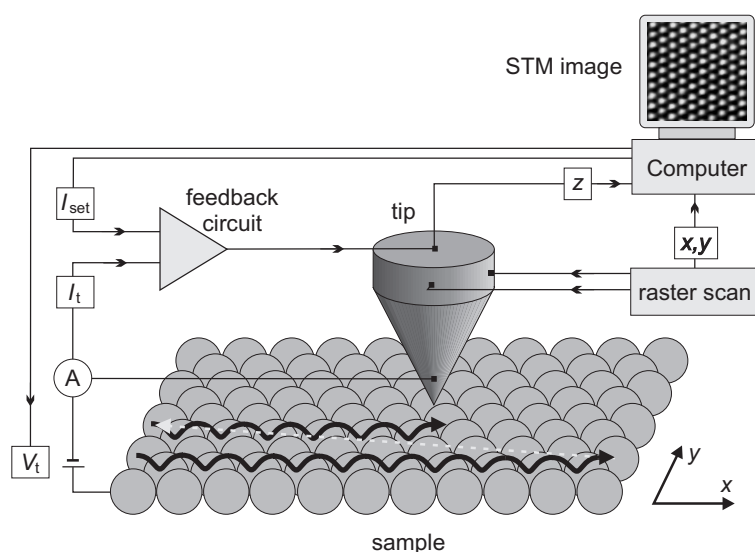


Figure 2.1: Schematic drawing illustrating the operation principle of a fully computer-controlled STM. Tip positioning with atomic precision is realized by piezo-electric elements (not shown). The current is recorded in a defined number of points (typically 256) while scanning the tip from left to right as indicated by the black line, but not during the fly-back to the next scan line (dashed line). See text for details.

2.2 Scanning tunneling microscopy

2.2.1 Basic principles

The STM is, as the name implies, based on the quantum mechanical *tunneling* effect. Roughly, the probability of electrons tunneling through a classically forbidden potential barrier depends exponentially on the barrier width. This extreme sensitivity is exploited for imaging surfaces with atomic resolution in the manner illustrated in Fig. 2.1.

An atomically sharp metal tip (mostly chemically etched tungsten) is brought into close proximity to the (conducting) sample of interest. By applying a small voltage V_t between them, electrons tunnel between the sample and the tip or vice versa, depending on the polarity. The exponential decay of the tip and sample wavefunctions into the vacuum gap requires their distance to be around 10 \AA in order to achieve a sufficient overlap and to measure a tunneling current I_t in the 1 nA range (for $V_t = 1 \text{ V}$).

The tip is raster-scanned across the surface by using, e.g. a piezo-electric tube (see Sec. 2.2.2). The atomic corrugation of the surface gives rise to variations in

the tunneling current with distance z between the sample and the tip.¹ As a rule of thumb, the current reduces an order of magnitude for an increase of the gap distance by 1 Å. This sensitivity leads to a high lateral and vertical resolution: the topmost atom at the tip-apex drags around 90% of the current (assuming that it protrudes ca. 1 Å further than other tip atoms). The whole STM operation is usually fully computer-controlled and the scanning parameters like V_t , I_t , and the raster speed are set via an interface.

There are basically two modes of operating the STM. In the *constant-current* mode, the current I_t is compared to a preset current by a feedback circuit. It provides a correction voltage to the scanner tubes which adjust the z position of the tip in order to keep I_t constant. The correction feedback signal is recorded together with the x - y position of the tip while raster scanning the surface, and hence the STM image is obtained. In the *constant-height* mode, the z -position of the tip is kept constant and the tunneling current is recorded as it varies while raster scanning the sample surface. Generally, the constant-current mode yields better resolution and the constant-height mode allows faster scanning.

2.2.2 Aarhus STM

This simple concept of the STM is contrasted by high demands on the construction, because the tip must be approached and stabilized with sub-Ångström precision above the sample by macroscopic devices with a size in the centimeter range. These problems have, however, been solved and the design of the STM in our group, referred to as the Aarhus STM, will be described here.

The design is sketched in Fig. 2.2 and the numbers in the following refer to this figure. The sample (3) is held in position by two leaf springs (5) which press the sample holder firmly against the top plate (2) of the STM. The top plate is itself connected to an Al cradle (1) suspended in springs (12). The STM housing (7) is for reasons of thermal insulation connected to the top plate via quartz balls (4) and holds a Zener diode (11) at its back.

The interior STM design consists of a piezo tube (6) for scanning (x - y - z movement) the tip at its end across the surface. It is glued on a SiC rod (10) that slides inside another piezo tube (9) used for the coarse approach of the tip to the sample (inchworm). The whole unit is connected to the housing by a ceramic disk (8).

This design provides insulation against mechanical vibrations in two ways. The tight connection of the STM unit and the sample protects against low-frequency vibrations as the whole assembly vibrates as one with no effect on the tip-sample distance. High-frequency insulation is achieved by springs supporting the heavy Al cradle which houses the STM. Together they yield an efficient vibrational insulation against incoming mechanical excitations.

The very compact STM possesses (x - y direction) and longitudinal (z direction) resonance frequencies as high as 8 kHz and 90 kHz, respectively. This reduces the sensitivity of the STM to external vibrations and allows for fast scanning:

¹The additional physical parameters that cause the tunneling current to vary will be discussed in Sec. 2.2.3.

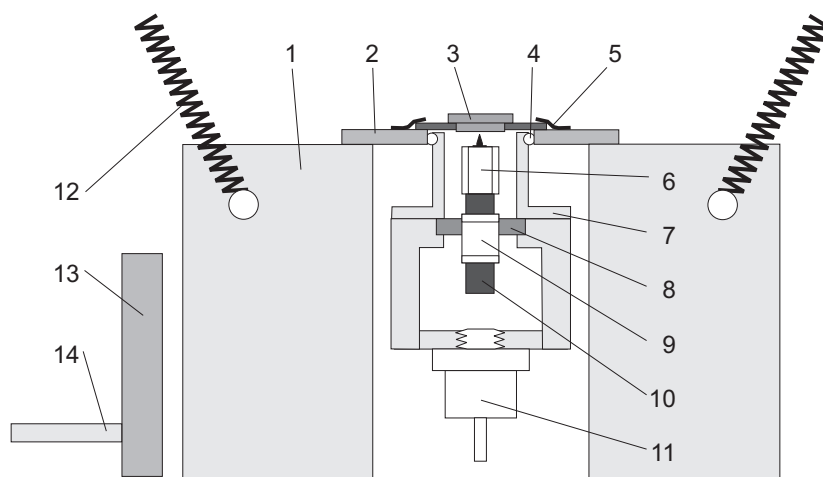


Figure 2.2: Cross-sectional side view of the Aarhus STM. Legend: (1) Al cradle; (2) top plate; (3) sample in sample holder; (4) quartz balls; (5) leaf springs; (6) scanner piezo tube and tip; (7) STM housing; (8) ceramic disc; (9) inchworm piezo tube; (10) SiC rod; (11) Zener diode; (12) suspending spring; (13) coldfinger; (14) liquid nitrogen feedthrough.

Constant-current images with 256×256 pixels can be recorded at approximately one image per second for image sizes up to $100 \times 100 \text{ \AA}^2$. Images as large as $2 \times 2 \mu\text{m}^2$ can be acquired in 100 seconds.

The inchworm enables the coarse approach of the tip towards the sample. Its piezo-electric tube (9) has three outer electrodes. The upper and the lower parts have bearings that fit very precisely onto the shaft (10) and are used for clamping the piezo tube to the shaft. The center piezo tube part can be expanded/contracted, and with a predefined sequence (upper clamping, lower un-clamping, center contraction, lower clamping, upper un-clamping, center expansion) the shaft can be moved relative to the fixed piezo tube. The coarse approach operates at a speed of approximately 1 mm/min and is computer-controlled: the tunneling current I_t is checked in every cycle until a preset value (usually 10 pA) is reached and tunneling is established.

The tube scanner (6) for x - y - z movement of the tip relative to the sample was invented by Binnig and Smith [114]. It consists of a piezo-electric tube (6) metal-coated on the inner and the outer side. The outer electrode is partitioned into four quadrants along the tube axis. By applying antisymmetric voltages to opposite segments (with respect to the inner electrode), one side expands and the other contracts which yields an overall bending of the tube towards one side.² Thus, the tube bending can be controlled by means of the four electrodes and move the

²Due to the enormous size difference between the scanner tube and the scanning area the actual bending of the tube is minute and even for a maximum scan size of $20 \mu\text{m}$ only around 0.05° .

tip in the x - y direction. Applying a voltage to the inner electrode allows control of the tip z position.

Variable-temperature measurements can be performed in the temperature range 100–400 K. Low temperatures are achieved via a liquid N_2 -cooled facility (13) which presses against the Al cradle during cool down. Due to the bad thermal contact of the cooling finger to the cradle, the top plate and finally the sample, the minimum temperature is reached only within 3 h. While performing a measurement, the finger is retracted to ensure vibration insulation of the STM. The large cradle acts as a heat reservoir and slows down warming-up of the sample to experimentally tolerable 5 K/h.

The inchworm coarse approach with the close fitting between rod and bearings makes the STM sensitive to low temperatures. Hence, the whole STM housing (7) is thermally insulated from the top plate (2) by three quartz balls (4), and can be counter heated with a Zener diode (11).³ This maintains a constant STM temperature around RT for all sample temperatures. Additionally, one avoids repeated calibrations of the STM resulting from temperature-related changes of the piezo coefficients. The design of a low- and variable-temperature STM with full temperature control down to 25 K is described in Sec. 2.3.

Elevated temperatures are reached by means of Zener diodes mounted on the Al cradle. Since they can be run also while acquiring STM images, the temperature can be controlled at all times. An upper limit of the sample temperature around 400 K is dictated by the Curie temperature of the piezo-electric elements: the STM unit heats up gradually and can not be cooled separately.

At all temperatures, the thermal drift in the z and the x - y direction can be kept low enough to enable the same area on the surface to be monitored (e.g. when recording STM movies), if a software-implemented drift compensation routine is used [115, 116]. The drift compensation is implemented in two stages:

A coarse drift rate is determined by pointing with a PC mouse on a prominent, immobile feature in two successive images. From the change in the pixel position and the time interval between images a drift rate is calculated; the drift correction is performed by accordingly changing the offset voltages applied to the scanner tube. A fine-adjustment of this drift rate is achieved via a template of a certain size, positioned around a stable structure in the image. An image-recognition algorithm tries to recognize the template in a certain area around the old position and updates the drift rate continuously from image to image. In an ideal situation the template rests on the same position in the image. With this method drift rates of < 1 nm/day have been achieved [117].

³The Zener diode is UHV compatible and the high Zener voltage offers the advantage of a relatively high power being dissipated at a low current so that thin wires can be used, which is important for the vibrational insulation from the surroundings. While heating, the Zener diode is connected to a power supply and the heating power is regulated by adjusting the current.

2.2.3 Theory of STM

An exact theoretical treatment of the tunneling process in STM is virtually impossible for several reasons. It requires a detailed description of the sample and tip states and their evanescence into the tunnel gap; this is not feasible for a low symmetry object like the tip with mostly unknown shape and exact chemical composition. Moreover, the tip apex structure can even change in the course of an experiment.

In the following models and theories treating this problem at different levels of approximation are described [118–120], which provide a foundation for understanding the results presented in this thesis.

An elementary model of the tunneling process in one dimension serves as an introduction to the concept of STM imaging [118].

Assuming a constant potential barrier U in a region $0 < z < d$, the wavefunction $\psi(z)$ describing an electron with energy $E < U$ moving in the $+z$ direction in a classically forbidden region is

$$\psi(z) = \psi(0) e^{-\kappa z} \quad (2.1)$$

with $\kappa = \sqrt{2m(U - E)}/\hbar$. Here m is the mass of an electron and \hbar the Planck constant. Hence, the probability w of observing an electron at the end of the potential barrier ($z = d$) is $w \propto |\psi(d)|^2 = |\psi(0)|^2 \exp(-2\kappa d)$. This exponential decay in the barrier region is illustrated in Fig. 2.3.

Now we consider a metal-vacuum-metal junction of two identical metals with sample states ψ_n and work function ϕ (playing the role of the potential barrier U), and we furthermore neglect the thermal excitation of electrons in the metal. If we assume $eV \ll \phi$ holds for the (positive) bias voltage V applied at the tip, the probability for an electron in the n th sample state with energy ε_n between the Fermi level ε_F and $\varepsilon_F - eV$ to be present at the tip surface is according to Eq. (2.1) given as $w \propto |\psi_n(d)|^2 = |\psi(0)|^2 \exp(-2\sqrt{2m\phi}d/\hbar)$.⁴

The tunneling current is then proportional to the total number of states on the sample surface within the energy interval eV (Fig. 2.3), leading to

$$I \propto \sum_{\varepsilon_n = \varepsilon_F - eV}^{\varepsilon_F} |\psi_n(d)|^2. \quad (2.2a)$$

If the density of electronic states does not vary significantly within $[\varepsilon_F - eV, \varepsilon_F]$, the result can be expressed with the *local density of states* (LDOS) $\rho_s(z = d, \varepsilon_F)$ of the sample at the Fermi level and the tip position $z = d$, and Eq. (2.2a) reads

$$I \propto V \rho_s(z = d, \varepsilon_F) = V \rho_s(z = 0, \varepsilon_F) e^{-\frac{2}{\hbar} \sqrt{2m\phi}d}. \quad (2.2b)$$

Accordingly, a constant-current STM image is a contour map of the sample surface LDOS at the Fermi energy and at the position of the tip surface — a result similarly obtained from the more sound Tersoff-Hamann theory later in this section.

⁴We used the approximation: $U - E = \phi - eV \approx \phi$.

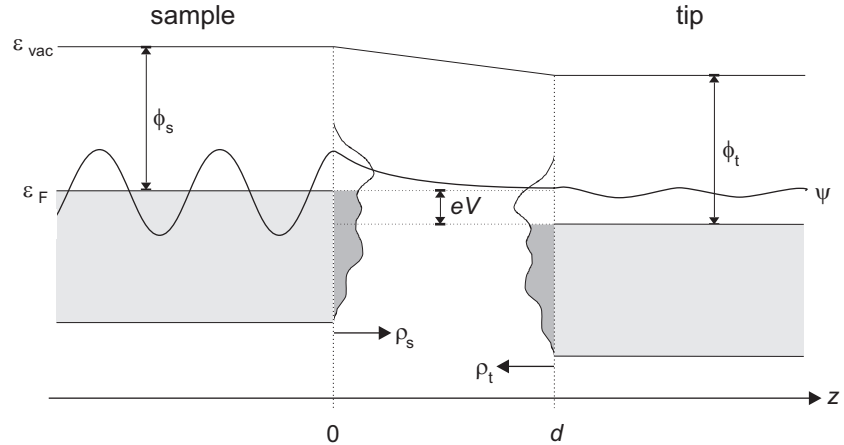


Figure 2.3: Schematic energy diagram for the sample–tip tunnel junction with a width d . A positive bias voltage V is applied to the tip, i.e. tunneling proceeds from occupied sample states to empty tip states (occupied states in the sample/tip are shaded grey). Tunneling is only permitted within the small energy interval eV . ϕ_s and ϕ_t are the (local) work function of the sample and the tip, respectively. The density of states ρ of the sample and the tip are sketched. ψ illustrates a wavefunction at the Fermi energy ε_F that decays exponentially in the junction but still has a non-zero amplitude at the tip position. ε_{vac} is the vacuum energy.

Eq. (2.2b) yields the well-known result that the tunneling current decreases about one order of magnitude if the tip–sample distance is increased by 1 Å (for common values of the work function of about 4–6 eV).

Bardeen found a method to circumvent the problems connected with a theoretical description of the complete tip–sample system as mentioned in the beginning of this section.⁵ He obtained the electronic wavefunctions ψ_t and ψ_s for the separate subsystems of the tip and the sample, respectively, by solving the stationary Schrödinger equation and calculated the rate of electron transfer, i.e. the tunneling current using time-dependent perturbation theory [121]. This concept was first applied by Tersoff and Hamann to treat the tunneling current, as summarized in the following.

From Fermi's golden rule [122] the probability w of an electron to tunnel between states ψ_s and ψ_t obeys

$$w = \frac{2\pi}{\hbar} |M|^2 \delta(\varepsilon_{\psi_s} - \varepsilon_{\psi_t}), \quad (2.3)$$

if only elastic tunneling is considered, i.e. tunneling between states with the same

⁵Even though this concept was developed long before the invention of the STM, we here present it applied to the tip–sample situation.

energy at both sides of the gap. The amplitude of electron transfer, the tunneling matrix element M , is determined by the overlap of the surface wavefunctions of the two subsystems at a separation surface S_0 as

$$M = \frac{\hbar^2}{2m} \int_{S_0} (\psi_s^* \nabla \psi_t - \psi_t \nabla \psi_s^*) dS. \quad (2.4)$$

The tunnel current is evaluated by summing over all states which for a (positive) bias voltage V applied at the tip yields

$$I = \frac{2\pi e}{\hbar} \int_{-\infty}^{\infty} [f(\varepsilon - eV) - f(\varepsilon)] \rho_s(\varepsilon - eV) \rho_t(\varepsilon) |M|^2 d\varepsilon \quad (2.5a)$$

with the Fermi distribution function $f(\varepsilon) = [1 + \exp((\varepsilon - \varepsilon_F)/kT)]^{-1}$ and the density of states (DOS) ρ of the two electrodes.⁶ For not too high temperatures the Fermi distribution can be approximated as a step function and Eq. (2.5a) can be recast in the simpler form

$$I = \frac{2\pi e}{\hbar} \int_{\varepsilon_F}^{\varepsilon_F + eV} \rho_s(\varepsilon - eV) \rho_t(\varepsilon) |M|^2 d\varepsilon. \quad (2.5b)$$

If the tunneling matrix element M does not change much in the energy interval eV , then the tunneling current is determined by the convolution of the tip and surface DOS, as is intuitively clear from Fig. 2.3. Furthermore, if the DOS of the tip can be regarded as constant, the current scales with the DOS of the sample.

Tersoff and Hamann applied Bardeen's formalism to the STM problem. The difficulty of evaluating the tunneling matrix M in Eq. (2.5) was tackled by approximating the tip to be of spherical symmetry with a radius of curvature R [123, 124]. Hence, it can simply be described by a symmetric s wavefunction (lending Tersoff and Hamann's approach the name *s-wave approximation*), which yields the tunneling matrix element

$$M \propto \kappa R e^{\kappa R} \psi_s(r_0). \quad (2.6)$$

Here $\kappa = \sqrt{2m\phi}/\hbar$ is the minimum inverse decay length for the wave functions in the vacuum gap with an effective local barrier height ϕ , and $\psi_s(r_0)$ is the sample wave function at the center of tip curvature r_0 .

⁶To avoid confusions, related parameters will be defined in the following:

The *density of states* (DOS) is the sum over all states i with energy ε : $\rho(\varepsilon) = \sum_i \delta(\varepsilon_i - \varepsilon)$.

The *local density of states* (LDOS) is furthermore weighted by the square of the wavefunctions ψ_i , yielding also a space dependence: $\rho(\varepsilon, \vec{r}) = \sum_i \delta(\varepsilon_i - \varepsilon) |\langle \psi_i(\vec{r}) \rangle|^2$.

The *charge density* is yielded by integration over all $\rho(\varepsilon, \vec{r})$: $\rho(\vec{r}) = \int \sum_i \delta(\varepsilon_i - \varepsilon) |\langle \psi_i(\vec{r}) \rangle|^2 d\varepsilon = \sum_i |\langle \psi_i(\vec{r}) \rangle|^2$.

The *projected density of states* is similar to the LDOS, but weighted by an overlap between the wavefunctions ψ_i and the projected state ϕ_a : $\rho_a(\varepsilon, \vec{r}) = \sum_i \delta(\varepsilon_i - \varepsilon) |\langle \psi_i(\vec{r}) | \phi_a(\vec{r}) \rangle|^2$.

Under the above assumptions they found that for small bias voltages V the simple result is

$$I \propto V \frac{R^2}{\kappa^4} e^{2\kappa R} \rho_t(\varepsilon_F) \rho_s(\varepsilon_F, r_0), \quad (2.7)$$

with the DOS of the tip ρ_t . Accordingly, the tunneling current is proportional to the Fermi level sample LDOS ρ_s at the center of curvature of the tip, similar to the result of the simple model in Eq. (2.2b), where an exponential dependence $I \propto \exp(-2\kappa d)$ on the gap-distance d was found. This is also reproduced here due to the exponential decay of the sample wavefunctions into the vacuum gap: Since $\rho_s = \sum_s |\psi_s(r_0)|^2 \delta(\varepsilon_{\psi_s} - \varepsilon_F)$ and $|\psi_s(r_0)|^2 \propto \exp(-2\kappa(R + d))$, we obtain from Eq. (2.7) the same decay behavior.

An advantage of the Tersoff and Hamann approach is that, assuming an s-wave for the tip, the current can be related to a property of the surface alone and hence the interpretation of (low-bias) constant-current STM images is straightforward: they reflect the contour of constant LDOS at the Fermi level. For metals the Fermi-level LDOS contour at a distance from the surface almost coincides with the total electron density, because of the faster exponential decay of the energetically deeper-lying occupied states. These surface charge density contours have the periodicity of the atoms in the surface and directly reflect the surface topology.

On the other hand, Tersoff and Hamann's approach is based on several important approximations: The tip and the surface are treated separately, which neglects any interaction between them and is valid only in the limit of large tip-surface distances. Moreover, a severe approximation is made on the structure of the tip apex and any tip dependence of the imaging is lost. The theory breaks down for small tip-sample distances and a non-perturbative approach is necessary, as described in the next section.

2.2.4 Imaging of adsorbates

One has to be aware that the simple topological height interpretation of metal surfaces is not valid in general for arbitrary adsorbates on surfaces. This is seen, e.g. for the counterintuitive imaging of O/Pt(111) [125, 126] or N/Fe(100) [127] as depressions with respect to the bare metal surface. Other examples are the imaging of CO on Cu(211) which can appear as a depression or protrusion, depending on the proximity of neighboring molecules and the modification of the tip with CO adsorbed to it [128, 129].

It is generally difficult to identify chemically different adsorbates in STM images. This arises from the fact that STM probes the electronic structure of the surface at the Fermi level and is therefore only indirectly sensitive to the position and chemical nature of the nuclei.

Before the first successful STM images of organic molecules were reported [61–64], it was debated if molecule imaging is possible at all. The doubts stem from Tersoff and Hamann's result that the tunneling current scales with the LDOS at the

Fermi level: most organic molecules have a large gap between the *highest occupied molecular orbital* (HOMO) and the *lowest unoccupied molecular orbital* (LUMO).

Adsorbate states away from the Fermi-level can, however, also induce changes in the Fermi-level LDOS, since they interact not just with a single surface state, but rather with a continuum of states in the (conduction) band [130–132]. Following the Newns-Anderson model [133, 134] for the case of “weak chemisorption” [130], a more or less broad band with a single resonance around the adsorbate state emerges which also affects the Fermi-level LDOS. This will be discussed in more detail in connection with the adsorption of molecules on surfaces in Chap. 3.

The pioneering work in clarifying the contrast mechanism of simple atomic adsorbates was performed by Lang, who proved Tersoff and Hamann’s result valid also for atomic adsorbates [135, 136]. Consequently adsorbates are imaged as protrusions or depressions, depending on how they modify the LDOS at the Fermi level compared to the bare surface, i.e. if they add or deplete electron density. A general rule is that with increasing electronegativity or decreasing polarizability of elemental adsorbates they tend to be imaged as depressions [137, 138].

For the calculation of the tunneling current (i.e. STM images) through adsorbates in general, the knowledge of the electronic structure of the system consisting of both surface and tip is a prerequisite; different approximations are used for the electronic structure calculation ranging from effective Hamiltonian approaches like extended Hückel to first-principles, self-consistent methods based mainly on density functional theory. When it comes to simulating an STM image from the electronic structure, again various levels of approximation are applied. The most popular class of methods relies on perturbation theory, following Bardeen, and Tersoff and Hamann, as sketched above.

The second class of methods goes beyond perturbation theory with a proper description of the interacting sample and tip in a scattering theory formalism. The basic idea is to consider the tunnel gap as a two-dimensional defect inserted between two semi-infinite periodic systems. The tunnel event is then viewed as a scattering process: incoming electrons, for example from the bulk of the sample, scatter from the tunnel junction and have a small probability to penetrate into the tip, and a large one to be reflected towards the bulk.

An example is the electron scattering quantum chemical (ESQC) approach by Sautet and Joachim [139]. The adsorbate is chemisorbed on the substrate surface, while the tip apex is modelled by a cluster of a few atoms attached to the second semi-infinite solid. Coupling with the tip and substrate electron reservoirs is hence taken fully into account. The Hamiltonian matrix elements of an orbital basis set which are the ingredients of the scattering matrix calculation, are obtained with an effective Hamiltonian approach, namely the extended Hückel theory. Maybe the most prominent example of a successful application of the ESQC method is for the adsorption of benzene on Pt(111), where three different experimental imaging modes [140] could be successfully modelled as corresponding to three different adsorption sites [141].

It is obvious from this short introduction that the contrast mechanism in STM imaging is generally not straightforwardly determined. A review of various theo-

ries used to calculate STM images of adsorbates is given in [142].

2.2.5 General remarks

STM has the clear advantage over spatial averaging methods (e.g. scattering methods like LEED) in gaining local structural information. This ability to investigate geometric and electronic structures at the atomic scale helped not only to clarify disputed structural models, but also enabled the investigation of dynamical processes. Even though STM is a powerful tool, there are certainly some disadvantages connected to it. One of the major drawbacks is the lack of chemical sensitivity. This does not only apply for cases where it is desirable to distinguish between different atomic adsorbates on the surface.

When working with large molecules the question often arises, whether the features imaged actually resemble the intact molecule on the surface or, e.g. a fragment of it due to decomposition during the deposition process. Assistance is available from theoretical calculations such as the ESQC approach which can be used to interpret the experimental images. This also allows one to distinguish between different conformations of a molecule on the surface [143–145]. Nevertheless, these calculations are still very demanding and not done routinely.⁷

Even without calculated STM images at hand, it is often possible to conclude indirectly if a molecule is decomposed or not. Molecules with a characteristic shape may be recognized in the images, if it resembles what is expected from molecular models. Imaging different features with variable size, on the other hand, makes a decomposition very likely.

Another problem with STM is connected with the stability of the tip which often varies in the course of an experiment. When working with molecules, there is the problem of picking up molecules by the tip apex in addition to the general problem related to morphological tip changes. This may lead to tunneling-gap instabilities as a result of, e.g. molecule diffusion in the tip apex region.

Furthermore, unusual imaging modes may be caused by such tip-adsorbed molecules as illustrated in Fig. 2.4. Sometimes, however, interesting or useful details appear as exemplified in Fig. 2.4B: additionally to the molecules revealed in an inverted manner, the usually not visible substrate structure is resolved. While the mechanistic details are far from understood, it has been shown that STM tips can be intentionally chemically modified to reach a sensitivity specific for certain subunits within a molecule [146].

The appearance of adsorbates in STM images can also depend on the polarity and magnitude of the bias-voltage applied as has been shown both experimen-

⁷In the paper of Moresco and co-workers [144] a combined molecular mechanics and ESQC approach is used to calculate the tunneling current during the manipulation of a molecule. By comparison to the experimentally determined current they claim that the current fine-structure is a result of the intramolecular bending motion of a subgroup in the molecule as it is manipulated across the surface. The calculated bending motion of the respective group is about an angle of only 0.5° which corresponds to lateral changes below 0.1 \AA . It seems surprising that such a degree of precision can be achieved, considering the approximations that have to be made for the molecular mechanics *and* the ESQC calculation.

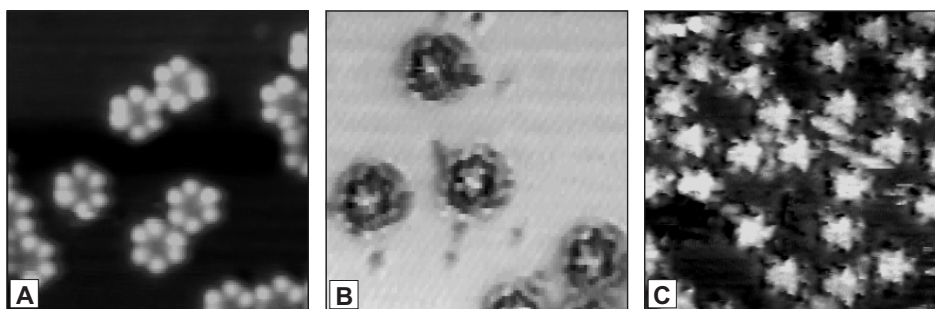


Figure 2.4: Constant-current STM images ($100 \times 100 \text{ \AA}^2$) illustrating different imaging modes of HtBDC molecules on Cu(110) (see Chap. 4). (A) “Regular” mode imaging six lobes of the molecules ($V = 1250 \text{ mV}$, $I = 0.42 \text{ nA}$, 26 K), (B) “Inverted” mode ($V = 884 \text{ mV}$, $I = 1.27 \text{ nA}$, 26 K). The additionally revealed row resolution of the Cu(110) substrate is hard to see in the image. (C) “Triangular” mode ($V = 1250 \text{ mV}$, $I = 0.76 \text{ nA}$, 116 K).

tally [147–149]) and theoretically [150]. STM images are, however, qualitatively often independent of the bias voltage. This is not only observed for metals, but also for large organic molecules (the studies of the molecules in this thesis neither revealed a bias dependence), and was explained by the close resemblance of the HOMO and LUMO of the investigated molecule [64].

2.3 Low- and variable-temperature STM

Due to the necessity to position the tip with sub-Ångström precision above the sample under investigation, the paramount consideration in the construction of an STM is the elimination or reduction of mechanical vibrations. This applies even more for studies below RT, since cooling may introduce new sources of mechanical vibrations, depending on the approach taken. If the ability to change the temperature on a relatively short time-scale (minutes) is of minor importance, a heat reservoir cooled down prior to the measurements can be used. This bath cryostat approach does not introduce additional vibrations and has been successfully applied on a number of STMs [105,106,108,151–153]. There, however, usually lack the ability to achieve fast temperature changes, if changing the temperature is at all possible.

For a quick change of temperature a design based on a flow cryostat is advantageous but also more challenging: cryostat vibrations, caused by boiling or flow of the coolant, or different thermal expansion coefficients of various materials require special considerations. A permanent connection between sample and cryostat to some extent bypasses the typical insulation against high-frequency vibrations from the surroundings by mounting the STM on a cradle suspended in springs [154]. The problems mentioned have been solved in various ways [107,

109, 110, 155–158]. A key feature has been shown to be mechanical decoupling of the sample-cryostat connection, thereby reducing the vibration amplitude [156].

Here we describe a low- and variable-temperature STM based on a liquid He flow cryostat that offers atomic resolution on metal surfaces in the temperature range 25–350 K. The work is a continuation of the general design and set-up initiated mainly by Petersen [113]. Basic features are

1. a small sample holder of low thermal mass to achieve fast temperature changes,
2. a small and compact, removable microscope of a scanner-tube/inchworm design adapted from the Aarhus STM; it is attached rigidly to the permanently mounted sample by a bayonet socket which at the same time provides thermal decoupling between sample and STM, allowing the STM temperature to be held constant, and
3. a thorough isolation of the entire UHV chamber from external vibration sources.

The general set-up is summarized in Sec. 2.3.1. The key features is a *permanent* sample-cryostat connection ensuring a controllable sample temperature while accessing or transferring between the different analytical tools available (AES, TPD, and STM) as well as during sample preparation, including evaporation of metals or molecules onto the surface. This turned out to be the crucial design issue and we focused on its modification to achieve good performance, while the rest of the set-up was only “fine-tuned”. The final solution for the connection of the sample to the cryostat is described in Sec. 2.3.2.

Compared to the Aarhus STM described in Sec. 2.2.2, the accessible sample temperatures are not only expanded towards much lower temperatures, but can also be stabilized in the entire range and are accessible within a much faster time-scale (minutes rather than hours). Sec. 2.3.3 demonstrates the performance.

2.3.1 General set-up

The UHV chamber is mounted on a steel frame which is supported by three pneumatic suspension legs with vertical and horizontal resonance frequencies below 1.5 Hz to provide an environment with sufficient vibrational insulation. This assembly rests on a 2000 kg concrete block which is itself vibrationally insulated from the laboratory floor by four air cushions. These measures were found to reduce the level of vibrations.

The chamber is pumped mainly by an ion getter pump and a low-vibration, magnetically levitated turbomolecular pump mounted on a vibration isolation bellows — this allows the turbo pump to run while STM measurements are performed with atomic resolution. Additional pumping is provided by a liquid-nitrogen-cooled titanium sublimation pump which has a particularly good pumping rate for hydrogen compared to the two other pumps. This leads to a base pressure below 1×10^{-10} mbar.

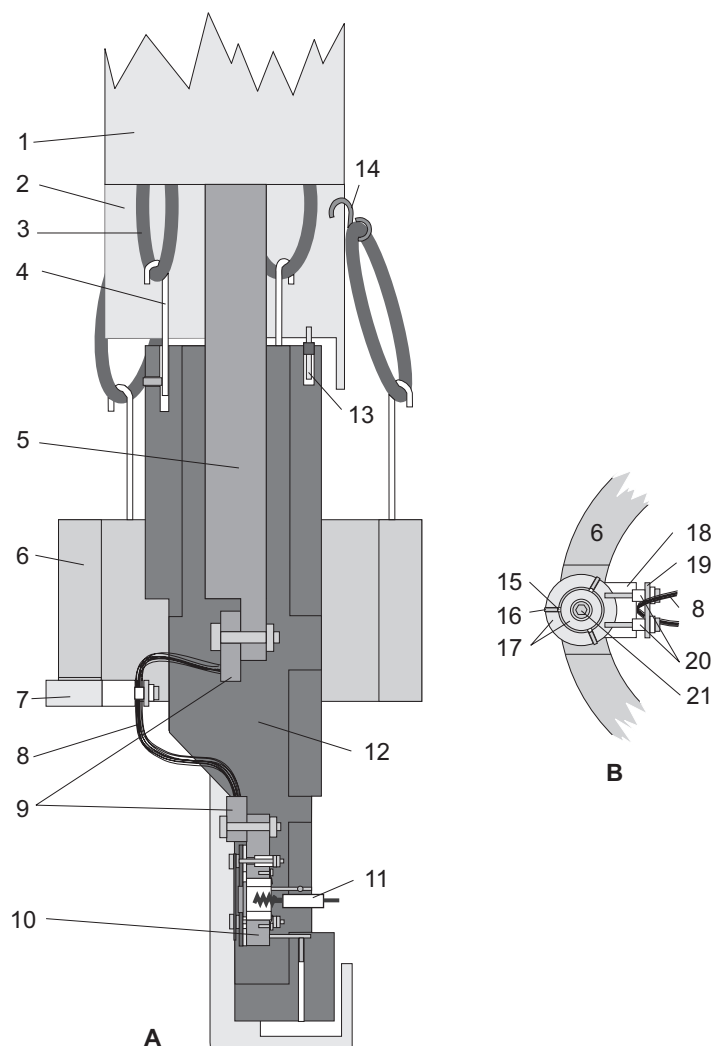


Figure 2.5: (A) Cross-sectional side view of the mounting of the STM and the sample holder on the large Cu block, and the connection to the cryostat. (B) Cross-sectional bottom view of the two-stage thermal insulation piece (7). Legend: (1) upper manipulator tube; (2) lower manipulator tube (removable); (3) Viton rings; (4) adjustable hooks; (5) bottom of the He cryostat; (6) mass for braid decoupling; (7) two-stage thermal insulation piece; (8) Cu braid; (9) braid end contact pieces; (10) STM mounted on the "sample sandwich"; (11) heating filament; (12) gold-coated Cu block; (13) wire connectors; (14) Cu hooks; (15) quartz balls; (16) screw-supporting quartz ball; (17) stainless steel rings; (18) macor piece; (19) stainless steel plate; (20) ceramic tubes; (21) screw.

The helium flow cryostat is coaxially positioned inside a stainless steel tube that serves as support for three levels of Viton sticks which press against the cryostat to reduce the amplitude of its vibrations and shift the resonance frequencies to higher values.⁸ The stainless steel tube also acts as a support for the sample holder; it runs through a rotary platform mounted on an *x-y-z* manipulator, thus yielding four degrees of freedom for positioning the sample inside the chamber.

Fig. 2.5A, to which the numbers in the following refer, illustrates the sample-holder support. The stainless steel tube (1 and 2) around the cryostat (5) supports the large copper block (12) with a mass of approximately 1 kg via three Viton rings (3) in the upper part; the block is gold-coated to minimize the emissivity and its suspension is an effective insulation against high-frequency mechanical vibrations (similar to the Aarhus STM). The lower part of this tube has been minimized with respect to its surface area in order to avoid contact with the large copper block and hence unwanted vibrations. It must fulfill two tasks: it provides a support for a heavy mass (6) described below and acts as a counterpart while mounting the STM on the sample holder (10). This sample holder is mounted on the large copper block via three thin, stainless steel hypodermic tubes (4); stainless steel has a relatively low thermal conductivity, and the hollow tubes have a high bending stiffness relative to a rod of the same conductance.

When cooling the sample with liquid He, the liquid is transferred from a Dewar container to the cryostat through a vacuum-shielded flexible transfer line by the overpressure that builds up in the He container. As soon as the overpressure drops below $\simeq 0.3$ bar, the container can be pressurized externally using room temperature He gas; this turned out to be necessary to maintain a very constant flow of liquid helium through the cryostat and hence a constant cryostat and ultimate sample temperature. To avoid that floor and building vibrations are transferred to the system through the transfer line, the liquid He container (60 l or 100 l) is placed on the vibrationally isolated concrete block.

The sample holder is very compact and of low thermal mass to provide the possibility of rapid temperature changes. The STM is mounted on this sample holder during measurements as described below. With this approach a transfer period of the sample, where the temperature can not be controlled, is avoided.

The design of the sample holder is depicted in Fig. 2.6 with the STM mounted. The numbers in the following refer to this figure. The cooled mass consists of a small Cu block (2) to which the Cu braid (1) coming from the cryostat is connected. On the Cu block, a Ta plate (8) is sandwiched between a Mo ring (9) for the STM

⁸The He flow cryostat itself is based on a design originally developed in the group of Comsa at KFA Jülich [107, 156, 159] and consists of two concentric tubes. The inner tube leads the liquid helium to the bottom of the cryostat, where it expands in a 65 mm long "baffle region". The evaporation of the liquid He ensures that the cooling is actually done by cold He gas. This is done for three reasons: i) to avoid vibrations from boiling liquid helium in the cryostat; ii) to use the heat of evaporation for cooling; and iii) to take advantage of the enthalpy change of the He gas when heating it [160]. The He gas then returns through the coaxial outer tube to the exhaust at the top of the manipulator and creates a "thermal shield" that minimizes the heating of the liquid He on its way through the cryostat to the baffle region.

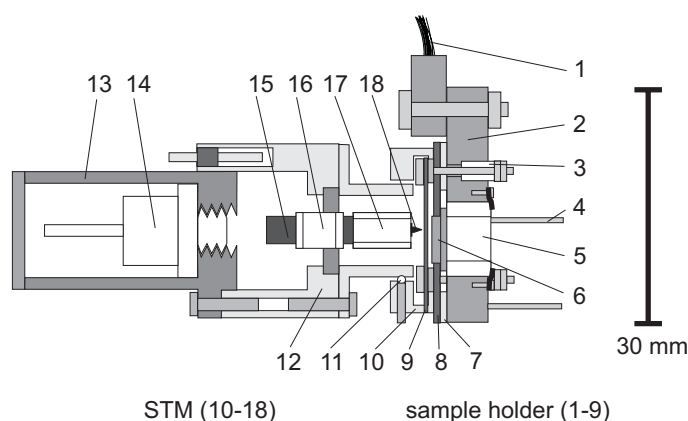


Figure 2.6: Cross-sectional side view of the sample sandwich with the STM mounted. Legend: (1) Cu braid to the cryostat; (2) small Cu block; (3) ceramic cylinder; (4) steel tubes; (5) small ceramic cylinder; (6) sample; (7) sapphire sheet; (8) tantalum base plate; (9) molybdenum ring (for STM); (10) STM foot (invar) with “hooks”; (11) quartz ball; (12) STM housing (Al); (13) handle for grabbing the STM; (14) Zener diode; (15) SiC rod; (16) piezo motor for coarse approach (15+16: inchworm); (17) scanner tube; (18) tip.

mounting (see below) and a sapphire sheet (7) with holes to accommodate screws and sample. The nuts on the stainless steel screws holding this sandwich together press on small ceramic cylinders (3); these contract less than the stainless steel screws when cooled, and thus the sample holder should be especially tight at low temperatures.

The sample (6) has a top hat shape and is pressed towards the Ta plate by a ceramic tube (5) held in place by two small leaf springs screwed into the Cu block. Between the ceramic tube and the back of the sample a thin Ta foil is placed on which chromel–alumel wires for measuring the sample temperature are spot-welded. The foil moreover ensures a more homogeneous heating of the sample by the filament placed behind it [(11) in Fig. 2.5A]. Because Cu contracts more than the ceramic material of the tube when cooled, the sample will be pressed even harder against the Ta plate at low temperatures (expansion coefficients: $\alpha_{\text{Cu}} \approx 17 \times 10^{-6} \text{ K}^{-1}$, $\alpha_{\text{cer}} \approx 6.5 \times 10^{-6} \text{ K}^{-1}$). This is important to avoid mechanical vibrations of the sample at low temperatures. Sapphire, an electric insulator, is a good thermal conductor at cryogenic temperatures, and hence the sapphire sheet serves to insulate the Ta plate and thus the sample electrically from the Cu block without losing thermal contact. Altogether, the sample holder provides a compact and mechanically stable unit of low (thermal) mass.

The STM must be very compact and with the lowest weight possible to ensure good mechanical stability and high resonance frequencies which are not easily excited (the STM essentially acts as a leaf spring mounted on the sample holder). Its

interior design is adapted from the Aarhus STM: a piezo tube for scanning (17) mounted on an inchworm (16) for coarse approach in the z direction perpendicular to the sample plane (see Sec. 2.2.2 for details); the bias voltage is applied to the sample with the tip at virtual ground.

The connection between the STM and the sample holder must be extremely rigid. This is obtained by means of a bayonet-type socket which consists of three hooks at the STM socket (10) fitting into a Mo ring (9) on the sample holder. By turning the STM approximately 40° , the bayonet socket is squeezed between the Mo ring and the Ta plate (8), yielding a stable mechanical contact. The mounting of the STM on the sample holder is done via a wobble stick grabbing the STM handle (13). The wobble stick is mounted on a 150 mm flange on the UHV chamber together with the feedthroughs for the wires to the STM.

The inchworm coarse approach with the close fitting bears the risk of malfunctioning at low temperatures. Hence, the whole STM housing (12) is thermally insulated from the STM foot (10) by three quartz balls (11) held by screws. Quartz was chosen since it has low thermal conductance at low temperatures [161]. This design provides a rigid mechanical connection with a small contact area between the cold STM socket and the rest of the STM. The STM temperature can be stabilized around RT by counter-heating the STM housing via a Zener diode (14) as described already in Sec. 2.2.2; this avoids malfunction of the inchworm and recalibrations of the scanner tube.

2.3.2 Cryostat sample holder connection

A permanent copper braid connection between the sample holder and the cryostat avoids unwanted and uncontrollable temperature changes of the sample during the transfer from a manipulator to the STM. This connection is probably the most crucial part of the cooling facility set-up, since its design has to be a compromise between two contradicting boundary conditions. On one hand, the transmission of vibrations from the cryostat has to be reduced to a minimum and hence sets a limit to the braid thickness; on the other hand, satisfactory low temperatures and *intentional* temperature changes should be achieved as quickly as possible. This requires a short braid with a large cross section.

The combination of an optimized braid together with mechanical decoupling succeeded in meeting both boundary conditions to a satisfactory extent in order to reach a minimum sample temperature of 25 K within a short time-scale. This is specified in the following; the numbers refer back to Fig. 2.5.

The copper braid can be modified by three parameters which influence the lowest possible sample temperature: the length, the cross section and the thermal conductivity (which is related to the Cu purity). It is very time consuming to test the optimal construction experimentally and we hence performed calculations as a guidance for estimating the influence of the three parameters on the lowest possible sample temperature. These are presented at the end of this section.

We used very clean Cu wire with a purity higher than 99.99 % to take advantage of the fact that the thermal conductivity of high-purity Cu increases approximately two orders of magnitude when going from 100 K to 10 K [161], in contrast to lower-purity Cu (e.g. oxygen-free, high conductivity Cu, OFHC).⁹ The ends of the braid (8) are clamped into two polished Cu pieces (9) pressed against the cryostat (5) and the sample holder (10); very thin gold leaf foils in between ensure good thermal contact. Occasional annealing of the braid at 900–1000 K in vacuum helps to get rid of dislocations in the copper and thereby keeping it soft.

To reduce transmission of vibrations from the cryostat to the sample, the Cu braid is made as soft and flexible as possible: It consists of approximately 10 000 Cu strands with a diameter of only 25 μm each, resulting in an overall cross sectional area of $\approx 5 \text{ mm}^2$. The length was demonstrated to have a minor influence on the temperature compared to the other parameters; 8 cm overall length was a necessary minimum in order to accommodate the mechanical decoupling piece.

The mechanical decoupling of the Cu braid to a heavy mass was demonstrated to be of utmost importance in order to reduce the amplitude of the vibrations introduced by the cryostat [156]. In our design the mass consists of a 1 kg heavy stainless steel ring (6) which is suspended by three Viton O-rings from the lower part of the manipulator tube (2). To provide a rigid connection and to minimize the thermal contact between the heavy stainless steel mass and the braid (8), the latter is clamped by a two-stage thermal decoupling piece (7) mounted on the decoupling ring.

The exact set-up of this thermal decoupling piece is shown in Fig. 2.5B. Quartz balls (15) and a Macor piece (18) — both with a low thermal conductivity — insulate the braid sufficiently and minimize the heat flow from the heavy mass to the braid. The minimum sample temperature is increased by less than 10 K because of the mechanical decoupling compared to the performance without decoupling. This is acceptable (but more than expected from our estimate below).

The estimation of the minimum sample temperature is based on an analogy between heat current and electrical current. The main objective is to obtain quantitative information on how the length, the cross section and the thermal conductivity of the braid influence the minimum sample temperature. It was used as a guideline to build a braid with proper dimensions. We have to stress the roughness of this estimate, since it uses various simplifications. The result, however, proves it to be quite good.

The thermal equivalent to Ohm's law for the electrical current is Fourier's law. Considering only the one-dimensional case, the thermal current \dot{Q} is given as

$$\dot{Q} = \frac{dQ}{dt} = -\kappa A \frac{dT}{dx}, \quad (2.8a)$$

where κ is the thermal conductivity, A is the cross-sectional area and dT/dx is the temperature gradient. In the simplest geometric approximation, A is replaced by

⁹Even higher purities are very costly and the gain in temperature is not significant (see Fig. 2.8).

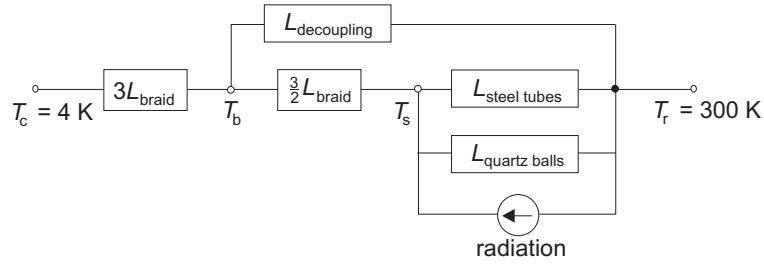


Figure 2.7: Electric equivalence circuit for the estimation of the sample temperature. T_c , T_b , T_s , and T_r are the cryostat, braid (at the contact point to the decoupling piece), sample and room temperature, respectively.

its spatial mean values \bar{A} , and the temperature gradient is taken to be constant ($\Delta T/\Delta x$), so that

$$\dot{Q} \simeq -L\Delta T \quad (2.8b)$$

with $L = \kappa\bar{A}/\Delta x$. The analogy with electricity is made by stating that the temperature difference ΔT is analog to the voltage difference and the thermal conductance L is analog to the electrical conductance.

Several components of the heat current then have to be taken into account in order to estimate the sample temperature:

1. the Cu braid connecting the sample and the cryostat,
2. the stainless steel tubes connecting the sample holder and the large Cu block,
3. the quartz balls connecting the STM via the “foot” to the sample holder,
4. the mechanical decoupling piece of the braid that is clamped approximately one third of its length away from the cryostat, and finally,
5. the net radiative heat current from the warm surroundings to the cold sample holder.

The latter is described by the Stefan-Boltzmann law as

$$\dot{Q}_{\text{rad}} = A_R\epsilon\sigma(T_r^4 - T_s^4) \approx A_R\epsilon\sigma T_r^4, \quad (2.9)$$

where A_R is the surface area of the sample holder, ϵ is the emissivity of the sample holder material, σ is the Stefan-Boltzmann constant, and T_r and T_s are room and sample temperatures, respectively.¹⁰ The approximation of neglecting the radiation emitted from the sample holder in Eq. (2.9) is better than 99% if $T_s < T_r/3$.

The radiative heat current is treated as a current source in the electrical analogy and the complete electric equivalence circuit is shown in Fig. 2.7. By use of

¹⁰Eq. (2.9) is in principle valid for two plane, parallel surfaces of area A with emissivities ϵ_1 and ϵ_2 , with $\epsilon = \epsilon_1\epsilon_2/(\epsilon_1 + \epsilon_2 - \epsilon_1\epsilon_2)$ [162]. Since the emissivities are hard to evaluate correctly and the surrounding surfaces at RT are somewhat close to the cooled sample holder, this approximation is good enough for our purposes.

Kirchhoff's first rule, the equations of the heat currents in the junctions T_b and T_s yield

$$3L_b(T_b - T_c) = \frac{3}{2}L_b(T_s - T_b) + L_d(T_r - T_b) \quad \text{and} \quad (2.10a)$$

$$\frac{3}{2}L_b(T_s - T_b) = (L_t + L_q)(T_r - T_s) + A_R \epsilon \sigma T_r^4. \quad (2.10b)$$

The indices of the temperatures T and the thermal conductances L refer to the cryostat (c), the braid (b), the sample (s), the decoupling piece (d), the quartz balls (q), the stainless steel tubes (t), and the surroundings (r).

For the final temperature estimation we assume the STM, the decoupling mass, the Cu cradle, and the surrounding chamber to be at RT, while the cryostat temperature T_c is assumed to be 4 K. The resulting sample temperature as a function of the length Δx_b [m], the cross-sectional area A_b [m²] and the thermal conductance κ_b [W/Km] of the Cu braid is hence given by¹¹

$$T_s = 0.3 \frac{6.0 \times 10^{19} \kappa_b^2 A_b^2 + 1.8 \times 10^{19} \kappa_b A_b \Delta x_b + 1.4 \times 10^{15} \Delta x_b^2}{4.5 \times 10^{18} \kappa_b^2 A_b^2 + 1.6 \times 10^{16} \kappa_b A_b \Delta x_b + 1.2 \times 10^{12} \Delta x_b^2}. \quad (2.11)$$

The information hidden in Eq. (2.11) is hard to grasp quantitatively from the given form. The parameter range of interest allows, however, to derive approximations which lead to results for every single parameter:¹²

$$T_s/\text{K} \approx 4 + 1.6 \Delta x_b \quad [\text{cm}], \quad (2.12a)$$

$$T_s/\text{K} \approx 4 + 60/A_b \quad [\text{mm}^2], \quad (2.12b)$$

$$T_s/\text{K} \approx 4 + 20000/\kappa_b \quad [\text{W/Km}]. \quad (2.12c)$$

From this we can now easily calculate that the length of the Cu braid has least influence on the sample temperature which changes only by 1.6 K/cm. The braid is as short as possible (8 cm) in order to connect the sample and the cryostat via the

¹¹From the serial arrangement of the Macor and the quartz balls in the decoupling piece (see Fig. 2.5B) we get $1/L_d = 1/L_q + 1/L_m$ with the Macor conductance L_m . We used the following parameters [161, 163]:

material	A [mm ²]	Δx [cm]	κ_{30} [W/Km]	κ_{100} [W/Km]
steel	3	1.5	15	40
quartz	5.3	0.1	0.1	0.5
Macor	10	0.1	0.1	0.1

The conductivity of the quartz balls could be confirmed experimentally from the power of the Zener diode used to keep the STM at RT, while the sample was at 30 K. Using once again Fourier's law we get $\dot{Q} = UI = \kappa A \Delta T / \Delta x$, and with $U = 75$ V and $I = 3.4$ mA we derive $\kappa = 0.19$ W/Km in good agreement with the listed values.

¹²For each equation two of the variables have been chosen from $\kappa_b = 1500$ W/Km, $A_b = 5$ mm², and $\Delta x_b = 8$ cm which are final braid parameters.

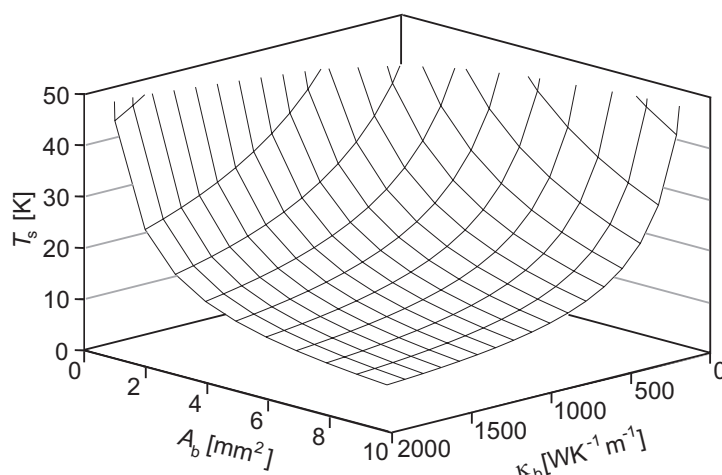


Figure 2.8: Minimum sample temperature T_s as a function of the braid cross-sectional area A_b and the thermal conductivity κ_b . The wire frame is drawn in spacing of 100 W/Km for κ_b and of 1 mm² for A_b .

decoupling piece. Using this value for Δx_b in Eq. (2.11), the sample temperature can be plotted as a function of κ_b and A_b .

This is shown in Fig. 2.8. We see that both the thermal conductance and the cross-sectional area influence the sample temperature significantly. From the graph we can deduce that with the values $A_b = 5 \text{ mm}^2$ and $\kappa_b = 1500 \text{ W/Km}$ a sample temperature of 17 K should be achievable.¹³ The purity of Cu must be better than 99.99% in order to yield κ_b up to 1500 W/Km at low T [162]; this is a direct consequence of defect scattering of electrons at low T [164].

From the calculation we chose our braid parameters as having a cross-sectional area of 5 mm² and a purity of 99.99%. A higher purity is unreasonable considering the much higher price in relation to the small gain in the final temperature according to our calculation. Similarly a larger cross-sectional area only has a small effect on the temperature, but leads to a stiffer connection between cryostat and sample holder, which causes an increase in the transmission of high frequency oscillations.

2.3.3 Performance

The cooling performance of the set-up described above is shown in Fig. 2.9 for liquid He and N₂ as coolants. All low temperatures have been measured with a chromel-alumel thermocouple referenced to a liquid nitrogen bath.

¹³This is in good agreement with our measured value of around 25 K. In the case of cooling with liquid nitrogen we calculate $T_s = 130 \text{ K}$ which is also reasonably close to the experimental result of 116 K (see Sec. 2.3.3).

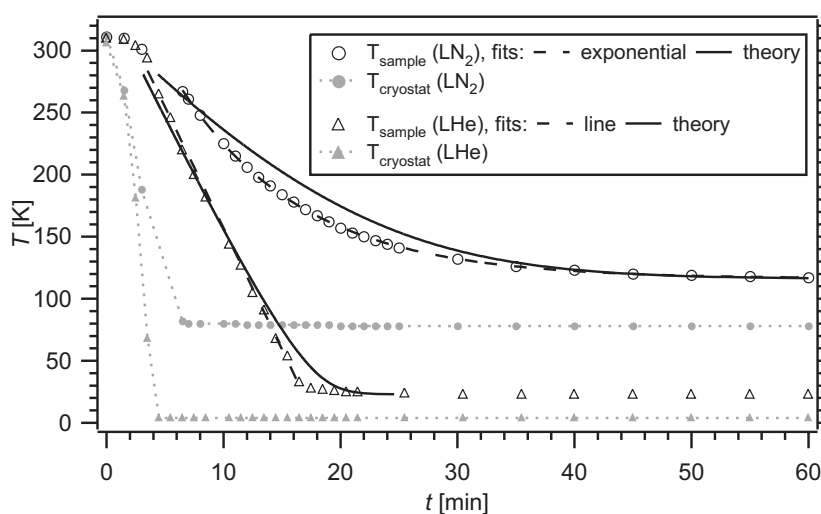


Figure 2.9: Cooling performance of the sample (STM mounted) with liquid nitrogen (black) and liquid helium (grey). The markers are experimental data points of the sample temperature (open) and the cryostat temperature (filled). The dashed lines are best fits and the solid lines are derived from a simple theory at the end of this section.

With liquid He the sample (mounted with the counter-heated STM) reaches a minimum temperature of 25 K within 20 min, in good agreement with the temperature estimate in Sec. 2.3.2.¹⁴ With liquid N₂ the sample reaches a minimum temperature of 116 K after 60 min, again in good agreement with our estimate. Looking at the plots in Fig. 2.9 it is obvious that the cooling behavior for the two liquids is not only quantitatively, but also qualitatively very different. For liquid He, the sample temperature drops *linearly* with a rate of of 20 K/min down to around 30 K and then equilibrates to 25 K within ca. 5 min. This is different for liquid N₂, where an *exponential* cooling rate is observed with a decay time of 10 min. We try to gain an understanding of this different behavior at the end of this section.

The imaging ability of the STM is quite excellent at all temperatures. This is shown with examples of an atomically resolved Cu(110) surface, imaged at different temperatures in Fig. 2.10. Atomic resolution is not only routinely achieved at the lowest temperature and at RT, but also at intermediate temperatures, where liquid nitrogen is used as a coolant. This is noteworthy, since liquid nitrogen boils very vigorously in the cryostat compared to helium. It demonstrates the efficiency of the decoupling piece in connection with the soft Cu braid. Notwithstanding, the noise spectrum of the tunneling current shows much larger vibrational ampli-

¹⁴The He consumption is estimated to be around 3 l/h, when maintaining the sample at 25 K.

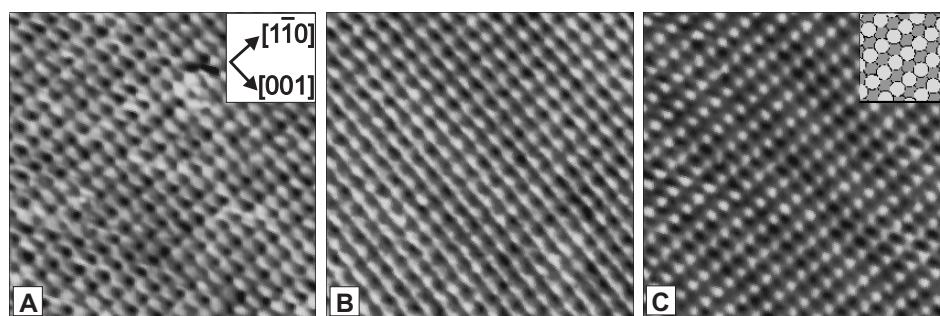


Figure 2.10: Constant-current STM image of Cu(110). (A) at 25 K ($V = 33.0$ mV, $I = 0.82$ nA, $50 \times 50 \text{ \AA}^2$). (B) at 116 K ($V = 2.4$ mV, $I = 0.98$ nA, $65 \times 65 \text{ \AA}^2$). (C) at room temperature ($V = 883.8$ mV, $I = 1.02$ nA, $65 \times 65 \text{ \AA}^2$). The Cu atoms are close packed along the $[1\bar{1}0]$ direction (the crystal directions are indicated) The insert shows a model of the Cu(110) surface with top layer (light grey) and the second layer atoms (dark grey).

tudes compared to the liquid helium set-up.

Even though the images in Fig. 2.10 are recorded at the lowest temperatures for the respective coolant, the set-up allows a truly variable-temperature performance, where all temperatures from 25–400 K can be accessed. This is done by radiative counter heating of the sample with the annealing filament which is regulated by a PID controller (Eurotherm) through a low-noise power supply (Good Will). In this way, the sample can be stabilized at any temperature up to at least 120 K (limited by the heating power of the filament), while maintaining the cryostat temperature constant at 4 K. With liquid N_2 as the coolant the temperature range up to RT can be bridged.¹⁵ This counter-heating ability has recently also been adapted to a low-temperature STM based on a bath cryostat [165].

With the heating filament it is also possible to reach temperatures above RT. Since the STM itself, however, can not be cooled, the temperature limit here is given by the Curie temperature (623 K) of the piezo elements used for the scanner tube and the inchworm coarse approach; temperatures above 400 K should hence be avoided. Also the close fittings in the inchworm cause malfunctioning at higher temperatures.

Due to the low thermal mass of the sample holder, temperature changes of the order of 100 K can be achieved within minutes by means of radiative heating. Within 5–10 min after a change of temperature, sufficient stability is reached to minimize thermal drift, especially in the z position of the tip. During temperature changes STM measurements are not feasible. It is generally crucial to keep the He

¹⁵Another way to adjust the sample temperature would be to reduce the coolant flow through the cryostat. It is, however, difficult and time consuming to stabilize the sample at temperatures higher than 25 K by simply trying to reduce the He flow, i.e. to reach a higher cryostat temperature. A flow control is moreover not possible with liquid N_2 which is simply poured through a funnel into the cryostat.

flow constant to avoid small temperature variations that would lead to thermal drift and distortions of the images; this is another consequence of the low thermal mass of the sample holder.

Another illustration of the capabilities of the STM is the imaging of standing waves in the electron density on Cu(110) surfaces at cryogenic temperatures [166]. The abilities of the instrument are further demonstrated in Chap. 4 in connection with imaging and manipulation of large molecules on a Cu(110) surface.

An estimation of the cooling behavior will be presented in the following, in order to gain a qualitative understanding of the different sample temperature decay for the liquid N₂ (exponential) and the liquid He coolant (linear).

The simple calculation of the sample temperature as a function of time is again based on Fourier's law [Eq. (2.8a)]. We consider only the one-dimensional case and assume the temperature gradient to be constant ($dT/dx \approx \Delta T/\Delta x$ with $\Delta T = T - T_f$; T_f is the final sample temperature). Using the thermodynamical relation $dQ = c_v dT$ with the specific heat c_v , we derive from Eq. (2.8a) after integration

$$\int_0^t -\frac{A}{\Delta x} dt = \int_{T_i}^T \frac{c_v}{\kappa(T - T_f)} dT. \quad (2.13)$$

Here T_i is the starting sample temperature and A is the cross-sectional area that is also approximated by a constant.

Integrating the right hand side of this equation is a formidable task due to the temperature dependence of the specific heat c_v (dominated by phonons) and the thermal conductivity κ (dominated by electrons in case of metals) of Cu [160, 164, 167]). In the simplest approximation both parameters can be assumed to be constant which then yields the well-known exponential temperature decay as a function of time. Even though this exponential functional behavior is observed in the case of liquid nitrogen cooling, it obviously does not apply to liquid helium cooling (see Fig. 2.9).

The temperature dependence of both c_v and κ is very complicated, since numerous different mechanisms are involved; in the case of κ a proper analytical description is even possible only for certain temperature intervals [164]. We are, however, not interested in reproducing our results quantitatively, but instead in trying to derive an analytical expression of the temperature dependence in order to gain a qualitative understanding. We therefore use the following approximations for c_v and κ .

The specific heat c_v is best described by the Debye theory which leads to an integral expression.¹⁶ The characteristic T^3 dependence for $T < \Theta_D/10$ (Θ_D is

¹⁶The correct expression from the Debye theory can be given in the form

$$c_v = 9nk \left(\frac{T}{\Theta_D} \right)^3 \int_0^{\frac{\Theta_D}{T}} \frac{x^4 e^x dx}{(e^x - 1)^2},$$

with $x = \hbar\omega/kT$, the electronic density n , the phonon frequency ω , Boltzmann's constant k , the Debye

the Debye temperature) does not have to be considered here, since we are using Cu ($\Theta_D \approx 315$ K [160]) for the thermal connection. For our estimation it is a good approximation simply to account for the decay with decreasing T in a linear fashion:

$$c_v = fT, \quad (2.14)$$

where f is a constant. We must, however, keep in mind that we hereby underestimate the decrease of c_v towards low temperatures.

From elementary kinetic theory the electronic thermal conductivity κ is given by $\kappa = \frac{1}{3}c_e v_e^2 \tau$ with the mean thermal electron velocity v_e (which can be considered temperature independent) and the electron relaxation time τ [164]. The electron specific heat follows $c_e \sim T$ [167]. For not too low temperatures the relaxation time is dominated by phonon-electron scattering processes which follow $\tau \sim T^{-n}$ at temperatures $T > \Theta_D/10$ [164]. n can be assumed to be unity for temperatures around Θ_D which is a good approximation even for T much lower than Θ_D .¹⁷ Hence, the thermal conductivity can be approximated as a constant g

$$\kappa = g. \quad (2.15)$$

By making these approximations we now underestimate the increase of κ with decreasing T at low temperatures.

These approximations enable us to solve Eq. (2.13) analytically and we derive

$$t = a \left[(T_i - T) + T_f \ln \frac{T_i - T_f}{T - T_f} \right], \quad (2.16)$$

where $a = f\Delta x/gA$ collects the temperature-independent parameters.

It can be seen that the time dependence of the temperature consists of two terms. The right term describes an exponential temperature decay as would be the case for $c_v/\kappa = \text{const}$ in Eq. (2.13). The left term results in a linear temperature decay due to the temperature dependence of c_v/κ as explained above. For $T \sim T_i$ the right term is negligible and the temperature decay is simply linear in the beginning. The right term plays an increasingly important role when T reaches T_f , and the smaller $T_i - T_f$. In other words: The lower the T_f (for a given T_i), the longer the linear decay dominates. This is exactly what is observed in our case: Cooling with liquid helium results in a linear decay, while liquid nitrogen as a coolant leads to a simple exponential decay.

temperature Θ_D and Planck's constant h [167].

¹⁷In a qualitative picture, a given electron is more likely to be scattered the more phonons are present to scatter, i.e. the phonon relaxation time τ decreases with increasing temperature. At higher T the total number of phonons present in the crystal is proportional to T and hence $\tau \sim T^{-1}$. Well below the Debye temperature, however, the number of phonons that can scatter an electron declines as T^2 . Moreover, the scattering rate is proportional to the square of the electron-phonon coupling constant which declines linearly with T well below Θ_D . Hence, $\tau \sim T^{-3}$ for very low temperatures, which are, however, not relevant in our case [167].

Based on this very simple theory, we can fit our experimental results in Fig. 2.9 with Eq. (2.16) using parameters a , T_i , and T_f .¹⁸ The results are included in Fig. 2.9 and if we consider the simplicity of our approach, the agreement is quite remarkable. A linear decay is reproduced in the case of liquid helium cooling, while the liquid nitrogen fit resembles an exponential decay.¹⁹ Moreover, the flattening of the liquid helium decay curve shortly before reaching the minimum temperature, as is observed experimentally in Fig. 2.9, is reproduced and demonstrates the importance of the second term in Eq. (2.16) towards low temperatures.

In conclusion, the different behaviors of the temperature decay was demonstrated to be due to the temperature dependence of the parameter c_v/κ which decreases towards lower temperatures. Our main approximation was an underestimation of the temperature decrease (increase) for c_v (κ) at low temperatures which therefore yields a lower bound to the decrease of the joint parameter c_v/κ , appearing in Eq. (2.13), with decreasing temperature. Taking this into account would yield higher order terms $(T - T_f)^n$ with $n > 1$, and as a result the temperature would decay faster and expectedly yield a better fit to our data.

2.4 Molecular evaporator

2.4.1 General design

The UHV chambers used are originally not designed for depositing molecules and hence lack a preparation chamber as is generally used to avoid molecule contamination of the main chamber. We constructed a molecule evaporator for depositing well-controlled amounts of a volatile molecule powder that is positioned inside a separately pumped facility and can be valved off from the main chamber by means of a manually actuated gate valve (Fig. 2.11A). In this position the contamination of the main chamber due to volatile molecules is avoided and the molecule

¹⁸ T_f should in fact be the coolant temperature. We use this approximation in order to neglect complications due to the external heat sources connected to the sample like the sample holder fixation or radiation from the surroundings which were included for estimating the minimum sample temperature in Sec. 2.3.2.

It is necessary to treat T_i as a fitting parameter, since it takes a certain time for the cryostat to cool down to 4/77 K, determining then the temperature gradient, i.e. the experimental initial temperature can not be used.

¹⁹The best exponential fit of the experimental data for liquid nitrogen yields

$$T/\text{K} = 116 + 283e^{-t/10 \text{ s}},$$

while the theory fit yields the parameters $a = 0.069 \text{ s}$ and $T_i = 320 \text{ K}$ which gives a time constant of 8 s for the exponential term in good agreement to 10 s from the purely exponential experimental fit.

The best linear fit of the experimental data for liquid helium yields

$$T/\text{K} = 352 - 20t/\text{s},$$

while the theory fit yields the parameters $a = 0.49 \text{ s}$ and $T_i = 340 \text{ K}$ which gives a linear decay rate of 20 K/s for the linear term, reproducing the purely linear experimental fit.

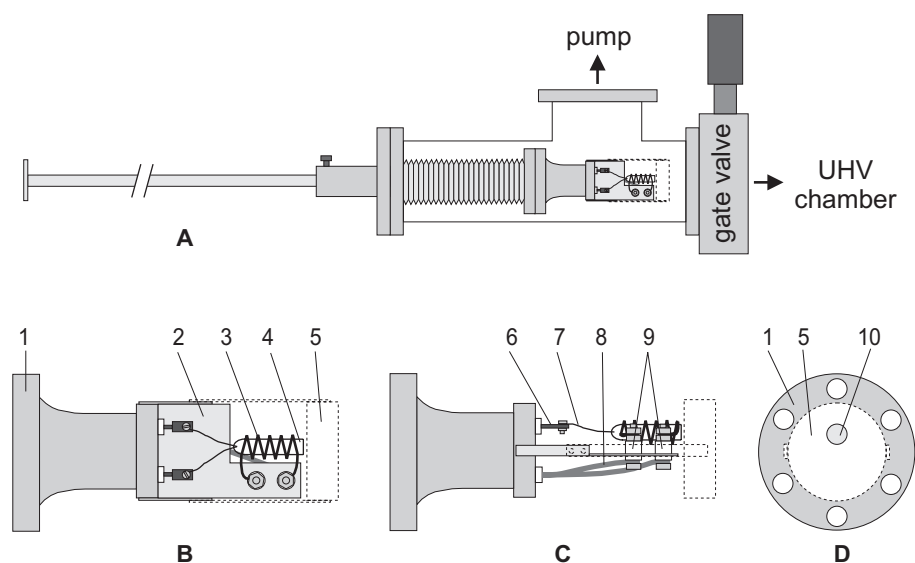


Figure 2.11: (A) Molecular evaporator construction showing the evaporator head at the end of the linear drive which is mounted inside a T-tube on a gate valve on the chamber. Front part of the evaporator head in (B) top view, (C) side view, and (D) front view. Legend: (1) flange (DN 16 CF); (2) stainless steel sheet; (3) Tantalum wire (\varnothing 0.25 mm); (4) glass crucible; (5) removable shield with orifice; (6) thermocouple feedthrough; (7) thermocouple wires; (8) power lead feedthroughs (Cu); (9) ceramic tubes; (10) shield orifice.

powder can furthermore be degassed prior to use.²⁰

The evaporator can be mounted after baking the main chamber and baked separately. This is useful when changing or refilling the evaporator (or dealing with a powder that can not withstand the bake-out temperature of 150 °C for the chamber) as it does not require breaking the vacuum in the main chamber. In order to deposit molecules on the sample, the evaporator with the molecules heated to the desired temperature is moved close to the front of the sample by means of a long linear drive (travels up to 50 cm in steps of 5 cm). The residence time of the evaporator inside the main chamber is thereby reduced to a minimum, i.e. the actual evaporation time.

The head part of the actual evaporator is drawn in Figs. 2.11B–D and the numbers in this section refer to that figure. It consists of a mini-flange feedthrough (1) (for a chromel–alumel thermocouple (6) and two power leads (8)) used in a reversed way, i.e. the usual UHV side is now at atmospheric pressure and vice versa. This was not found to cause any problems concerning the quality of the vacuum.

²⁰The studies of molecules on surfaces in vacuum, deposited by organic molecular beam deposition (OMBD) [59], have the advantage of providing both layer thickness control and an atomically clean environment and substrate compared to conventional Langmuir-Blodgett film deposition [168].

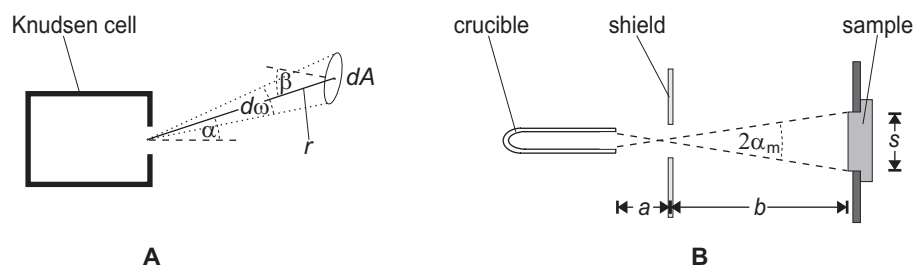


Figure 2.12: (A) Schematic drawing of a Knudsen cell defining the emission and deposition angles α and β , respectively, the solid angle $d\omega$, the surface unit area dA , and the distance r of the surface from the Knudsen cell. (B) Schematic drawing of the molecule flux out of the crucible in our set-up, defining the sample diameter s , the crucible-orifice and orifice-sample distances a and b , respectively, and the maximum angle α_m under which the molecules hit the sample.

A thin stainless steel sheet (2) is welded along the center of the feedthrough axis as a support for a small glass crucible (4), in which the molecule powder is stored. The tube is held in place by a Ta-wire filament (3) that is wound around the crucible and used for resistive heating via the power lead feedthroughs. The temperature can be monitored via a thermocouple wire connection (7) melted into one end of the glass crucible. In addition, the steel sheet supports a removable shield (5) with a 4 mm wide orifice (10) for collimating the molecule beam during the deposition process. This prevents the surroundings of the sample and the rest of the chamber from being contaminated with molecules.

The glass crucible, which holds the powder, can be heated up to at least 500 K within minutes. The evaporator can therefore be utilized for a great variety of molecules. However, not all molecules can be deposited on the surface by this method, since they might fragment before reaching a sufficient vapor pressure.

Care has to be taken in order to clean the molecule powder from impurities. In the beginning, the heating of the powder is usually accompanied by a pressure rise of around one to two orders of magnitude which can be reduced by thorough outgassing of the powder for several hours.

2.4.2 Uniformity of the deposited layer

The flux of molecules out of the crucible is collimated by a shield with an orifice/aperture as sketched in Fig. 2.12B. This shield protects the remote surroundings of the sample from unnecessary contamination with molecules. The question arises, if the flux of molecules hitting the sample is homogeneous over the entire sample area, since the intensity of the flux out of a crucible depends on the emission angle α with respect to the crucible axis.

To a good approximation, the effusion of molecules out of the crucible can be compared to a Knudsen cell. Based on Knudsen's so-called *cosine law* [169, 170],

the angular distribution of the number of molecules deposited per unit area can be calculated to be given by

$$\hat{N} = \hat{N}_0 \cos^4 \alpha \quad (2.17)$$

with the maximum number per unit area \hat{N}_0 at $\alpha = 0^\circ$ [171].²¹

The maximum angle α_m under which the molecules hit the surface depends on the sample diameter s and the crucible-sample distance ($l = a + b$) as specified in Fig. 2.12B. An upper bound can be given as $\alpha_m = \arctan(s/l) \approx 10^\circ$, using typical parameters $s = 5$ mm, $a = 5$ mm and $b = 25$ mm. Hence, $\hat{N}/\hat{N}_0 = 95\%$ and the uniformity of the deposited molecules across the surface is quite good.

Certainly the coverage is homogeneous in the small area sampled by the STM. However, the sample is removed from the STM between experiments and the tip hits different spots on the sample, varying from experiment to experiment. In order to be able to work at reproducible coverages, it should be homogeneous also over the whole sample.

²¹The number N of evaporated molecules in the solid angle $d\omega$ is given by the cosine law

$$dN = N \cos \alpha \frac{d\omega}{\pi},$$

where N is the total number of the evaporated molecules and α the emission angle (see Fig. 2.12A). The area dA of the surface (at a distance r from the effusion source) upon which the molecules are condensed under the deposition angle β is $dA = (r^2 / \cos \beta) d\omega$, and the number of deposited molecules per unit area \hat{N} is thus

$$\hat{N} = \frac{dN}{dA} = \frac{N}{\pi r^2} \cos \alpha \cos \beta.$$

For a plane surface oriented perpendicular to the effusion-cell axis at a distance l , $\alpha = \beta$ and $r = l / \cos \alpha$ which leads to Eq. (2.17) with $\hat{N}_0 = N / \pi l^2$.

CHAPTER 3

Bonding of molecules to surfaces

In this chapter theoretical concepts describing the bonding of adsorbates to surfaces are described. This provides a theoretical basis for understanding the experimental results in this thesis.

3.1 Introduction

The interaction of adsorbates with metal surfaces is an important issue in many research topics. The understanding of the mechanism determining an adsorbate-metal interaction to be “weak” or “strong” and the respective influences of the adsorbate and the metal is a prerequisite for understanding complex processes such as diffusion, self-assembly or even catalytic reactions.

It is instructive to compare the bonding of molecules to surfaces and to single metal atoms which is the equivalent to surface adsorption in chemical complexes. We will do that in the following by concentrating on adsorbates with a π -system, not only because this is a common structure of the molecules investigated in this thesis, but because this often gives rise to the leading interaction.

Historically, the first alkene complex was Zeise’s salt, $\text{K}[\text{PtCl}_3(\eta_2\text{-C}_2\text{H}_4)]\text{H}_2\text{O}$,¹ synthesized by the Danish pharmacist Zeise in 1827 [172, 173]. The first aromatic complex was the famous ferrocene complex, $\text{Fe}(\eta_5\text{-C}_5\text{H}_5)_2$, which was synthesized in 1951 [174, 175].² The correct sandwich structure with the Fe ion being intercalated between the two cyclopentadienyl-ligands (C_5H_5^-) was, however, first correctly predicted independently by Wilkinson/Woodward [176] and Fischer [177].³ Similar complexes are known for benzene; an example is $\text{Cr}(\eta_6\text{-C}_6\text{H}_6)_2$ which is isoelectronic to ferrocene [177].

A sound understanding of the bonding in these complexes was not available before the work of Dewar in the beginning of the fifties [178], a work which was elaborated by Chatt and Duncanson [179]. The model is described in Sec. 3.2 and may be considered as a chemist’s view of chemical bonding since it concentrates on the aspect of molecular orbital interaction with respect to the orbital symmetry.

By going from the bonding in complexes to the bonding on surfaces in Sec. 3.3, more quantitative concepts are presented that focus much on the relative position of energy levels with respect to the Fermi level of the surface. This concept hence resembles a physicist’s approach to bonding mechanisms based on solid state theories. We try to provide a basic understanding of the adsorbate bonding by outlining general trends rather than an accurate description. The great similarity of the bonding concepts for single complexes and those for extended surfaces and solids was excellently pointed out in a book by Hoffmann [180].⁴

The concepts presented are not restricted to interactions with π -systems, but are generally applicable to all kinds of bonding situations. Very weak interactions (e.g. in the bonding of aliphatic groups) are, however, not covered completely by

¹The prefix η_i denotes that i centers of a ligand are equally connected to the metal center. In the case of ethylene these are the two carbon atoms: the C-C bond is located perpendicular to the quadratic-planar coordination sphere around the Pt center.

²The name ferrocene has been proposed in analogy with benzene, as the cyclopentadiene rings would undergo classical aromatic reactions. The name metallocenes was given to the class of similar sandwich molecules.

³Their work on elucidating the structures and opening the area of metallocene chemistry was honored with the Nobel Prize in Chemistry for Wilkinson and Fischer in 1973.

⁴A comparison focusing on C-H and H-H bond activation by transition metals can be found in [181].

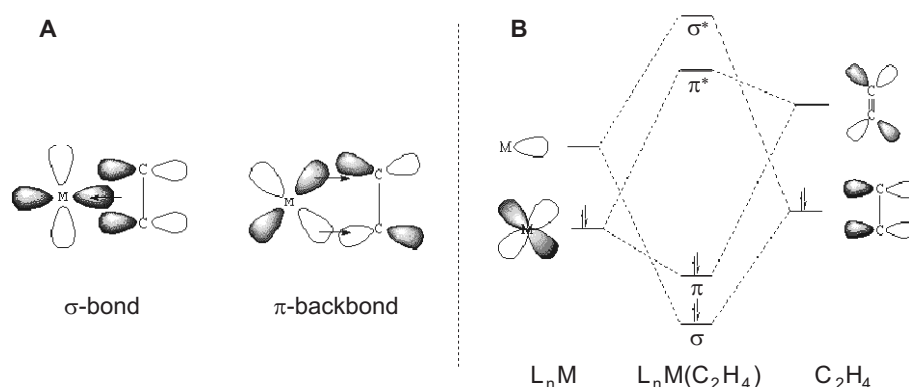


Figure 3.1: Qualitative drawing of the bonding situation according to the Dewar-Chat-Duncanson model for a complex formed by ethylene (C₂H₄) and a metal atom (M). The shading of the orbital lobes refer to their relative sign. (A) Interacting orbitals forming a σ and a π bond. (B) Molecular orbital energy diagram. The left- and right-hand sides are the levels of the metal atom M (binding n other ligands L) and the ethylene ligand (C₂H₄), while the center region represent the complex L_nM(C₂H₄).

these concepts. The reason is that the weak van-der-Waals forces become more important. These are therefore briefly outlined in Sec. 3.4.

3.2 A chemist's view

The Dewar-Chat-Duncanson model provides a solid framework for a qualitative understanding of organometallic π -complex chemistry, i.e. alkenes and aromatic compounds coordinated as ligands to a metal center [178, 179, 182].⁵

The model by Dewar-Chat-Duncanson proposes a bonding of the (alkene) ligand to the transition metal by a σ and a π bond. This is illustrated in Fig. 3.1. The σ bond is formed by overlap of a filled π orbital of the olefin with an empty (hybrid) orbital of the metal, while the π bond forms by overlap of an empty (antibonding) π^* orbital of the olefin with a filled (hybrid) orbital of the metal.⁶ This yields a donor-acceptor synergistic bonding situation: the greater the sigma donation to the metal, the greater the π backbonding in order to compensate for the excess of electron density at the metal center.

The greater the electron density back-donated into the π^* orbital on the alkene, the greater the reduction in the C=C bond order. An alternative way of stating this would be to say that the hybridization of the alkene carbon changes from

⁵Basic theoretical concepts of organometallic chemistry are reviewed in [183].

⁶Do not get confused by the fact that a π orbital forms a σ bond. The orbital prefix refers to the molecule (ligand) symmetry, while the bond prefix refers to the symmetry of the whole metal-ligand complex (see Fig. 3.1A).

sp^2 to sp^3 as back-donation increases. Either formalism describes two limiting structures: a planar alkene adduct and a metallocyclopropane ring explain the geometrical changes that are confirmed by X-ray crystallographic studies: as the C-C bond length increases, the CH_2 plane is distorted from the ideal planar geometry of an alkene.

In the light of this backbonding concept, distortions of the aromatic molecule from the planar gas-phase structure upon adsorption on a metal surface can be explained. The metal surface donates electrons back into benzene π^* orbitals as in a complex, leading to a distortion. For recent experimental studies of benzene on metal surfaces see Refs. [53, 54].

Besides a bonding through π orbitals, ligands can be expected to bind through their σ orbitals. The first complex of such type was unambiguously revealed for the bonding of H_2 in $W(CO)_3(P^iPr_3)_2(\eta_2-H_2)$ in 1983 by Kubas [184, 185], nearly 150 years after the first alkene complex representing a π coordination. This dihydrogen complex is the archetype of a σ complex: the σ -bonding electron pair of H_2 binds the ligand to the metal, and back-donation from the metal goes into the empty σ^* orbital of the H_2 bond, as predicted by the Dewar-Chatt-Duncanson model. The back-donation controls the activation of the H_2 bond towards cleavage, then forming a dihydride complex [186]; in the mentioned complex the H-H bond distance is stretched about 20% over its value in free H_2 .

By now a variety of σ bonds that interact with metal centers are found, and in principle any X-Y bond can coordinate to a metal center, provided steric and electronic effects are favorable. Steric hindrance may arise from substituents at X or Y blocking the metal's access. Back-donation is always a critical point in stabilizing the bond and is, e.g. very weak for alkanes, primarily because of energy mismatch between the metal d and the C-H σ^* orbitals [181].

The Blyholder model was developed specifically for the adsorption of CO on metal surfaces [187]. Even though the concept is not directly concerned with alkene adsorption, we will see that it is a simple qualitative extension of the Dewar-Chatt-Duncanson model to adsorption at surfaces which bears much of the idea of back-bonding, as was just discussed for alkene complexes.

Blyholder considered the bonding of CO to a surface as the formation of a complex with a metal atom at the surface as the central atom and the surrounding metal atoms and the CO as the ligands [187]. In analogy with the Dewar-Chatt-Duncanson model, the lone pair (5σ orbital) at the carbon atom of CO forms a coordinate bond with suitable metal d-orbitals to produce a σ bond. This puts a large formal negative charge on the metal atom and again a back-donation from a metal d -orbital to the antibonding $2\pi^*$ molecular orbital on the CO ligand is proposed.

This weakening of the ligand C-O bond can be observed experimentally by infrared spectroscopy, since it influences the CO stretching frequency. The Blyholder model could then nicely explain the shift towards lower wavenumbers in the CO mode with increased back-donation.

The strength of back-donation depends on the extent of competition from the

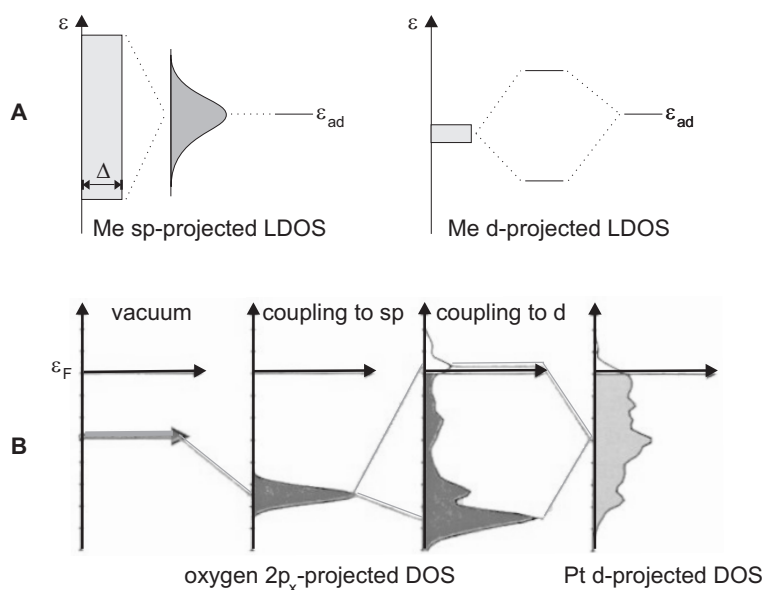


Figure 3.2: (A) Local density of states at an adsorbate in the Newns-Anderson model. Coupling of adsorbate states with a broad sp band (with energy independent LDOS of width Δ) leads to a single resonance around ϵ_{ad} , while a narrow d-band can be regarded as the simple two-level problem. (B) Change of the local electronic structure at an oxygen atom upon adsorption on Pt. The vacuum state of O interacts with the Pt sp band (not shown) into a broad, down-shifted resonance. This resonance interacts with the d-band and forms covalent bonding and anti-bonding states below and above the initial states roughly in accordance with the Newns-Anderson model. The figure is adapted from [132].

surrounding metal atoms for suitable electrons. The number of surrounding metal atoms varies for different local surroundings at different crystal faces, edge sites or kink sites, and hence the competition for electrons will vary (higher degree of back-donation for lower coordinated sites). The bonding strength moreover depends on the filling of the metal d-bands: the higher the filling degree (towards the right in the periodic system of elements), the stronger the back-donation.

3.3 A physicist's view

The Newns-Anderson model and theories based upon it explain the bonding situation in a more quantitative way [131–134]. As opposed to the case of molecular complexes discussed above, adsorbate states interact not just with a single metal state, but rather with a continuum of states in the (conduction) band. This leads to two limiting cases as explained in Fig. 3.2A.

If the metal band is broad (sp-band) with a local projection of the metal density

of states on the adsorbate state approximately constant, a resonance then forms centered at the initial adsorbate state. This can be viewed as a consequence of the finite lifetime of an electron in the adsorbate state. For a narrow band (d-band), on the other hand, one encounters a situation similar to a simple two-level interaction so sharp bonding and antibonding states are formed above and below the initial states; accordingly the splitting of the levels depends on the orbital overlap and the relative energy of the states. The two idealized cases of sp- and d-band interaction represent weak and strong chemisorption, respectively [130].

This model is applied in Fig. 3.2B for the real situation of oxygen adsorption on a Pt surface. The calculation is performed in two steps to show the influences of the two band types: Interaction with the sp-band leads to a resonance. This then interacts with the d-band which gives rise to a splitting into bonding and anti-bonding states.

The d-band model explains the adsorbate bonding strength from the position of the d-band center ε_d with respect to the Fermi level [131, 132]. The focussing on the d-bands is in accord with results from the Newns-Anderson model, since the interaction of adsorbate states with metal sp-bands is very similar for different transition metals.

Different transition metals possess different degrees of filling of the d-band and hence have varying positions of the d-band center, as illustrated in Fig. 3.3A. By going from Ag to Pd and Ru (i.e. towards the left in the periodic table of elements), the d-band center moves up in energy. The interaction with an adsorbate (here oxygen atoms) then produces more and more empty antibonding states above the Fermi level as the d-band center shifts up which leads to a stronger bonding [132].

This result can be derived from second-order perturbation theory for two interacting states i and j with energies ε_i and ε_j coupled by the matrix element V_{ij} . The hybridization energy E_{hyb} per electron is then given by

$$E_{\text{hyb}} \simeq \frac{V_{ij}^2}{\varepsilon_i - \varepsilon_j}. \quad (3.1)$$

For a constant coupling strength of the adsorbate to the metal states, the amount of antibonding states above the Fermi level hence crucially depends on the position of the d-band center. It is noteworthy that not only the relative energies of the metal and adsorbate states are important, but also their coupling which scales with the orbital overlap [131]. By going from the two-level problem to the interaction with bands, the general form stays valid with an additional factor taking the fractional filling f of the d-band into account [131].⁷

⁷For adsorbate states below the Fermi level, the factor is $(1 - f)$, while for adsorbate states above the Fermi level it is f . Roughly speaking, this takes into account that filled adsorbate states interact with empty metal states and vice versa. Accordingly, for completely filled bands basically only the backbonding to empty adsorbate states (above ε_F) can make a bonding contribution, while for empty bands only bonding from the filled adsorbate states (below ε_F) contributes [188].

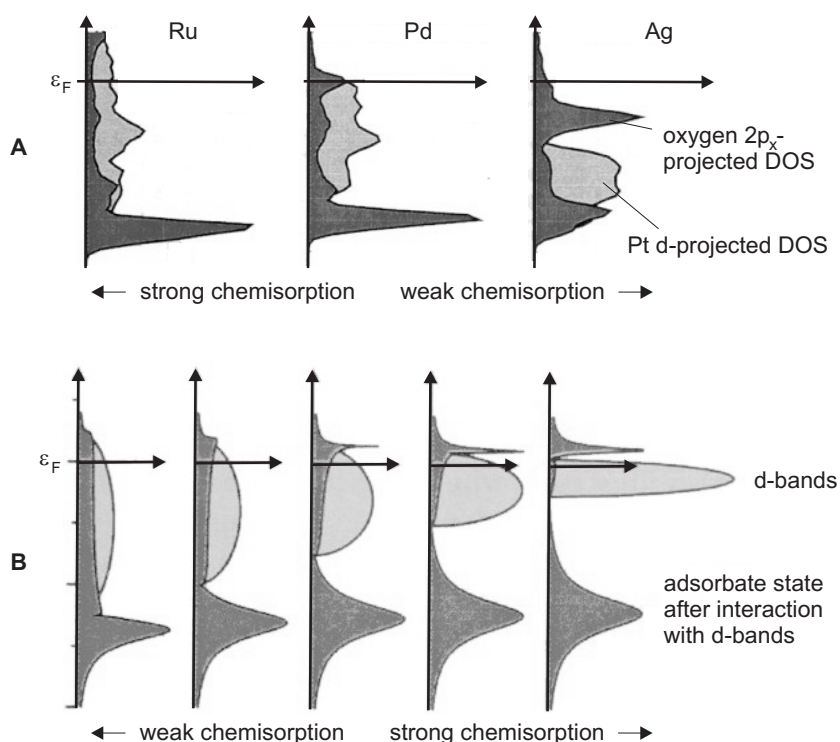


Figure 3.3: Dependence of the adsorbate states on the center of the d-band. **(A)** LDOS projected onto the oxygen $2\pi_x$ state (shaded dark) for different 4d transition metals. The light shaded area gives the metal d-band before oxygen adsorption, showing clearly how the d-band center moves up towards the left. Hence, more antibonding states move above the Fermi level ϵ_F and the bonding becomes stronger. **(B)** Variation of the d-band center with the band width. To maintain a constant filling, the d-band center shifts upwards as the band width decreases. Again, more antibonding states move above ϵ_F , increasing the bond strength. The figures are adapted from [132].

If we instead of atomic adsorbates (like O on Pt in Fig. 3.2B) want to treat more complex molecules like CO, ethylene or eventually large molecules, only little changes in the general picture: several adsorbate states are important for the bonding. For, e.g. CO adsorption, the occupied 5σ orbital (below ϵ_F) and the empty $2\pi^*$ orbital (above ϵ_F) will dominate the bond formation. Similar to the result in Fig. 3.2B, the interaction of both states with the metal d-band gives rise to bonding and antibonding states below and above the Fermi level, respectively [132]. This resembles the qualitative picture of bonding and backbonding as discussed in the Blyholder model. It is shown that the (back)bonding through the $2\pi^*$ orbitals dominates the bonding, since the interaction with the metal produces new, filled bonding states below the Fermi level.

Apart from being applicable to different adsorbates, the d-band model can account for different metal-substrate configurations. The often preferred bonding of adsorbates to lower-coordinated adsorption sites (step or kink environments) can be explained in the same way in that the position of the d-band center varies with the metal coordination number. The smaller the metal coordination number, the narrower the d-band; in order to maintain its filling, the d-band center moves up in energy (for more than half-filled d-bands) as explained in Fig. 3.3B, leading to a stronger bonding as predicted by Eq. (3.1).⁸ The same argument applies for bonding to surfaces with different (low) Miller indices. The more open the surface, the lower the coordination number and the stronger the bonding of adsorbates.

With the basic concepts at hand, the preferred binding of aromatic π systems with the aromatic plane parallel to the surface can be explained. Generally, the HOMO and the LUMO orbital of the molecules are π and π^* orbitals, respectively, which are hence closest to the Fermi energy and also to the d-band center of the metal to which they are adsorbed. According to Eq. (3.1), this causes HOMO/LUMO hybridization energies to dominate over other states which are further away from the Fermi level. These HOMO and LUMO states would, however, not be accessible in a perpendicular bonding configuration of the aromatic system to the surface which would yield a reduced interaction compared to the π -system interaction.

An experimental STM study comparing the aromatic heterocyclic molecules thiophene (C_4H_4S) and pyrrole (C_4H_4NH) to their saturated analogues, tetrahydrothiophene (C_4H_8S) and pyrrolidine (C_4H_8NH), revealed that only the aromatic forms adsorb parallel to the surface, while the saturated forms bind with the heteroatom (S/N) to the surface, the residual ring pointing away from the surface [190]. This demonstrates that the π interaction even dominates over the electrostatic interaction via the heteroatom. In molecules with several structural elements, it is hence a good first approximation that the π system, if available, is bound parallel to the surface.

Even though the weak bonding of aliphatic groups — through σ and σ^* states of the C-H bonds [181] — can be described with the outlined concept, the dominating interaction may result from so-called van-der-Waals forces which are described in the following.

3.4 van-der-Waals bonding

van-der-Waals bonding is usually applied to describe weak bonding situations (physisorption) as a result of attractive long-range interactions. The forces are named after the Dutch physicist van der Waals, who in 1873 first postulated these intermolecular forces when developing a theory to account for the properties of real gases.

⁸In the same line of reasoning, a band upward shift in connection with a band narrowing has been demonstrated by going from the bulk (high coordination) to the surface (low coordination) [189].

This kind of bonding is abundant and common in gases and organic liquids/solids. It not only describes the forces responsible for the condensation of noble gases and other closed shell particles (CH_4 , H_2), but also their bonding to surfaces. In the same way it is the main effect behind the physisorption of aliphatic molecules on surfaces.

There are three different sources of forces between molecules and surfaces summarized under the name van-der-Waals force [191].

1. Parallel dipoles attract, since they have a tendency to align with each other. Since electrons “spill out” into the vacuum region, the center of negative charge of the electrons and the center of positive charge of the atomic nuclei do not coincide at surfaces [192]. An electrostatic dipole layer is thereby created that may interact with a polar molecule.
2. Polar molecules temporarily induce image dipoles in the surface charge distribution (equivalently, the surface dipole moment temporarily distorts the charge distribution in molecules) which causes an attractive interaction for aligned dipoles or components thereof.
3. Even for molecules without a permanent dipole moment, the center of negative charge of the electrons and the center of positive charge of the atomic nuclei are not likely to coincide. The fluctuation of electrons thus makes molecules time-varying dipoles, even though the average of this instantaneous polarization over a brief time interval may be zero. Such time-varying dipoles induce image dipoles in the substrate, resulting in attractive forces. These forces, arising from electron fluctuations in molecules (known as London forces) are present also for molecules with permanent dipole moment.⁹

The attractive van-der-Waals energy for an adsorbate on a surface depends on the adsorbate-surface distance R as $E_{\text{att}} = -c_1 R^{-3}$ [192]. Qualitatively, c_1 has the form of a product of dipole moments — one for the adsorbate, scaling with the polarizability, and one for the image dipole, scaling with the adsorbate dipole moment.¹⁰

At very close distances, however, short-range repulsive interactions become important which can be viewed as caused by filled orbital interactions [192]. They are characterized by $E_{\text{rep}} \sim n(R) = c_2 \exp(-c_3 R)$, where $n(R)$ is the charge density of the surface that decays exponentially into the vacuum, and c_2 and c_3 are constants. The overall expression of the van-der-Waals interaction energy E_{vdW} is hence given by¹¹

$$E_{\text{vdW}} = E_{\text{rep}} + E_{\text{att}} = c_2 e^{-c_3 R} - \frac{c_1}{R^3}. \quad (3.2)$$

⁹At least in the case of intermolecular interactions this is, generally, the largest of the three contributions [191].

¹⁰For interactions between molecules, on the other hand, the situation is somehow different. The field E of a dipole which induces a dipole moment in an adjacent molecule, decays as R^{-3} (R being the molecule-molecule distance here). Hence, the overall interaction energy decays like $E_{\text{att}} \sim -R^{-6}$ [191].

¹¹For the van-der-Waals interaction between molecules the famous Lennard-Jones potential $E_{\text{vdW}} = c_2 R^{-12} - c_1 R^{-6}$ is sometimes used with the power law to describe the repulsive interaction instead of the exponential dependence.

The physisorption potential invariably has a shallow minimum a few Ångström from the surface. Compared to the strong chemisorption energy of typically 1–5 eV, the van-der-Waals energy for noble gases and small gaseous molecules is in the range 0.01–0.1 eV, depending mainly on the polarizability of the adsorbate [193]. For large molecules, which have a large contact area to the surface, the single van-der-Waals contributions add and may lead to a very strong overall bonding.

CHAPTER 4

HtBDC on Cu(110)

In this chapter the interaction of large organic molecules (HtBDC) with a Cu(110) surface is reported. These findings have been published in the papers [II] and [III]. By combining the imaging and manipulation capabilities of the STM, details of the molecule adsorption are unravelled. The molecules induce a restructuring of the metal surface underneath them, which anchors the molecules on the substrate and is the driving force for a self-assembly process of the molecules into characteristic molecular double rows. Effective medium theory calculations are presented with the attempt to explain different aspects of the structure. An important and unexpected detail is the chirality of the restructuring which extends over the entire flat terraces of a single crystal surface at higher coverages. Large enantiomorphic domains can be formed, thereby creating a perfectly ordered chiral metal surface.

4.1 Introduction

Organic molecules on surfaces studied with the STM have been an object of investigation quite soon after the invention of the STM, and important insight into the bonding and ordering of such molecules to metal and semiconductor surfaces could be gained [61–64]. The self-assembly of molecules on surfaces plays a vital role in many fields, e.g. the rapidly growing area of nanotechnology, especially within areas such as molecular electronics, nanodevice fabrication and molecular recognition [35–40].

Self-assembled monolayers are the result of a subtle balance between the competing intermolecular and molecule-substrate interactions. It is therefore necessary to understand how this balance affects the molecules' nucleation and growth in order to control these processes in a desired way. Often, non-covalent molecule-molecule interactions dominate the supramolecular aggregation over the molecule-substrate interactions [77, 78, 81, 82]. The evolving adsorbate layers range from complicated patterns, if directional bonds are present (hydrogen bonds [77, 78] or electrostatic interactions [79, 80]), to simple close packed layers [82, 83]. The metal surface is often considered a static checkerboard that provides bonds and specific adsorption sites to the molecules.

When the adsorbed molecules become large and complex, however, the complexity of the interaction between the substrate and the molecules may increase. In a few cases it has been indicated, mainly from measured height corrugations of the adsorbed molecules, that a restructuring of the substrate may exist underneath the molecular adsorbate layer of polar (thiols, amino acids, etc. [71, 194–197]) and non-polar molecules (C_{60} , etc. [74, 93, 198–203]). Nevertheless, often no firm conclusions could be reached and in some cases conflicting evidence has been published [72, 73, 204].

The STM opens up the possibility of investigating restructuring processes directly underneath the molecular adsorption layer, since it allows not only the imaging of the matter at the atomic scale, but also the interaction with it in a controlled manner [26–28, 30]. This is demonstrated in this chapter where we investigate the adsorption of the aromatic HtBDC molecules on a Cu(110) surface (Sec. 4.2).¹

We show directly that the adsorption of large molecules can be associated with a restructuring of the surface layer underneath (Sec. 4.3). These results prove that molecule-surface interactions can be a controlling driving force for the self-assembly of molecules on surfaces. Identifying the exact nature of such a restructuring would have been difficult using an *averaging* surface sensitive probe such as standard scattering techniques. Furthermore, aspects connected with the chirality of the restructured holes underneath the molecules, will be discussed in Sec. 4.4.

The HtBDC molecule is interesting to study for several reasons. It is relatively rigid and stable and may hence be seen as a model system for large molecules

¹The related decacyclene (DC) molecule, which comprises only the aromatic core of HtBDC (see Fig. 4.1), is treated in Chap. 5.

in general. Moreover, it possesses the basic structural features required for future molecular building blocks for nanoelectronic devices: a conducting backbone (aromatic π system) and spacer groups (*tert*-butyl groups), separating the conducting parts of the molecule from the substrate [17].

From a technological point of view, molecules with extended aromatic units have the property to adsorb light in the visible range. This not only gives them intense and beautiful colors [95], but also makes them interesting candidates as dyes in emissive devices. This was, e.g. demonstrated for decacyclene (DC) as dopant in an electroluminescent device with high luminance and a long lifetime [43] and a LED based on Langmuir-Blodgett films [205]. Other practical applications of optoelectronic devices as photodiodes require the use of inexpensive organic thin-films [44, 60]. Again, the understanding of the growth and crystallization is strongly desired to tailor such process in a desired way.

4.2 HtBDC molecule

The investigated molecule 2,5,8,11,14,17-hexa-(*tert*-butyl)decacyclene (HtBDC, $C_{60}H_{66}$, $M = 787.2$ a.u.) is illustrated in Fig. 4.1A.² The molecule consists of a center aromatic ring system (decacyclene [207]) of condensed five-membered and six-membered rings arranged in a threefold rotational symmetry; six *tert*-butyl groups surround the molecules and are attached to the naphthalene subunits [208]. It is noteworthy that the aromatic DC core can be viewed as a precursor to the C_{60} fullerene molecules. By establishing a C-C bond between the (3,4), (9,10) and (15,16) positions (see Fig. 4.1A), a C_{60} hemisphere is created; this was recently utilized in a first rational synthesis of C_{60} [209].

The overall conformation of the molecule in the gas phase is determined by the steric repulsion of the (3,4), (9,10) and (15,16) hydrogen atoms at the peripheral naphthalene groups. The intersection of their van-der-Waals radii leads to a distortion of the molecule from the preferred planar geometry of aromatic compounds. This results in local conformations, where, e.g. the 3-hydrogen is located above or below the adjacent 4-hydrogen, referred to as local “a” or “b” conformation, respectively. Overall four stereoisomers exist:³ aaa, bbb, aba and bab, which are all sketched in Figs. 4.1B and C (aab/baa and bba/aab are the two possible permutations of aba and bab, respectively and reproduce the same molecule rotated by $\pm 120^\circ$).

aaa and bbb, on one hand, and aba and bab, on the other, are enantiomers, i.e. chiral molecules that are like image and mirror image to each other. The first conformation leads to a chiral, propeller-shaped molecule with D_3 symme-

²The HtBDC molecule has been synthesized at the Risø National Laboratories (Risø, Denmark) by Johannsen, starting from the plain center part DC via a Friedel Craft alkylation [206]. The powder has a yellow color and a melting point of 692 K, but is supposed to decompose at lower temperatures if heated in air.

³All chemical expressions concerning chirality and its description are summarized in App. A.

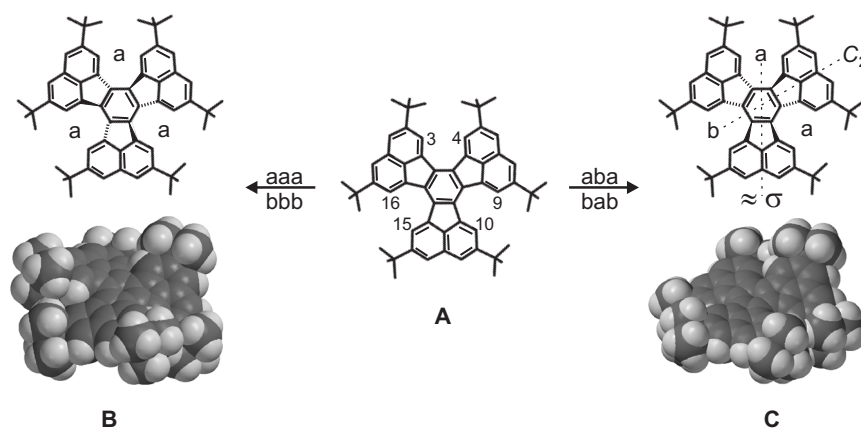


Figure 4.1: (A) Molecular structure of 2,5,8,11,14,17-hexa-*tert*-butyl decacyclene (HtBDC). HtBDC consists of an aromatic ring system built from a centered benzene ring interconnected by three five-membered rings to three naphthalene subunits (each with two *tert*-butyl groups ($-C_4H_9$) attached to it). The numbers label positions of the H atoms responsible for the distortion from a planar molecule conformation, leading to the local a and b conformation (see text for details). (B) Propeller shape or aaa/bbb conformation with D_3 symmetry (rotation axis runs perpendicular to the paper plane through the center of the molecule). The triangular and dashed bond shapes indicate a bond pointing above and below the paper plane, respectively. (C) Folded shape or aba/bab conformation with C_2 symmetry (rotation axis is indicated). It is only slightly distorted from an achiral conformation with a C_s symmetry (the quasi-mirror plane σ is also indicated).

try (Fig. 4.1B) [207],⁴ whereas the second conformation leads to a folded-shaped molecule with C_2 symmetry that is slightly distorted from the achiral C_s symmetry (Fig. 4.1C) with a 0.13 eV higher energy, according to simple force field calculations [208]. The latter is, however, the form found in HtBDC crystals which is ascribed to a better stacking of the *tert*-butyl groups.

All four stereoisomers easily interchange conformation, since the activation energy of this process, requiring a switch from a local “a” to a local “b” conformation, is fairly low. From semiempirical molecular orbital calculations the activation energy for the enantiomerization of the closely related DC molecule was calculated to be no more than 0.13 eV [207].

The two main conformations in HtBDC with D_3 and C_2 symmetry were also found in similar aromatic molecules [210]. It is a common feature in both conformations that the distortion is mainly caused by bending the 5-membered rings,

⁴The HtBDC molecule has then D_3 symmetry and can be denoted according to the P-M nomenclature for helical chirality (see App. A).

whereas the benzene and naphthalene subunits remain planar. This maintains the aromatic character of the naphthalene and benzene subunits, thus minimizing the overall energy of the molecules.

The deposition of the HtBDC molecules onto the Cu(110) surface (cleaned by cycles of 2.0 keV Ne ion bombardment followed by annealing at 820 K) was performed by organic molecular beam deposition (OMBD) using the molecule evaporator described in Sec. 2.4.

The HtBDC powder was heated to 470 K which resulted in a typical deposition rate of around 0.0001 ML/s (one monolayer (ML) is defined as the number of atoms per unit area in the unreconstructed Cu surface layer; note that a close-packed layer of HtBDC equals a coverage of 0.031 ML, as will be discussed in Sec. 4.4).⁵ The amount of dosed HtBDC molecules on the surface was controlled by keeping the crucible temperature constant and varying the exposure time (5-600 s); the absolute coverage was determined by STM. The adsorption of the molecules on the Cu(110) surface was studied by means of the low- and variable-temperature STM described in Sec. 2.3.

Prior to the very first use the HtBDC powder was degassed in UHV at 400 K for several hours in order to clean it from impurities. In the beginning, the main impurity was tetrachlormethane (CCl_4 , identified by the characteristic MS fragmentation pattern [211]), and even thorough outgassing could not purify the powder to a satisfactory extent. The STM images of HtBDC on Cu(110) revealed a well ordered, but different structure than the one described in Sec. 4.3. This must be due to the presence of chlorine on the surface which was detected by AES.⁶ The powder was finally cleaned chemically by recrystallization from ethyl acetate ($\text{CH}_3\text{COOC}_2\text{H}_5$). After this no chlorine impurities were detected.

4.3 Restructuring of the surface

4.3.1 Double row structure

Single HtBDC molecules are randomly distributed over the terraces upon deposition of the molecules onto the cold Cu(110) surface ($T < 150$ K), as illustrated in Fig. 4.2A. When following the time-evolution of this distribution, no diffusion was detected at these low temperatures. This is confirmed by the fact that no pronounced step decoration is observed, i.e. the molecules more or less stay where they hit the surface in the deposition process.

Fig. 4.2B shows a high resolution STM image revealing that single molecules are imaged as six lobes arranged in a distorted hexagon with only threefold rotation symmetry. The lobe distances are 5.5 ± 0.5 and 7.2 ± 0.6 Å, in accordance

⁵It should be mentioned already here that a variation in the deposition rate due to a change of the evaporation temperature or the sample-evaporator distance had no influence on the surface structures found by STM.

⁶More evidence to this notion is given by $c(2 \times 2)$ domains which were occasionally observed. This structure is known for halide adsorption (Cl, Br) on the similar Cu(100) surface [212].

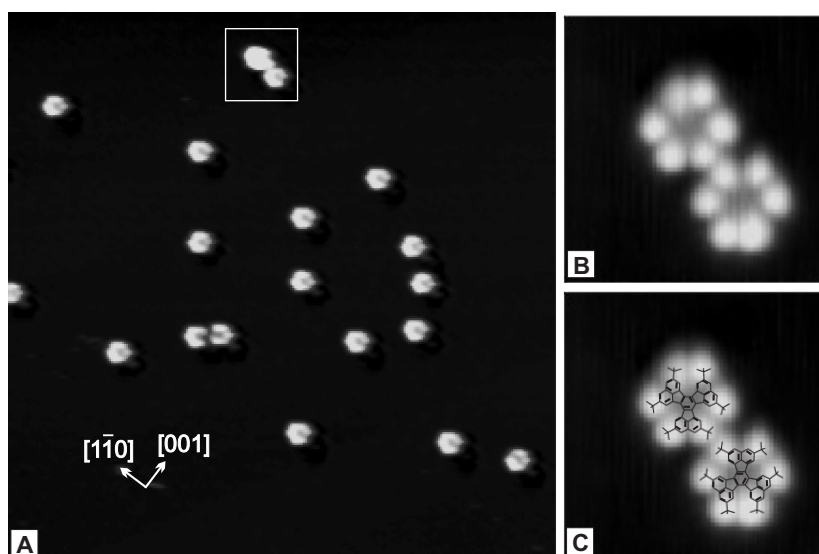


Figure 4.2: Constant-current STM images of HtBDC on Cu(110) at 25 K ($V = 1250$ mV, $I = 0.34$ nA). (A) Single molecules are spread over the surface ($500 \times 500 \text{ \AA}^2$). The crystal directions are indicated and the area marked with a square is enlarged in (B) and (C). (B) The high-resolution image ($50 \times 50 \text{ \AA}^2$) reveals the pronounced internal structure of six lobes which show a distorted hexagonal geometry. Two mirror symmetric forms are found on the surface. (C) The molecular structure of the HtBDC molecules is superimposed on the image in (B), showing that there are two distinct adsorption geometries on the Cu(110) surface, which is in accordance with the mirror symmetry of the Cu(110) surface. As can be seen, each lobe in the image corresponds to the position of a *tert*-butyl group. This reflects the threefold rotation symmetry of the molecules.

with the molecular model (5.6 and 7.6 Å). It becomes obvious from Fig. 4.2C that each lobe can be assigned to one of the *tert*-butyl appendages of a planar adsorbed molecule. This was confirmed by ESQC calculations, as shown in Fig. 4.3; similar results have been found for HtBDC on a Cu(100) surface [67].⁷

The dimensions of the six-lobed structure fit those expected from the molecule, pointing to an intact molecule on the surface: two lobes with a wider spacing (7–9 Å) correspond to *tert*-butyl groups connected to the same naphthalene subunit,

⁷In other investigations of larger aromatic compounds on metal surfaces [213, 214], STM images could reveal a structure within the aromatic system. This has been interpreted as corresponding to the HOMO (highest occupied molecular orbital) or LUMO (lowest occupied molecular orbital) distribution over the π system that had been imaged (depending sometimes on the polarity of the bias voltage; see also Sec. 2.2.3).

In the case of HtBDC, the *tert*-butyl groups separate the aromatic π system from the metal support. The tunneling current is dominated by tunneling through these *tert*-butyl groups, and the core area shows no further structure in the ring core. This might be the reason why reversing the bias voltage does not lead to a different imaging mode of the molecule.

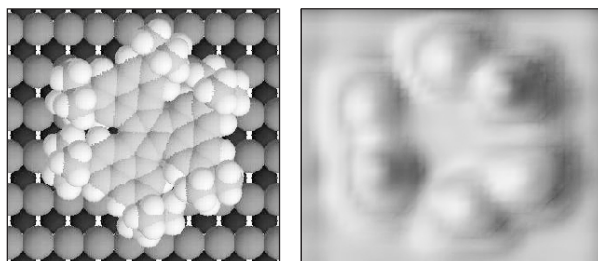


Figure 4.3: (A) Model of the HtBDC molecule on the Cu(110) surface. (B) Calculated ESQC images that confirm the experimentally found six-lobed structure, where each lobe corresponds to a tunneling path through the *tert*-butyl legs.

whereas two lobes with a smaller spacing (5–6 Å) correspond to *tert*-butyl groups connected to adjacent naphthalene subunits. From this it can be concluded that the molecules do not decompose during the evaporation or adsorption process.⁸

With increasing temperature ($T > 160$ K) the molecules start to diffuse on the terraces. This diffusive motion was studied extensively, and will be presented separately in Chap. 7. When reaching a step, the molecules attach to it and do not diffuse further. This is due to the increased bonding strength of the lower coordinated Cu step atoms (see Chap. 3) and leads to a gradual decoration of the steps.

The registry of the molecule on the Cu(110) lattice could not be determined exactly. It was generally not possible to achieve atomic resolution on the Cu lattice, when molecules were adsorbed due to the large tunneling resistances required to avoid manipulation of the molecules. Figs. 4.2B and C reveal two distinct, but equivalent, adsorption conformations of HtBDC which are mirror-symmetric to each other.

The fact that only two adsorption conformations are observed indicates, however, that specific adsorption sites exist. This was confirmed from images, in which single HtBDC molecules are manipulated by the STM tip along the [110] direction during the scanning process and thereby imaged repeatedly.⁹ An example

⁸Occasionally, the HtBDC molecules are imaged with five instead of six lobes. This could result from a partial decomposition. It seems, however, more likely to be the result of an incomplete chemical reaction while synthesizing the molecules.

⁹Such manipulations, first reported for Ag atoms and anthracene molecules on Ag(110) [215, 216], were named *scanning mode manipulations*. The maximum tunneling resistances for these manipulations to occur are 1, 100, and 1000 MΩ for Ag atoms, anthracene, and HtBDC, respectively, pointing to the differences in the interactions of the two adsorbate systems. The lower value needed to manipulate anthracene compared to HtBDC seems reasonable, because the aromatic π system of the HtBDC molecule (which is thought to give the largest contribution of the molecule–surface interaction) is separated from the surface due to the *tert*-butyl legs. The high value for HtBDC demonstrates the small forces necessary to move the molecules and give a lower boundary for the tunneling resistance in diffusion studies to avoid tip interaction (Sec. 7).

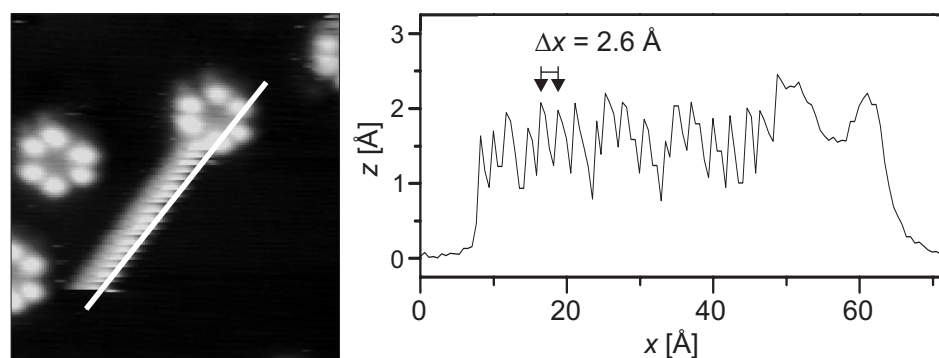


Figure 4.4: Scanning mode manipulation at 35 K ($V = 486$ mV, $I = 0.52$ nA, $56 \times 66 \text{ \AA}^2$). The line in the image marks the position of the height profile shown in the graph. The average peak distance in the height plot is 2.6 \AA in agreement with the NN distance of the Cu substrate (2.56 \AA). This demonstrates that HtBDC has specific adsorption sites.

is shown in Fig. 4.4. The average peak distance in the height plot is 2.6 \AA in agreement with the nearest-neighbor (NN) distance of the Cu substrate (2.56 \AA). The existence of specific adsorption sites was confirmed in diffusion studies, showing the molecules to jump in multiples of the NN distances (see Chap. 7).

A double row structure of HtBDC molecules nucleates homogeneously on the plain terraces at sample temperatures above 250 K. The rows are aligned along the equivalent $[\bar{1}12]$ and $[1\bar{1}2]$ directions and are comprised of two parallel chains of molecules (Fig. 4.5A). The structures are randomly distributed over the terraces, and there is no indication that they grow preferentially from a step edge. STM movies (series of STM images [218]) at RT demonstrate that the double rows have a fixed position on the surface but fluctuate in size on a time-scale of seconds: double rows disappear or nucleate and grow or shrink at the row ends. On a time-scale of seconds one can observe that, on one hand, new rows nucleate (containing at least two or three HtBDC molecules), while on the other hand, existing rows disappear. An illustration of these fluctuations is shown in Fig. 4.6.

In between the double row structures streaks are imaged with the same height as the lobes in the double rows, as is illustrated in a height profile below Fig. 4.5A. This together with the observation of the fluctuating double row size indicates a

Recording the tip height during controlled lateral manipulations along a straight line across the surface — as first demonstrated for the manipulation of CO and Pb atoms [217] — did not lead to the typical plots as in Fig. 4.4, but only revealed featureless structures. It was therefore not directly possible in these cases to differentiate between “pulling”, “pushing” and “sliding” manipulations. From the shape of the scanning mode manipulations in Fig. 4.4, it becomes, however, apparent that the molecule is manipulated in the *pulling mode*. The repeatedly imaged HtBDC lobe is cut off at the bottom with a straight line and the corresponding height plot (Fig. 4.4) reveals the typical pulling mode “quarter-circle” shapes [217].

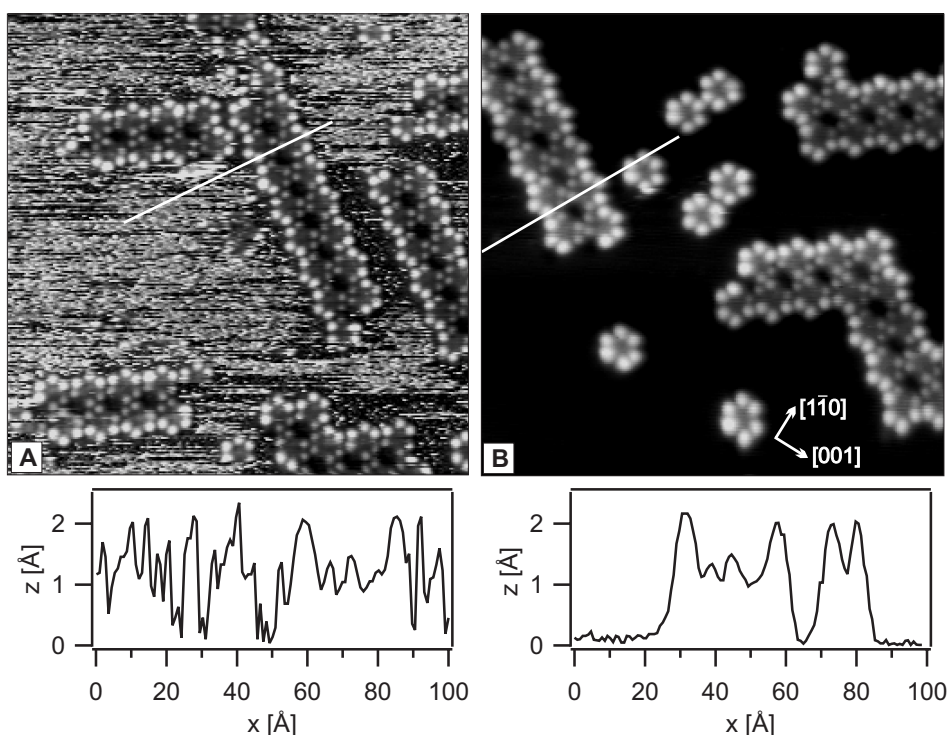


Figure 4.5: Low coverage, constant-current STM images ($200 \times 200 \text{ \AA}^2$) of HtBDC on Cu(110). (A) at RT ($V = 1051 \text{ mV}$, $I = 0.43 \text{ nA}$). (B) at $T \simeq 26 \text{ K}$ ($V = 1250 \text{ mV}$, $I = 0.42 \text{ nA}$). The arrows indicate the crystal directions. The white lines mark the position of the height plots presented below the respective images. The noisy streaks at RT appear with the same height as the double rows. Notice also that the single molecules have lobes of identical height, while those in the double rows are different.

fast diffusion of molecules, much faster than the time-scale of STM imaging (the residence time of a molecule in an adsorption site is too short to be imaged completely).¹⁰ This notion is confirmed by imaging the surface structure (prepared at RT) after cooling it below the onset-temperature of molecule diffusion. When doing this single molecules become visible in between the double rows, while the rest of the substrate surface appears plain with no impurities adsorbed onto it — the diffusion is frozen out completely (Fig. 4.5B).

Three main questions remain:

1. Why is the double row structure formed and stable in position compared to the single molecules?
2. What is the reason for the rows to grow along the equivalent $[\bar{1}12]$ and $[1\bar{1}2]$ directions?

¹⁰This is generally observed for fast diffusing adsorbates [94, 219].

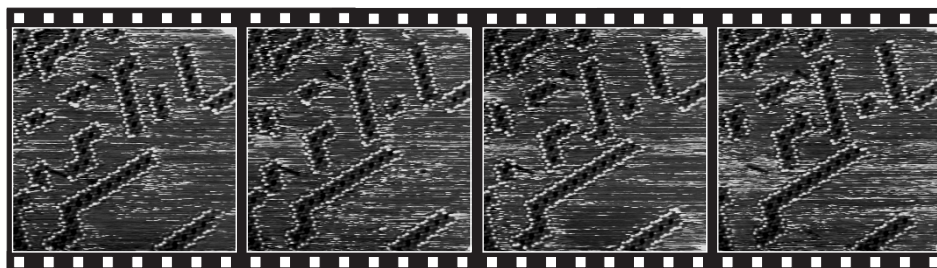


Figure 4.6: Stills from a constant-current STM movie of HtBDC molecules on Cu(110) at room temperature ($V = -743$ mV, $I = -0.46$ nA, $300 \times 300 \text{ \AA}^2$). The time per image is 15.6 seconds. The nucleation and fluctuation of double rows is clearly seen. See the complete movie under <http://www.ifa.au.dk/camp/movies/htbdc.mpg>

3. Why do the molecules appear differently in the rows than when they are adsorbed individually?

The latter fact is evident from Fig. 4.5B. The single molecules have lobes with an almost identical height of $\approx 2.2 \pm 0.2 \text{ \AA}$ relative to the Cu(110) substrate. For the molecules within a double row, however, the three lobes at the rim of the row are imaged much brighter than the three lobes pointing towards the interior of the double row (see line-scan in Fig. 4.5B) and the molecules seem to be tilted inwards.

A purely electronic reason for these imaging differences due to the proximity of neighboring molecules can be excluded. On one hand, adjacent molecules with six identical lobes are present (Fig. 4.5B) and, on the other hand, manipulating two single, individual molecules “into contact” did not lead to any change in their appearance. The experiments in the following section provide answers to all the questions raised.

4.3.2 STM manipulation experiments

The height difference of the lobes in the double rows scatters around 1 \AA . Comparing this with the height of a step on a Cu(110) surface (1.28 \AA) it can be speculated, if some kind of step restructuring is involved in the build-up of the row structures. This, however, seems to contradict the fact that non-molecule covered areas *within* the molecule rows — in between two molecules aligned along the $[1\bar{1}0]$ direction — are imaged as having the same height as the surrounding plane Cu surface.

To shed light on the situation, we have utilized the unique ability of the STM to manipulate single molecules on surfaces at the atomic scale [26–28, 30].¹¹ The

¹¹Not until the early 90ies was the STM used as a tool to manipulate matter in a controlled way on the atomic scale. The first lateral manipulations (i.e. parallel to the substrate) were shown with xenon atoms on a nickel surface at 4 K [26], and the first reversible, vertical manipulations (i.e. perpendicular to the surface) were demonstrated on a Si(111) surface and again on the Xe-Ni(110) system [220, 221].

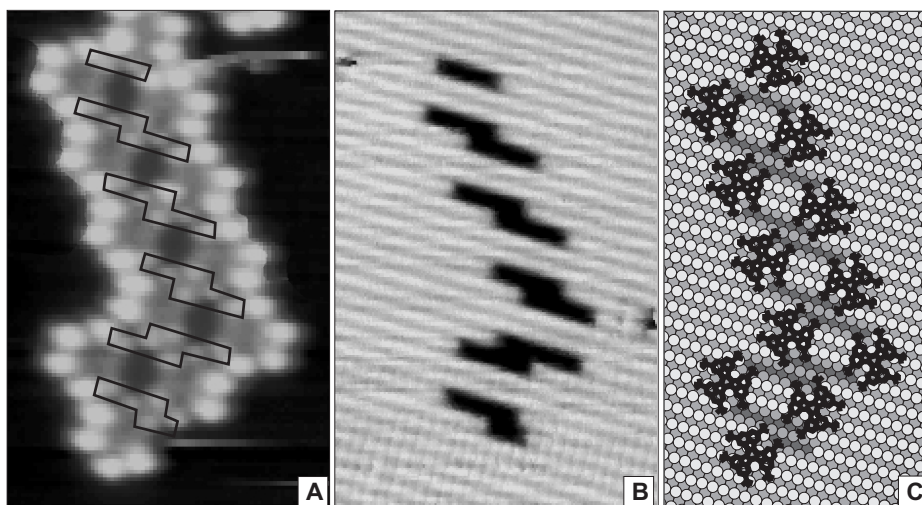


Figure 4.7: Constant-current images ($105 \times 69 \text{ \AA}^2$) at 41 K. **(A)** HtBDC double row structure ($V = 1070 \text{ mV}$, $I = 0.45 \text{ nA}$). The holes in the underlying surface are sketched. **(B)** The holes in the surface layers are disclosed after manipulating the molecules aside ($V = 7 \text{ mV}$, $I = 1.82 \text{ nA}$). Atomic resolution along the close-packed direction was obtained in the lower part of the image (horizontal fast-scanning direction), whereas it was lost when the tip scanned the restructured area. **(C)** Ball model of the double row structure — the substrate atoms are shaded darker the deeper the layers lie, while the molecules are shown in black.

controlled manipulation of the molecules is performed by reducing the tunneling resistance from $1 \text{ G}\Omega$ to $1 \text{ M}\Omega$ by changing the tunneling current or voltage or both.¹² According to the theory presented in Sec. 2.2.3, this corresponds to a tip surface approach of around 3 \AA . When scanning with this reduced tunneling resistance, all HtBDC molecules will be pushed outside the scanned area after 2–4 scans.

In Fig. 4.7 an STM image is shown recorded at 41 K of (A) an area with double rows of molecules *before* manipulation, and (B) the “cleaned” surface area *after* the molecules have been pushed aside. The latter STM image directly discloses the existence of a local disruption of the topmost Cu surface layer. Surprisingly, we find that ≈ 14 Cu atoms are expelled from the surface in two adjacent $[1\bar{1}0]$ rows,

It was further shown that this vertical manipulation process could be utilized for modifying the tip apex specifically and therefrom gain chemical contrast in the STM images [30]. From tip height measurements during the lateral manipulation process of CO molecules and Pb atoms along a straight line it was possible to differentiate between several manipulation modes [217]: “pulling”, “pushing” and “sliding”, where the molecule is behind, in front of or right under the tip with respect to the manipulation direction, respectively.

¹²The tunneling resistance is a qualitative measure for the sample–tip distance and thus a measure of the force applied to the molecules [222].

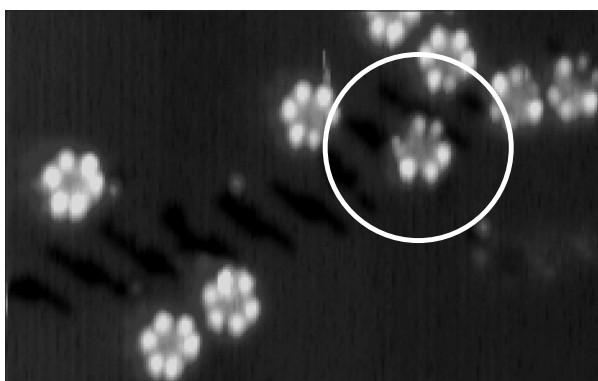


Figure 4.8: Single molecules residing on the restructured surface after an incomplete manipulation at $T \simeq 32$ K ($V = 354$ mV, $I = 0.30$ nA, $200 \times 100 \text{ \AA}^2$). The molecules in the upper right corner appear different, depending on their exact localization with respect to the holes. The small protrusions are probably single Cu atoms on the surface, as can be deduced from their height compared to the hole depth. The circle marks the molecule which has a conformation as in a double row. See text for details.

forming local holes for anchoring of the molecules.¹³ In Fig. 4.7C a schematic ball model of this structure is shown. As can be seen, the *tert*-butyl groups of the HtBDC molecule inside the double rows lie in the hole, whereas the outer *tert*-butyl groups lie on the plain Cu(110) surface (see also Fig. 4.7A). The registry of the molecules in the double rows with respect to the holes could be gained from images that contain a double row of molecules *and* a cleaned reconstruction area (see an example in Fig. 4.9).¹⁴

The manipulation of molecules out of the double rows is sometimes incomplete. Then single molecules may reside on the structure and provide information on the adsorption site. This is exemplified in Fig. 4.8, where several molecules

¹³We performed the manipulations at very low temperatures to avoid unwanted manipulation effects or diffusion of the Cu substrate atoms which could affect our observations. Effective medium theory results fortunately show that it is easier to freeze out vacancy diffusion than adatom diffusion. The activation energies E_d for the respective processes are [223]:

	jump		exchange
	[1 $\bar{1}$ 0]	[001]	[001]
$E_d(\text{adatom})/\text{eV}$	0.292	0.826	0.419
$E_d(\text{vacancy})/\text{eV}$	0.506	0.921	-

The diffusion activation energy for a vacancy along the [1 $\bar{1}$ 0] direction is larger by a factor of almost two compared to the adatom diffusion barrier in the same direction and still around 0.1 eV larger than the adatom diffusion along the [001] direction via an exchange mechanism.

¹⁴From such images also the partial registry of the *singly* adsorbed molecules on the plain surface can be determined: the central benzene subunit is located above a trough in between two adjacent close-packed Cu rows — just like the molecules in the row structure are. The registry along the close-packed rows was not accessible due to the lack of lattice resolution, as mentioned before.

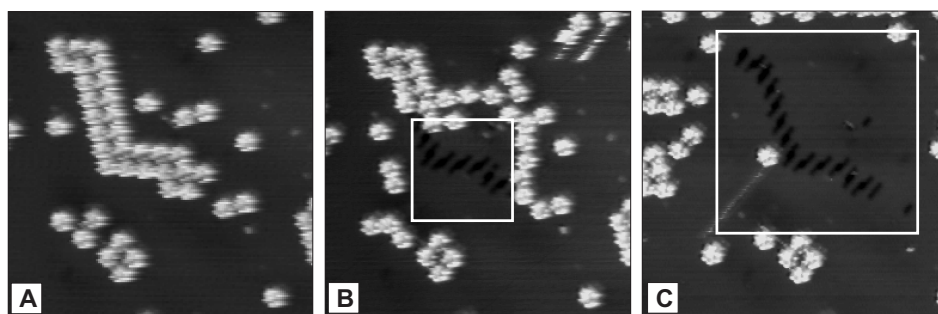


Figure 4.9: Successive cleaning of surface areas by pushing molecules aside at 33 K ($366 \times 382 \text{ \AA}^2$). (A) Original configuration before manipulation ($V = 354 \text{ mV}$, $I = 0.29 \text{ nA}$). (B) Cleaning of the marked area of around $100 \times 100 \text{ \AA}^2$ ($V = 420 \text{ mV}$, $I = 0.47 \text{ nA}$). (C) Further cleaning of the marked area of around $200 \times 200 \text{ \AA}^2$ ($V = 297 \text{ mV}$, $I = 0.35 \text{ nA}$). Small holes in the center and lower-right part of the cleaned area indicate the nucleation of new double rows.

are located on top and aside a restructured area. Of course the imaged molecules could be moved from the original position during the manipulation. Nevertheless, one molecule is visible (marked by a circle in Fig. 4.8) which is imaged as in the double row structure (three dim and three bright lobes). Its adsorption position reveals what is proposed in the model in Fig. 4.7C: the dim lobes are on top of the holes, two of them located to the left and to the right of the ridge between two adjacent holes.

The possibility that the holes are created while the molecules are manipulated and therefore are build up by expelling Cu atoms due to a strong molecule-Cu interaction can be ruled out. There was no indication of Cu adatoms (in an equivalent amount to the number of missing atoms in the holes) or Cu-molecule complexes after the manipulations.¹⁵ Moreover, the manipulation of single molecules (having six identical lobes) never revealed a restructured surface underneath.

Fig. 4.9 shows a sequence of images that reveals the step-by-step cleaning of the surface by moving the adsorbed molecules within the scanning area aside. After imaging the undisturbed structure (A), small areas inside the image are successively cleaned from molecules (B and C). The manipulated molecules are located outside the rim of the cleaned area with no sign of destruction.¹⁶ There

¹⁵The possibility remains of a direct removal of the surface atoms by the STM tip after manipulation of the molecules. Such processes have been observed on a Cu(211) surface at tunneling resistances below $100 \text{ k}\Omega$ [29] and occasionally also in our studies on Cu(110) (then even at higher tunneling resistances). However, in these cases removed adatoms are not found during the manipulation. Such processes would neither yield a regular restructuring pattern.

¹⁶The molecules are located at the left, right or the top side of the previously scanned area, but not at the bottom. Since the x direction is the fast scanning direction and the slow scanning along the y direction starts at the bottom, this indicates that the molecules had been manipulated in the pushing mode.

is no indication of molecule complexes or disrupted molecules which indicates a manipulation of entire, intact molecules.

The results presented so far partly answer the questions raised at the end of Sec. 4.3.1: the local restructuring leads to lower coordinated Cu atoms which yield a stronger molecule bonding (anchoring), as is explained by the d-band model described in Chap. 3. We come back to this in the next section, where we discuss the energetics of the restructuring.

4.3.3 Driving force for the restructuring

What is the origin and driving force of the hole formation in the surface layer? In general, the binding of adsorbates will induce a restructuring of the surface only if the gain in the adsorption energy ΔE_{ad} of the molecules on the disrupted surface, as compared to the virgin surface, is sufficiently high to balance the energy cost ΔE_{metal} required to break the metal bonds, i.e. the energy difference between the disrupted and the virgin *clean* surface. Even though the gain in the adsorption energy is difficult to calculate for such large molecules, the restructuring energy is accessible. This allows us to estimate a lower bound for the gain in adsorption energy. Moreover, the details of the restructuring energy provide an indication of why the rows grow along the two observed directions.

An estimate for the energetic situation of the removal of Cu atoms from a plain Cu(110) surface can be made by means of effective medium theory (EMT) [224, 225]. According to this, the energy E_i of an atom i in an FCC structure can be calculated as a function of its NN and next-nearest neighbor (NNN) coordination numbers N_1 and N_2 , respectively. If all interatomic distances are fixed to their bulk equilibrium values, it is

$$E_i(N_1, N_2) \simeq V_2(12 - N_1) + \frac{1}{2} V_3(12 - N_1)^2 + V_2'(6 - N_2). \quad (4.1)$$

Here $V_2 = 0.109$ eV and $V_2' = 0.0246$ eV are the effective NN and NNN pair interactions and $V_3 = 0.0023$ eV is the effective NN three-body interaction for a Cu lattice [224].

Now the energy change caused by the extraction of an atom out of the surface and moving it somewhere else can be calculated. In order to calculate the energetic effect ΔE_i for the whole process of moving an atom i , we have, however, not only to consider that the atom moved from the initial and to the final adsorption site, but also that all the surrounding atoms change their coordination number in the cause of this process.

This calculation has been performed in two steps. First, the energies necessary to move an atom out of the plain surface onto a single adsorption site on top of the plain surface (vacancy adatom situation) were calculated. Next, the energy necessary to move this adatom to a kink site is calculated. It is useful for our discussion later to remove the atoms one after another instead of creating the hole restructuring at once. The results are presented in Tab. 4.1, and the labelling of the atoms there and in the following refers to Fig. 4.10.

The question why these areas stay uncovered at all, i.e. why the two molecules aligned along the $[1\bar{1}0]$ direction are not located closer to each other, can be answered using our EMT results.

The spacing between two molecules aligned along the $[1\bar{1}0]$ direction enables one *tert*-butyl appendage of a third molecule to be located in the “cavity” which exists between these two molecules. Their mutual distance of around four lattice distances seems to be the optimum in order to locate two *tert*-butyl groups of the third molecule in the hole of the two adjacent short missing rows. For shorter distances this would no longer be possible because of the van-der-Waals repulsion. It would hence be necessary to have a third, short missing row adjacent to the two existing ones which, however, would require more energy than extending the existing two rows along the close-packed direction, as we saw above.

In conclusion, the double-row structure and the growth along the $\langle\bar{1}12\rangle$ directions are the result of an interplay between a close packing of the molecules and an energetically efficient way of binding to the restructured surface. The formation energy of the holes, $\Delta E_{\text{metal}} = 0.89$ eV, that has to be balanced yields a lower bound of the gain in adsorption energy of the HtBDC molecules in the double rows of 0.45 eV (there are two molecules adsorbed per hole).¹⁷

The remaining question is the origin of the increase in adsorption energy which leads to an anchoring of the molecules to the restructured surface. It seems very unlikely that this is simply a geometrical effect, where the *tert*-butyl groups bind stronger due to an increased contact area in the holes. Also theoretical results (Chap. 3) and known difficulties in C-H-bond activation of alkanes in catalysis [226–228] and organometallic chemistry [229] seem to rule out such a significant interaction.

An obvious reason is that the hole-restructured surface has low-coordinated Cu atoms (step- and kink-sites) which — according to the d-band model (Chap. 3) — lead to a stronger bonding. Moreover, there is an important geometrical effect. The holes enable the *tert*-butyl groups to sink into the surface. The π system hence approaches the reactive, lower-coordinated Cu atoms and causes a strong bonding as compared to the weak van-der-Waals bonding of the aliphatic groups on the plain surface.¹⁸ The strong bonding of the aromatic compounds as described in Chap. 3 seems also here to be the main driving force of the restructuring. HtBDC and the similar DC have been found with various bonding situations in organometallic complexes, demonstrating that very complicated bonding mecha-

¹⁷EMT calculations give reasonable evidence why no reconstruction was observed on the close-packed Cu(100) surface [67]: the vacancy adatom formation energy is too high — increasing in the order Cu(110), Cu(100), and Cu(111) as would be expected simply from the number of NN of the topmost surface atoms — and can not be compensated by the gain in adsorption energy of the HtBDC molecules.

¹⁸The tilted appearance of the molecules in the row structure is not necessarily due to a physical tilt of the molecule on the restructured surface. It could also be a gap between the *tert*-butyl group (staying in the same height position as on the unrestructured surface with respect to the Cu top layer) and the underlying surface. This seems, however, unlikely since the major bonding part with the π system would then not contribute significantly.

nisms may be active with multiple local bonding centers.¹⁹

We can think of the formation of the double row structure in the following way. In a random process a single Cu atom jumps out of the plain surface and leaves behind a vacancy.²⁰ A HtBDC molecule is then pinned to this vacancy when it meets a vacancy — a row nucleates (the random nature of the vacancy formation is in accordance with the random nucleation of the molecules on the Cu terraces). The growth of the rows proceeds when the Cu vacancy expands to a missing string/double string. Another molecule is pinned to the growing hole which then optimizes its shape, and eventually a neighboring vacancy starts to build up (probably assisted by the molecule) and so forth.

This growth mode also provides an understanding of why double-row structures can not be formed by depositing HtBDC on a cold sample, as was described in Sec. 4.3.1. The limiting factor is the activation energy for the first vacancy adatom formation which must be larger than the vacancy adatom formation energy of 0.56 eV. At low temperatures ($T < 250$ K) apparently, not enough thermal energy is available to promote the vacancy adatom formation on the Cu substrate. Additionally, the molecule diffusivity is reduced and diminishes the probability of a vacancy and a molecule to meet.²¹

Up to this point, we have discussed the general phenomenon and energetic aspects of the restructuring underneath the HtBDC molecular double rows. We ignored, however, mentioning a detail which maybe the most peculiar about the restructuring: The holes in the metal surface are chiral. Since chirality is usually not encountered in connection with metal surfaces, this topic will be discussed separately in the next section along with the growth towards a full monolayer.

¹⁹The bonding of HtBDC molecules in organometallic complexes have been reported in [208], where a $\text{Cr}(\text{CO})_3(\text{HtBDC})$ complex was synthesized. The pure aromatic core system DC was even found in a multidecker sandwich complex $\text{Ag}_2(\mu - \text{tetra} - \eta^2\text{-DC})(\text{ClO}_4)_2(\text{benzene})$, where every DC molecule binds simultaneously to 4 Ag ions (as assigned by the descriptor μ) in a η^2 manner at its periphery [230]. The DC dianion was even found to show different bonding behavior in the $\{(\eta^5\text{-Me}_4\text{EtC}_5\text{Co})_2(\mu\text{-}\eta^5\text{:}\eta^4\text{-DC})\}$ and $\{(\eta^5\text{-Me}_4\text{EtC}_5\text{Ni})_2(\mu\text{-}\eta^3\text{:}\eta^3\text{-DC})\}$ complexes, where the metal atoms are coordinated from more central units of the DC molecule [231, 232].

²⁰The descent of a diffusing Cu atom in this vacancy is probably impeded due to the Schwoebel-Ehrlich barrier and the vacancies therefore have a reasonable lifetime [233, 234]. It seems moreover unlikely for the adatom and the vacancy to meet again, before the adatom is trapped at a step.

²¹It may seem surprising that a process can be initiated at temperatures where the thermal energy kT (0.022 eV at 250 K) is much lower than the activation energy. From a kinetic point of view, this is, however, not a contradiction since the rate of formation — generally expressed in an Arrhenius form — simply becomes very low at low temperatures, but does not vanish completely. A thermodynamic argument can be given by noticing that not only the energy, but also the entropy of the process is important. The entropy gain of the adatom-vacancy formation process is enormous and the main driving force (the extracted Cu atoms can diffuse between numerous adsorption sites on the surface). This is comparable to the vaporization of a liquid: Trouton's rule ($\Delta s_{\text{vap}} = \Delta h_{\text{vap}}/T_b \simeq 10k$) states that the molecular entropy of vaporization Δs_{vap} at the boiling point T_b equals a constant of approximately ten times Boltzmann's constant k (Δh_{vap} is the enthalpy of vaporization) [235]. As with the adatom-vacancy formation, the evaporation process takes place even though the thermal energy is only about a tenth of a fraction of the enthalpy of the corresponding process. The reason is the enormous entropy gain when going from the condensed phase to the gas phase.

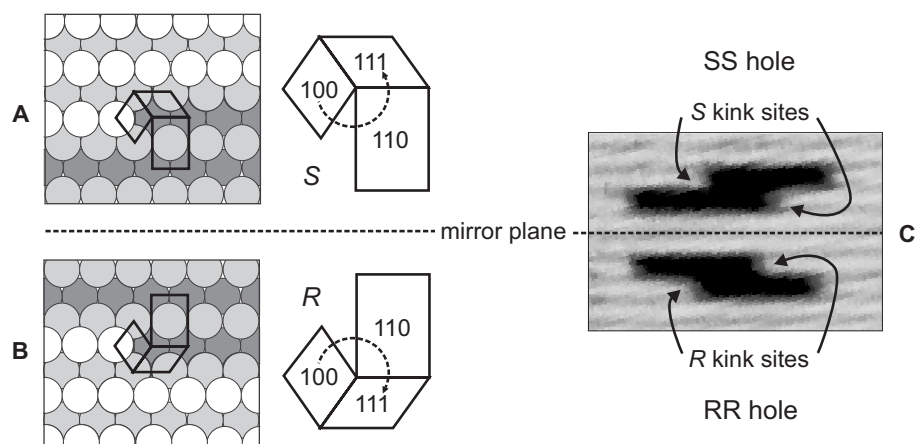


Figure 4.11: Illustration of chirality and nomenclature of kink sites on an FCC{110} surface [242]. The black frames in the ball models mark the unit cells of the three surface orientations — (100), (110), and (111) — involved in the kink formation, as labelled in the enlarged drawings (see text for details). **(A)** *S* configuration. **(B)** *R* configuration. **(C)** STM image of the two hole types, demonstrating their chirality due to kink sites.

4.4 Chirality of the restructuring

Chirality is a property commonly associated with organic molecules, biological materials or inorganic salts. A metal (and its associated surfaces) is normally achiral due to the mirror symmetry of its close-packed structures. Chirality can, however, be added to the surface by adsorbing chiral auxiliary molecules onto the substrate surface — a phenomenon often referred to as “chiral modification”. A number of studies have reported on the nucleation and growth of such chiral structures within the adsorbed molecular monolayer by the deposition of chiral/prochiral molecules on an achiral substrate surface [40, 57, 78, 236–241].

It was recently pointed out that metal surfaces can themselves be chiral due to kink sites which possess an intrinsic chirality [242, 243]. By cutting single crystals along certain high Miller index directions, surfaces that exclusively contain kink sites of a specific chirality can be formed [242–249]. The chirality of kink sites and the nomenclature according to Ahmadi *et al.* are shown in Figs. 4.11A and B [242]. When the surface is viewed from above, a kink site is of *R* configuration if the sequence of the surface orientations meeting at the kink site runs clockwise in the order {111}-{100}-{110}, and of *S* configuration if the orientation runs counter-clockwise.²²

²²The order of the low-index surfaces follows a decreasing density of atoms in the topmost layer, in analogy with the Cahn-Ingold-Prelog sequence rules known in organic chemistry [250, 251]. See

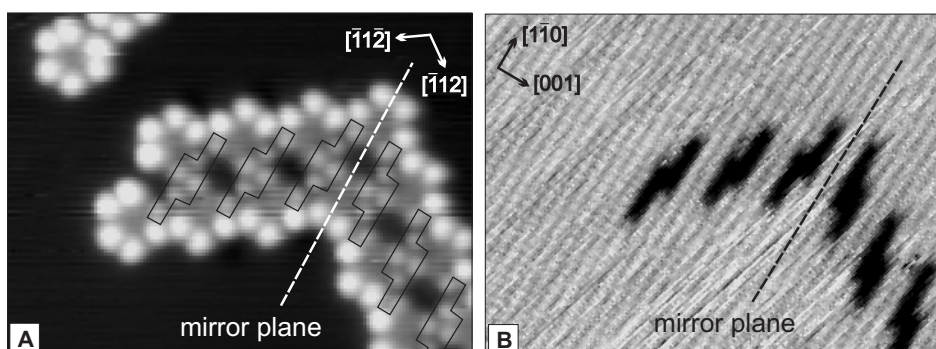


Figure 4.12: (A) Constant-current images ($110 \times 82 \text{ \AA}^2$) of the HtBDC double row structure and immobilized single molecules at 25 K ($V = 1250 \text{ mV}$, $I = 0.42 \text{ nA}$). Holes in the restructured surface are framed black. (B) Holes underneath the molecules after pushing the molecules aside. They consist of ~ 14 Cu atoms expelled from the surface in two adjacent $[\bar{1}\bar{1}\bar{0}]$ rows ($V = 10 \text{ mV}$, $I = 1.78 \text{ nA}$).

As shown in Fig. 4.11C the holes contain either two *R* or two *S* kinks, in the following referred to as RR and SS holes, and are consequently *chiral*, i.e. non-superimposable by simple translation or rotation. The mirror symmetry of not only the holes underneath the molecular double row structure, but also of the molecular overlayer itself is illustrated in Fig. 4.12.

The imaging of the double row structures seems to reflect the molecules' different conformations, as explained in Fig. 4.13. All molecules along the $[\bar{1}\bar{1}\bar{2}]$ rows are imaged identically reflecting a certain conformation whereas the molecules along the $[\bar{1}\bar{1}\bar{2}]$ rows have the enantiomorphic conformation — the molecules within a given double row are superimposable by a 180° rotation. The two molecule conformations are hence chiral and non-superimposable.

If we tentatively assume that the STM images of the molecules can be interpreted as simple geometric height corrugations, then the molecules along the rows correspond to the aaa and bbb conformations of the HtBDC molecule: three bright and three dim lobes of the molecules reflect the two sets of three *tert*-butyl groups lying in two parallel planes, as seen in the propeller conformation (aaa/bbb) model in Fig. 4.1B. Within this interpretation the molecules at the elbows interconnecting the rows correspond to the folded conformations (aba/bab): The four bright and two dim lobes (or two bright and four dim lobes) reflect the two sets of four and two *tert*-butyl groups lying in two parallel planes (see model of the folded conformation in Fig. 4.1C).²³

This argumentation lacks the explanation why the molecules on the plain sur-

App. A for details.

²³Moreover, the mirror plane between the two double-row orientations goes right through an elbow and therefore through the (adsorbed) molecules which are (in the gas phase) almost mirror symmetric, as discussed in Sec. 4.2.

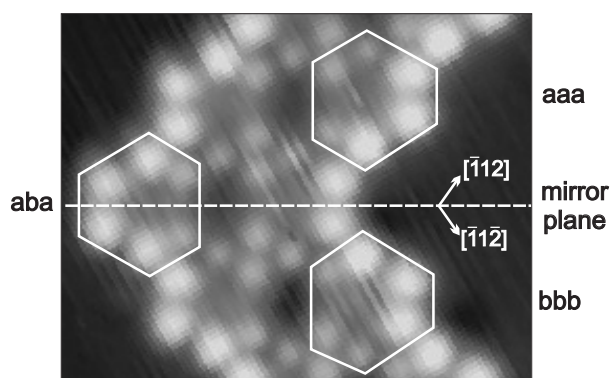


Figure 4.13: STM images of the double row structure. Chiral aaa and bbb conformations along the rows and achiral aba conformation in the elbows are indicated.

face are imaged as having six equivalent lobes. If we assume, for example, a propeller-shaped conformation on the plain surface, the alternating height pattern of the six lobes within one molecule would be expected; this was not observed unambiguously, even though slight height variations are usually seen (Fig 4.5B). Molecule–surface interactions, however, may lead to severe distortions within the molecules (at least, such an increased molecule–surface interaction leads to the hole reconstruction of the surface). Moreover, we must keep in mind that in principle STM images do not simply reveal geometrical height contours (see Sec. 2.2.3).

In conclusion, it is speculated that the chirality of the Cu surface is imprinted into the surface by the chiral molecules: the adsorption of chiral molecules on top of chiral holes leads to diastereomeric complexes with different interaction energies. The aaa (bbb) conformation may, for example, have a lower interaction energy with RR (SS) holes than with SS (RR) holes. Accordingly, one type of enantiomeric hole will be decorated with one and only one enantiomeric conformation of the molecule. It would therefore be very interesting to perform theoretical STM simulations of the different conformations and compare them with the experimental findings.

Higher coverages of approximately 0.01 ML, 0.02 ML, and 0.03 ML are depicted in Figs. 4.14A–C, respectively.²⁴ At 0.01 ML (Fig. 4.14A), the surface shows a preferred step decoration and random distribution of double rows with large spacings as described in Sec. 4.3. The intermediate areas are dominated by fast-diffusing single molecules. The molecular rows grow in length and density with increasing coverage (Fig. 4.14B), and the zigzag rows, alternating irregularly along the $[\bar{1}1\bar{2}]$ and $[\bar{1}12]$ direction, eventually cover the entire surface (Fig. 4.14C).

²⁴Since the HtBDC molecules are fairly large (diameter ≈ 15 Å), a saturated molecular overlayer corresponds to a coverage of only ≈ 0.03 ML (see below).

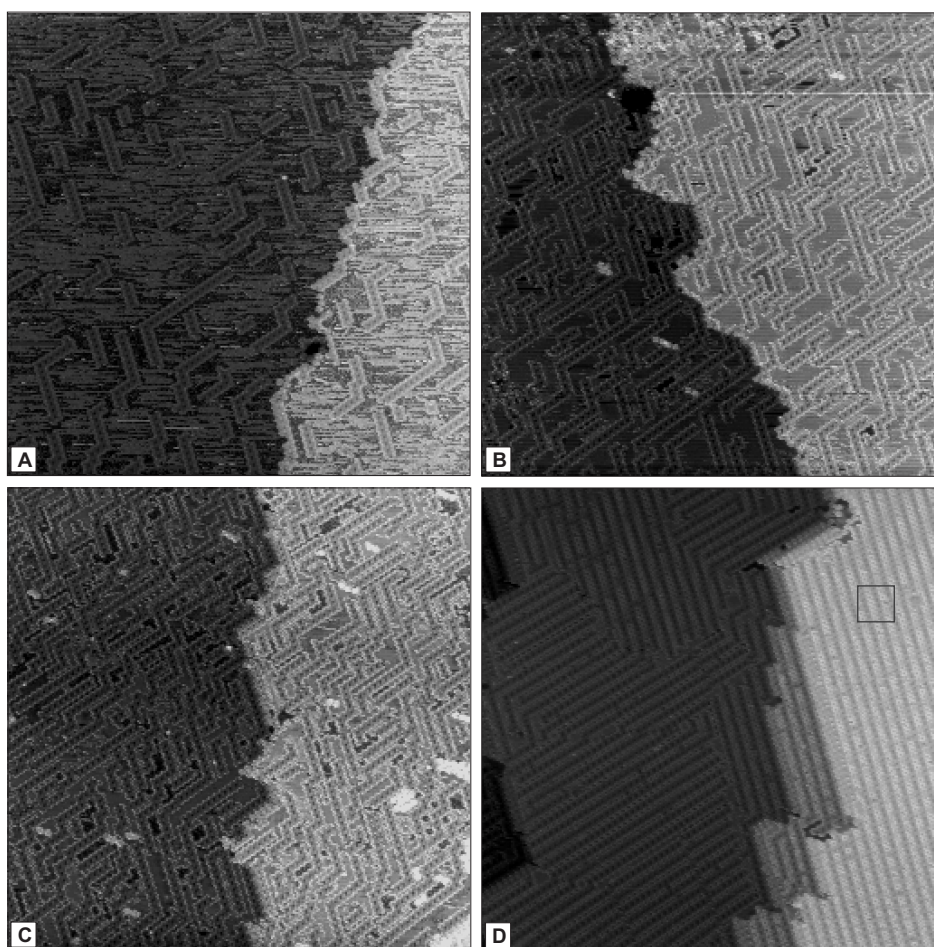


Figure 4.14: Constant-current images ($1000 \times 1000 \text{ \AA}^2$) of HtBDC on Cu(110) after different deposition times at RT: **(A)** 3 min ($V = 1250 \text{ mV}$, $I = 0.44 \text{ nA}$). **(B)** 6 min ($V = 1250 \text{ mV}$, $I = 0.65 \text{ nA}$). **(C)** 9 min ($V = 1250 \text{ mV}$, $I = 0.55 \text{ nA}$). The density of the zigzag row increases. **(D)** Domains of densely packed molecules along the $[\bar{1}1\bar{2}]$ and $[\bar{1}12]$ directions build up after annealing the fully covered surface shown in Fig. 4.14C at 410 K for 10 min ($V = 1250 \text{ mV}$, $I = 0.51 \text{ nA}$). The square marks the area that is shown enlarged in Fig. 4.15A.

The extraction of Cu atoms out of the surface in the process of the restructuring has two consequences which can be seen in Figs. 4.14B and C. Firstly, the Cu atoms diffuse on the terraces and eventually attach at a step edge. The step shapes hence change with increasing molecule coverage and become more fringed (note that almost 25% of the surface atoms move over distances of a step terrace, i.e. in the order of magnitude of 1000 \AA). Secondly, above a certain coverage bright spots

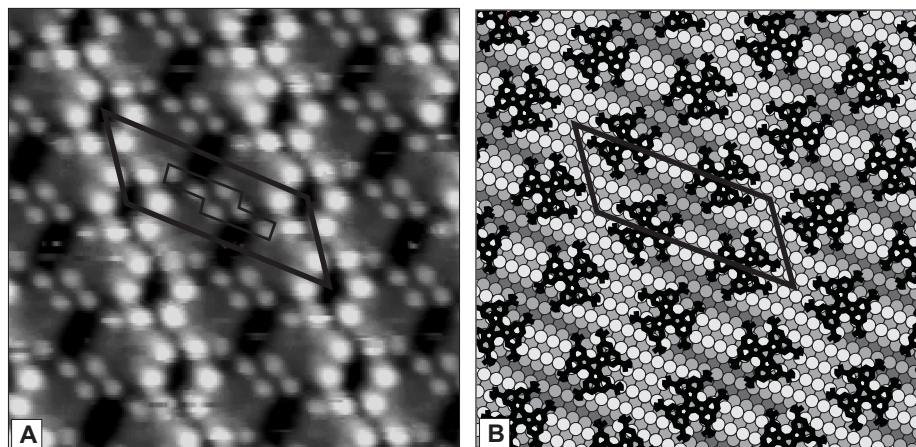


Figure 4.15: (A) Constant-current STM image ($100 \times 100 \text{ \AA}^2$, $V = 1768 \text{ mV}$, $I = 0.30 \text{ nA}$) at RT after annealing the fully covered surface to 410 K (zoomed in on a spot marked in Fig. 4.14D): the $\begin{pmatrix} 4 & 4 \\ 16 & 0 \end{pmatrix}$ unit cell and the hole contour are framed black. (B) Ball model of the double row structure — the substrate atoms are shaded darker whenever the layers lie deeper. Molecules are shown in black and the unit cell is indicated.

appear on the terraces consisting of a few molecules in between the double rows. We suggest those to be molecules adsorbed on top of local Cu islands which are confined by close-packed double rows and therefore prevent Cu atoms to diffuse to a step edge of a terrace.²⁵ These small spots of mainly 2–4 molecules seem to be aligned preferentially along the $[\bar{1}10]$ direction. The growth of a second layer of molecules could not be studied due to the loss of resolution.

If unordered saturated overlayers are annealed at 410 K for around 10 min, uniform domains with diameters in the range of 100–1000 Å build up (Fig. 4.14D). Each of these domains consists of densely packed rows along the $[\bar{1}1\bar{2}]$ or $[\bar{1}12]$ direction exclusively which demonstrates that the straight double row structure is indeed thermodynamically stable and energetically preferred with respect to the zigzag rows.

A close-up of a domain is shown in Fig. 4.15 together with a model of the monolayer structure, showing the commensurable superstructure of the molecules. The $\begin{pmatrix} 4 & \pm 4 \\ 16 & 0 \end{pmatrix}$ unit cell contains two HtBDC molecules and 64 Cu atoms,

²⁵It could not be completely excluded that these are molecules in a second layer on top of the row structure, but there are four indications against it: i) the molecules are always imaged as having six lobes of equivalent height; ii) they are imaged with the height analog to the molecules on the neighboring terrace; iii) when the Cu atoms are no longer confined they diffuse away, leaving behind stripe patterns of diffusing molecules and iv) an increasing coverage — as can be seen from Figs. 4.14B to C — does not lead to the expected increase of the number of bright spots if this would be molecules in a second layer.

i.e. the saturated coverage is $2/64 \approx 0.031$ ML. Due to an unequivocal correlation between the row direction and the hole chirality underneath, we conclude that the holes within a given domain are all alike and hence *the domains are homochiral*.²⁶ Moreover, every molecule is connected to a chiral kink site, demonstrating how the molecules induce chirality to the extended terraces of the metal crystal surface.

The uncovered areas in between the double rows imply that a denser packing could be possible. However, the hole reconstruction and the well-defined adsorption sites on top of these prevent arbitrary molecular double-row positions on the surface. They can only be shifted by a whole lattice constant along the $[1\bar{1}0]$ and $[001]$ direction and hence a closer packing is indeed not possible because of repulsive interactions.

Since a domain contains molecules of one enantiomeric conformation exclusively, an explanation of how the two conformations separate into domains, i.e. how the adsorbate layer rearranges from unordered zigzag rows into large chiral domains, is necessary. Due to the dense packing, separation by diffusion seems rather unlikely. A local rearrangement seems, however, possible because of the low inversion energy between the HtBDC conformations aaa and bbb. At the same time the holes underneath the molecular layer in the Cu surface can easily be converted from RR to SS by diffusion of Cu atoms. Owing to the conformational flexibility of the HtBDC molecules, the overall surface is racemic, consisting of equal amounts of both domains.

To investigate the possibility of chiral imprinting, we are collaborating with Krebs from Risø National Laboratories on synthesizing a chiral version of the HtBDC molecule. In order to do this, we aim at inserting three additional methyl groups in the 3, 9, and 15 positions; this should prevent the enantiomerization process without affecting the general restructuring process. The synthesis is, however, very demanding, since the molecule's periphery becomes sterically crowded. Moreover, only the racemate can be synthesized, and this has to be separated in the two enantiomers afterwards, which again is not an easy task.

4.5 Conclusion

In this chapter we reported STM results on the nucleation and growth of HtBDC monolayers on a Cu(110) substrate. The molecules adsorb with their aromatic plane parallel to the surface and diffuse rapidly on the plane surface for $T > 160$ K. Above 250 K the HtBDC molecules aggregate into double rows of molecules that grow along two equivalent directions of the surface. This anchoring of the molecules to the surface is associated with a restructuring of the surface underneath the molecules.

This could be demonstrated directly by using the STM tip to manipulate the molecular adsorption layer aside (in contrast to other results proposing a struc-

²⁶The correlation was confirmed by manipulating several molecular double row structures and checking the restructuring underneath. Attempts to push molecules away from densely packed domains did not succeed in resolving the underlying restructured surface directly.

turing from height corrugations within the molecular adsorption layer [71, 74, 93, 194–202]). A local disruption of the surface layer underneath the molecules was revealed that is comprised of around 14 Cu atoms being removed from the surface layer in two neighboring close-packed rows. EMT calculations attempted to give a plausible explanation of the specific double row structure.

These results prove that molecule-substrate interactions can be a controlling factor for self-assembly of molecules on surfaces even at low coverages. We propose that the driving force is the approach of the molecule's π system to the kink-sites in the restructured surface; the gain in adsorption energy compensates the energy necessary for restructuring the surface. On a Cu(100) surface no restructuring occurs [67]. Accordingly the molecule-substrate interaction is weak in this case and structure formation has not been observed at low coverages; simple quasi-hexagonal, close-packed domains evolve at high coverages [67].

We saw that the surface restructuring on Cu(110) is chiral: the holes contain two kink sites of equal chirality. We find that at full coverage *every molecule* is associated with *one chiral kink site* in the underlying surface. The observed molecule hole complexes extend homogeneously over the entire surface and segregate spontaneously into enantiomeric domains upon gentle annealing, thereby creating a perfectly ordered chiral metal surface.

The results demonstrate, how chirality is induced on a metal surface in a *chemical way* due to the adsorption of molecules. This is very different from the *physical* preparation (cutting and polishing) of surfaces which has been used as enantiospecific adsorbents [242–249]. Earlier attempts to create a chiral metal surface used the chirality of a homochiral substrate material like quartz as a chiral template for a deposited metal film [252–254], but structural information about the metal films is not available. A recent study indicated that adsorption of L-lysine on an achiral Cu(100) surface may lead to the partial formation of chiral kink sites at step edges in connection with a step faceting process [255, 256]; the overall fraction of such facets was, however, very small compared to the entire surface area.

Chiral surfaces are generally of great interest in fields like heterogeneous asymmetric catalysis, chemical sensors, and for studying the separation of chiral compounds and nonlinear optical materials [96, 97, 257, 258]. In the past, chiral surfaces have mainly been formed by adsorbing chiral molecules onto an achiral surface, forming molecular overlayer domains which are chiral [40, 78, 236, 237, 239–241]. Our finding of chirality in a metal surface itself may shed new light on the mechanistic understanding of the catalytic behavior of chirally modified surfaces. Generally, catalytic surfaces are considered as a static checkerboard providing adsorption sites for the chiral auxiliary and the reactants, while we have shown that a chiral restructuring of the substrate surface may have to be taken into account.²⁷

²⁷It was recently demonstrated that the adsorption of chiral amino acids on calcite crystals (a form of CaCO_3) leads to chiral surface morphology changes [259].

CHAPTER 5

DC on Cu(110)

In the present chapter the adsorption of decacyclene (DC) molecules on a Cu(110) surface is reported and compared to results from the previous chapter on HtBDC. Opposite to HtBDC, no restructuring underneath the DC molecules is found and no ordered structures are observed at low coverages. This difference to HtBDC is discussed in terms of molecule-substrate and molecule-molecule interactions. Close to full monolayer coverage, ordered domains with different molecule density are found and described in a model.

5.1 Introduction

Aromatic molecules play an essential role in different fields of interest, ranging from catalytic processes to applications in organic LEDs and thin film transistors [43–45]. Detailed knowledge of the structure and bonding of these molecules on metal and semiconductor surfaces is therefore of fundamental importance. This is seen by the many studies investigating single molecules on surfaces (e.g. rehybridization effects [52–54]), the formation of ordered monolayers [55, 56, 58], and thin film growth [59, 60].

The aim of studying the adsorption behavior of decacyclene (DC) was to compare it to the adsorption behavior of HtBDC molecules. This direct comparison of related molecules sheds further light on the driving forces for the HtBDC structure formation on Cu(110), as discussed in the previous chapter.

We will see in the present chapter that DC occupies specific adsorption sites on the Cu(110) substrate (Sec. 5.3). The lack of directional intermolecular bonding possibilities prevents the formation of close-packed structures up to very high coverages (Sec. 5.4). This is different from the substrate-mediated structure formation of HtBDC which was a result of the restructuring of the Cu substrate.

5.2 DC molecule

The molecule under investigation, decacyclene (DC, $C_{36}H_{18}$, $M = 450.5$ a.u.), is illustrated in Fig. 5.1.¹ The constitution of DC is identical to the aromatic center part of the HtBDC molecule [207]. The conformational information provided in Sec. 4.2 for HtBDC hence also applies to DC and we refer thereto for details.

We briefly summarize that the steric repulsion of hydrogen atoms between adjacent peripheral naphthalene groups leads to distortions from a planar conformation with a local “a” and “b” structure. Overall this results in two enantiomorph conformations: a propeller-shaped molecule with D_3 symmetry (Fig. 5.1A) found in DC crystals [207], and a folded-shaped molecule with C_2 symmetry (Fig. 5.1B). The energy barrier between the different conformations is low, allowing the molecule conformations to easily interchange.

The deposition of the DC molecules was performed as in the case of the HtBDC molecules (Sec. 4.2). The powder was outgassed at 400 K and deposited at 450 K for 5–1200 s.

5.3 Low coverages

When DC is deposited on the Cu(110) surface at RT, the molecule is observed to diffuse readily on the terraces. This results in only occasional imaging of entire

¹DC is commercially available (Sigma-Aldrich) and has been further purified by recrystallization and sublimation at the Risø National Laboratories (Risø, Denmark) by Johannsen. The powder has a yellow color and a melting point of 660 K [43].

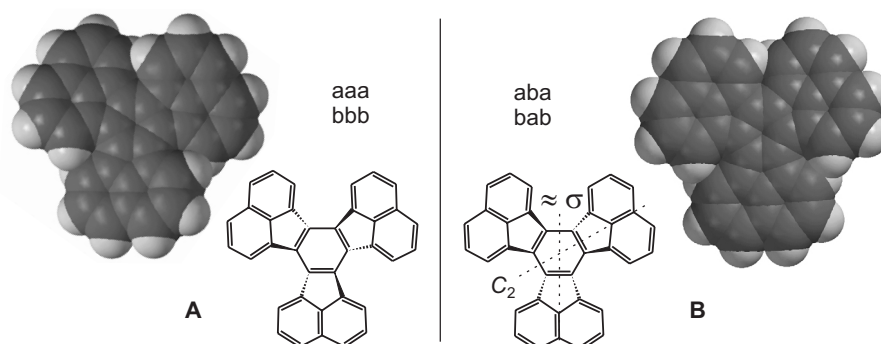


Figure 5.1: Molecular structure and space-filling model of decacyclene (DC). DC consists of an aromatic ring system built from a centered benzene ring interconnected by three five-membered rings to three naphthalene subunits. In analogy with HtBDC (see Fig. 4.1 for details), interacting H atoms lead to distortions from the planar geometry which lead to two low-energy conformations. **(A)** Propeller shape or aaa/bbb conformation with D_3 symmetry (a rotation axis runs perpendicular to the paper plane through the center of the molecule). The triangular and dashed bond shapes indicate a bond pointing above and below the paper plane, respectively. **(B)** Folded shape or aba/bab conformation with C_2 symmetry (rotation axis is indicated). It is only slightly distorted from an achiral conformation with a C_s symmetry (the quasi-mirror plane σ is also indicated).

molecules as seen in Fig. 5.2A. The images are dominated by streak patterns running preferentially along the $[1\bar{1}0]$ direction. This indicates a high mobility along these directions, much faster than the time-scale of STM imaging. The diffusion of DC molecules is discussed in detail along with the HtBDC diffusion in Chap. 7.

As in the case of HtBDC, the molecule's mobility can be frozen out by cooling the sample below 220 K. This is much less than required in the case of HtBDC ($T < 160$ K) and is a first indication of a stronger molecule-substrate interaction for DC. It is shown in Fig. 5.2B that at these low temperatures individual molecules are visible. The molecule height of the molecules is $1.3 \pm 0.1 \text{ \AA}$.² Its diameter is $14.8 \pm 1.9 \text{ \AA}$ in agreement with the molecular dimensions in the gas phase model (around 13.3 \AA). This confirms the expected planar adsorption of DC which provides the strong interaction with the Cu substrate through the aromatic π system.

At closer inspection the adsorption conformations reveal an internal structure that is much less pronounced than in the case of HtBDC (which was dominated by the *tert*-butyl appendages). However, high resolution images as in Fig. 5.3A show a molecular structure with an internal mirror symmetry defined by the (001) plane of the substrate surface.³ Two equivalent conformations are found that are super-

²Coincidentally, this corresponds to the height of a Cu(110) single step. It can, however, be excluded that the streaks in Fig. 5.2A result from diffusing Cu adatoms, since they are not observed on a clean Cu substrate.

³It may be speculated, if this is connected with the quasi mirror-symmetric aba/bab conformation

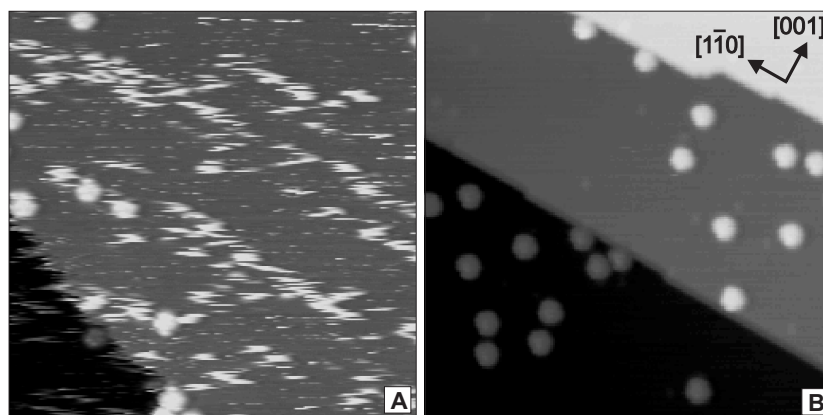


Figure 5.2: Constant-current STM images of DC on Cu(110) at low coverages ($300 \times 300 \text{ \AA}^2$, deposition time: 1 min). **(A)** At RT only few molecules are imaged. The streaks run preferentially along the close-packed Cu-direction, indicating fast molecule diffusion ($V = -884 \text{ mV}$, $I = -0.35 \text{ nA}$). The Cu-step appears fringed due to the high mobility of the Cu kink atoms. **(B)** At 96 K the diffusion is frozen out and single molecules are visible ($V = -1250 \text{ mV}$, $I = -0.34 \text{ nA}$). Also Cu kink atom mobility is reduced and the steps are stable with single kinks visible.

impossible by mirroring at a $(1\bar{1}0)$ plane and shown in Fig. 5.3A. This is equivalent to the case of HtBDC on the unstructured Cu(110) surface.

The occurrence of only these two adsorption conformations restricts the possible adsorption geometries of DC to those shown in Fig. 5.3B, if we assume well-defined adsorption sites.⁴ From the low-coverage images, an unambiguous identification of the two adsorption geometries with the imaged molecule shapes is not possible. The assignment given in Fig. 5.3B can, however, be deduced correctly from the packing of molecules in domains at high coverages (see Sec. 5.4).

The registry along the $[001]$ direction is accessible from images with inverted contrast which also resolve the close-packed rows of the Cu substrate as in Fig. 5.3C. The molecule center benzene ring is located between close-packed rows.⁵ The registry along the $[1\bar{1}0]$ direction could not be unravelled.

Unlike HtBDC molecules, DC molecules do not preferentially decorate step edges. This may be explained by the strong, direct interaction of the aromatic

of the DC molecules known from the gas phase (Fig. 5.1B). We must, however, keep in mind that the strong interaction with the substrate may have an important influence on the adsorption geometries. An assignment to one of the presented gas-phase conformations would therefore generally be questionable.

⁴An adsorption conformation that would be rotated out of the high symmetric form shown in Fig. 5.3B would lead to four distinguishable conformations.

⁵It may be interesting to note that benzene molecules on Cu(110) occupy long-bridge adsorption sites which yields equivalent positions on the troughs between close-packed Cu rows as the DC and also HtBDC molecules [260].

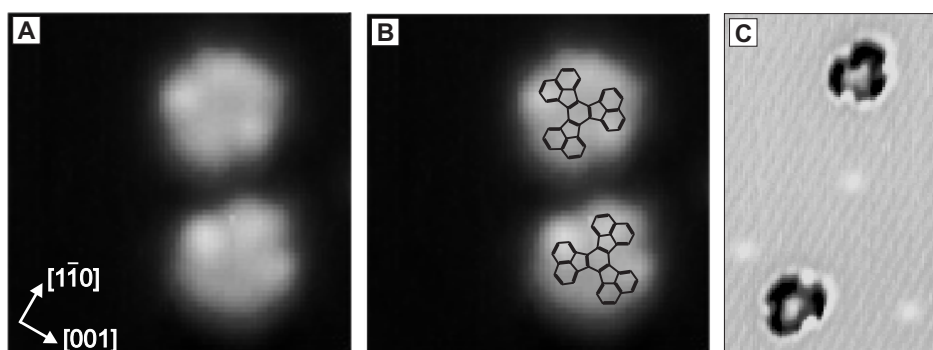


Figure 5.3: (A) High-resolution image ($50 \times 50 \text{ \AA}^2$, $V = -1215 \text{ mV}$, $I = -0.11 \text{ nA}$, $T=96 \text{ K}$) revealing the internal structure of the DC molecules. As in the case of HtBDC, two mirror symmetric forms are found on the surface (compare to Fig. 4.13). (B) The molecular structure of the DC molecules is superimposed on the image in (A). (C) Inverted imaging contrast with additional resolution of the close-packed rows ($70 \times 1100 \text{ \AA}^2$, $V = -1250 \text{ mV}$, $I = -0.27 \text{ nA}$, $T=96 \text{ K}$). From this, the registry of the DC molecules along the $[001]$ direction can be determined: the molecule center benzene ring is located between close-packed rows.

system with the substrate and the thereby reduced mobility compared to HtBDC. A further difference compared to HtBDC is that no tendency to form clusters is found in the case of DC at low coverages, because of the lack of directional, intermolecular forces. In contrast to this, we saw in Chap. 4 that the separation of the aromatic π system in HtBDC from the surface is the reason for the restructuring of the surface which eventually is responsible for the formation of ordered HtBDC double rows, even though intermolecular forces are absent also here.

It was shown by STM manipulation experiments that in fact no restructuring is induced by the adsorbed DC molecules (Fig. 5.4).⁶ This confirms a strong interaction of the aromatic system of the DC molecules with the substrate: a possible gain in adsorption energy cannot compensate for the energy necessary to restructure the Cu surface. DC does not even adsorb across Cu step atoms which indicates that the energy gain due to adsorption at low-coordinated Cu atoms is negative. A reason for this may be a better interaction of the π system with the flat surface than in a tilted configuration at a step edge.

5.4 High coverages

With increasing coverage the amount of streaks in the STM images reduces, while the density of entirely imaged DC molecules increases (Fig. 5.5A): the closer pack-

⁶The two adsorption geometries can interchange in the course of a manipulation, confirming that they represent the same molecule.

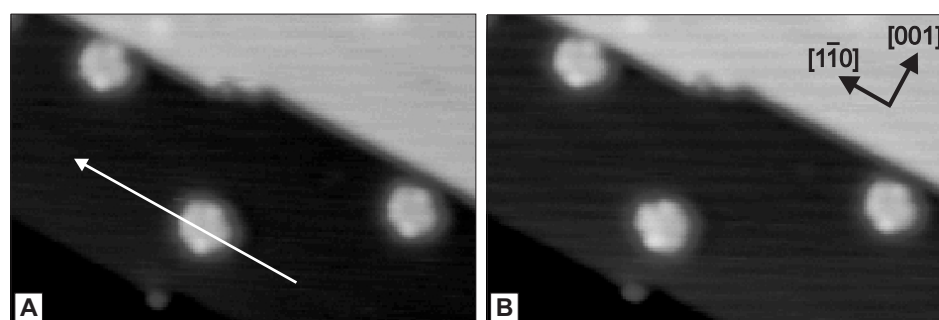


Figure 5.4: Manipulation experiments of single DC molecules along the $[1\bar{1}0]$ direction ($150 \times 100 \text{ \AA}^2$, $V = -1215 \text{ mV}$, $I = -0.31 \text{ nA}$, $T=96 \text{ K}$). (A–B) Manipulation results in a short lateral displacement accompanied by a rotation of the molecule (tunneling parameters for manipulation: $V = -105 \text{ mV}$, $I = -0.35 \text{ nA}$).

ing of molecules hinders the diffusion process. The tendency to form ordered domains is, however, fairly low even at coverages close to a full monolayer (Fig. 5.5B). Annealing of the deposited overlayer does not improve this situation.⁷ Attractive intermolecular forces are basically absent and the molecule coverage is not high enough to force the molecules into an ordered arrangement.

Pronounced long-range order is only observed if the molecules are deposited over a longer period of time onto a heated Cu surface (450 K). Fig. 5.6A reveals that three types of domains appear: two striped domains consisting of double rows of molecules (denoted “r-t” and “l-t”) and domains of quasi-hexagonal symmetry (denoted “hex”). The striped phases are very regularly ordered. They are chiral and of enantiomorph symmetry, superimposable upon mirroring at the $(1\bar{1}0)$ plane.⁸ The quasi-hexagonal domains are less strictly ordered. This can be understood from the different packing density of the molecules in these two domains, as illustrated in the following.

A common structural element in these domains are pairs of DC molecules along the $[1\bar{1}0]$ direction, as seen in Fig. 5.6B.⁹ A conclusive model of the domain structures can be given by assuming that all DC molecules occupy well-determined, identical adsorption sites.¹⁰ Since we do not observe different ad-

⁷DC molecules seem very robust towards decomposition. Heating to 700 K did not lead to noticeable changes in the molecule’s appearance. At higher temperatures, however, the molecules seem to decompose which results in a completely disordered overlayer of probably carbonaceous compounds.

⁸Note that the chirality of the domains refers exclusively to the arrangement of molecules on the surface. The furthermore possible chiral conformations of the molecules are not considered.

⁹These pairs should not be understood as a result of intermolecular attraction, but simply as a result of close packing at high coverages. Diffusion studies show that molecule pairs which occasionally form at low coverages readily dissociate again.

¹⁰In the model the center benzene ring of the DC molecules is assumed to be located on top of fourfold hollow sites, in agreement with the position on top of the troughs in between close-packed Cu-rows.

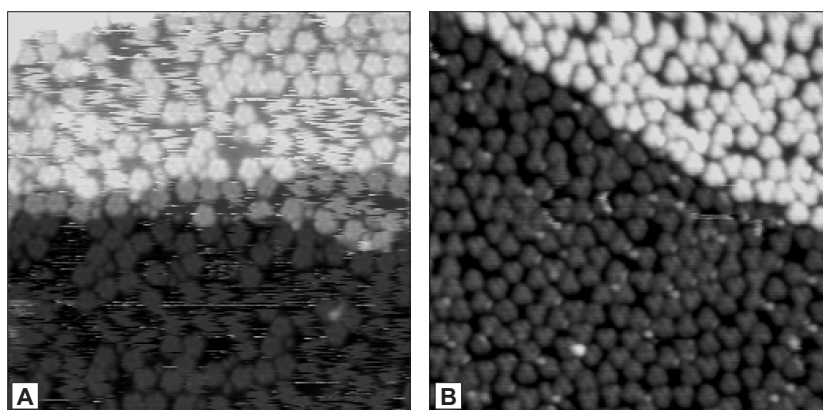


Figure 5.5: Images with increasing coverage of DC on Cu(110) at RT ($300 \times 300 \text{ \AA}^2$). (A) Due to the close packing, the molecules become partly immobilized. Streaks of diffusing DC molecules are still visible ($V = -2102 \text{ mV}$, $I = -0.32 \text{ nA}$, deposition time: 5 min). (B) At almost full monolayer coverage, molecule diffusion is hindered. No particular ordering of the molecules is found even after annealing of the surface to 450 K ($V = -2500 \text{ mV}$, $I = -0.39 \text{ nA}$, deposition time: 8 min).

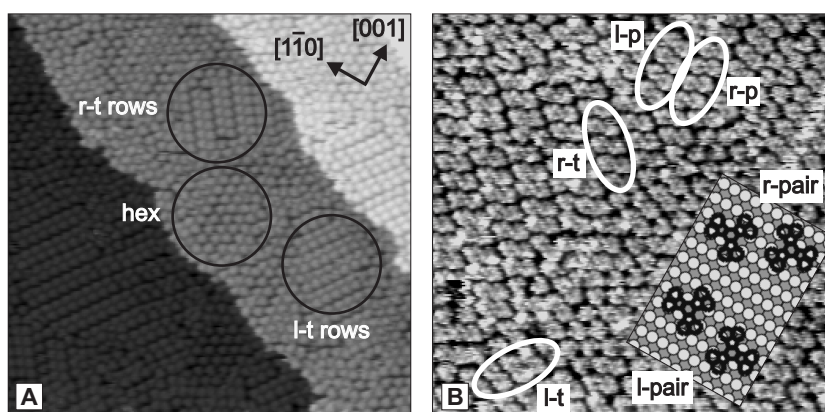


Figure 5.6: Ordered phases of DC molecules appear on the surface after a deposition time of 15 min at elevated sample temperatures (450K). The images are acquired at RT. (A) Basically three types of domains appear and are marked by circles: striped domains consisting of double rows of molecules (denoted “r-t” and “l-t”) and quasi-hexagonal domains ($500 \times 500 \text{ \AA}^2$, $V = -1768 \text{ mV}$, $I = -0.43 \text{ nA}$). (B) Mixture of different domains resulting from l- and r-pairs (see model inset) of DC molecules ($300 \times 300 \text{ \AA}^2$, $V = -526 \text{ mV}$, $I = -0.33 \text{ nA}$). Four kinds of row structures can be formed out of these: l-p, r-p, r-t, and l-t; see text for details.

sorption geometries at high coverages other than the two found at low coverages, this seems to be a reasonable assumption.

The inset in Fig. 5.6B shows a model of the DC pairs: two molecules are positioned so that pairs of naphthalene subunits face each other. A close, staggered packing is enabled by side-shifting of one molecule to the neighboring trough along the [001] direction. This staggered adsorption can be achieved in two ways. We call them *l-pair* and *r-pair*, since in a top view of the surface along the [110] direction the lower molecules within a molecule pair is shifted to the left (“l”) or to the right (“r”). These enantiomorph pairs constitute the basic building blocks, from which the dense packing into enantiomorph domains can be explained.

A close packing of DC pairs can be achieved by ordering like pairs into rows. Two different row types evolve, depending on whether a naphthalene subgroup of the upper or lower molecule in a DC pair is located in the cavity of its adjacent DC pair. The resulting rows are aligned either parallel (“p”) or twisted (“t”) to the [001] direction. Hence, four (idealized) packing situations emerge that can be assigned to one of the four combinations l-p, r-p, l-t, and r-t.

These different cases are illustrated in Fig. 5.7. The parallel l-p and r-p domains are ordered in a quasi-hexagonal manner. Since the change of adsorption geometry of single molecules within the p domains does not result in unfavorable intermolecular repulsion (see the circled molecule in Fig. 5.7A), each molecule has the freedom to adsorb in either of the two mirror-symmetric conformations. Accordingly, a loose ordering into a quasi-hexagonal arrangement is observed. A strict ordering, as in the model of the parallel domains, is rarely encountered.

In the twisted l-t and r-t domains, however, severe repulsive interactions occur if the adsorption geometry of single molecules switch to their mirror symmetric form (see the circled molecule in Fig. 5.7F). The twisted t domains are therefore ordered very strictly as described in the model. This is simply a result of a closer packing in the twisted domains. The $\begin{pmatrix} 8 & \pm 4 \\ 3 & \mp 3 \end{pmatrix}$ unit cell (Figs. 5.7A and B), contains two DC molecules and 36 Cu atoms in the topmost layer which corresponds to a coverage of $2/36 \approx 0.056$ ML. This is an increase of 10% compared to the parallel p domains with a $\begin{pmatrix} 10 & \pm 3 \\ 0 & 4 \end{pmatrix}$ unit cell (Figs. 5.7F and G).¹¹ These contain two DC molecules and 40 Cu atoms in the topmost layer, i.e. the coverage is only $2/40 = 0.050$ ML.

From the close packing of molecules within the twisted row domains, we can deduce the correct adsorption geometry as shown in Fig. 5.3B. If the molecules in the twisted row domains had been assigned the opposite conformation to the one presented in Fig. 5.3B, the DC pairs within the unit cell would not have a staggered arrangement of naphthalene units in adjacent molecules. Instead an eclipsed arrangement of two naphthalene subgroups would be the result which is subject to strong repulsive interactions.

The closer packing of the twisted row domains is also demonstrated if a completely saturated monolayer of DC molecules is prepared. This can be achieved by depositing DC for a very long time onto the Cu(110) substrate held at 450 K.

¹¹All unit cells reflect the (chiral) C_2 symmetry of the molecule pairs.

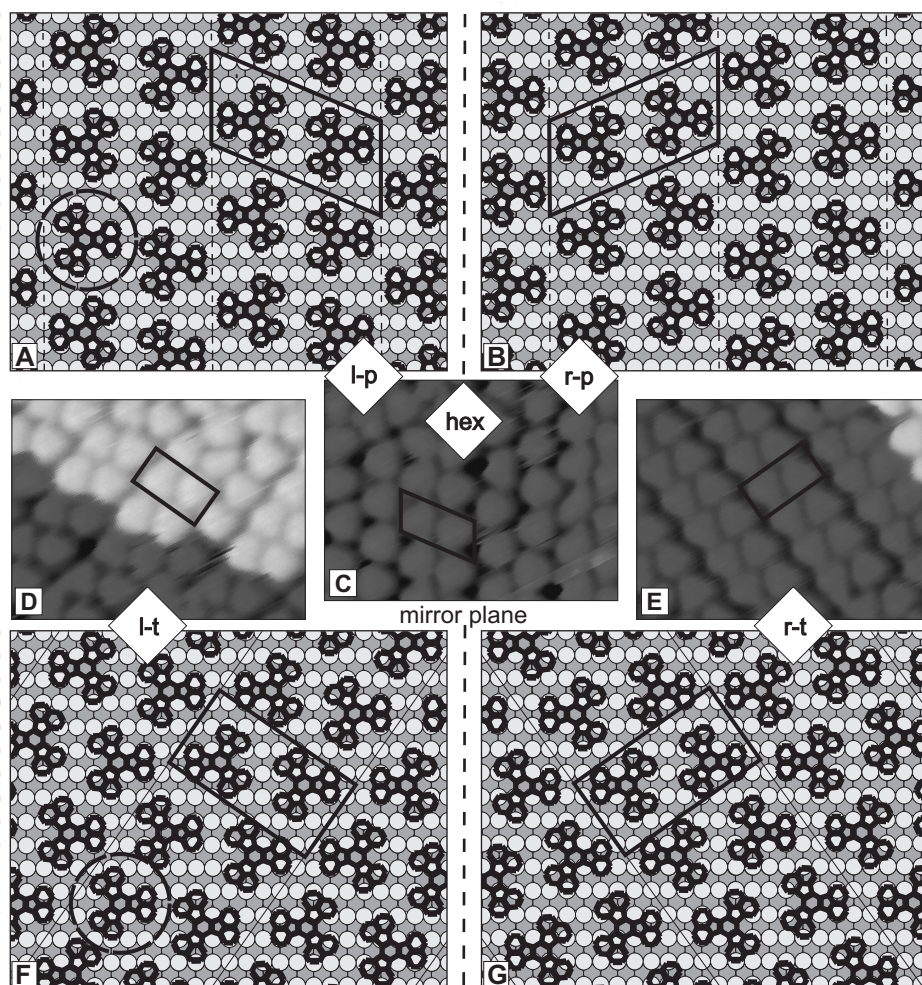


Figure 5.7: Illustration of the four idealized ways of packing DC molecules on Cu(110). The dashed line through the figure center indicates a mirror plane. **(A–B)** Models of l-p and r-p domains, respectively. The rhomboidal $\begin{pmatrix} 10 & \pm 3 \\ 0 & 4 \end{pmatrix}$ unit cells are indicated. The dashed lines parallel to the [001] direction within the models are guidelines to better identify the rows. The circled molecule has mirror symmetric adsorption geometry with respect to the ideal l-p packing; no pronounced repulsive interaction is expected in this conformation. **(C)** STM image of the quasi-hexagonal domain partially containing l-p rows. **(D–E)** Image of l-t and r-t domains, respectively ($100 \times 75 \text{ \AA}^2$, $V = -1768 \text{ mV}$, $I = -0.36 \text{ nA}$). **(F–G)** Models of l-t and r-t domains, respectively. The rectangular $\begin{pmatrix} 8 & \pm 4 \\ 3 & \mp 3 \end{pmatrix}$ unit cells are indicated. The twisted rows run along the $[\bar{1}12]$ and $[1\bar{1}2]$ direction. The circled molecule has mirror symmetric adsorption conformation with respect to the ideal l-t packing. Severe repulsive interaction is expected: the lower left naphthalene subunit is very close to the adjacent molecule.

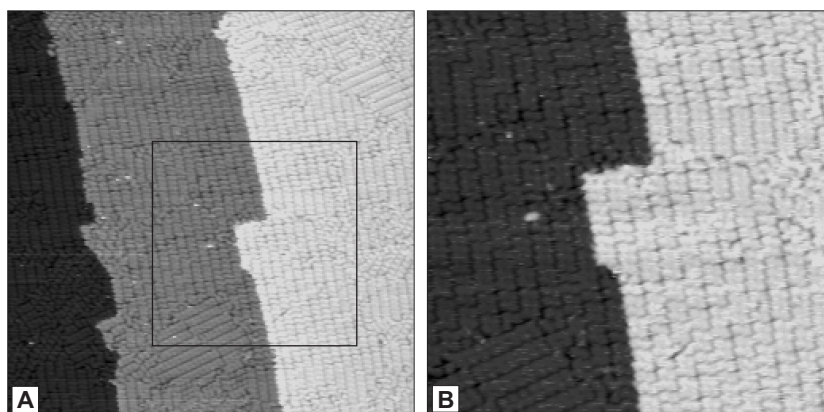


Figure 5.8: (A) Saturated monolayer of DC molecules on a Cu(110) surface (deposition time: > 20 min at sample temperature of 450 K). ($1000 \times 1000 \text{ \AA}^2$, $V = -2500 \text{ mV}$, $I = -0.37 \text{ nA}$). (B) Zoom-in of the area marked in (A) ($500 \times 500 \text{ \AA}^2$).

The result is shown in Fig. 5.8. Almost the entire surface is then covered with DC-molecules in the strictly ordered twisted-row domains. Only small islands with quasi-hexagonal symmetry remain.

5.5 Conclusions

We reported on the adsorption behavior of DC molecules on a Cu(110) surface. Single DC molecules have adsorption sites similar to HtBDC molecules on the unstructured surface. However, the direct, strong interaction of the aromatic π system with the substrate — spacer groups as in the HtBDC molecules are missing — prevents a surface restructuring. This, together with the absence of directional intermolecular forces, explains the low tendency of DC to form ordered domains, in contrast to the substrate-mediated formation of HtBDC structures that occurs already at low coverages.

Since only weak van-der-Waals forces are active between DC molecules, the molecules are forced into ordered domains first at almost saturated coverages. The evolving structures are simply close-packed domains that can be viewed as a repeated arrangement of molecule pairs. The domain structures can be understood by assuming well-determined, identical adsorption site of the DC molecule on the substrate. The molecules are then arranged in a way that minimizes the repulsive interactions between them. In this respect the structure formation is also ruled by dominating molecule-substrate interactions as in the case of HtBDC molecules.

CHAPTER 6

Lander molecules on Cu(110)

In this chapter the adsorption of so-called Lander molecules on a Cu(110) surface is reported. Different molecule conformations are present on the surface which order only partially into small domains. At step edges the adsorption of Lander molecules is accompanied by a restructuring of the surface underneath the molecules. This is similar to the case of HtBDC on Cu(110) and is again revealed by STM manipulation experiments. EMT calculations are presented in order to elucidate the restructuring process. Parts of this chapter are summarized in paper [V].

6.1 Introduction

The interaction between complex organic molecules and crystal surfaces has recently been investigated extensively because of prospective applications in nanoelectronics [17, 18, 65–69]. Single molecule conductance is of great importance when using molecules as building blocks in electronics applications. Often, specifically designed, large molecules are investigated [17].

The fact that the ability of deforming an object scales with its size does not only apply to the macroscopic world, but is also found on the molecular scale. While benzene can be considered a very rigid molecule, units of several condensed benzene rings are much more sensitive to distortions out of the planar configuration (a well-known example is the helical helicenes [261]). Conformational changes are hence very likely to happen if external forces are exerted on large molecules as in the case of adsorption processes on a surface.

The Lander molecules are models of molecular conductors [17]. They are comprised of an aromatic board, representing the molecular wire which is separated through spacer groups from the surface and surrounding molecules. Conductance measurements performed along the aromatic center of a molecule at a double step of a Cu(001) surface have been reported in Ref. [262]. For a correct interpretation of such measurements, detailed information about the exact bonding geometry of molecules on the surface is crucial. Different conformations may influence the interpretation of conductance measurements. The size of the molecules in and the flexibility of their spacer legs give in fact rise to different conformations, as could be observed for similar molecules [143–145].

Here we report on the adsorption behavior of large Lander molecules on a Cu(110) substrate. The interplay between experimental STM data and theoretical calculations disclosed different molecular conformations. It was revealed that the spacer groups do not provide the predicted task of electrically insulating the board from the substrate. The reason is the enormous flexibility of the large molecule, as will be reported in Sec. 6.3.

The similarity of the molecular geometry of the Lander and HtBDC molecules (Chap. 4) raises the question if comparable restructuring processes occur during adsorption. This is indeed the case as will be demonstrated by means of STM manipulation experiments in Sec. 6.4.

6.2 Lander molecule

The investigated molecule, shown in Fig. 6.1, is in the following referred to as “Lander” ($C_{90}H_{98}$, $M = 1179.7$ a.u.).¹ It is 17 Å long and 15 Å wide and consists of a central polyaromatic unit (4.5 Å wide): An anthracene unit is terminated at both ends by a five-membered ring connected to a naphthalene subunit (fluoranthene group). This board is surrounded by four 3,5-di-*tert*-butylphenyl “spacer

¹The molecules have been synthesized at the CEMES - CNRS (Toulouse, France) by Gourdon. The powder has a yellow color and a melting point above 550 K.

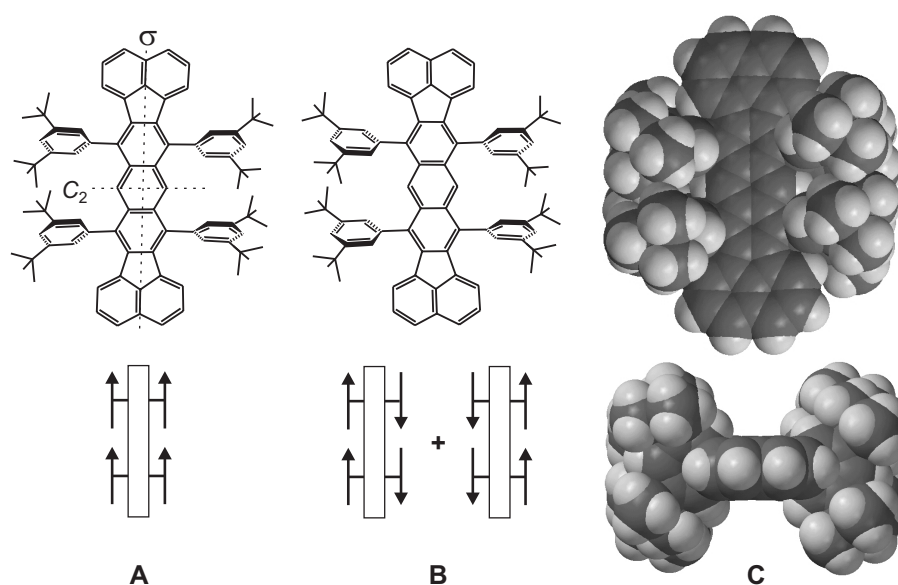


Figure 6.1: Molecular structure of the Lander molecule ($C_{90}H_{98}$) consisting of a central polyaromatic board terminated by two fluoranthene groups and four spacer legs (3,5-di-*tert*-butylphenyl substituents). **(A)** achiral form with C_{2h} symmetry: eclipsed conformation of legs on opposite sides of the board (indicated in the schematic drawing where the arrows represent the spacer groups). The symmetry elements (rotation and mirror axis) are indicated. The triangular and dashed bond shapes indicate a bond pointing above and below the paper plane, respectively. **(B)** chiral form with C_2 symmetry: staggered conformation of legs on opposite sides of the board which results in two enantiomers (indicated in the schematic drawing). The rotation axis runs perpendicular to the paper plane through the center of the molecule. **(C)** Space-filling model of a chiral form: top-view and side-view (along the board) showing how the spacer legs separate the central board from the surface.

legs". They are designed to elevate the central part of the molecule by a nominal distance of 5 Å above the substrate when adsorbed on the surface (assuming an unperturbed adsorption geometry as in the gas phase; see Fig. 6.1C). This should electronically isolate the board from the surface and exhibit a low leakage current to the substrate when the Lander board acts as a molecular wire [262].

In the gas phase the molecule can adopt different conformations, because the spacer groups are to some extent rotatable around the σ bond connecting them to the center board. The minimum energy conformation is reached by a rotation of the spacer legs out of the right-angled orientation relative to the board plane. This rotation approaches the two benzene rings in the spacer groups which leads to an energetically favorable π - π stacking [263].²

²In the right-angled orientation of the spacer groups the benzene groups are separated by 5 Å which

Two spacer groups exist on each side of the center board which can both be tilted to the left or to the right out of the right-angled orientation (Fig. 6.1). Hence, three minimum energy conformations are found: an achiral form with C_{2h} symmetry (eclipsed conformation of legs on opposite sides of the board — Fig. 6.1A) and two enantiomeric, chiral forms with C_2 symmetry (staggered conformation of legs on opposite sides of the board — one form is shown in Fig. 6.1B).

In analogy with the deposition of HtBDC and DC, the Lander molecules were deposited by molecular vapor deposition from a heated crucible. The deposition was performed at a temperature of 550 K after outgassing at 500 K. The exposure time was varied between 5-600 s.

6.3 Adsorption geometries

Upon submonolayer deposition of the Lander at RT, the molecules preferentially decorate the edges of a step (see Sec. 6.4). At higher coverages, the terraces become covered with molecules and single molecules adsorbed in a second layer are visible as bright spots. No particular ordering of the molecules is found, as seen from Fig. 6.2A, except that they all adsorb in the same orientation with respect to the [110] direction of the Cu substrate.

High resolution STM images reveal the Lander molecules as four lobes with an apparent height of $4.8 \pm 0.4 \text{ \AA}$ (Fig. 6.2B). The lobes are arranged in three different ways: two mirror-symmetric, rhomboidal shapes and one rectangular shape.³ This suggests a one-to-one correlation with the minimum energy conformations of the molecules in the gas phase as presented in Fig. 6.1, where also two chiral conformations (rhomboidal shape) and one achiral conformation (rectangular shape) are found.

The four lobes in the STM images seem to correspond to tunneling paths through the spacer legs of the molecule. The two lobes aligned along the close-packed Cu direction are separated by $5.8 \pm 1.1 \text{ \AA}$. This is in good agreement with the distance of spacer groups attached to the same side of the board as expected from the gas-phase molecular model (5.0 Å). In the rhomboidal conformation, the two groups of lobes along the close-packed direction are displaced by $3.1 \pm 1.2 \text{ \AA}$ out of the rectangular arrangement, again in accordance with the model (around 2.5 Å). The lobe distance perpendicular to the close-packed direction, however, is $6.8 \pm 1.9 \text{ \AA}$, much less than expected from spacer-group distances in the gas-phase model (around 10 Å).

To obtain further insight into the adsorption geometries, ESQC calculations have been performed by Jiang and Joachim (CEMES - CNRS, Toulouse, France).⁴

is substantially longer than the equilibrium distance in, e.g. graphite (3.4 Å [173]) or benzene dimers (3.5–3.8 Å [263]). Calculations demonstrate, however, that attractive interactions should be active even at a separation of 5 Å [263].

³The same shapes of the Lander molecules have been found on a Cu(001) surface [264].

⁴The ESQC routine is based on the calculation of the full scattering matrix of the STM tunnel junction [139, 265]. It was used together with a standard molecular mechanics calculation (MM2 routine

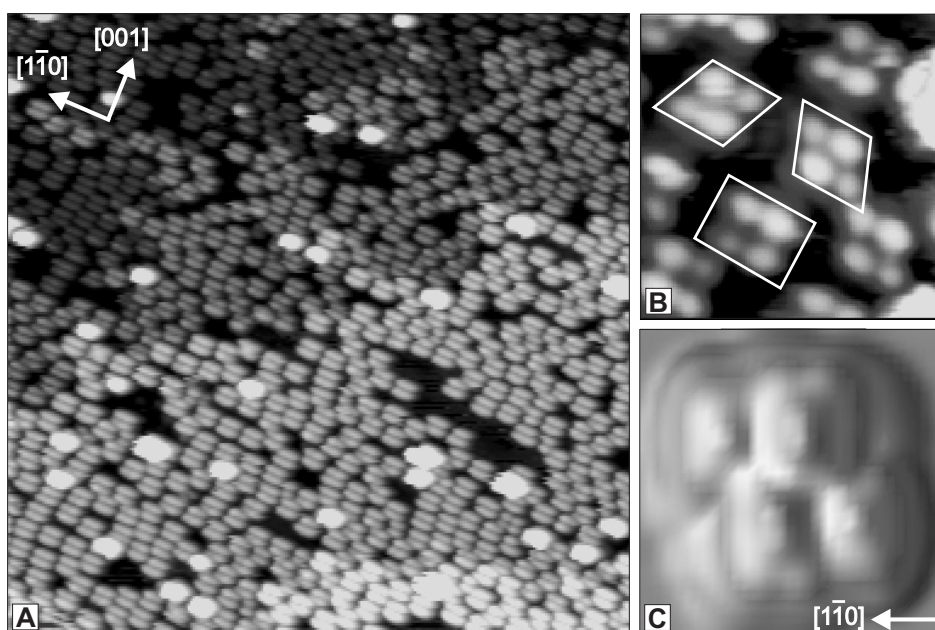


Figure 6.2: (A) STM image of Lander molecules on Cu(110) at RT ($500 \times 500 \text{ \AA}^2$, $V = -955 \text{ mV}$, $I = -0.29 \text{ nA}$). On the Cu terraces (represented as different grey-shades of the molecules) no particular ordering is visible, except that all molecules align along the close-packed Cu direction (indicated in the image). The bright spots are molecules in a second layer. (B) High-resolution STM image ($50 \times 50 \text{ \AA}^2$, $V = -1000 \text{ mV}$, $I = -0.21 \text{ nA}$) of Lander molecules showing three possible geometrical conformations, two molecules for each conformation: rhomboidal shape (top and middle) and rectangular shape (bottom). One of each is marked by a white frame. The three molecular shapes correspond to the three possible molecule conformations shown in Fig. 6.2. (C) Calculated constant-current STM image of the Lander in a chiral conformation revealing the rhomboidal shape (note that in this image the close-packed Cu direction runs horizontally).

In Fig. 6.2C we present a calculated STM image of an isolated molecule with rhomboidal conformation on the flat Cu(110) terrace, using tunneling parameters identical to the experimental ones. The agreement with experiment is very good (allowing for the fact that the tip used in the simulations was atomically sharp, thereby reducing tip convolution effects). The calculations reproduce the rhomboidal arrangement of the four lobes, associated with tunneling channels through the four spacer legs, while the molecular orbitals of the board do not contribute to the contrast — in agreement with experiment.

The ESQC calculations show that the two dimmer lobes are each due to a tun-

with a generalized potential for surface metal atoms) to optimize the conformations of the Lander molecules.

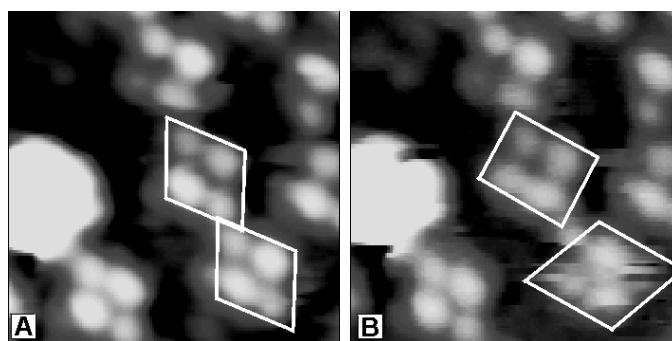


Figure 6.3: STM images of Lander molecules revealing conformational changes ($50 \times 50 \text{ \AA}^2$, $V = -1000 \text{ mV}$, $I = -0.25 \text{ nA}$). **(A)** The center and lower-right molecule show the same rhomboidal shape. **(B)** The center molecule changed to the rectangular shape, while the lower-right molecule reveals a fluctuating conformation while imaging with a dominating rhomboidal shape mirror-symmetric to the original shape.

neling path through one leg only: the top of the leg and then the vacuum before the surface. The two brighter lobes are due to a combination of tunneling channels through two legs on the same side of the Lander: through the top of one leg and then to the bottom of the other leg.

The discrepancy of the lobe distances on opposite sides of the board in the gas-phase model and on the surface is clarified by the ESQC calculations. A strong attraction of the π system of the board towards the metal surface (which was also found for similar molecules [145]) introduces a severe constraint on the legs which leads to an out-of-plane distortion of each leg-board σ bond. In turn, this has the effect of approaching opposite spacer groups as seen in the model in Fig. 6.8B. The calculations hence confirm the notion that all Lander molecules adsorb with the board parallel to the close-packed Cu direction. In summary, the three different molecular shapes found in the STM images correspond to the three possible geometrical conformations of the molecule on the surface (compare to Fig. 6.1).

At RT the molecular conformations sometimes change during the imaging process as demonstrated in Fig. 6.3. The center molecule switches from a rhomboidal conformation to a rectangular shape. The molecule in the lower-right corner which initially has a rhomboidal conformation (A) seems to change its appearance repeatedly during the imaging process in (B). This is indicated by the stripes through the molecule; the dominant shape is the enantiomeric rhomboidal conformation to the one in (A). Switching between the two conformations of the molecule is also possible by STM manipulation at reduced tunneling resistance which is generally accompanied by a lateral displacement.⁵

Lander molecules do not tend to arrange into ordered structures, not even close to full monolayer coverages (Fig. 6.2A). Occasionally, a partial ordering is ob-

⁵Both observations prove that the different conformations belong to the same molecule.

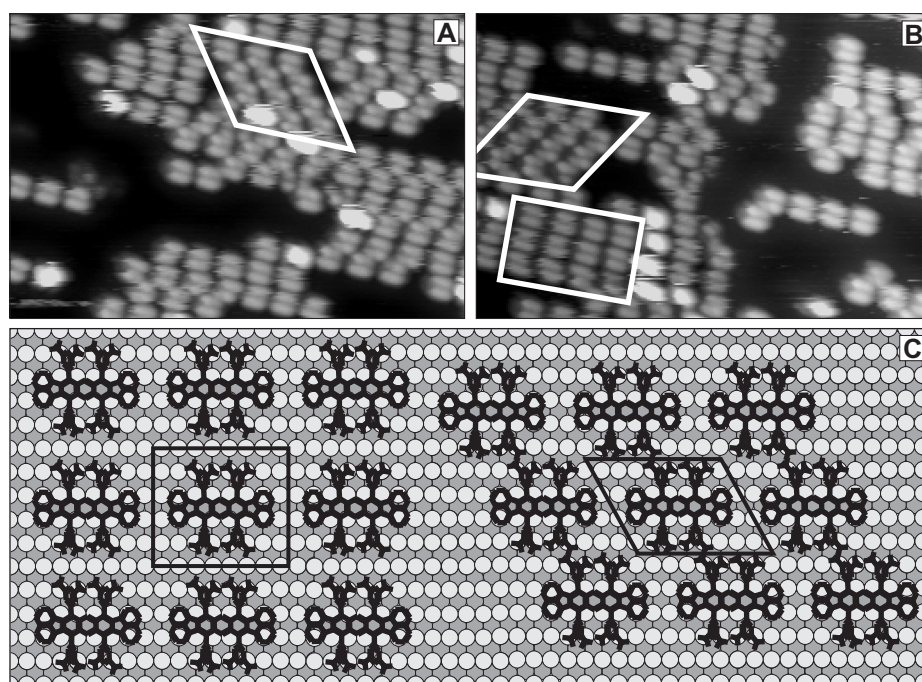


Figure 6.4: Higher coverages of Lander molecules with partial ordering after annealing to 473 K ($300 \times 200 \text{ \AA}^2$, $V = -7071 \text{ mV}$, $I = -0.32 \text{ nA}$). (A) A domain of rhomboidally shaped molecules. (B) Domains of rhomboidally and rectangularly shaped molecules. Note that there is a vertical step edge running through the center of the image; this is why the molecules on the right-hand side are imaged brighter. (C) Ball model of the double row structure. Molecules are shown in black and the unit cells of the rectangular $p(8 \times 5)$ structure and the rhomboidal $\begin{pmatrix} 3 & 4 \\ 8 & 0 \end{pmatrix}$ unit cell are indicated.

served, especially if a RT-deposited film is annealed to around 400 K (or likewise, if the molecules are deposited onto a sample at elevated temperatures). Three different structures are then found which reflect the rhomboidal and rectangular adsorption geometries of the single molecules described above (Fig. 6.4).

In all three domains the molecules are aligned in rows along the $[1\bar{1}0]$ direction with a molecule-molecule distance of around $20 \pm 2 \text{ \AA}$. This corresponds to the van-der-Waals distance of the molecules (see Fig. 6.4C). As revealed in Figs. 6.4A and B, rows of chiral, rhomboidal molecules order into chiral domains that reflect the C_2 symmetry of the molecule. Equivalently, the achiral molecules form achiral, rectangular domains (Fig. 6.4B). Fig. 6.4C shows a model of the domain structures with commensurate superstructures of the molecules. The rectangular $p(8 \times 5)$ and rhomboidal $\begin{pmatrix} 3 & 4 \\ 8 & 0 \end{pmatrix}$ structures are indicated. They differ in the density of molecules in the adsorbate layer: the coverage is $1/40 = 0.025 \text{ ML}$ in the

rectangular and $1/32 \approx 0.031$ ML in the rhomboidal domains.

We can only speculate about the origin of the different domain structures. A closer packing of the rhomboidal compared to the rectangular molecules perpendicular to the close-packed Cu rows may be possible due to the orientation of spacer groups of neighboring Lander molecules pointing in opposite directions. This leads to a staggered approach and avoids steric hindrance between the bulky *tert*-butyl parts of the spacer groups. We do, however, not understand why the molecules in the rectangular domains actually order parallel to each other along the [001] direction. The weak van-der-Waals forces may prevent an arbitrary shifting of neighboring rows along the [110] direction.

It is peculiar that the Lander molecules do not form extended, ordered domains on the Cu(110) surface, while they do so on the even less corrugated Cu(001) surface [264]. In the latter case chains of rhomboidal molecules form already at low coverages along specific crystal directions of the Cu(001) surface and constitute large domains close to monolayer coverage. Chain formation is also observed on the Cu(110) surface (Figs. 6.4A and B). The attractive interaction responsible for this is most likely due to van-der-Waals forces.⁶

6.4 Restructuring processes

The resemblance of the Lander to HtBDC — both exhibiting spacer groups separating the aromatic center part from the substrate — is seemingly not reflected in their adsorption behavior. No particular adsorption geometries or lobe appearances are observed that would indicate a substrate restructuring as in the case of HtBDC adsorption. We nevertheless investigated the adsorption of Lander molecules on Cu(110) in more detail and the results are reported in the following.

As mentioned above, the Lander anchors preferentially to the step edges upon submonolayer deposition at RT, as shown in Fig. 6.5A. To investigate this anchoring, STM manipulation experiments were performed around 100 K on isolated molecules (deposited at RT) adsorbed on step edges. We used the STM tip as a tool to push the molecules away from the step edge in a gentle manner. This manipulation was obtained by reducing the resistance in the STM tunneling junction by about two orders of magnitude, from 5 G Ω to about 50 M Ω (by either increasing the tunneling current or reducing the tunneling voltage, or both), corresponding to a tip-surface approach of about 2 Å. By controlling the precise tip position along the [110] direction during the manipulation, we are able to manipulate individual molecules one at a time, leaving the rest of the scan area unperturbed.

Surprisingly, such manipulations disclose an underlying restructuring of the monoatomic Cu steps induced by the docked molecules. A manipulation sequence is shown in Figs. 6.5A–F in which neighboring molecules [labelled (1–5) in the images] are successively removed from the step edge. A tooth-like metal nanostructure appears at the site where the molecules were previously attached

⁶The recently reported ordering of pentacene molecules on Cu(110) due to a substrate-mediated repulsion [58] does not seem to be a reasonable explanation of the attractive interaction in our case.

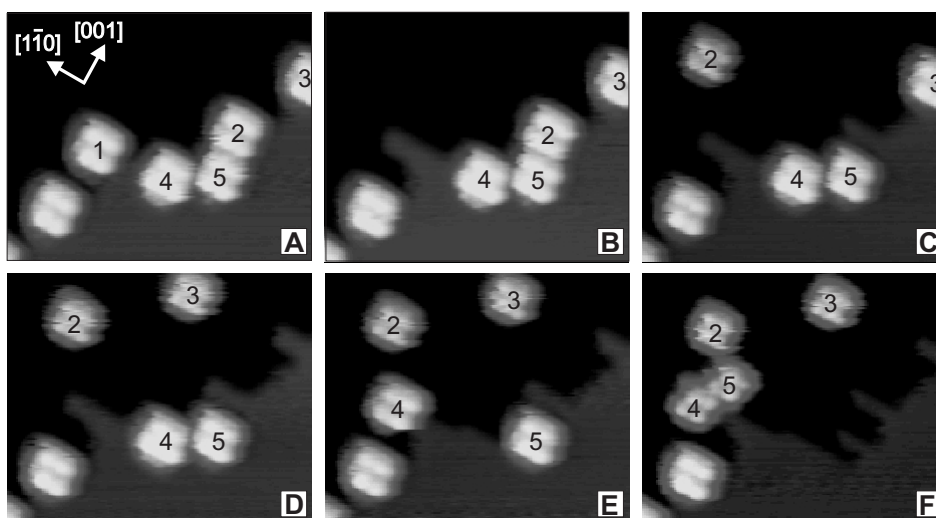


Figure 6.5: (A-F) Manipulation sequence of the Lander molecules from a Cu(110) step edge showing the tooth restructuring underneath ($136 \times 112 \text{ \AA}^2$, $V = -1768 \text{ mV}$, $I = -0.37 \text{ nA}$, $T = 95 \text{ K}$). The molecule numbers (1-5) label their order of manipulation along the $[1\bar{1}0]$ direction (tunneling parameters for manipulation: $V = -55 \text{ mV}$, $I = -1.05 \text{ nA}$). Note that molecule (1) is located outside the imaging area after the manipulation. Molecule (4) is not located on a tooth before the manipulation, but is then moved onto the tooth formerly occupied by molecule (1).

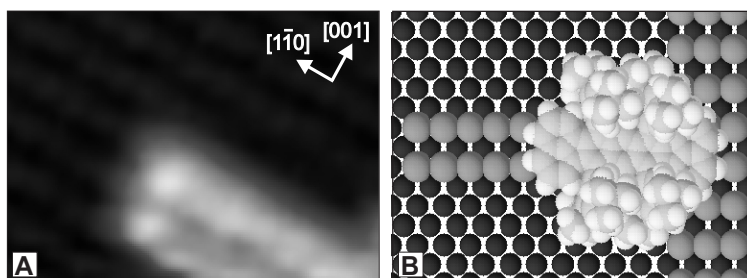


Figure 6.6: (A) Zoom-in of smooth-filtered STM image ($41 \times 25 \text{ \AA}^2$, $V = -1770 \text{ mV}$, $I = -0.75 \text{ nA}$) showing the characteristic two row width of the tooth-like structure after removal of a single Lander molecule from the step edge. The Cu rows of the surface terrace are also visible and the arrows indicate the directions on the surface. (B) Model of the Lander on the tooth-like structure with the board parallel to the tooth. For clarity, the length of the tooth is extended beyond the molecule.

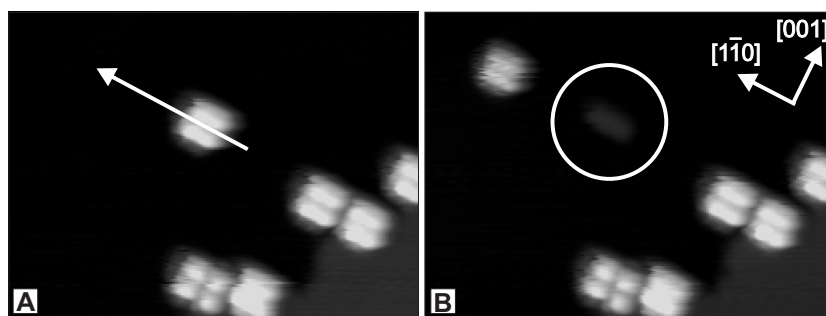


Figure 6.7: Manipulation of a Lander molecule on a Cu(110) terrace at 95 K ($200 \times 150 \text{ \AA}^2$, $V = -1769 \text{ mV}$, $I = -0.28 \text{ nA}$). (A) Before manipulation. The arrow marks the manipulation direction. (B) After manipulation (tunneling parameters for manipulation: $V = -55 \text{ mV}$, $I = -1.05 \text{ nA}$). The circle marks the Cu rows that are found where the molecule was adsorbed initially.

[except for molecule (4) which was located on the upper terrace]. We can rule out that the tooth-like structures are induced by the STM tip, since no such structures are formed when we perform exactly the same manipulation at a step region where no molecules were present initially.⁷

The tooth-like structures are atomically resolved in Fig. 6.6A. They have a width of $7.5 \pm 0.5 \text{ \AA}$ which, taking possible tip convolution effects into account, agrees with the dimension of two neighboring, close-packed Cu-rows (6.2 \AA). The length is $18.5 \pm 3.5 \text{ \AA}$ (corresponding to around 7 atoms per row). For comparison, the aromatic board of the Lander has comparable dimensions, being 17 \AA long and 5.8 \AA wide. Fig. 6.6B presents the conformation of the molecule adsorbed on a tooth-like structure consisting of two Cu rows along the $[1\bar{1}0]$ direction.

As opposed to the manipulation of molecules at steps, which nearly always disclosed the underlying restructured tooth, the manipulation of molecules on the Cu terraces did usually not reveal a restructured surface. It was, however, possible to find molecules, where an equivalent tooth structure was formed on the plane surface (Fig. 6.7). The dimensions of these teeth are identical to the teeth attached to a step.⁸

ESQC calculations confirm that adsorption of the Lander board parallel to the copper rows on the tooth is energetically preferred relative to the perpendicular orientation. Calculated scans across the Lander on the tooth (Fig. 6.8A) and on a flat terrace (Fig. 6.8B) imply a different height (5.0 versus 4.5 \AA) and width (8.3 versus 6.3 \AA) of a molecule in the two adsorption environments due to a more vertical conformation of the legs when adsorbed on the tooth compared to its

⁷At 100 K the mobility of Cu kink atoms is practically frozen out and the step edge shape is stable over time.

⁸A restructuring similar to the HtBDC molecules, forming holes in the surface under the spacer groups, can be excluded from the lobe heights on the plane terrace.

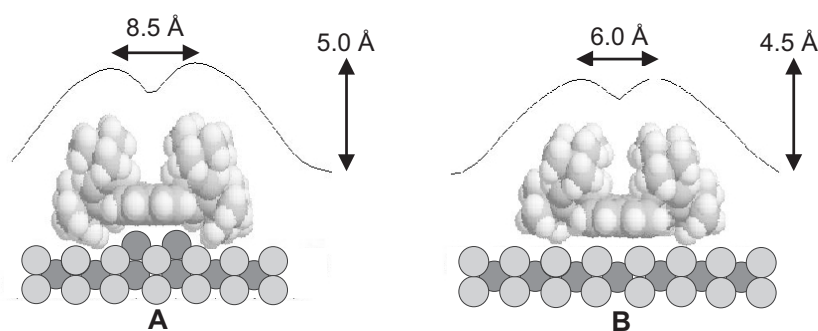


Figure 6.8: Cross-sectional view of the Lander on (A) a tooth and (B) a terrace. The plots are from calculated STM images, showing the width of two spacer groups across the tooth and their height with respect to the Cu(110) surface.

conformation on the flat terrace.

The reason is the almost restored planarity of the leg-board σ bonds relative to the board. When the Lander is on the tooth, its board is lifted up relative to the surface. This reduces the steric constraint on the leg-board σ bond and leads to an increased width and height. This was confirmed by our experimental results. The lobe distances across the tooth decrease from 8.5 ± 2.5 Å on the tooth to 6.8 ± 1.9 Å on a flat Cu(110) terrace, and in the same way, the molecules' height decreases from 5.8 ± 0.5 to 4.8 ± 0.4 Å.⁹ The reduced height on the terrace is clearly seen in Fig. 6.5.

In analogy with Sec. 4.3.3, EMT calculations were performed by means of Eq. (4.1) to shed light on the energetics of the restructuring process. The energy necessary to move a kink atom (k) to a position i in the tooth structure is calculated successively. The labelling of the atoms in the following refer to Fig. 6.9, and the results are presented in Tab. 6.1.

For the tooth at the step only the formation of the first row (1-7) costs energy (0.04 eV per atom mainly due to NNN changes), while the formation of the second row does not lead to energy changes. Overall, the creation of a step tooth requires an energy of 0.28 eV.

As a result of the reduced number of nearest neighbors of the terrace atoms ($\bar{1}$) and ($\bar{8}$) compared to the step atoms (1) and (8), the situation is slightly different for a tooth on a terrace. The movement of kink atoms (k) to the positions ($\bar{1}$) and ($\bar{8}$) therefore requires a large formation energy (0.28 and 0.24 eV, respectively), while the other atoms ($\bar{2}$ - $\bar{7}$) and ($\bar{9}$ - $\bar{14}$) encounter the same energetic situation as the equivalent atoms in the step tooth, (2-7) and (9-14). The formation of a terrace

⁹To ascertain that the STM tip did not influence the conformation of the molecules during the manipulation process, we checked the internal distances of more than 100 molecules on bare terraces. The values found are consistent with the ones obtained from manipulated molecules, and we therefore rule out the possibility that the conformational change may be induced by the STM tip.

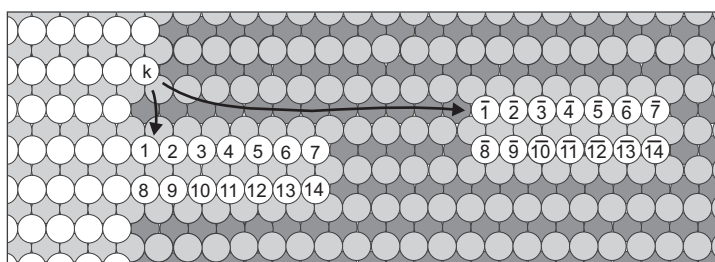


Figure 6.9: Labelling of tooth atoms attached to a step (1-14) and on the terrace ($\bar{1} - \bar{14}$) referring to Tab. 6.1. “k” marks a kinkatom.

atom label i	at step		on terrace			
	1-7	8-14	$\bar{1}$	$\bar{2}-\bar{7}$	$\bar{8}$	$\bar{9}-\bar{14}$
ΔE_i	0.04	0.0	0.28	0.04	0.24	0.0
$\sum_1^{14} \Delta E_i$	0.28		0.75			

Table 6.1: Formation energies ΔE_i of the step-tooth and terrace-tooth atoms out of kink atoms on Cu(110) in eV obtained successively corresponding to their label numbers (Fig. 6.9) by means of EMT via Eq. (4.1).

tooth requires an overall energy of 0.75 eV.

This tooth formation energy has to be balanced by the gain in the molecule’s adsorption energy. A lower bound for the gain in adsorption energy is hence given by the terrace-tooth formation energy $\Delta E_{\text{metal}} = 0.75$ eV. The lower value for the tooth formation at a step leads to a much higher energy gain and explains the dominance of step-tooth structures.¹⁰

The driving force behind the restructuring is the increase in adsorption energy on the tooth structure. One contribution is the increased interaction of the aromatic π system of the Lander board with the surface due to their closer proximity. Additionally, the tooth contains reactive low-coordinated Cu atoms (see Chap. 3 for details). We saw in the ESQC calculations that on a plane surface such an interaction is only possible when accompanied by severe spacer group deformations (Fig. 6.8B). Adsorption on a tooth is hence accompanied by a strain release in the σ bond of the spacer groups to the aromatic board (Fig. 6.8A) which is the second contribution to the energy gain.

The overall process for the anchoring of a molecule to a Cu nanostructure can thus be described qualitatively as follows. At RT the molecules adsorb on the surface and migrate towards the steps edges which appear frizzy in STM images

¹⁰A tooth structure is more likely to grow on a step, since the supply of Cu atoms is much larger than on a terrace, where only diffusing adatoms are available (see below).

due to the high mobility of Cu kink atoms even at RT.¹¹ Due to a strong interaction with the π system of the molecule, it encourages the fluctuating Cu step adatoms to arrange themselves in the tooth-like structures, and at the same time locally anchors to the nanostructure at the step edges. Equivalently, on a terrace the tooth structure growth is initiated when a molecule meets a Cu adatom. Subsequently more adatoms are captured to form the structure.

6.5 Conclusions

In this chapter, we studied the adsorption of the Lander molecule on a Cu(110) surface. Different conformations of the molecules are found on the surface, all with the aromatic board parallel to the substrate. The orientations of the spacer groups then determine the final conformation. The Lander molecules barely order into domains; only small domains (reflecting the symmetry of the molecule conformations) are occasionally observed.

By STM manipulation we have shown that the Lander molecule locally restructures monatomic steps, acting as a pinning center for step edge fluctuations on the Cu(110) surface. By means of a thermally activated process portions of step edges are reshaped into teeth which are two atomic rows wide and around seven atoms long.

The teeth are the preferential adsorption sites for the Lander molecules. As in the case of HtBDC molecules on Cu(110), an important interaction between the molecule and the substrate is achieved through the aromatic π system. This is emphasized by the fact that the bond of the spacer groups to the aromatic board is severely bent to enable bonding of the aromatic board to the substrate. The lift-up of the aromatic board on top of the tooth enables a better π interaction with the substrate while at the same time strain is released in the spacer group bond. A lower bound for the gain in adsorption energy on the tooth structure was calculated from EMT to be 0.75 eV.

The results demonstrate that large and hence flexible molecules can adopt adsorption structures on metal surfaces which may involve unpredicted restructuring of the surface. In contrast to HtBDC on Cu(110) and other studies where a surface restructuring was indicated by height corrugations of the molecule adsorption layers in STM images, a restructuring would hardly be postulated underneath the Lander molecules just judging from adsorption geometry.

Together with the examples of HtBDC molecules this emphasizes not only the importance of manipulation experiments to investigate the adsorption of large molecules on surfaces, but also suggests that surface-restructuring processes may be more common than generally believed for the adsorption of large molecules. In general, the separation of a strongly bonding molecule part (π system) from a metal surface seems to be a driving force behind the restructuring of the metal surface in order to adjust a suitable interaction geometry.

¹¹At 300 K the mean residence time for a step is shorter than the time needed to scan across the corresponding distance of kink sites [266].

Inspired by molecular electronics, the formation of the tooth structure can be interpreted as a process, where a single Lander molecule creates its own metallic nanocontact at a step edge. These nanocontacts may provide a route to self-fabricate appropriate electronic interconnects. This extends the general vision of self-assembled devices to self-fabricated contacting to the outer world at the atomic scale. The contact formation to single molecules is, in spite of achievements in lithography, still a basically unsolved task. Its importance is fundamental also for the current research field of measuring the conductance through single molecules [267].

CHAPTER 7

Surface diffusion of large molecules

In this chapter the one-dimensional diffusive motion of large organic molecules on Cu(110) is investigated using scanning tunneling microscopy. The diffusion properties of two chemically closely related molecules are investigated: decacyclene (DC) and hexa-*tert*-butyl decacyclene (HtBDC). Beside the Arrhenius parameters (activation energy and prefactor), the root mean-squared jump length is determined using a new and simple approach based on a fundamental statistical relation of the random walk process. It is demonstrated that a simple model including only nearest neighbor hopping is not valid and that long jumps thus participate in the diffusion process. Monte Carlo simulations are presented in order to evaluate the validity of the approach. The chapter is based on paper [IV].

7.1 Introduction

The migration of atomic and molecular adsorbates across surfaces plays an important role for physical and chemical processes like chemical reactions, epitaxial film growth, and crystallization. A profound knowledge of adsorbate migration is hence a prerequisite for understanding these complex processes. A delicate balance between the adsorbate-adsorbate and adsorbate-substrate interactions determines the nucleation and growth of nanostructures at the molecular level. Accordingly, it is important not only to learn about the *static* behavior of adsorbates (as was done in the previous chapters), but also their *dynamic* behavior.

The first indication that the growth of crystals is not only governed by adsorption and desorption processes but also by surface diffusion dates back to 1921 when Volmer and Estermann investigated the growth of Hg platelets with a light microscope [268]. The aspect ratio (diameter–thickness) of the platelets was as large as $\approx 10^4$ and prompted them to deduce the process of surface diffusion of deposited Hg atoms on the basal plane of the platelet. Since then numerous studies have tried to elucidate the involved microscopic processes. The experimental techniques used to study surface diffusion can roughly be divided into two groups [85]. These will be described in the following.

In the first group, concentration profiles of adsorbates and their evolution in time are measured. The initial profile represents a non-equilibrium distribution of the adsorbates and the spatio-temporal evolution is governed by Fick's second law

$$\frac{\partial n}{\partial t} = -D^* \nabla^2 n, \quad (7.1)$$

where n is the density of adsorbates and D^* is the chemical diffusion coefficient. Historically, data on surface diffusion have been obtained by techniques like scratch smoothing, grooving of grain boundaries or changes in the shape of field emitters, which all measure mass transfer involving a rearrangement of the surface itself [269]. Even today, the majority of techniques applied (like laser induced thermal desorption (LITD) [270]) are integral. These have the disadvantage to average over all surface features such as flat terraces, step edges, kinks, and defects, i.e. it is not possible to separate the individual contributions.

The second group summarizes the so-called equilibrium methods, where the diffusive motion of the adsorbates is followed for adsorbates homogeneously distributed over the surface. The two outstanding methods used for this are field ion microscopy (FIM) and STM which set one into position to follow the temperature-dependent movement of individual adsorbates on a well-defined, defect free surface terrace.¹ This was for the first time demonstrated using FIM by Ehrlich and

¹Within the field of STM the rate equation approach is a widely used method to derive quantitative information on surface diffusion by investigating the temperature dependence of the island number density [271, 272]. This is, however, an indirect way that does not require one to follow individual adsorbates, and is not discussed further here.

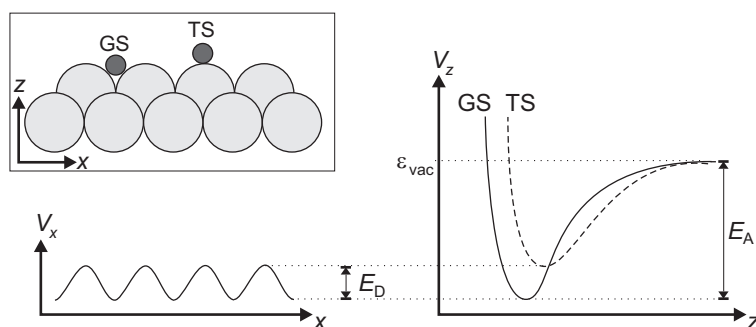


Figure 7.1: The frame shows a side-view of a substrate (grey circles) with adsorbates (black circles) in the ground state (GS) and the maximum energy transition state (TS). Cross sections of the potential energy hypersurface are shown parallel to the surface (x direction, left-hand side) and perpendicular to it (z direction, right-hand side). The adsorption energy E_A , the energy barrier for diffusion E_D , and the vacuum level ε_{vac} are indicated.

Hudda in 1966 [273].² From these studies the so-called tracer diffusion coefficient D can be determined which is connected with random motion of individual particles, and is defined by the long-time limit of the mean-squared displacement $\langle(\Delta x)^2\rangle$ in the time interval t as

$$D = \lim_{t \rightarrow \infty} \langle(\Delta x)^2\rangle / 2mt, \quad (7.2)$$

where m is the dimensionality of the system, i.e. 1 or 2 for one- and two-dimensional diffusion, respectively, as will be discussed in more detail in Sec. 7.3. The difference between D^* and D can be ascribed a thermodynamic factor by $D^* = D[\partial(\mu/kT)/\partial \ln \theta]_T$ (μ is the chemical potential and θ the coverage of the adsorbates) [85]. Both diffusion constants depend on the temperature and the coverage, and tend to be identical for $\theta \rightarrow 0$. This was demonstrated in an ingenious experiment at the atomic scale using STM [276].

A qualitative picture describing the microscopic situation of surface diffusion is sketched in Fig. 7.1. Adsorbates occupy specific sites of lowest potential energy on an ordered substrate and have an adsorption energy E_A with respect to the vacuum level. As seen from the cross section of the potential energy hypersurface at the surface, the minimum energy adsorption sites (ground state) are connected by transition states which represent local maxima in the adsorption energy. The energy difference between the ground state and the transition state is E_D and usually amounts to 10-30% of E_A [277]. An adsorbate is therefore able to move from one adsorption site to another without detaching from the surface.

²Since then FIM has been used intensively for atomic-scale diffusion studies [84]. The first STM study on diffusion was performed by Binnig and coworkers in 1986 [274], but it was not until 1992 that displacements of individual adsorbates have been followed [275].

The energy required to overcome the diffusion barrier E_D stems generally from the substrate in the form of thermal energy supplied by the phonon bath. Hence, the diffusion rate does not only depend on E_D and T , but also on the coupling of the adsorbate to the substrate, determining the speed of excitation and de-excitation of the adsorbates. A strong coupling leads to a fast de-excitation of the excess energy gained while passing over the transition state. In this case the particle will spend a certain time in its adsorption site before again gaining enough energy to move further. If this time is long compared to the time needed to surpass the transition state (typically in the order of a period of a vibrational mode, i.e. 10^{-12} s), the particle loses all memory of the direction where it came from, leading to a random walk process. The random walk picture is no longer valid if the thermal energy $kT \gtrsim E_D$; the adsorbate then moves quasi continuously over the surface.

Atomic-scale diffusion studies of metal/semiconductor adatoms have been performed quite detailed by FIM [84, 278, 279] and recently also by STM [91, 218, 280–286]. Details of the diffusion process — beyond the usual determination of the activation energy for diffusion and the prefactor — have also been addressed. A fundamental question is if *long jumps* (i.e. jumps of length beyond the NN distance) are important for the microscopic description of the diffusive motion. Only few FIM and STM studies of metal-on-metal diffusion have treated this problem and revealed jumps up to 3 NN distances in length [89–91, 287]. These studies rely on a statistical analysis of the *complete* displacement distribution, if an atomically resolved data set is available, as demonstrated by Ehrlich [89, 287].

Even though STM — as opposed to FIM — also allows the study of non-metallic adsorbates and molecules [87, 125, 127, 219, 276, 288–290], very little is known about the basic diffusion parameters of organic molecules on surfaces. Most of the available data for organic molecules result from integral LITD studies [291], while atomic-scale STM data for molecule diffusion are rare. So far results have been obtained mainly for small molecules like acetylene and benzene and are often based on rough estimates of the diffusion barriers (assuming standard attempt frequencies) [292–295]; larger organic molecules are hardly ever investigated [92–94].

This lack of information for larger molecules was the motivation for our study of the diffusion of large organic molecules. We aimed to set up a detailed diffusion study in order to compare results gained through fundamental properties: the tracer diffusion constant D and the hopping rate h (see Sec. 7.3 for details). Furthermore, to the best of our knowledge, no previous experimental studies address the important question of long jumps in connection with molecules, even though MD simulations predicted long jumps to play an important role [296]: the molecule-substrate interaction is reduced for molecules as compared to metal-on-metal diffusion.

The reason why long jump data lack for organic adsorbates is related to the normal procedure for extracting this information which goes back to Ehrlich (see Sec. 7.4.1). Such an analysis not only requires a huge and lattice-resolved data set which is often not available for large molecules since a simultaneous resolution

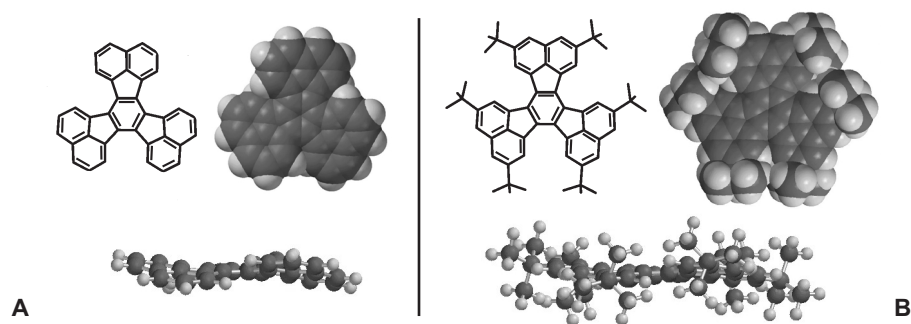


Figure 7.2: Chemical structure and space-filling model (top) of (A) decacycene (DC) and (B) hexa-*tert*-butyl decacycene (HtBDC). The additional *tert*-butyl groups in the HtBDC molecules separate the centered π system from the substrate as is seen from the side-view (bottom).

of the molecules and the substrate is in most cases not achievable. It moreover becomes practically inapplicable if jump lengths of up to several NN distances contribute.

We demonstrate a new and simple approach to gain information about the root mean-squared (RMS) jump length that is feasible even if exact displacement distributions are not available or very long jumps contribute. The method utilizes the fact that D and h are connected via the RMS jump length λ through a well-known statistical relation [Eq. (7.6) in Sec. 7.3.1]. This approach must have been overlooked in earlier studies since all experiments based on D have, in principle, also h available, as will be demonstrated.

A general motivation to study *large molecules* is their actual and future importance in fields and applications concerned with thin organic films. The two molecules investigated, HtBDC and DC, have been described in detail in Chap. 4 and 5 and are for reasons of comparison shown again in Fig. 7.2. Their similar chemical structure allows a direct comparison of the microscopic diffusion mechanisms: we expect that the presence/absence of spacer groups modulates the diffusivities of the DC and HtBDC molecules on the Cu(110) surface. The conformational rigidity of the molecules avoids possible complications in the diffusion mechanism as is the case with flexible molecules like alkanes [270, 297, 298].

7.2 Data acquisition

The experiments were performed in a UHV chamber equipped with a variable-temperature STM of the Aarhus type (Sec. 2.2.2). The HtBDC and DC molecules were deposited onto the clean Cu(110) surface as described in Chap. 4 and 5, respectively. There we saw also that at RT HtBDC molecules anchor to the substrate via a restructuring of the topmost Cu layer. In order to study the diffusion of

HtBDC molecules on the *plane* Cu(110) surface, it was therefore necessary to deposit the HtBDC at a substrate temperature below 250 K. It is possible to deposit DC at RT since no substrate restructuring occurs for this molecule.

After deposition of the molecules, the sample was transferred to the STM (pre-cooled to the desired temperature) for imaging. Series of time-lapse STM images (256×256 pixels) are acquired in the constant-current mode using active drift compensation to keep the same section of the surface in view. When these images are played back as an STM movie they impart a vivid impression of the diffusion process.³

The image size of $500 \times 500 \text{ \AA}^2$ was chosen as a compromise between two opposing requirements: On one hand, the sample temperature increases slightly during data acquisition (see Sec. 2.2.2) which limits the accessible time for collecting data in a narrow temperature range ($< 2 \text{ K}$) to about 30 min. In order to collect a data base with appropriate statistics (around 1000 observations) during this time, large scale images are needed to image a reasonable number of molecules (considering that the molecules are fairly large and mutual molecule interactions have to be avoided by working at low coverages). On the other hand, small-scale images are needed to resolve the hopping distances as accurately as possible and to reduce the image acquisition time.

An example of successive images from an STM movie of HtBDC on Cu(110) at $T = 194 \text{ K}$ is shown in Fig. 7.3. The molecules' internal structure is hardly resolved in the large-scale images and they are mainly imaged as protrusions. The diffusion of DC and HtBDC is observed to be one-dimensional, parallel to the $[1\bar{1}0]$ direction of the Cu(110) substrate.⁴ In the case of HtBDC, this can be explained by assuming that the *tert*-butyl groups "slide" into the troughs of the close-packed Cu rows which results in a lower activation energy for diffusion parallel to the $[1\bar{1}0]$ direction rather than perpendicular to it. A similar explanation is questionable for DC which lacks the protruding *tert*-butyl groups. DC is, however, not just a plane molecule but exists in a distorted configuration which seemingly must be responsible for its preferential one-dimensional movements.

The lack of attractive molecule-molecule interactions prevents clustering into islands, and the molecules hence are distributed randomly over the surface. A certain fraction of them is pinned to step edges, but only those on the terraces are considered for diffusion analysis. The average distance between molecules is around 100 \AA which is sufficiently large for mutual molecule-molecule interactions to be neglected.

The temperature range in which the diffusion could be studied was around 170–200 K for HtBDC and 220–250 K for DC. The lower limit is given at temperatures where the number of jump events is zero in the limited time frame available. The upper limit is set by the temperatures where the displacements of single molecules can be followed unambiguously without mixing up molecules.

³Examples can be found at: <http://www.ifa.au.dk/camp/stmmovies.htm>.

⁴Displacements of molecules along the $[001]$ direction occasionally occurred at elevated temperatures. This does, however, not influence our analysis since diffusion parallel and perpendicular to the $[1\bar{1}0]$ direction can be considered as independent.

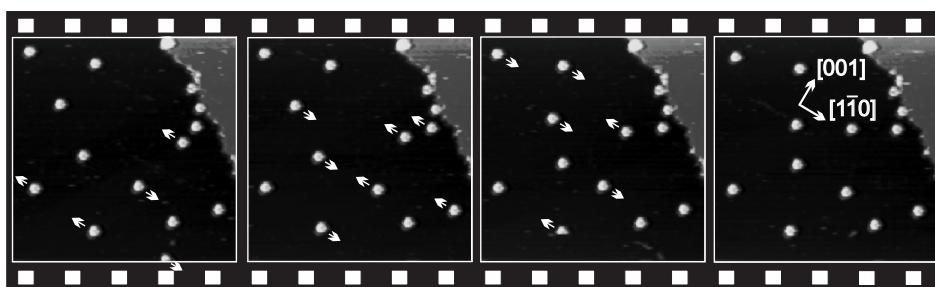


Figure 7.3: Stills from a constant-current STM movie of HtBDC molecules, imaged as bright spots, on Cu(110) at $T = 194$ K ($V = -1768$ mV, $I = -0.61$ nA, $500 \times 500 \text{ \AA}^2$). The arrows clarify the one-dimensional motion of the molecules between successive images along the $[1\bar{1}0]$ direction of the Cu substrate (crystal directions are indicated in the last frame). Molecules are immobilized at the step edge in the upper right corner. Each frame is acquired in 13.9 s. Find the complete movie under <http://www.ifa.au.dk/camp/movies/ht79.mpg> (total length 32 min, 143 frames).

For both molecules around 10 STM movies have been recorded where the number of image-to-image observations of molecules amounts to 400-2500 for each movie. In order to analyze this large data set a semiautomatic pattern-recognition routine was used. The routine is based on the same image recognition algorithms for fine-tuning the drift rate as described in Sec. 2.2.2. A template is placed around a molecule and the algorithm tries to find a match with this template in the following image. The found position has to be confirmed manually and is stored; the program then proceeds to the next image.⁵ This must be done for all molecules in the field of view.

It is in principle then possible to calculate the displacements from the changes in the pixel positions. This requires, however, the drift in the recorded movies to be exactly zero, which is usually not possible to achieve in practice. It is therefore necessary to track the position of an immobile feature like a kink site or an immobilized molecule at a step edge. The displacements can now be calculated from the pixel positions of the tracked molecules *relative* to the pixel positions of the immobile feature. The displacements are finally converted from values given in pixel positions to values measuring Ångström via the (calibrated) image size.

7.2.1 Tip influence

It was demonstrated in the early 1990ies that the STM tip can not only be used to image surfaces and adsorbates but also to manipulate them [26, 220, 221]. When studying diffusion of adsorbates any influence from the tip must be avoided. Such influences are encountered even for the strong interaction of atomic metal and

⁵The algorithm checks only a certain area around the original position, i.e. for very long displacements the template has to be set again manually.

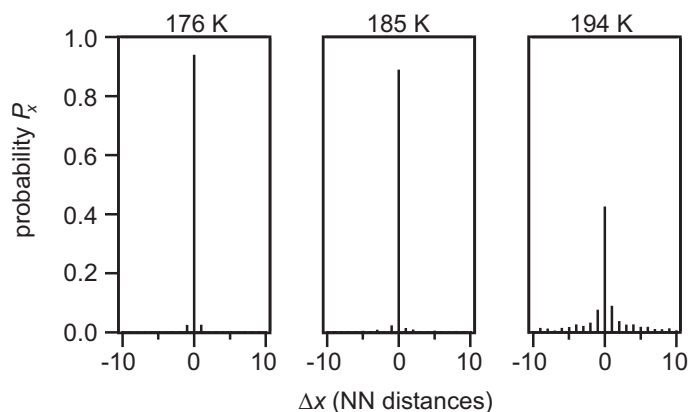


Figure 7.4: Example of normalized displacement distributions of HtBDC as deduced from STM movies with image acquisition times of 13.7 s at 176 K, 185 K, and 194 K (883, 1020, and 1297 observations, respectively). The distributions are symmetric and the mean values $\langle \Delta x \rangle$ are located close to 0 NN distances (0.03, 0.04, and 0.12, respectively). The accelerated evolution of the mean-squared displacement with increasing temperatures is clearly seen.

semiconductor adsorbates [275, 299–301]. The phenomenon was also treated theoretically and revealed that besides a direct attractive/repulsive interaction between the adsorbate and the tip, the tip can also modulate the potential energy hypersurface and thereby indirectly influence the diffusion process via the activation energy of the diffusion process [302–304].

By choosing proper tunneling conditions all influence of the scanning process on the displacement or the hopping rate of the DC and HtBDC molecules can be avoided. This is discussed in further detail in the following.

In general, we tried to minimize the tip influence by usually scanning with a tunneling resistance above 5 G Ω ($V \approx -1500$ mV, $I \approx -0.3$ nA). To clarify whether or not the tip influences the diffusion process we inspected the displacement distributions. Displacement distributions were binned according to the lattice constant of Cu(110) along the $[1\bar{1}0]$ direction (2.56 Å), since we known from high resolution, small-scale images that the molecules indeed have specific adsorption sites which are spaced in integral multiples of the NN lattice distance. As exemplified in Fig. 7.4, the resulting displacement distributions are symmetric with mean values $\langle \Delta x \rangle = 0.0 \pm 0.8$ Å, indicating no tip influence.

We further investigated possible tip artifacts by varying the “interaction” time between the molecule and the tip, i.e. the time the tip actually scans right over a molecule. This was done by either changing the image size and/or acquisition time which resulted in a variation of the interaction time between 30% and 300% (compared to regular 500×500 Å² images acquired in ≈ 14 s). No deviation beyond the usual spread around the linear Arrhenius plots was obtained. This

confirms that there is no influence of the scanning process, neither on the hopping rate nor on the hopping displacements.

Finally, the tip influence was investigated by performing controlled STM manipulation experiments. It was impossible to manipulate DC and HtBDC if tunneling resistances above 100 M Ω and 1 G Ω were used, respectively which is well below the values used for imaging. All the results support the conclusion that the obtained diffusion parameters are not influenced by the scanning process.

7.3 Theoretical background

This section summarizes the background necessary to analyze our experimental data [84, 85, 305–307]. Restricting us to the one-dimensional case only, the fundamental parameters describing a diffusion process are defined in Sec. 7.3.1. Theories dealing with diffusion rates are discussed in Sec. 7.3.2.⁶

7.3.1 General relations

The jumps of an adsorbate, migrating from adsorption site to adsorption site, can be considered as being independent of each other if the duration of a hop (the correlation time) is orders of magnitude shorter than the time between hops (the residence time). In this case the particle loses its memory about the previous jump direction, because of its vibrational motion in the adsorption site. The migration can hence be described as a symmetric random walk, where it is equally likely to hop in either direction. A theoretically appropriate representation of such a process is the *Poisson process* that is characterized by a mean hopping rate h [311].⁷ The mean-squared displacement $\langle(\Delta x)^2\rangle$ of an adsorbate during the time interval t is then given by⁸

$$\langle(\Delta x)^2\rangle = \lambda^2 ht. \quad (7.3)$$

Herein the root mean-squared (RMS) jump length λ is defined as

$$\lambda^2 = \sum_i p_i \lambda_i^2. \quad (7.4)$$

The probability p_i of making a jump of length $\lambda_i = i$ NN distances is generally referred to as the jump length distribution function (jump lengths will throughout the chapter be denoted in units of the NN distance of the substrate atoms). It is

⁶Mathematical aspects of the random walk can be found in Refs. [308, 309]; special aspects of exponentially distributed jump lengths are considered in Ref. [310].

⁷Details on the definition of a Poisson process, as well as a discussion of the validity of describing diffusion as a Poisson process, can be found in App. B.

⁸Note that we define the hopping rate h as the *overall* number of hops out of the adsorption site irrespective of its direction. This differs throughout the literature where it is often defined as the number of hops in a *certain* (of all possible symmetry-equivalent) directions, which then leads to a *directional* hopping rate reduced by a factor 2.

noteworthy that Eq. (7.3) does not have any restrictions on p_i , even though it is often stated only for the case of NN hopping $\lambda = 1$ (i.e. $p_1 = 1$) [296, 312].

It is a characteristic property of a diffusion process that the mean-squared displacement $\langle(\Delta x)^2\rangle$ scales linearly with t , as seen from Eq. (7.3). It is therefore convenient to define the tracer diffusion coefficient D as a time-independent constant of the diffusion process by⁹

$$D = \lim_{t \rightarrow \infty} \frac{\langle(\Delta x)^2\rangle}{2t}, \quad (7.5)$$

which by means of Eq. (7.3) can also be expressed as

$$D = \frac{1}{2}\lambda^2 h. \quad (7.6)$$

The temperature dependence of the hopping rate h is often expressed in a way (generally referred to as the *Arrhenius form*) that was first proposed by Arrhenius for thermally activated processes [315]:

$$h = h_0 e^{-E_D/kT}. \quad (7.7)$$

Here, h_0 is the hopping rate prefactor, E_D the activation energy for the diffusion process, k Boltzmann's constant, and T the temperature. The activation energy of diffusion E_D is typically extracted from a so-called Arrhenius plot ($\ln h$ versus $1/kT$) along with the hopping prefactor h_0 .

Due to the connection of D and h through Eq. (7.6) the temperature dependence of D is given in a similar way:

$$D = \frac{h_0 \lambda^2}{2} e^{-E_D/kT} \equiv D_0 e^{-E_D/kT} \quad (7.8)$$

with the tracer diffusion prefactor D_0 . Again, E_D can be extracted from an Arrhenius plot ($\ln D$ versus $1/kT$), this time along with the tracer diffusion prefactor D_0 .

It follows from Eqs. (7.6), (7.7) and (7.8) that an equivalent relation as Eq. (7.6) holds for the prefactors:

$$D_0 = \frac{1}{2}\lambda^2 h_0. \quad (7.9)$$

⁹In an STM measurement t is determined by the time lapse between two images which is typically a few seconds. The question arises if these short times satisfy the condition to define D ($t \rightarrow \infty$). The "idea" behind the condition $t \rightarrow \infty$ is to avoid statistical fluctuations by collecting data of as many hopping events as possible. Fluctuations of the mean-squared displacement $\langle(\Delta x)^2\rangle$ around the linear t -dependence have also been demonstrated theoretically for very short times (ps) and are due to the oscillating motion between barriers [296, 313]. A more fundamental condition in the definition of D would be via the number of hopping events N as $N \rightarrow \infty$.

This can be rationalized from the ergodic theorem stating that the time average for a given system is equal to the ensemble average at a given time [314]. While the above given definition for $t \rightarrow \infty$ is based on the time average of a single particle followed in time, STM measurements represent an ensemble average: every image obtained in a (short) time interval t collects information on many particles and this is done repeatedly in several images, hence the overall information represents an ensemble average.

In the next section it is discussed how the phenomenological Arrhenius dependence of h and D (that is often observed in experimental measurements) can be explained from a theoretical point of view, and what is the physical significance of the prefactors h_0 and D_0 . It is explained under which assumptions a simple Arrhenius dependence appears to be a good and reasonable rate description.

7.3.2 Rate theories and multiple jumps

The theory of diffusion can be seen as a special case of the general rate theories for (chemical) reactions. Roughly, two major directions treat multiple jump lengths: as a dynamical correction to transition state theory (TST) [296, 316], and in the context of generalized Langevin equation (GLE) models [313, 317–321]. Both will be discussed briefly in the following.

TST was a major development in the description of rate equations. It describes particles as moving on a potential energy (hyper)surface, as is illustrated in Fig. 7.1 [305, 322]. Simple TST is based on two assumptions:

1. Adsorbates in the transition state are at equilibrium with those in the ground state (strong coupling assumption).
2. Any adsorbate trajectory reaching the transition state leads to a successful hop over the barrier; recrossing of the transition state is not considered.

The rate is governed by the number of particles reaching the transition state, and has been expressed in the famous result by Eyring [323] as

$$h_{\text{TST}} = \frac{kT}{h} K_{\text{TS}} = \frac{kT}{h} \frac{z_{\text{TS}}}{z_{\text{GS}}} e^{-E_{\text{TST}}/kT} \quad (7.10a)$$

with Planck's constant h , the equilibrium constant K_{TS} ,¹⁰ and the partition functions z_{TS} and z_{GS} for the transition and ground state, respectively. The activation energy E_{TST} is the difference in adsorbate energy in the transition state and the ground state. The factor kT/h ($\approx 10^{13} \text{ s}^{-1}$ at RT) can in the simplest case be described as the frequency ν_0 of the adsorbate in the ground state. Therefore, ν_0 is sometimes called the attempt frequency.

Using the thermodynamic relations for equilibrium systems described by an equilibrium constant $K = \exp(-\Delta F/kT)$ and the Helmholtz free energy $F = E - TS$, Eq. (7.10a) can formally be recast as

$$h_{\text{TST}} = \nu_0 e^{S_{\text{TST}}/k} e^{-E_{\text{TST}}/kT}, \quad (7.10b)$$

where S_{TST} is the entropy difference between the transition and ground state.

TST reproduces the qualitative Arrhenius result of Eq. (7.7) in Sec. 7.3.1 and provides a physical meaning to the prefactor h_0 which is temperature depen-

¹⁰Strictly speaking, K_{TS} is only a *pseudo* equilibrium constant since z_{TS} is the partition function of the transition state reduced by one degree of vibrational freedom, namely the one transforming into translational motion over the transition state.

dent.¹¹ The theory was quite successfully applied to explain experimental results of, e.g. metal-on-metal diffusion, where the strong coupling assumption is often valid and NN jumps are dominant.

Obstacles of TST are basically twofold: firstly, jumps are intrinsically restricted to NN sites, and secondly, dynamical effects such as a recrossing of the transition state are ignored [324]. It has been shown that TST always gives an upper bound for the true hopping rate. A dynamical correction factor $f_d \in (0, 1]$ was hence introduced which accounts for recrossing and multiple jumps and adjusts the TST rate [305]:

$$h = h_{\text{TST}} f_d. \quad (7.11)$$

It was demonstrated that an analog expression to Eq. (7.11) exists for any hopping rate h_i of jumps with a length i [316]

$$h_i = h_{\text{TST}} f_{di}. \quad (7.12)$$

This reproduces the result for the overall rate $h = \sum_i h_i$ given in Eq. (7.11) with $f_d = \sum_i f_{di}$. Accordingly, the tracer diffusion constant can be expressed as¹²

$$D = D_{\text{TST}} \lambda^2 f_d. \quad (7.13)$$

Due to the λ^2 dependence of D , D_{TST} is not necessarily an upper bound for D .

The general Arrhenius dependence [Eqs. (7.7) and (7.8)] is not affected by applying dynamical correction factors. The temperature dependence is, however, extended into the prefactor due to the temperature dependence of the dynamical correction factors f_{di} which implicitly cause λ to be temperature dependent as well. The dynamical correction factor is not just an empirical correction value, but can be expressed in the form of a time-correlation function that can be evaluated

¹¹Note that the experimentally determined diffusion barrier E_D is defined from an assumed Arrhenius dependence ($h = h_0 \exp(E_D/kT)$) by

$$\frac{d \ln h}{d(1/T)} = -E_D/k.$$

Theoretically predicted barriers, however, can deviate from these experimental values due to the temperature dependent prefactor which affects the experimentally determined barriers [322]. TST, for example, leads from Eq. (7.10a) to

$$\frac{d \ln h_{\text{TST}}}{d(1/T)} = -(E_{\text{TST}} + kT)/k,$$

i.e. the theoretically predicted barrier E_{TST} differs from the experimental value E_D by kT which may be a large fraction. This is, however, often ignored, when experimental and theoretical data are compared.

¹²From Eq. (7.6) we get

$$D = \frac{1}{2} \lambda^2 h = \frac{1}{2} \sum_i \lambda_i^2 h_i = \frac{1}{2} h_{\text{TST}} \sum_i \lambda_i^2 f_{di} = D_{\text{TST}} \sum_i \lambda_i^2 f_{di} = D_{\text{TST}} \lambda^2 f_d$$

by making use of the relation $\lambda^2 = \sum_i p_i \lambda_i^2$ with $p_i = h_i/h = f_{di}/\sum_i f_{di}$. From Eq. (7.6) we defined also $D_{\text{TST}} = \frac{1}{2} h_{\text{TST}}$ since TST assumes only NN jumps ($\lambda = 1$).

from molecular dynamics simulations [316]. A physically intuitive interpretation is, however, still not available.

A starting point for a more complete rate description, *a priori* capable of explaining phenomena like recrossing and long jumps, goes back to Kramers [325]. He considered interactions of the adsorbates with the substrate not only through a periodic potential but also through a frictional force exerted to the adsorbate by the substrate. The nature of this frictional force is a coupling to the substrate phonons.

Kramers' theory considers a particle of mass m in a potential $U(x)$ and is governed by the classical equation of motion

$$m\ddot{x} = -\frac{dU}{dx} - \eta m\dot{x} + \xi(t). \quad (7.14)$$

Here $\xi(t)$ is a Gaussian white noise fluctuation force that is responsible for the excitation over the diffusion barrier and η is a friction coefficient describing the relaxation. Both are connected via the fluctuation-dissipation theorem [305]. Eq. (7.14) builds the foundation for the GLE approach — or equivalently the Fokker-Planck (or Klein-Kramers) equations — which focuses on the time evolution of the probability density in phase space instead of the equation of motion [305, 307].

In the rare event regime with $E_D/kT \gg 1$ one can roughly distinguish between a high friction regime where NN jumps prevail and the TST result is reproduced, and a low friction regime where long jumps play a role [305, 307].¹³ Another advantage of Kramers' approach is that it can be applied beyond the rare event regime, i.e. where $E_D/kT \lesssim 1$ and quasi-continuum diffusion prevails.

Even though the theoretical evaluation of the friction force is not straightforward, Kramers' rate concept seems physically more sound and intuitive compared to the approach of dynamical correction factors to TST. The diffusion rates are frequently described in the form

$$h_{\text{GLE}} = f(\eta, T) e^{-E_{\text{GLE}}/kT} \quad (7.16)$$

which gives an expression that is formally equivalent to Eq. (7.11) but provides an interpretation of the prefactor in terms of the friction force η which is (although maybe tough to evaluate) easy to understand intuitively.

It has been pointed out in Ref. [307] that the barrier plays an important role in rate theory, but is nevertheless only an equilibrium property. It is rather the prefactor which contains all the true dynamical information as is obvious from Eqs. (7.11) and (7.16). For a quantitatively correct theoretical rate description the prefactor is therefore of utmost importance. This importance is often ignored in experimental studies which normally focus on the barrier: the large error bars

¹³This can be defined quantitatively: for example the low friction regime is given from the condition

$$kT/E_D > \eta/\omega_D \quad \text{and} \quad \eta/\omega_D < 1 \quad (7.15)$$

with the transition state frequency ω_D [305].

connected with experimental prefactors do often not allow a detailed comparison with theory in order to unravel details of the model.

An important aspect of the diffusion dynamics is the jump-length distribution function p_i . Both analytical and numerical results show that the decay is asymptotically exponential for large i , while it can be even faster for very small jump lengths [296, 313, 318, 320, 321, 326–328]. An exponential decay was also phenomenologically derived in [329], assuming that the relaxation process of lateral translational motion can be characterized by a lifetime of the excited adsorbates as

$$p_i = c e^{-ai} \quad (7.17)$$

with the decay constant a determining the relative probability that an adsorbate takes a jump of length i and a normalization constant $c = (e^a - 1)$.¹⁴ Most other results for the jump-length distribution can only be evaluated numerically. An analytical expression based on Kramers' theory was given in Ref. [328] as

$$\frac{p_i}{p_1} = \frac{h_i}{h_1} = \frac{2(i-1)^{-3/2}}{\sqrt{\pi \Delta E_f / kT}} e^{-(i-1)\Delta E_f / 4kT} \quad (7.18)$$

for $i \geq 2$ and $\Delta E_f > kT$. The average energy loss ΔE_f of a particle to the dissipative environment (substrate) as it traverses from one barrier to the next is directly related to the added activation energy with increasing jump length i (obviously $\Delta E_f = \Delta E_f(\eta)$).¹⁵ This demonstrates that jumps of different length are associated with different barriers which can be expressed as a temperature dependence of the prefactor. Moreover, the prefactor has a \sqrt{T} dependence, as is also found in the so-called transition path theory [331].

From the theoretical considerations it is concluded that an Arrhenius behavior as is stated in Eqs. (7.7) and (7.8) is in principle confirmed. The fact that long jumps may cause deviations from the Arrhenius law is understood by realizing that all jumps of different length are associated with different barriers, and the simple Arrhenius law gives an average over the different processes. The differences in the activation energies can, however, be gathered in an accordingly temperature-dependent prefactor. This explains the deviation from the simple Arrhenius behavior of h and D for experiments that are carried out over large temperature intervals.

7.4 Data analysis

The extraction and comparison of the diffusion parameters (activation energy, prefactor, and jump length) is done using two observables: the mean-squared

¹⁴The decay constant a is then related to the lifetime τ by $a = 1/\bar{v}\tau$ (with the average translational velocity \bar{v} of the adsorbates through the transition state) [329]. The probability of relaxation of a translating adsorbate within a potential well can be expressed as $\hat{p} = (1 - e^{-a})$ [330].

¹⁵Eq. (7.18) can be seen as equivalent to the dynamical correction factor method with $f_{di}/f_{d1} = p_i/p_1$. Note that for large i it describes indeed an exponential decay, as $p_{i+1}/p_i = (1 - 1/i)^{3/2} \exp(\Delta E_f / 4kT)$.

displacement $\langle(\Delta x)^2\rangle$ and the hopping rate h (furthermore we use the parameter t which is the time it takes to acquire an image). The mean-squared displacement can be extracted from the STM movies by following the displacement of all the molecules between images.

It is, however, not straightforward to extract the hopping rate which is concealed in the displacement distribution. Since exact displacement distributions are not available in our case, we instead use the approximative methods described in Sec. 7.4.1. Their validity is investigated by means of kinetic Monte Carlo simulations (KMC) in Sec. 7.4.2.

7.4.1 Extraction of the hopping rate

A characteristic property of the Poisson process is that the time intervals between hops are exponentially distributed, and the probability $p(0)$ of no jump to occur during t is given by

$$p(0) = e^{-ht}. \quad (7.19)$$

In principle, this opens up the possibility of determining h from a residence time distribution fitted to an exponential function if the time resolution of the measurement is good enough (indicated in Fig. 7.5A); only in a few examples has this been achieved [281, 286, 295]. Generally, it is only possible to observe *displacements* of a certain length after a time interval t which can comprise several individual *jumps* (see Fig. 7.5B).

The theory of the statistical analysis to extract h from such a displacement distribution was developed by Ehrlich, who encountered this situation in FIM studies [234, 273]. The analytical expression for the displacement distribution ${}^\gamma P_x$ of finding a particle at a distance x from the origin ($x = 0$) after time t , crucially depends on the number γ of different jump lengths participating in the random walk and their actual lengths λ_j [89].¹⁶

In the simplest case, where only NN jumps occur with rate h_1 ($\gamma = 1$ and $\lambda_1 = 1$), the displacement distribution is given by

$${}^1 P_x = e^{-h_1 t} I_x(h_1 t). \quad (7.20a)$$

I_x is the modified Bessel function of the first kind of order x . The function is defined in App. B; its behavior is also illustrated there. Taking double jumps ($\gamma = 2$) with rates h_1 and h_2 for $\lambda_1 = 1$ and $\lambda_2 = 2$ into account yields

$${}^2 P_x = e^{-(h_1+h_2)t} \sum_{j=-\infty}^{\infty} I_j(h_2 t) I_{x-2j}(h_1 t). \quad (7.20b)$$

¹⁶In App. B details on how Eq. (7.20a) is derived and how Eqs. (7.20b) and (7.20c) can be interpreted in a more physical manner are presented.

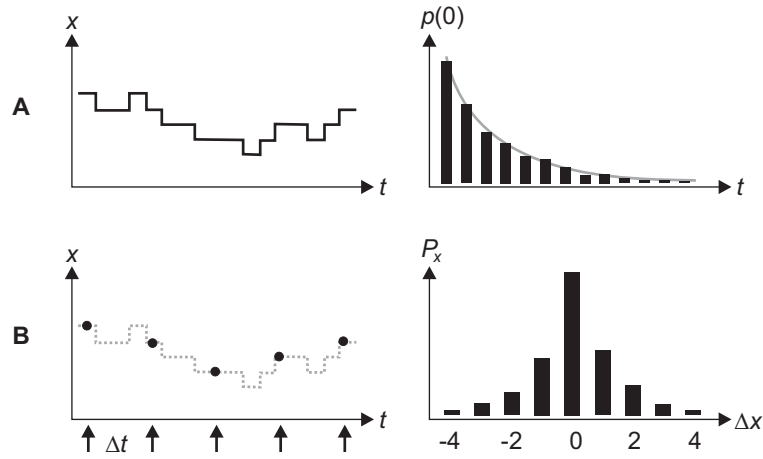


Figure 7.5: Illustration of the analytical differences encountered in a continuous and discrete time observation of a random walk, sketched as position x versus time t (left). **(A)** A (quasi-)continuous time resolution allows one to detect all jumps *and* their distribution of residence times in between jumps $p(0)$. This yields the hopping rate via an exponential fit to Eq. (7.19) (grey line, right plot). **(B)** A discrete time separation between observations only resolves displacements (black circles) and not the individual jumps (dotted line). From the displacement distribution P_x the hopping rate is then accessible through Eq. (7.20a)

Adding finally also triple ($\gamma = 3$) with rates h_1 , h_2 , and h_3 for $\lambda_1 = 1$, $\lambda_2 = 2$, and $\lambda_3 = 3$) gives

$${}^3P_x = e^{-(h_1+h_2+h_3)t} \sum_{k=-\infty}^{\infty} I_k(h_3 t) \sum_{j=-\infty}^{\infty} I_j(h_2 t) I_{x-2j-3k}(h_1 t). \quad (7.20c)$$

It is obvious from Eqs. (7.20a–c) that the analytical expressions become very complicated when the number of different jump lengths increases. Ehrlich's approach to extract the hopping rates relied on the best fit of the analytical expressions ${}^\gamma P_x$ through the parameters h_i to the experimentally found, lattice-resolved displacement distribution. Such an analysis is not feasible in our case of large molecules. Firstly, we are not able to unequivocally assign jump lengths to integer multiples of the NN lattice spacing. Secondly, the RMS jump length is so large that the expression for ${}^\gamma P_x$ should include up to almost 20 different jump lengths — this would be complicated to handle in practice. A way out of this dilemma is demonstrated in the following.

The lack of a lattice-resolved displacement distribution is overcome by focussing only on the probability ${}^\gamma P_0$ that the molecules reside at their original positions ($x = 0$) after the time interval t , instead of regarding the entire distribution ${}^\gamma P_x$. For $ht \ll 1$, ${}^\gamma P_0$ can be approximated as

$$P_0 \approx e^{-ht}, \quad (7.21)$$

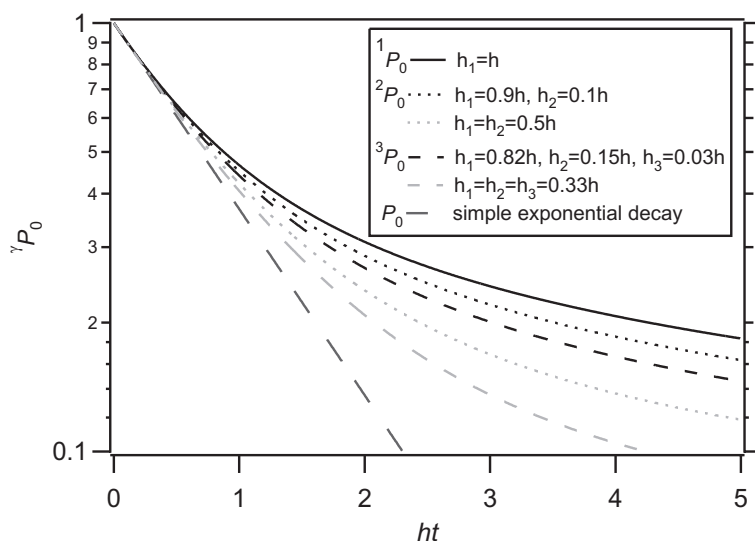


Figure 7.6: Probability ${}^\gamma P_0$ of finding a particle at the same position after the time interval t as a function of the parameter ht . 1P_0 , 2P_0 , and 3P_0 are the correct analysis for 1, 2, and 3 different jump length participating in the diffusion process as given in Eqs. (7.20a–c); P_0 is the simple exponential approximation from Eq. (7.21) which represents ${}^\gamma P_0$ the better, the larger γ , i.e. the larger λ : For 2P_0 and 3P_0 the curves are plotted for the two cases of an exponential jump length distribution and equal jump probabilities. In the first case the RMS jump lengths are $\lambda = 1.14$ (for $h_1 = 0.9h$, $h_2 = 0.1h$) and $\lambda = 1.30$ (for $h_1 = 0.82h$, $h_2 = 0.15h$, $h_3 = 0.03h$), and in the second case $\lambda = 1.58$ (for $h_1 = h_2 = 0.5h$) and $\lambda = 2.15$ for $h_1 = h_2 = h_3 = 0.33h$.

which reproduces the residence time distribution of Eq. (7.19). This expression was often used for analyzing STM diffusion data [92–94, 289, 290]. One must, however, be careful about the validity of the approximation. This is illustrated in Fig. 7.6. For small P_0 the simple exponential approximation results in significant deviations in the extracted ht towards too low values: in these cases the (real) hopping rate h is so large that molecules perform jumps in between consecutive images. Due to the limited time resolution of the STM, these jumps either did *seemingly* not occur (if the molecule jumped back and forth and ended on the same adsorption site again) or are observed as longer displacements (if the molecule jumped multiple times). The validity of the exponential approximation increases with γ , i.e. with increasing RMS jump length λ .

This seemingly surprising behavior is explained in Fig. 7.7. With an increasing hopping rate h (or more precisely: with increasing ht), jumps in between observations are more likely to occur. For $\lambda = 1$ and not too high hopping rates ($h\Delta t < 1$), jumps back and forth between images are still likely to result in an observation with no net-displacement ($\Delta x = 0$), and will thus contribute to P_0 (Fig. 7.7A).

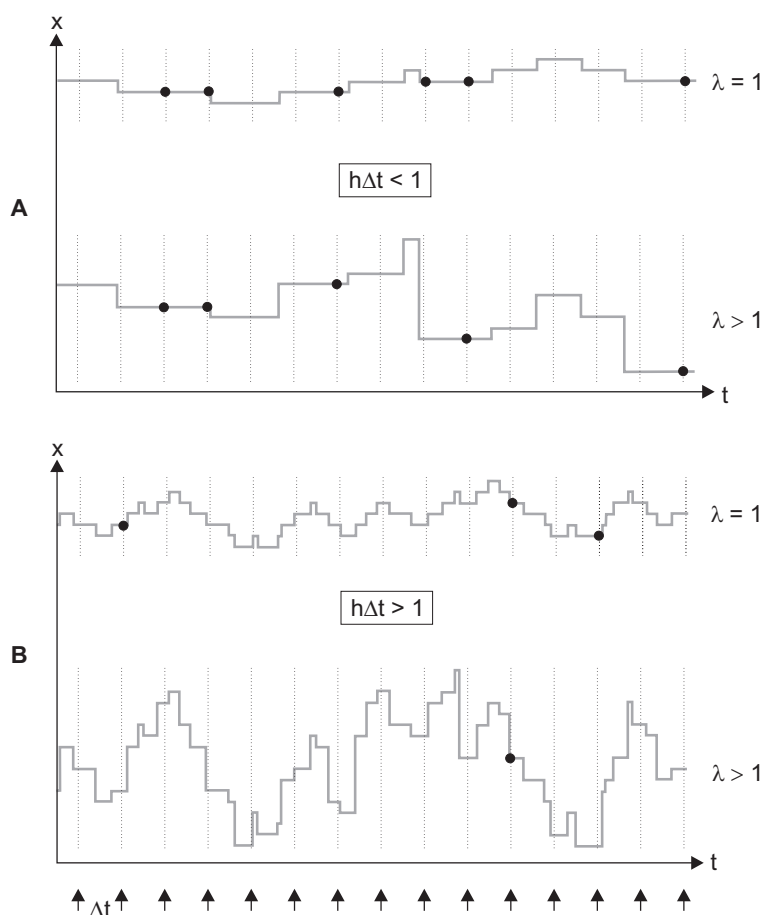


Figure 7.7: Influence of the RMS jump length λ on the probability P_0 of observing an adsorbate at the same x position as in the previous observation (marked with \bullet ; P_0 is the number of filled circles relative to the total number of observation!). The real time evolution of the jumps is plotted as a grey line, while the time intervals Δt of an (STM) observation are marked by vertical lines. Note that in both graphs the residence times and the direction of each jump are identical for the plots $\lambda = 1$ and $\lambda > 1$. **(A)** For $h\Delta t < 1$, multiple jumps in Δt are rare. If, however, e.g. jumps back and forth do occur (see center region of the plot), they are more likely to be observed at the previous x position for $\lambda = 1$ (top) than for $\lambda > 1$ (bottom) due to the different jump lengths participating in the latter case. P_0 therefore decreases with increasing λ (for the same ht). **(B)** For $h\Delta t > 1$, P_0 is reduced compared to $h\Delta t < 1$ due to the fact that it is more and more unlikely to return to the same x position if many jumps occur. This effect is even more pronounced for $\lambda > 1$ compared to $\lambda = 1$ for the reasons discussed under (A).

With increasing λ such jumps back and forth will with increasing probability result in a finite displacement ($\Delta x \neq 0$) and yet P_0 is reduced.¹⁷ This trend is even more pronounced for $h\Delta t > 1$ (Fig. 7.7B). Therefore, for a given ht , ${}^\gamma P_0$ decreases with increasing λ (i.e. γ) and approaches the simple exponential decay function P_0 [Eq. (7.21)].

With respect to using the expressions ${}^\gamma P_0$ to extract h from an experimentally determined P_0 , we can conclude as follows: Eq. (7.20a) can for $x = 0$ be written in the form

$${}^1 P_0 = e^{-ht} I_0(ht), \quad (7.22)$$

which will from now on be referred to as the *Bessel analysis*. It considers only jumps to NN sites and leads to an upper bound of the extracted hopping rate h . The simple exponential expression Eq. (7.21) that will from now on be referred to as the *simple analysis* seemingly gives a lower bound for h .¹⁸ Both equations are obvious and well suited candidates for analyzing h . They not only result in upper and lower bounds, but are moreover only dependent on *one* hopping rate h . In order to obtain a quantitative estimation of how well these two equations represent P_0 , we performed KMC simulation.

7.4.2 Kinetic Monte Carlo simulations

Since the molecules have well-defined adsorption sites in registry with the substrate lattice, a Monte Carlo simulation can easily be applied to simulate their one-dimensional random walk [332–334]. We performed KMC simulations¹⁹ for many sets of λ and ht within the parameter space of interest.

The basic idea is to derive displacement distributions — representing our STM experiments — from which we can calculate the mean-squared displacement and determine the (approximate) hopping rate. The latter is derived by the Bessel and the simple analysis, as discussed in Sec. 7.4.1; the results can be directly compared to the input hopping rate of the simulation and serve as a measure of how good our approximation is. In a second step, the same is done for the RMS jump length. In the following, the parameters fed into the simulation are denoted as λ_{in} and $h_{\text{in}}t$, and those calculated from the simulated displacement distribution as λ_{out} and $h_{\text{out}}t$.

¹⁷This can be seen quantitatively from the Gauss distribution

$$\tilde{P}_x = \frac{1}{\sqrt{2\pi ht\lambda^2}} e^{-x^2/2ht\lambda^2},$$

which is a good approximation of ${}^\gamma P_x$ for very large ht [234]. Accordingly, $\tilde{P}_0 = 1/\sqrt{2\pi ht\lambda^2}$ decreases with increasing λ .

¹⁸This seems to be the case for an exponential jump length distribution. It is not obvious from Fig. 7.6, only from the results derived by KMC simulation in Fig. 7.8.

¹⁹In *Monte Carlo* simulations the hopping rate depends merely on the relative energies of the configurations before and after hopping, while in *kinetic Monte Carlo* simulations the barrier between the configurations plays an essential role [332].

According to the discussion in Sec. 7.3.2, jumps of length i are — as a very good approximation — assumed to be exponentially distributed: $p_i = c \exp(-ai)$.²⁰ Since the overall jump rate $h = \sum_i h_i$ is given as the sum over all the rates for jumps with a certain length i , the individual rates are given as $h_i = p_i h$.

In the following we describe the principles of the simulation routine together with the results obtained for h_{out} and $\lambda_{\text{out}} t$. We conclude the result of the KMC simulations by providing a recipe of how to extract excellent approximated hopping rates from experimental data.

The simulation routine used here is in line with theoretical foundations of KMC simulations summarized in Ref. [335]. It is based on a modified and extended program already used for other KMC simulations [91] which has been developed by Linderoth [336].

We are considering an adsorbate moving in one dimension with a given overall rate $h = \sum_i h_i$. A RMS jump length λ is chosen which determines the probabilities p_i of making a jump of distance i via Eq. (7.17) and hence the individual hopping rates $h_i = p_i h$. Which jump length actually occurs in the simulation is chosen randomly but is weighted with the probabilities p_i .²¹ Furthermore, the direction of the jump was chosen, having equal probabilities for movements to the right and to the left.

As a result of the Poisson process the time between individual hops is exponentially distributed with a mean residence time $\tau = 1/h$ [Eq. (7.19)]. Hence, after each adsorbate jump the time is incremented by $t = -\tau \ln r$, where r is a random number with $r \in (0, 1]$. This was demonstrated to be correct also for processes with different hopping lengths [335]. In order to mimic an STM experiment correctly with time intervals Δt between observations, the times between consecutive hops are summed until they exceeded Δt .²² If this is the case, the displacement from the last observation is denoted. This was repeated until 1000 observations were made leading to the desired displacement distribution. Simulations were performed for each parameter set $(\lambda_{\text{in}}, h_{\text{in}} t)$.

The correctness of the simulation routine was tested by ensuring that the following two parameters are reproduced:

²⁰From exponentially distributed jump lengths, the RMS jump length λ can be calculated to be [310]

$$\lambda^2 = \sum_{i=1}^{\infty} p_i \lambda_i^2 = \sum_{i=1}^{\infty} p_i i^2 = \frac{1 + e^{-a}}{(1 - e^{-a})^2}.$$

The result leads to $\lambda \rightarrow 1$ for $a \rightarrow \infty$ which is the value expected when only NN jumps participate ($p_i = 1$ for $i = 1$ and $p_i = 0$ else).

²¹In practice, from the probabilities p_i we define intervals $I_i = (\sum_{k=1}^i p_{k-1}, \sum_{k=1}^i p_k]$ for $i = 1, 2, \dots, 100$ (with $p_0 = 0$). The jump length is then determined to be i , if a randomly chosen number $r \in (0, 1]$ is an element of the interval I_i .

Including jump lengths of a distance up to $i = 100$ was demonstrated to be sufficient for $\lambda < 10$, i.e. jumps beyond λ_{100} occur so rarely that they practically do not contribute to the RMS jump length λ [Eq. (7.4)].

²²More precisely, an observation was made if $\sum t/\Delta t \geq n$, where the sum goes over all residence times Δt in the simulation and $n \in \mathbb{N}$ is a counter for the observations.

1. The overall number of jumps divided by the time necessary for 1000 observations to occur must be equal to h_{in} .
2. The RMS jump length λ calculated from the mean-squared displacement $\langle(\Delta x)^2\rangle$ and $h_{\text{in}}t$ via Eq. (7.3) must yield λ_{in} .

Results for h_{out} were extracted from the displacement distributions of the simulation via the non-hopping probability P_0 by using the simple analysis [Eq. (7.21)] and the Bessel analysis [Eq. (7.22)].

Fig. 7.8 illustrates how the approximation $h_{\text{out}}t$ is affected by $h_{\text{in}}t$ and λ_{in} . In order to get a good measure of the relative error induced by the approximative analysis, we scaled $h_{\text{out}}t$ by the input parameter $h_{\text{in}}t$. For both analyses this gives values that are easy to compare.

From Fig. 7.8C it is clearly seen that the Bessel analysis always overestimates and the simple analysis always underestimates the (real) hopping rate (h_{in}). In both cases the errors increase with $h_{\text{in}}t$ (for a given λ_{in}). There are, however, pronounced differences depending on the values of λ_{in} .

For $\lambda = 1$ the Bessel analysis obviously yields the correct result, since it is the correct analytical expression for this situation. The simple analysis is a good approximation only for $h_{\text{in}}t \ll 1$. The underestimation of the hopping rate is a result of hops back and forth in between observations that are not observed; this becomes worse with increasing $h_{\text{in}}t$ (see Fig. 7.7).

It is noteworthy that the simple analysis leads to values for h_{out} that improve with increasing λ_{in} . In contrast to this, the Bessel analysis becomes worse with increasing λ_{in} . As seen in Fig. 7.8C, the simple analysis is superior to the Bessel analysis for $\lambda_{\text{in}} \gtrsim 2$. The reason is that different jump lengths make it more unlikely to observe zero net-displacements ($\Delta x = 0$) due to jumps back and forth in between observations. The experimentally observed value P_0 is hence reduced which according to Eq. (7.22) leads to an increase of h_{out} from the Bessel analysis. The same argumentation applies likewise to the simple analysis [Eq. (7.21)]; nevertheless, here we have the fortunate situation that this effect compensates the general underestimation of h_{out} in the case $\lambda = 1$.²³

We conclude that the results of both analyses are comparably good for $ht < 1$, irrespective of the RMS jump length λ . For $ht > 1$ the Bessel analysis is good only for $\lambda \approx 1$, while the simple analysis is much better for $\lambda \gtrsim 2$. From Fig. 7.8C it even seems that the simple analysis approaches the correct result for h_{out} in the limit $\lambda \rightarrow \infty$; we do, however, not have a proof of this.

Results for λ_{out} were calculated from the mean-squared displacement $\langle(\Delta x)^2\rangle$ and the result for $h_{\text{out}}t$ by using Eq. (7.3). To illustrate how λ_{out} is affected by the approximation of h_{out} from the Bessel and the simple analysis, Fig. 7.9 shows a plot of $\lambda_{\text{out}}/\lambda_{\text{in}}$ versus $h_{\text{in}}t$ and λ_{in} — equivalent to the plot of $h_{\text{out}}/h_{\text{in}}$ in Fig. 7.8.

²³The situation has already been discussed in connection with Ehrlich's analytical results of γP_0 in Fig. 7.6. See Sec. 7.4.1 and Fig. 7.7.

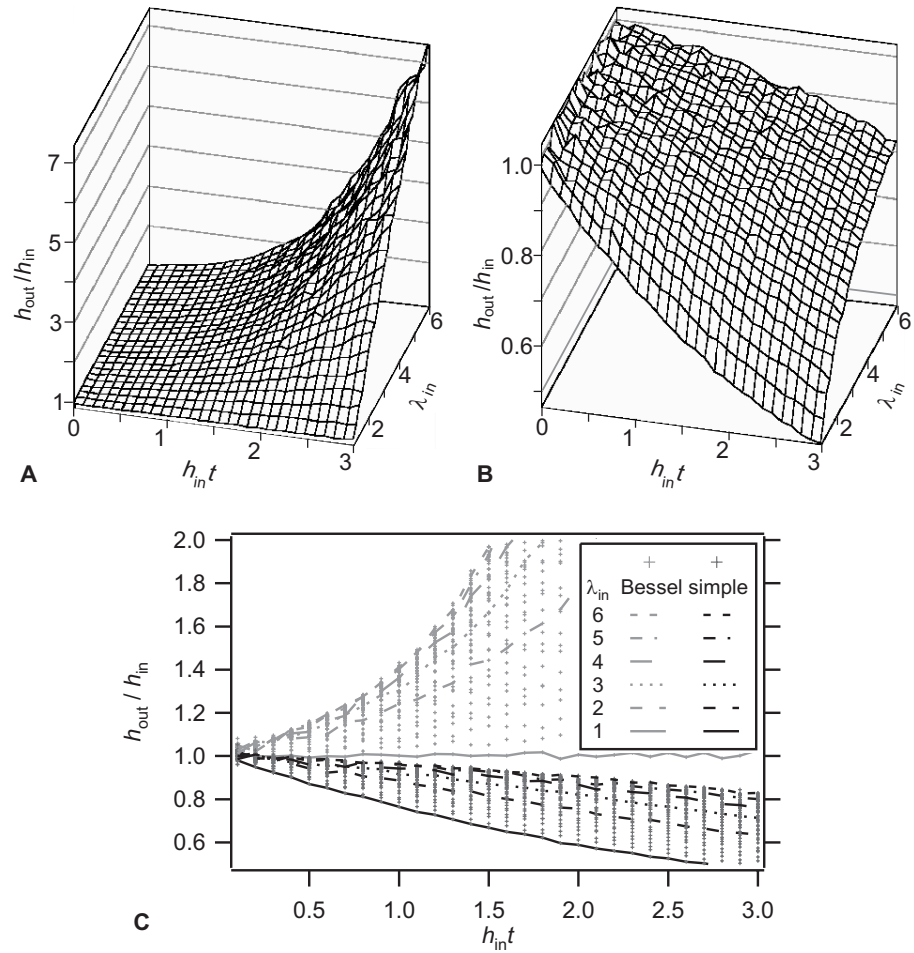


Figure 7.8: Results of the KMC simulations for $h_{\text{out}}/h_{\text{in}}$ as a function of $h_{\text{in}}t$ and λ_{in} derived via (A) the Bessel analysis and (B) the simple analysis. Note that the values extend over a much larger interval in the case of the Bessel analysis. (C) two-dimensional projection of the plots in (A) and (B) along the λ_{in} axis, where plots for integer values of λ_{in} are highlighted. It can be seen that the Bessel analysis (A) always overestimates and the simple analysis (B) always underestimates the real hopping rate (h_{in}). See text for details.

According to Eq. (7.3), an underestimation of h_{out} results in an overestimation of λ_{out} and vice versa. Hence, the Bessel analysis underestimates and the simple analysis overestimates the (real) RMS jump length (λ_{in}), as is seen best in Fig. 7.9C.

Due to the close connection between λ_{out} and h_{out} , the conclusions drawn in the previous section apply also for the results of λ_{out} , and can be summarized as follows:

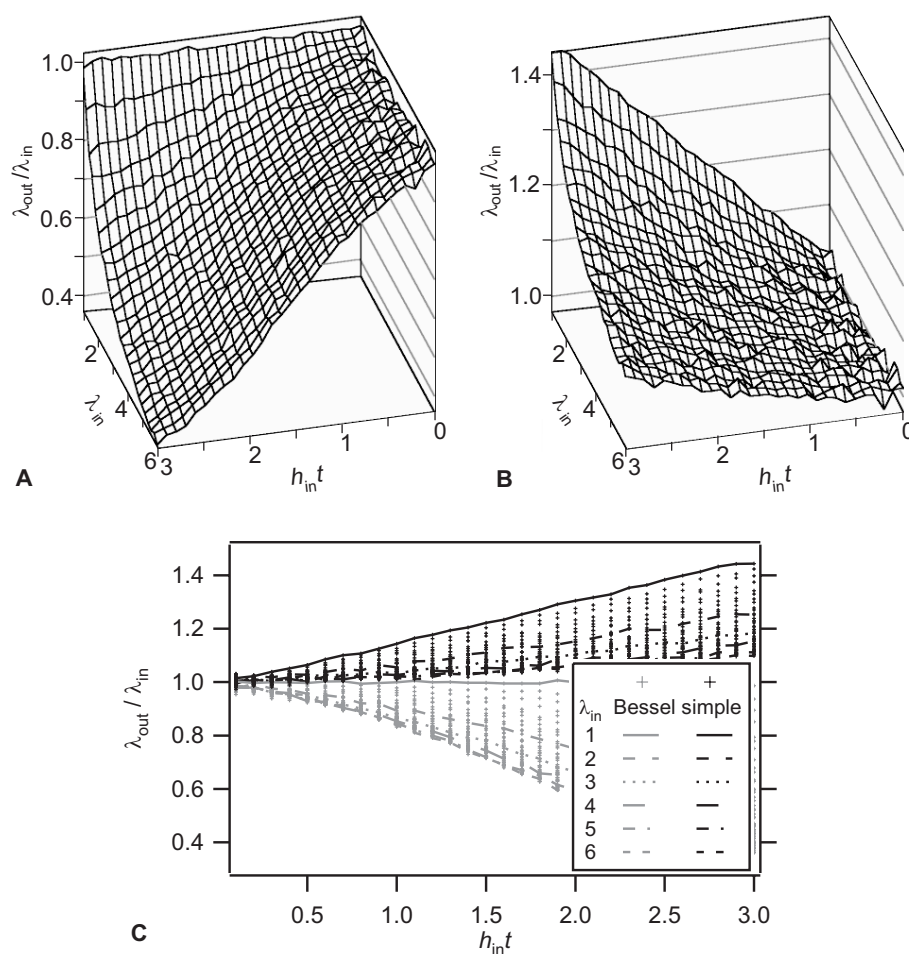


Figure 7.9: Results of the KMC simulations for $\lambda_{\text{out}}/\lambda_{\text{in}}$ as a function of $h_{\text{in}}t$ and λ_{in} derived via (A) the Bessel analysis and (B) the simple analysis. The direction of the $h_{\text{in}}t$ axis is opposed to that in (A) and (B). (C) two-dimensional projection of the plots in (A) and (B) along the λ_{in} axis where plots for integer values of λ_{in} are highlighted. It can be seen that the Bessel analysis (A) always underestimates and the simple analysis (B) always overestimates the real RMS jump length (λ_{in}). See text for details.

1. For small ht both methods are comparably good.
2. The errors increase with $h_{\text{in}}t$ (for a given λ_{in}).
3. For $ht > 1$ the Bessel analysis is good only for $\lambda \approx 1$, while the simple analysis is much better for $\lambda \gtrsim 2$.

It should be noted that the minor relative error of λ_{out} compared to h_{out} for a given set of λ_{in} and $h_{\text{in}}t$ is a direct consequence of the square-root dependence of λ

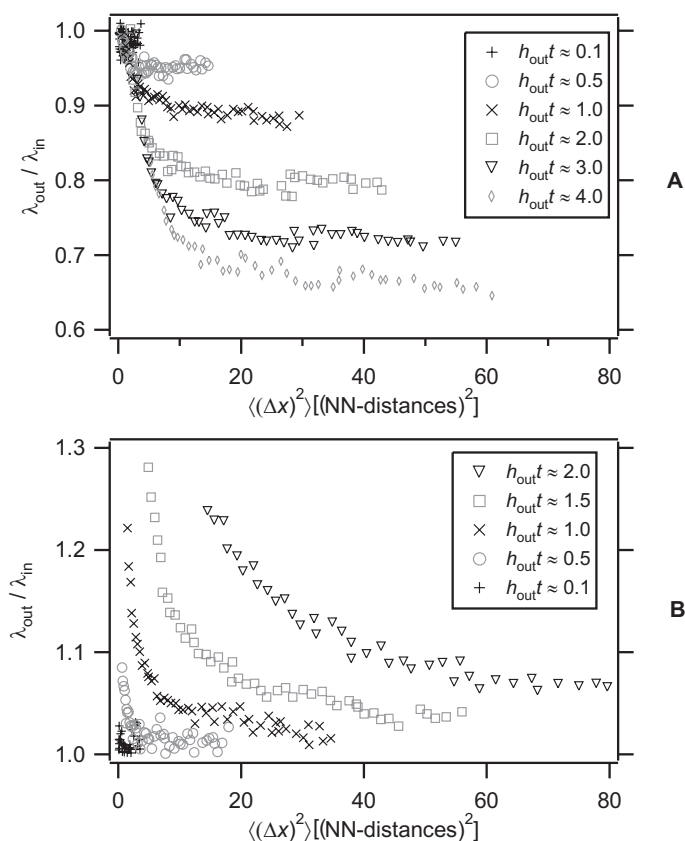


Figure 7.10: Results of the KMC simulations for $\lambda_{out}/\lambda_{in}$ as a function of the experimental available parameters $\langle(\Delta x)^2\rangle$ and $h_{out}t$. The latter is derived via (A) the Bessel analysis and (B) the simple analysis. These plots enable us to directly evaluate the error of λ_{out} for a set of the experimentally gained $\langle(\Delta x)^2\rangle$ and $h_{out}t$. To understand the plots better, note that the plots for a given $h_{out}t$ are a result of the different λ_{in} in a way that the data points towards larger values of $\langle(\Delta x)^2\rangle$ are connected with increasing values of λ_{in} .

on h as seen in Eq. (7.3). For example, for $h_{in}t = 3$ and $\lambda_{in} = 6$ the Bessel analysis of h_{out} is wrong by a factor of 7 (Fig. 7.8), whereas the corresponding result for λ_{out} is off by only a factor around $1/2.5$.

The discussion above provides a general quality evaluation of the two hopping rate approximations, but it is not suitable to estimate errors directly from *experimentally* determined data. In this case it is not the parameters λ_{in} and h_{in} that are available, but $\langle(\Delta x)^2\rangle$ and $h_{out}t$. We therefore plotted $\lambda_{out}/\lambda_{in}$ versus these two experimentally relevant parameters in Fig. 7.10.

The plots reproduce the findings from Fig. 7.9, namely that for a given ht the Bessel analysis leads to *large* errors that increase with λ , i.e. $\langle(\Delta x)^2\rangle$ (Fig. 7.10A).

The simple analysis, on the other hand, gives *small* errors with increasing λ (Fig. 7.10B). With these plots we are in the position to directly evaluate the error of λ_{out} for a set of experimentally extracted values of $\langle(\Delta x)^2\rangle$ and $h_{\text{out}}t$. Hence the best method of analysis — Bessel or simple — can easily be determined.²⁴

Conclusions from the KMC simulations

Which of the two methods is more favorable to extract the hopping rate can be concluded from the plots in Fig. 7.10 for every single data point ($\langle(\Delta x)^2\rangle$ and $h_{\text{out}}t$). We saw that it is the magnitude of λ that determines which of the two methods is better. Around a critical value $\lambda \lesssim 2$ both methods lead to comparable results (for $ht < 2$).

Since the Bessel and the simple analyses yield lower and (probably) upper bounds of the RMS jump length λ , a general “recipe” for analyzing diffusion data is provided in the following routine:

1. Determine an upper bound of h via the Bessel analysis [Eq. (7.22)] and from this h and the experimental $\langle(\Delta x)^2\rangle$ a lower bound of λ [Eq. (7.3)].
2. If $\lambda < 2$, stick with the results for h and λ .
3. If not, recalculate (a lower bound of) h with simple analysis [Eq. (7.21)] and therefrom λ [Eq. (7.3)].

7.5 Results and discussion

In this section the results gained from STM data are presented based on the considerations of Sec. 7.4. The independent determination of D (respectively $\langle(\Delta x)^2\rangle$) and h opens up the opportunity to discuss two topics. Firstly, the temperature dependence of both parameters provides two independent ways to extract the Arrhenius parameters (activation energy of diffusion E_{D} , prefactors h_0 and D_0). This will be done in Sec. 7.5.1. Secondly, the RMS jump length λ can be obtained as is demonstrated in Sec. 7.5.2.

While D is directly determined from the mean-squared displacement, the hopping rate h can only be approximated by either the Bessel or the simple analysis (Sec. 7.3). We applied the recipe described in Sec. 7.4.2 and found that due to the large RMS jump lengths of both molecules (Sec. 7.5.2) the simple analysis of the hopping rate h via Eq. (7.21) is clearly superior.

The error bars given in Figs. 7.11 and 7.13 are calculated based on the statistical spread σ of the probability P_x of finding a particle with a displacement Δx in a displacement distribution which is given by $\sigma(P_x) = \sqrt{N_x(1 - N_x/M)}/M$ [287]. The hopping rate error bars are then accessible from $P_0 = \exp(-ht)$ as $\sigma(h) = \sigma(P_0)/P_0t$ and the diffusion error bars are $\sigma(D) = \sum_x \sigma(P_x)(\Delta x)^2/2t$, since $D = \langle(\Delta x)^2\rangle/2t = \sum_x P_x(\Delta x)^2/2t$ (see also [277]).

²⁴A likewise plot as in Fig. 7.10 could have been provided for $h_{\text{out}}/h_{\text{in}}$, but would lead to no new results as the better method to determine λ_{out} is also the better method to determine h_{out} . Similarly, Fig. 7.9 does not contain new information compared to Fig. 7.8.

7.5.1 Arrhenius parameters

The activation energy of diffusion E_D and the prefactors h_0 and D_0 are accessible through the Arrhenius plots of D and h [see Eqs. (7.8) and (7.7)]. The results in Fig. 7.11 show that the data points neatly fall on a straight line, as it is expected from a simple Arrhenius behavior. This applies for both case (h and D) of DC and HtBDC.²⁵ The quantitative results of the activation energy of diffusion E_D and the prefactors h_0 and D_0 found from the best linear fits to the data are summarized in Tab. 7.1.

The activation energies from both analyses agree quite well within the experimental uncertainties and yield average activation energies of 0.73 eV for DC and 0.59 eV for HtBDC.²⁶ This reproduces what was anticipated from qualitative considerations: HtBDC has a lower activation barrier for diffusion compared to DC. This is a result of the reduced bonding strength of HtBDC to the surface, caused by the presence of *tert*-butyl spacer groups separating the generally strongly bound aromatic π system from the substrate surface (see Fig. 7.2). The results therefore directly relate diffusion properties to the chemical constitution of the molecules, showing in a unique manner the influence of the molecule-substrate interaction on the diffusivity of the molecule itself.

The agreement of the two methods (h and D) is expected from the discussion in Sec. 7.3.2 on the theoretical foundation of the Arrhenius behavior. Based on the dynamical correction factor description [Eqs. (7.11) and (7.13)], an Arrhenius dependence is still valid even though the temperature-dependence of the correction factors is to be considered. This possible effect can, however, not be unravelled from our data for two reasons. Firstly, the small temperature range makes a prominent effect of the temperature dependent correction factors unlikely to play a significant role. Secondly, the statistical fluctuations are too large. This is due to the relatively small amount of events exploited for each data point.

Hence, if the temperature dependence of the correction factor f_d and λ is small, the *overall* temperature dependence of the rate is dominated by the expo-

²⁵Note that for low temperatures where only a few percent of the molecules are actually jumping, the obtained (small) mean-squared displacement values can be dominated by single, long jumps. We observed single displacements of up to 20 NN lattice spacings between consecutive images, while all other displacements in the movie are only to NN or NNN places. Such long jumps are not believed to be artifacts (e.g. tip-influenced), because they are also observed at higher temperatures (but do then not influence the mean-squared displacement as significantly, since the fraction of total jumps is much higher). The observation of few jumps in combination with the occurrence of long jumps could be the reason for the more pronounced deviation of some of the low temperature data points from the Arrhenius fit.

²⁶As a rule of thumb, diffusion barriers are expected to amount to 10–30% of the adsorption energy. Adsorption energies could not be determined in our case, since we were not able to obtain TPD data. This relates to the fact that the sticking coefficient of these large molecules is so high that it is almost impossible to measure a signal with the mass spectrometer at the end of the 10 cm long collector tube in front of the mass spectrometer. Moreover, the molecular masses of DC and HtBDC by far exceed the mass range of our spectrometer of only 200 a.u. Another problem arises with DC that decomposes before it desorbs; this is most likely due to the stronger interaction with the substrate compared to HtBDC.

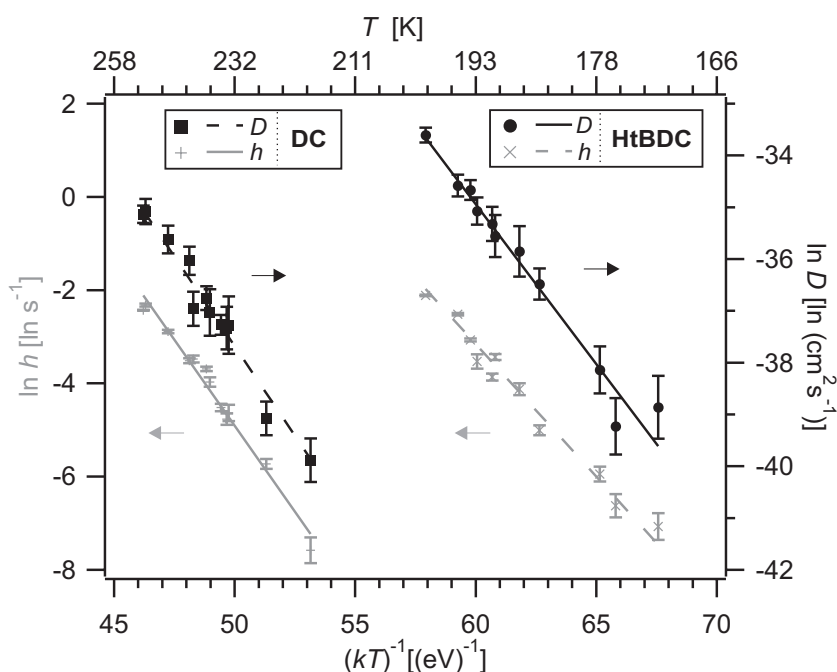


Figure 7.11: Arrhenius plots of the hopping rates h and tracer diffusion coefficient D for DC and HtBDC. The data for h are drawn in grey, while the data for D are black; the arrows mark the axis belonging to the respective plots. The lines are the best linear fits. Note that the error bars of h are calculated from the statistical spread of P_0 and do not explicitly take into account the approximative estimation of h . It will be shown in Sec. 7.5.2 that this error is for all data points below 4% except for the two highest temperature data points, where it is still below 9%. The effect is, however, small as seen in Tab. 7.1.

ponential dependence on the diffusion barrier, and both h and D should according to Eqs. (7.11) and (7.13) yield the same activation energy. This is confirmed by our analysis within the experimental error bars.

Other studies of organic molecules on single crystal metal surfaces have also observed an Arrhenius dependence of either h or D , but have never compared the two methods. 4-Trans-2-(pyrid-4-yl-vinyl)benzoic acid (PVBA) on Pd(110) led to an activation energy of 0.83 eV [92]. Although PVBA is an aromatic molecule without spacer groups and in this respect resembles DC, the data are difficult to compare because the influence of the different surfaces is not easily quantified. A rough estimate of 0.7 eV for sub-phthalocyanine on Ag(111) was given in [94], but was determined only by using a standard prefactor h_0 and is also affected by a high coverage of around 40%. An unusually large activation barrier of 1.4 eV was found for the one-dimensional diffusion of C_{60} on Pd(110) [93].

Another study, comparing diffusion barriers with the structure of the mole-

	DC		HtBDC	
	dis	hop	dis	hop
E_D/eV	0.71 ± 0.05	0.74 ± 0.03 (0.75)	0.62 ± 0.04	0.57 ± 0.02 (0.58)
h_0/s^{-1}	-	$10^{13.9 \pm 0.7}$ ($10^{14.3}$)	-	$10^{13.5 \pm 0.4}$ ($10^{13.7}$)
$D_0/\text{cm}^2\text{s}^{-1}$	$10^{-1.0 \pm 1.0}$	-	$10^{0.9 \pm 1.0}$	-

Table 7.1: Diffusion parameters for DC and HtBDC derived from analyses of the mean-squared displacements (dis) and the hopping rates (hop). The error bars are calculated from the deviations of the data from the best fit. This does in the case of the hopping rate not explicitly take into account the approximative estimation of h . The values in parenthesis result from the *corrected* hopping rates according to the errors calculated from the KMC simulations (see Fig. 7.13); it demonstrates that this correction effect towards higher activation energies is rather small and accounts for the underestimation of h in the simple analysis.

cules, was performed for a number of n -alkanes on Ru(0001), demonstrating a linear relation between chain length and activation energy (0.13 eV for propane up to 0.21 eV for n -hexane) [270]. These data are, however, obtained by LITD and must therefore be considered as an average over different surface features like steps or kinks.

The prefactors h_0 and D_0 in Tab. 7.1 are somewhat higher compared to “standard” values $h_0 = 10^{13} \text{ s}^{-1}$ and $D_0 = 10^{-3} \text{ cm}^2\text{s}^{-1}$ that are frequently found for metal-on-metal diffusion.²⁷ The pronounced difference between the experimental values of h_0 that match the standard values quite well, and those for D_0 which are significantly higher, is readily explained by Eq. (7.9): D_0 accounts for the large RMS jump lengths. We will see in Sec. 7.5.2 that the values of λ are ca. 4 and 7 NN distances for DC and HtBDC; this yields an increase by a factor 100 based on the experimental h_0 , i.e. $D_0 \approx 1 \text{ cm}^2\text{s}^{-1}$. This agrees well with the experimental values of D_0 .

The slight increase in h_0 and D_0 — disregarding the influence of the RMS jump length — does not come as a surprise taking into account that we are studying large organic molecules and not single atoms. Such large molecules possess numerous internal degrees of rotational and vibrational freedom not present in single atoms. One can easily imagine that they may have a significant influence on the prefactor as is seen from TST [see Eq. (7.10a)]. The partition functions contain many more factors due to the internal degrees of freedom, and these can have distinct values in the ground state and the transition state.

The increase of h_0 and D_0 could result from the varying bonding strength of the molecule in these two states. A looser bound transition state may lead to ad-

²⁷This is a result of the fact that simple TST is often well suited to describe metal-on-metal diffusion. Hence, the TST result $h_0 = kT/h$ reproduces for temperatures around RT the standard value h_0 and also D_0 if only (or dominantly) NN hops participate in the diffusion process.

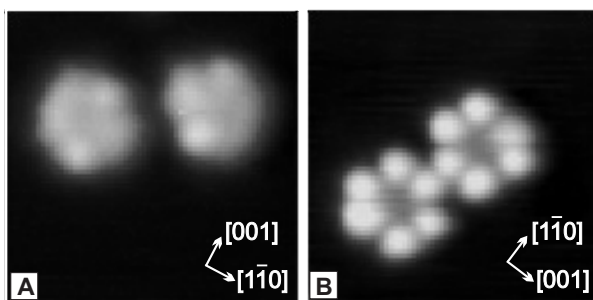


Figure 7.12: High resolution, constant-current STM images ($50 \times 50 \text{ \AA}^2$) of (A) DC ($T = 96 \text{ K}$) and (B) HtBDC ($T = 25 \text{ K}$). Both images reveal two distinct adsorption geometries which are each superimposable by mirroring them on a plane perpendicular to the $[1\bar{1}0]$ direction or — equivalently rotations of odd multiples of 60° . The pronounced internal structure of HtBDC is caused by the six *tert*-butyl groups which give rise to six lobes.

ditional rotational degrees of freedom (corresponding to frustrated vibrations in the ground state) and increase the transition state partition function, or — following the terminology of Eq. (7.10b) — be the reason for an increase in the entropy of the transition state. This entropy effect is often considered not to play a role for metal-on-metal diffusion ($S_D = 0$), which is reasonable because of the lack of internal degrees of freedom [84].²⁸

An indication of our notion concerning an additional rotational degree of freedom is found directly from experimental observations from STM movies at small-scale images which also revealed the adsorption geometry of the molecules. Additional to the diffusive motion of DC and HtBDC, rotational motion could be observed, since the threefold rotational symmetry of the molecules leads to two distinct adsorption geometries on the twofold rotational symmetric Cu(110) substrate as it was described in Chap. 5 and 4 (Fig. 7.12). Rotations of odd multiples of 60° hence lead to distinguishable adsorption geometries and can unambiguously be ascribed to molecule rotation (see Fig. 7.15).

The rotation of molecules can *not* be observed independently from diffusion: at temperatures too low for a diffusion process to occur we never observed a purely rotational motion (i.e. on the same adsorption site). This indicates that the activation energy for rotation must be even higher than for the diffusion process, as opposed to results reported for acetylene on Cu(100) [295]. This can be explained by the size of the DC and HtBDC molecules, extending over $\simeq 4$ close-packed rows on the Cu(110) substrate: a purely diffusive motion is only affected by the smooth corrugation along the $[1\bar{1}0]$ direction, whereas a rotational process also includes interactions with the rougher corrugation along the $[001]$ direction.

Other contributions to large prefactors may result from the vibrational degrees

²⁸It was, however, demonstrated theoretically that vibrational contributions to the activation entropy S_D may not be neglected [337–339].

of freedom in connection with the shape of the potential energy surface. This explanation goes back to the harmonic approximation of TST derived by Vineyard, who found that $h_0 = \prod_m \nu_{GS} / \prod_{m-1} \nu_{TS}$, where ν_{GS} and ν_{TS} are the normal-mode frequencies of the m vibrational degrees of freedom in the ground and transition state [305, 340]. It was shown theoretically for the diffusion of two-dimensional Ir₁₉ clusters on an Ir(111) surface that the energy surface along the diffusion path is flat in the vicinity of the transition state and steep near the adsorption sites [341]. This suggests that at least some normal modes at the transition state have lower frequencies than those in the ground state, thereby producing a high prefactor which agreed well with the experimental value [342]. A similar situation may be imagined for the case of large molecules that experience a smoother potential energy surface in the transition state which gives rise to large prefactors.

Exploiting these arguments from TST, we must remember that this is only an approximative theory which is not directly applicable for diffusion processes including long jumps as in our case. Moreover, the deviations from the standard values are not as significant, if we consider the large error bars which are mainly a result of the narrow temperature interval.

Prefactors deviating from “standard” values are frequently reported in the literature on diffusion but usually unmentioned. High prefactors have been found by STM studies, e.g. for acetylene on Cu(100) ($h_0 \approx 10^{14} \text{ s}^{-1}$) [295], C₆₀ on Pd(110) ($h_0 \approx 10^{14.4} \text{ s}^{-1}$) [93], N on Ru(0001) ($D_0 \approx 10^{-1.7} \text{ cm}^2 \text{ s}^{-1}$) [276], and by integrating LITD studies for alkanes on Ru(0001) ($D_0 \approx 10^{-0.5} \text{ cm}^2 \text{ s}^{-1}$) [270]. In the latter case the prefactors were attributed to long jumps, and theoretical simulations derived a prefactor in good agreement with the experimental one [297, 298]. A low prefactor of $h_0 \approx 10^{10.3} \text{ s}^{-1}$ has been found for PVBA on Pd(110) which was proposed to be the result of a bonding configuration with a reduced entropy in the transition state [92]. This seems rather unlikely from our consideration given above. For CO on Cu(110) the low prefactor of $h_0 \approx 10^7 \text{ s}^{-1}$ was rationalized by only a rather low fraction of thermally accessible configurations of CO which actually can lead to a hopping event [289].

The compensation effect or Meyer-Neldel rule is an empirical rule which predicts a correlation between the prefactor and the activation energy for related activated processes with Arrhenius dependence [343–346]. In the case of activated diffusion (following $h = h_0 \exp(-E_D)$) the rule states

$$h_0 = h_{00} e^{E_D/E_{D0}} \quad (7.23)$$

with a constant h_{00} and the Meyer-Neldel energy E_{D0} . An increase in the activation energy E_D is thus “compensated” by an increase in the prefactor h_0 .

The compensation effect can be understood with simple physical arguments. The curvature of the potential around the adsorption site increases with the barrier heights. A higher curvature is then associated with a larger attempt frequency. A deeper theoretical understanding along with a physical interpretation of h_{00} and E_{D0} is, however, missing even though E_{D0} was predicted to be of the size of a typical excitation energy (the Debye frequency) [347]. The rule is anticipated to apply

for processes where the activation energy is much larger than a typical excitation energy, i.e. if a multiple excitation is needed for the process to occur [345].²⁹

Quite a large number of processes, like solid state diffusion in crystals and electronic conductivity in amorphous semiconductors, obey the Meyer-Neldel rule [345, 346], but an experimental study proving this for surface diffusion processes is, to the best of our knowledge, not available.³⁰ Nevertheless, a MD study of the surface self-diffusion of various metals showed that the rule is obeyed: the data all fall on a straight line in a Meyer-Neldel plot ($\ln h_0$ versus E_D) and a Meyer-Neldel energy $E_{D0} = 0.19 \pm 0.02$ eV has been found.

The diffusion data (Tab. 7.1) for HtBDC and DC fall also on the predicted straight line and we extract $E_{D0} = 0.15$ eV. This agreement with the theoretical diffusion data raises the question if E_{D0} is a universal constant for surface diffusion processes. We therefore checked other atomic-scale diffusion studies which we expected to resemble the MD data of metal-on-metal diffusion much better than our data due to the atomic nature of the adsorbates [87, 91, 126]. These results are, however, not at all in agreement with the Meyer-Neldel plot.

A simple explanation comes from the different lattice parameters of the substrates which influence the curvature of the potential energy surface even for identical barrier heights. This lattice effect was pointed out to be responsible for the occurrence of an anti-compensation effect, i.e. a decrease in the prefactor with increasing barriers [350]. Certainly there are open questions on how to interpret the mismatch of the experimental data, but we must keep in mind that it is still only an empirical rule which lacks a fundamental connection to rate theories.

7.5.2 RMS jump lengths

As mentioned, the hopping rate was determined via the simple analysis, since the determined RMS jump lengths from the Bessel analysis were found to exceed 2 NN distances by far (see Tab. 7.2). In our new approach, the RMS jump length can be deduced from a plot $\langle(\Delta x)^2\rangle$ versus ht which according to Eq. (7.3) has the slope λ^2 . The results for DC and HtBDC are shown in Fig. 7.13.

Best linear fits (least squares under the constraint of passing through the origin) yield $\lambda = 3.9 \pm 0.2$ for DC and 6.8 ± 0.3 for HtBDC.³¹ Since we know that the simple analysis leads to an upper bound for λ , it is useful to test the result versus the lower bound found from the Bessel analysis. The values are compared in Tab. 7.2 and demonstrate that differences are well within the error bars of both methods.

The stated error bars are calculated from the deviations of the data from the best fit and do not explicitly take into account the approximative estimation of h . We can make use of our KMC simulation result in Fig. 7.10 to see that the errors introduced by this approximation are below 2% for all experimental data points,

²⁹This is the subject of ongoing discussion [348, 349].

³⁰For the hopping of oxygen atoms between different adsorption sites on Si(111) a correlation according to the compensation rule was indicated, but a quantitative analysis is missing [288].

³¹Relaxing the fitting constraint and the weighting does not change λ within the error bars.

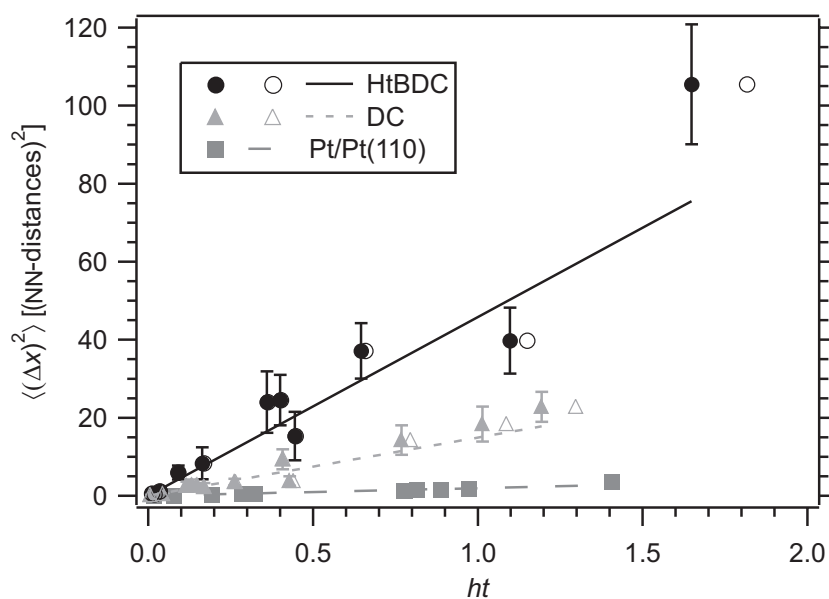


Figure 7.13: Plot of the mean-squared displacement $\langle(\Delta x)^2\rangle$ versus ht according to Eq. (7.3). The lines are the best linear fits under the constrain to pass through the origin. The filled symbols represent the measured data points, while the open symbols in the case of DC and HtBDC are values that have been corrected according to the error estimated in the KMC simulation (see Fig. 7.10). Note that the data density is very high for $ht < 0.3$. Also presented are data from the diffusion of Pt on Pt(110) [91].

except the two highest temperature values, where they, however, are still below 5%.³² This is illustrated in Fig. 7.13, where the *corrected* data points — recalculated according to this error — are included. In a further analysis we can now estimate the *corrected* RMS jump lengths from this. The effect is rather small as seen in Tab. 7.2, demonstrating the excellent approximation of our approach for long RMS jump lengths.

Another potential source of error is the temperature dependence of the RMS jump length. If this was important a plot of $\langle(\Delta x)^2\rangle$ versus ht would not necessarily lead to a straight line. MD simulations showed that long jumps become increasingly important at higher temperatures [296, 316, 324, 351]. On the other hand, only a weak temperature dependence of λ was found in MD simulations for CO on Ni(111) ($\lambda = 2.8$ NN distances) over temperature intervals much larger than considered in our experiment [296].³³ We must, however, consider that in

³²From this we can calculate the errors introduced in h due to the approximation to be below 9% for all data points, as mentioned in the caption of Fig. 7.11.

³³The contradiction may arise from competing influences depending on the temperature range: i) at very low temperatures the adsorbate kinetic energy in the transition state is small and long jumps are

	simple	corrected	Bessel
HtBDC	6.8±0.3	6.7±0.3	6.4±0.4
DC	3.9±0.2	3.8±0.2	3.6±0.2
Pt/Pt(110)	1.41±0.06	-	1.11±0.01

Table 7.2: RMS jump length (in NN distances) derived from Fig. 7.13. The *corrected* values correspond to the data in Fig. 7.13 that were recalculated with the error estimated from the KMC simulations. For comparison, the data via a Bessel analysis are also noted since they represent a lower bound for λ .

our case the temperature interval is quite narrow and significant deviations are not expected.

In principle, information about the jump length could also be obtained from the prefactors via Eq. (7.9). This is frequently done in the literature to estimate RMS jump lengths — often by determining only D_0 experimentally and assuming a standard h_0 [270]. Calculating λ from our experimental prefactors (Tab. 7.1) yields $\lambda = 2 \pm 3$ for DC and $\lambda = 28 \pm 39$ for HtBDC and does not lead to conclusive data due to the large error bars associated with the prefactors. This is avoided by our method which instead of the prefactors concentrates directly on D and h (or equivalently on $\langle(\Delta x)^2\rangle$ and ht).

An analysis of our data through Ehrlich’s formalism is not feasible here as already mentioned in Sec. 7.4.1. Nevertheless, it appears useful to compare our approach with the one introduced by Ehrlich. In order to do so, data from a diffusion study of Pt on Pt(110) [91] have been reanalyzed. In the original study that utilizes Ehrlich’s method, the fraction of NNN jumps amounts on average to around 10% in the temperature interval 300–380 K, corresponding to $\lambda = 1.14$. The result based on our method is included in Fig. 7.13 for a simple analysis of the hopping rate. The result of $\lambda = 1.41 \pm 0.06$ clearly shows the overestimation of this approximation for small λ . Using, however, the Bessel analysis to determine h yields $\lambda = 1.11 \pm 0.01$ in excellent agreement with Ehrlich’s method which has an uncertainty of at least 10% [352]. This demonstrates nicely that our two methods of analyzing h must be chosen according to our recipe given in Sec. 7.4.2, and yield upper and lower bounds for λ .

Fig. 7.14 illustrates how a given RMS jump length λ actually looks in terms of the individual jump probabilities p_i for jumps of different lengths i . Different values of λ are chosen, including those for the systems Pt/Pt(110) and DC and HtBDC on Cu(110). Note that in the case of DC and HtBDC very long jumps are still likely to occur. p_i is still $\approx 0.5\%$ even for $i = 11$ (DC) and $i = 18$ (HtBDC) and such long jumps are also frequently observed in our KMC simulations.³⁴

unlikely to occur, but the probability of their occurrence increases with T , ii) dissipative forces increase with T and reduce λ at high temperatures, and iii) at very high temperatures the diffusion becomes quasi-continuous and frictional forces may become less important.

³⁴We should note that even long jumps with a small probability p_i can significantly contribute to

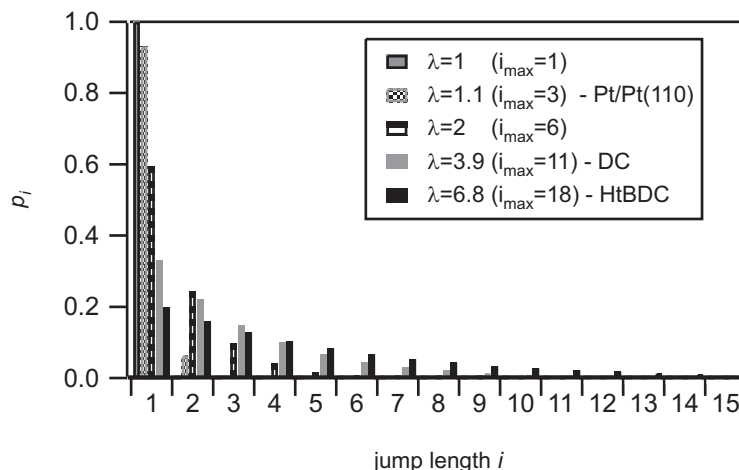


Figure 7.14: Exponential jump length distributions for different RMS jump length λ . We presented distributions for our experimental results and the arbitrary values $\lambda = 1$ and 2 . i_{\max} denotes the maximum jump length i in the distribution with $p_i \approx 0.5\%$, i.e. there are still between 5 and 10 jumps of this length if there are around 1000 events overall.

It is not possible to detect such long jumps directly from our experiments due to the limited time resolution. Nevertheless, we find two strong indications from the STM images in addition to our analytical results: Firstly, occasionally only a fraction of a molecule was imaged, i.e. the molecule jumped away while scanning a single line; typically half a molecule was imaged (Fig. 7.15). The time needed to scan a single line (≈ 0.05 s) is too short for multiple jumps to occur with any significant probability ($h < 1$ s $^{-1}$ and hence $\tau > 1$ s). This implies that single jumps with a length of at least half a molecule diameter occur, i.e. with a length of 6–8 Å. Secondly, at low temperatures (and hence low hopping rates) single observations of very long displacements (up to ca. 20 NN distances) indicate jumps farther than to NN sites, since multiple jumps are very unlikely within the image acquisition time.

The very long RMS jump lengths determined here for DC and HtBDC on Cu(110) seem quite surprising compared to other studies where long jumps could be revealed by means of FIM [90, 287], He-atom scattering [353], and STM [91, 280] and they rarely exceeded NNN distances. An explanation is indicated from theoretical studies (see Sec. 7.3.2): If the thermal energy (≈ 0.02 eV at RT) is much lower than the diffusion barrier (≈ 0.6 eV), long jumps are believed to play a roll when the energy dissipation to the substrate lattice is weak [305].³⁵ The only study

³⁵ $\lambda^2 = \sum_i p_i i^2$, since they are multiplied by i^2 .

³⁵Following Eq. (7.15), the friction (i.e. energy dissipation) must be very low for the two molecules on Cu(110).

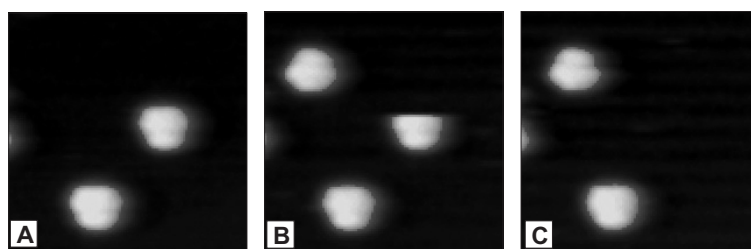


Figure 7.15: Consecutive constant-current images of DC on Cu(110) at $T = 237$ K ($V = -1768$ mV, $I = -0.19$ nA, $80 \times 80 \text{ \AA}^2$). Each image is acquired in 9 s. The bottom molecule stays at its position and is used as a reference for the hopping molecule: (A) Original positions. (B) After more than half of the center molecule is imaged, it hops towards the top and is imaged there again. The displacement is $\approx 40 \text{ \AA}$. Note that this hop is connected with a rotation, since the adsorption geometry of this molecule changed to its mirrored form. (C) The top molecules resides at its position and is no longer imaged at its former position.

known to us which demonstrates an RMS jump length comparable to our results is a MD study of the diffusion of CO on Ni(111), calculating $\lambda = 2.8$ [296]. The transfer of energy between lateral translational motion and the surface was described by a weak friction model as done by Kramers which predicts an increase in jump length (and decreasing equilibrium rate to initiate jumps) with increasing molecular mass.³⁶

It was pointed out in Ref. [355] that additional degrees of freedom are an important difference between molecules and atomic adsorbates: If the lateral molecular motion is weakly coupled to the surface, then the energy exchange between lateral motion and other internal adsorption modes becomes comparably important, i.e. the molecule (may) act as its own heat bath. This was demonstrated again for CO on Ni(111), where the lateral translational motion couples more strongly to the frustrated rotation of the adsorbate (which itself couples to the surface) than directly to the surface. The larger RMS jump length of HtBDC compared to DC can be explained in accordance with the weak friction model: the strong interaction of the aromatic π system of DC with the surface leads to an increased friction and coupling of molecular modes to the surface.

The most reliable atomic-scale data on long jumps result from extensive FIM and STM data of metal-on-metal diffusion, where the fraction of jumps to NN and NNN sites could be extracted [89–91]. Brand *et al.* proposed a very large jump

³⁶Energy transfer is known from classical mechanics to be most efficient when the masses of the adsorbate and substrate atoms are identical (as in the case of surface self-diffusion). It was, however, shown by MD simulations [296] that it is the lower velocity of the heavier molecules that leads to a smaller friction compared to lighter, faster molecules (as seen from the simple Kramers model) rather than the reduced energy transfer in a direct impulsive coupling through a collision with substrate atoms (as predicted in [354]). In our case the molecules have a weight of 450.5 a.u. (DC) and 787.2 a.u. (HtBDC), much heavier than the Cu atoms (63.5 a.u.).

length of 40–50 Å for alkanes on Ru(0001) in order to match the tracer diffusion prefactors to “standard” hopping rate prefactors [270], while theoretical work of alkanes on Pt(111) predicted only jumps to NN and NNN sites to occur [298]. Other studies often more or less speculate about jump lengths or simply consider only NN jumps. Weckesser *et al.* claim from the Arrhenius behavior of their data of PVBA on Pd(110) that only NN jumps are present [92]. Nevertheless, their data analysis is based entirely on partly imaged molecules as in Fig. 7.15. Therefore, jump lengths of at least half a molecule diameter must be present which in their case is ≈ 6 Å; this strongly indicates long jumps and not only jumps to Pd(110) NN adsorption sites (separated 2.76 Å).

It is finally noted that the interpretation of jump spanning multiple NN sites is not straightforward. This was demonstrated for the diffusion of Pt on Pt(110) where 5-10% of the jumps were determined to go to NNN sites [91]. Surely one would on a first glance assume that the Pt atoms jump directly to the NNN site. It was, however, shown theoretically that the (111) microfacets along the troughs in the (1×2) -reconstructed Pt(110) surface offer an alternative pathway. This path is almost equally likely compared to the direct jump path and hence is an important and competing diffusion route [356, 357]. Nevertheless, the statistical analysis could be applied successfully in Ref. [91], the reason being that the adsorption sites on the microfacets of the troughs represent very shallow minima in the potential energy hypersurface. This results in very short residence times of the molecules which can hence not be imaged in these positions.

The same situation as for the Pt diffusion could be the case for the diffusion of large molecules. A jump of for example 10 NN distances does not have to be a direct jump. It could in principle be a path along shallow local minima, where the molecule-surface conformation adopts in a certain way through the many molecular degrees of freedom to result in a preferred or at least competitive diffusion path to the direct jump. This is, however, very speculative.

7.6 Conclusions

In this chapter a comprehensive study of the diffusion of large molecules on single crystal metal surfaces is reported. Even though large molecules have numerous internal degrees of freedom compared to atomic adsorbates and therefore interact with the substrate via a much more complex potential energy surface, the diffusion processes observed in this study could be described by simple Arrhenius behavior of the hopping rate h and the tracer diffusion coefficient D . This can be expected from theoretical consideration for a rare event diffusion process even when long jumps play a role, if the temperature dependence of the prefactor is small or the investigated temperature interval is narrow.

The activation energies of diffusion for DC and HtBDC on Cu(110) were determined to be 0.73 eV and 0.59 eV, respectively. This difference in the barriers resembles the qualitative understanding of the process: the aliphatic spacer groups in HtBDC weaken the otherwise dominant interaction of the DC π system with the

Cu substrate. The prefactor h_0 was determined to be slightly elevated compared to standard values and this was discussed in relation to rate theories. The prefactor D_0 is significantly larger compared to standard values because of the large RMS jump length.

A new and simple approach to determine the RMS jump length was presented. It is based on an independent determination of the tracer diffusion coefficient D and the hopping rate h from experimental data. The precision of the determined hopping rates h was assessed by KMC simulations and enabled us to present a recipe of how to extract values with minimal error. RMS jump lengths of 3.9 (DC) and 6.8 (HtBDC) NN distances are, to the best of our knowledge, the largest reported in the literature so far. Again, the difference is related to the chemical structure: the stronger bonded molecule has a shorter RMS jump length and vice versa. The results stress not only the importance of taking long jumps into account for the diffusive motion of large molecules. It moreover presents a way, how molecules can be tailored to possess particular diffusion properties.

We want to emphasize an important result of the KMC simulations: depending on the parameter range of h , D and especially λ , large errors can be involved in the approximative determination of the hopping rate. This is especially true for the often used, simple exponential analysis, if long jumps participate in the diffusion process. It is therefore of utmost importance to focus not only on the hopping rate but also to determine the tracer diffusion constant. This enables a quantitative estimation of which method of analysis is better suited. Generally, diffusion data gained via D may be considered more reliable, since they intrinsically take the RMS jump length into account. Moreover, from such data the hopping rate can always be estimated and hence the RMS jump length can be determined — a fact that up to now has not been exploited.

CHAPTER 8

Summary

Molecules on surfaces play a fundamental role in many fields of interest like epitaxial thin film growth, heterogeneous catalysis, biomaterials interfaces, molecular electronics and the formation of nanostructures in general. In all these areas the delicate balance between the competing intermolecular and molecule-substrate interactions is a key factor and their detailed understanding is important for controlling the mentioned processes in a desired way. In the present thesis fundamental aspects of the bonding, ordering and mobility of large organic molecules on metal surfaces were studied at the atomic scale by means of scanning tunneling microscopy (STM).

A main objective of this thesis was to investigate molecular assembly mechanisms at surfaces. This supramolecular aggregation is often governed by directional, intermolecular interactions, while the metal surface is considered a static checkerboard that provides only weak bonding to the molecules. This thesis clearly demonstrates that the latter assumption is not necessarily true. It is shown that molecule-substrate interactions can be a dominating effect for large molecules with weak intermolecular interactions (van-der-Waals forces).

Three similar molecules (HtBDC, DC, Lander) were investigated which all possess a conducting backbone (aromatic π system) as a key structural element thought to be important in building blocks for possible future molecular electronics devices. The aromatic system adsorbs parallel to the metal surface and is surrounded by spacer groups. These groups differ within the three molecules which leads to a varying strength of the molecule-substrate interaction. The study of such related molecules on the same Cu(110) surface elucidates important, funda-

mental aspects of the bonding and ordering mechanism of large adsorbates.

It is shown that the varying bonding strength to the surface has consequences not only for the *static* aspects of the adsorption, i.e. the structure of the adsorbate monolayer and the underlying surface, but also for the *dynamic* behavior of the adsorbate, e.g. the diffusion activation energy and the jump length. The microscopic understanding gained in these model systems is valuable for eventually extending this understanding to more applied systems.

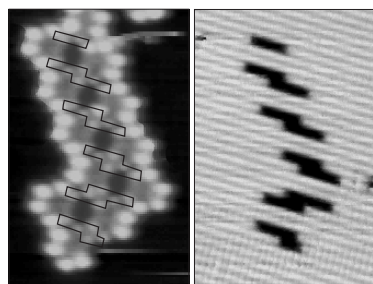


Figure 8.1: Adsorption structure of HtBDC and surface restructuring underneath.

The first part of this thesis focused on the static aspects of the molecule-substrate interaction which was investigated for the three different molecules. It was shown that HtBDC molecules form stable, double rows along specific surface directions even though intermolecular forces are minimal (Chap. 4). This assembly process was associated with a local restructuring of the surface underneath the molecules. The ability of the STM to manipulate matter at the atomic scale was exploited, when pushing the molecular adsorption layer aside, directly revealing the restructured Cu surface (Fig. 8.1). Effective medium theory calculations were

used to yield insight into the specific double row structure.

Even more surprising was that the disclosed restructuring was chiral, a fact that has not been observed before. The holes in the Cu substrate are enantiomorph, each containing two kink sites of identical chirality. This shows how chirality is locally induced on a metal surface due to the adsorption of molecules, and since every molecule is associated with one kink site it was speculated if the molecules themselves transfer a specific kink site chirality to the surface in a chiral imprinting process. This may shed new light on the mechanistic understanding of the asymmetric catalytic behavior of chirally modified surfaces.

The driving force behind the surface restructuring was proposed to be the approach of the molecule's π system to the kink sites in the restructured surface. This enables the strong molecule-substrate interaction to be restored after being weakened through the spacer groups on the plane surface. Improved insight into the different bonding situations was achieved by comparing the adsorption of HtBDC molecules to the adsorption of the very similar DC molecules (Chap. 5).

DC consists of the same aromatic center as HtBDC, but does not possess the spacer legs. No surface restructuring was found underneath the DC molecules even at elevated substrate temperatures, which is a consequence of the strong, direct interaction of the aromatic π system with the substrate. In contrast to the substrate-mediated formation of HtBDC double rows occurring already at low coverages, DC has a very low tendency to form ordered structures which occur only at almost saturated coverages.

These results prove that molecule-substrate interactions can be a controlling factor for self-assembly of molecules on surfaces — even at low coverages and

when directional intermolecular forces are absent. In general, the intentional separation of a strongly bonding molecular subunit from a metal surface seems to be a driving force behind a restructuring of the metal surface in order to regain a suitable interaction geometry.

This notion turned out to be a central theme in the investigation of Lander molecules (Chap. 6) which comprise an aromatic π system surrounded by spacer groups similar to HtBDC. It was shown that the Lander molecules also locally restructure the surface, forming tooth-like structures at monatomic Cu steps underneath the molecules (Fig. 8.2).

It is interesting that a surface restructuring does not occur on the terraces in the case of Lander molecules. Electron scattering quantum chemistry (ESQC) calculations indicated that this is a consequence of the high flexibility of the Lander spacer groups: they are bent such that the aromatic board can adsorb already strongly on the plain terraces. Lifting the board onto a tooth mainly releases the strain in the spacer group bonds and this energy gain is not large enough to compensate for the surface restructuring on the terraces. Accordingly, Lander molecules barely order into domains, since directional, intermolecular forces are absent as in the case of DC.

In conclusion, the results in Chaps. 4–6 demonstrate that large organic molecules can adopt adsorption conformations on metal surfaces which may or may not involve unpredicted restructuring of the surface depending on the precise chemical structure of the adsorbate. Apart from emphasizing the importance of manipulation experiments to investigate the adsorption in detail, this suggests that surface-restructuring processes may be more common than what is generally believed for the adsorption of large molecules.

The second main topic of this thesis deals with the mobility of adsorbates on surfaces (Chap. 7). While the understanding of metal-on-metal diffusion has reached a very detailed level, much less is known about surface diffusion of (large) molecules. This was for the first time thoroughly and comprehensively investigated in this thesis focusing on the two molecules HtBDC and DC. The diffusion was studied by means of STM movies which enabled one-dimensional displacements of individual molecules on the Cu(110) surface to be followed.

A key result from these investigations is that the diffusion of the two molecules is *dominated* by long jumps. Surprisingly, root mean-squared (RMS) jump lengths of 6.8 and 3.9 Cu lattice spacings have been determined for HtBDC and DC, respectively, demonstrating that only a minority of jumps occurs between nearest-neighbor sites. This is in strong contrast to the conventional nearest-neighbor hopping picture which is generally found for metal-on-metal diffusion.

The RMS jump lengths λ were extracted in a new approach which, to the best of our knowledge, has been overlooked in the existing literature. It is based on an independent determination of the tracer diffusion coefficient D and the hopping

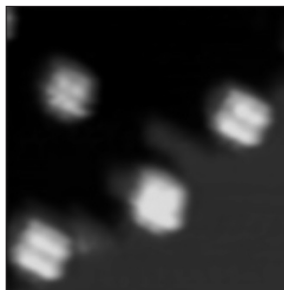


Figure 8.2: Tooth restructuring of Cu steps due to Lander molecules.

rate h from the STM data. From the well-known statistical relation $D = \lambda^2 h/2$, the RMS jump length can be extracted from the slope of a D - h plot (Fig. 8.3). Kinetic Monte Carlo simulations have been performed to quantify with which precision h can be determined from experimental data.

Finally, it was shown that the diffusion follows a simple Arrhenius behavior with diffusion activation energies of 0.59 eV (HtBDC) and 0.73 eV (DC). The difference for the two molecules can be related to the chemical structure: By raising the aromatic plane common to DC/HtBDC away from the surface by spacer groups in the case of HtBDC, this molecule is endowed with a much higher diffusivity both due to larger RMS jump lengths and a lower activation barrier for diffusion. This demonstrates the possibility of tailoring the molecular diffusion properties which may play an important role for building self-assembled molecular electronics devices.

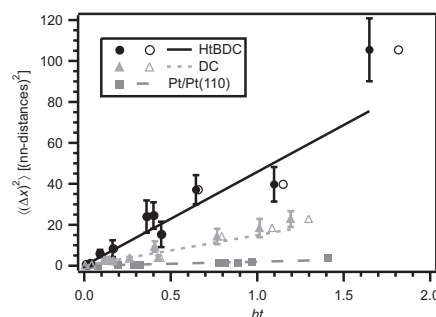


Figure 8.3: Different RMS jump lengths are indicated by the slopes of D - h plots.

APPENDIX A

Stereochemical principles

The following chapter deals with fundamental principles of stereochemistry and the conventions that have been adopted to describe the spatial arrangements of molecules [358, 359].

A.1 General definitions

When structures of the same *constitution*, i.e. with the same sequence of bonding of the atoms differ in *configuration*, i.e. spatial arrangement, they are *stereoisomers*. Stereoisomers that are related by being non-superimposable mirror images are *enantiomers*; stereoisomers that are not enantiomers are *diastereomers*.

In addition to constitution and configuration the *conformation* as a third significant level of structure describes discrete molecular arrangements that differ in spatial arrangement as a result of facile rotations around single bonds. When rotation about single bonds is restricted by steric or other factors, the different conformations can be separated and are called *atropisomers*.

Structures that have non-superimposable mirror images are called *chiral*. It is possible to separate the enantiomers of chiral compounds, and samples containing only one enantiomer are called *enantiomerically pure* or *homochiral*. One characteristic of chiral molecules is that the separated enantiomers cause the plane of polarized light to rotate in opposite directions.

Samples that have equal amounts of the two enantiomers are called *racemic mixtures* and show zero net rotation. Racemic crystals can be divided into two types: *racemic compounds* and *conglomerates*. The first type consists of a perfectly

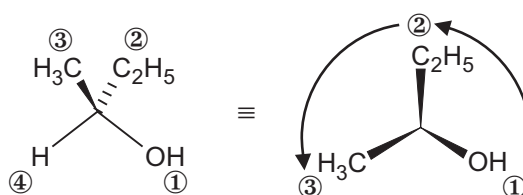


Figure A.1: The Cahn-Ingold-Prelog convention exemplified for (*S*)-2-butanol. The substituents are marked from highest priority (1) to lowest priority (4). On the right-hand side the molecule is oriented in a way which makes the assignment of the *S* configuration obvious (see text for details).

ordered crystal of both enantiomers — a 1:1 addition complex — while the second type consists of a mechanical mixture of homochiral (micro-)crystallites of the two enantiomers.

The *enantiomeric excess* (ee) of a mixture of two enantiomers is defined via their molar concentration n as

$$\text{ee} [\%] = 100 \frac{n_{\text{major}} - n_{\text{minor}}}{\Sigma n} \quad (\text{A.1})$$

In order to distinguish between the chirality, or handedness, of stereoisomeric compounds, the configuration must be specified. The conventions used nowadays are described in the next section.

A.2 Cahn-Ingold-Prelog convention

The Cahn-Ingold-Prelog (CIP) convention is based on (arbitrary but consistent) sequence rules to assign a priority order to the substituents on the atom to which a configuration is being assigned¹. The substituent atoms are assigned decreasing priority in the order of decreasing atomic numbers and when two or more of the substituent atoms represent the same element, the next attached atoms in those substituents are compared. This process of substituent comparison is continued until the order of priority of all substituents has been established².

The molecule is now viewed in an orientation which places the lowest-priority substituent behind the chiral center (Fig. A.1). If the remaining three substituents decrease in priority in a clockwise or counterclockwise manner, the configuration is assigned the descriptor *R* (rectus = right) or *S* (sinister = left), respectively.

Beside the *R* and *S* numerous other descriptors exist to describe special stereochemical situations. One of those is for molecules with a helical structure, where

¹Compounds in which chirality is the result of an *asymmetric carbon atom* having four nonidentical substituents (*stereogenic center*) represent the largest class of chiral molecules. Molecules possessing other forms of chiral elements like a *stereogenic axis* or *plane* are not considered here.

²The process of hierarchical assignment of the substituents can in certain cases be very complicated and puzzling. The reader is referred to the original papers for details [250, 251]

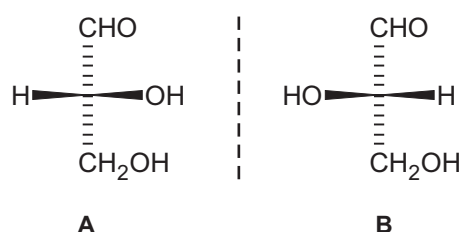


Figure A.2: Structure of (A) D-glyceraldehyde and (B) L-glyceraldehyde, the reference molecule for the Fischer convention.

the (overall) configuration is designated *P* (plus) and *M* (minus) for right- and left-handed helices, respectively.

A.3 Fischer convention

The Fischer convention, employing the descriptors D (dexter = right) and L (laevus = left), is historically important and is still used in sugar chemistry and for α -amino acids. Glyceraldehyde is the point of reference and the two enantiomers were originally arbitrarily assigned the configurations D and L by Fischer (Fig. A.2) which were later established to be the correct ones.

The molecules are oriented with the major carbon chain aligned vertically with the most oxidized carbon atom at the top. The vertical bonds at each carbon are directed back, away from the viewer, and the horizontal bonds are directed forward to the viewer. The configuration by any other chiral molecule to be assigned in the Fischer convention is done according to whether the configuration at the highest numbered stereogenic center is equivalent to D- or L-glyceraldehyde.

The Fischer convention is hence only a *relative* assignment, whereas the CIP convention is an *absolute* assignment. Moreover, many molecules are chiral even though they do not possess a stereogenic center and can therefore only be categorized by the CIP rules. It is important to note that there is no direct relationship between the configurational descriptors *R* and *S* on one hand, and D and L on the other hand.

APPENDIX B

Random walk theory

Here details of random walk theory are presented and some useful background information with respect to the analysis of the adsorbate diffusion process in Chap. 7 is summarized.

B.1 Poisson process

The mathematical model treating completely random series of events is the *Poisson process* that is characterized by a mean rate h [311]. The conditions for a Poisson process to occur are:

1. the number of events (jumps) N occurring in a time interval dt is statistically independent of the number and position of events in dt .
2. at very short time intervals dt , the probability of no event to occur is $p(N = 0) = 1 - hdt + o(h)$, and
3. the probability of one event to occur is $p(N = 1) = hdt + o(h)$.

$o(h)$ denotes any quantities that tend to zero more rapidly than h as $h \rightarrow 0$, i.e. $\lim_{h \rightarrow 0} o(h)/h = 0$. Hence, from (2) and (3) the probability $p(N > 2)$ of more than one event to occur in dt tends to zero (more precisely, $p(N > 2) = o(h)$).

A characteristic property of the Poisson process is that the number of jumps N , occurring in the time interval of length t , has a Poisson distribution with mean value ht :

$$p(N) = \frac{(ht)^N e^{-ht}}{N!}. \quad (\text{B.1})$$

As a direct consequence, the time intervals between events are exponentially distributed, and the probability $p(0)$ of no jump to occur during t is

$$p(0) = e^{-ht}. \quad (\text{B.2})$$

It is a feature of the Poisson process that an ensemble of independent Poisson processes will behave as one Poisson process characterized by the individual ones. For example, we have different hopping rates h_i for jumps characterized by a length i which are all described by a Poisson process; then Eq. (B.1) does not only hold for the individual h_i , but also for the overall process characterized by $h = \sum_i h_i$ and $N = \sum_i N_i$ [335].

One must be aware that the Poisson process is a mathematical concept and whether a real process is in accord with a Poisson process is ultimately an empirical matter. The most prominent example is probably the emission from a radioactive source. The three conditions necessary for a Poisson process to occur seem reasonable also in the case of the diffusion of adsorbates on a substrate. Maybe the best "proof" is the exponential decay of the residence times $p(0)$ [Eq. (B.2)] that could be observed experimentally in a few cases [281, 286, 295].

B.2 Displacement distributions

The statistical framework of how an analytical expression of the displacement distribution is calculated for the case of discrete time intervals in between observations was developed by Ehrlich [234, 273]. The crucial parameter coming into play, beside the hopping rate h and the time interval t , is the number of different jump lengths λ_i (measured in multiples i of the NN distances of the substrate) which participate in the diffusion process. This has a pronounced influence on the displacement distribution.

We are interested in an expression for the displacement distribution ${}^\gamma P_x$ of finding a particle at a distance x from the origin after time t , if we take γ different jump lengths into account. Even though the general expression can be difficult to derive, it is straightforward and instructive for the simplest case of only NN jumps to occur ($\gamma = 1$ and $\lambda_1 = 1$) with the rate h_1 . This will be shown in the following.

The probability of observing a particle with the starting position $x = 0$ at $t = 0$ at a position x after a time interval t during which it made a total of N jumps is given by the binomial expression

$$p_x(N) = \left(\frac{1}{2}\right)^N \frac{N!}{\left(\frac{N+x}{2}\right)! \left(\frac{N-x}{2}\right)!}. \quad (\text{B.3})$$

Hence, the probability ${}^1 P_x$ of finding a particle at a distance x from the origin after time t (independent of the number N) can be obtained by folding $p_x(N)$ with the

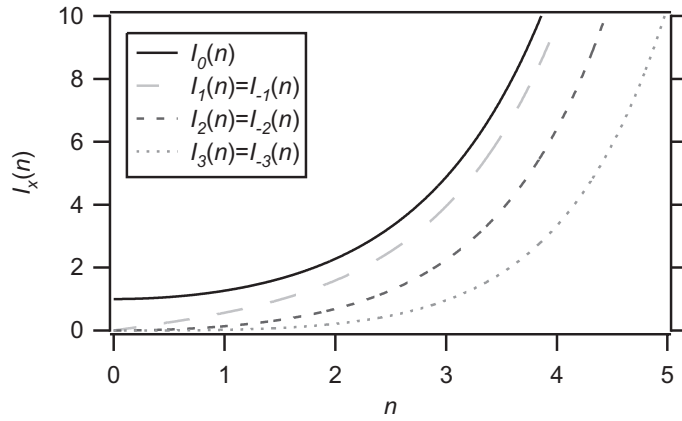


Figure B.1: Modified Bessel functions of the first kind $I_x(n)$ plotted for the order $x = 0, \pm 1, \pm 2,$ and ± 3 . Note that $I_x(n) = I_{-x}(n)$.

probability $p(N)$ of the particle to perform N jumps [Eq. (B.1)] and summing over all possible numbers N :

$${}^1P_x = \sum_{N=0}^{\infty} p_x(N)p(N) \quad (\text{B.4a})$$

$$= e^{-h_1 t} \sum_{N=0}^{\infty} \frac{\left(\frac{h_1 t}{2}\right)^N}{\left(\frac{N+x}{2}\right)! \left(\frac{N-x}{2}\right)!}. \quad (\text{B.4b})$$

If we take into account that odd/even displacements x can only be achieved by an odd/even number of displacements with $N > x$, it is convenient to rewrite Eq. (B.4b) by substituting $N = 2k + x$ which leads to

$${}^1P_x = e^{-h_1 t} \left(\frac{h_1 t}{2}\right)^x \sum_{k=0}^{\infty} \frac{\left(\frac{h_1 t}{2}\right)^{2k}}{(k+x)!k!} \quad (\text{B.4c})$$

$$= e^{-h_1 t} I_x(h_1 t), \quad (\text{B.4d})$$

with I_x being the modified Bessel function of the first kind of order x that is defined as [360]

$$I_x(n) = \left(\frac{n}{2}\right)^x \sum_{k=0}^{\infty} \frac{\left(\frac{n}{2}\right)^{2k}}{(k+x)!k!}. \quad (\text{B.5})$$

Its functional behavior is illustrated in Fig. B.1 for some low values of x .

If jumps to more remote adsorption sites are relevant, the deduction of the displacement distributions becomes complicated and does not provide new features; it can be found in Ref. [89]. The results, however, can be interpreted in a straightforward manner as will be demonstrated for two more cases.

Taking double jumps ($\gamma = 2$ and $\lambda_2 = 2$) with rate h_2 into account yields

$${}^2P_x = e^{-(h_1+h_2)t} \sum_{j=-\infty}^{\infty} I_j(h_2t) I_{x-2j}(h_1t) \quad (\text{B.6a})$$

$$= \sum_{j=-\infty}^{\infty} {}^1P_{2j}(h_2t) {}^1P_{x-2j}(h_1t). \quad (\text{B.6b})$$

The latter was rewritten in a physically more meaningful form using ${}^1P_x(h_1t) = \exp(-h_1t) I_x(h_1t)$ and ${}^1P_{2j}(h_2t) = \exp(-h_2t) I_j(h_2t)$ for the probabilities if only single or double jumps occur. Hence, P_x can be expressed as the sum over all possible paths by which an adsorbate reaches an intermediate position $x - 2j$ by single jumps and goes back to x by double jumps.

Adding also triple ($\gamma = 3$ and $\lambda_3 = 3$) with rate h_3 gives

$${}^3P_x = e^{-(h_1+h_2+h_3)t} \sum_{k=-\infty}^{\infty} I_k(h_3t) \sum_{j=-\infty}^{\infty} I_j(h_2t) I_{x-2j-3k}(h_1t) \quad (\text{B.7a})$$

$$= \sum_{k=-\infty}^{\infty} {}^1P_{3k}(h_3t) \sum_{j=-\infty}^{\infty} {}^1P_{2j}(h_2t) {}^1P_{x-2j-3k}(h_1t), \quad (\text{B.7b})$$

where ${}^1P_{3k}(h_3t) = \exp(-h_3t) I_k(h_3t)$ is now the probability that only triple jumps occur. As in the former case the result can be interpreted as a sum over all possible paths of jump combinations.

The analytical solution for the exponentially distributed jump lengths $p_i = h_i/h = (e^a - 1) \exp(-ai)$ with $h = \sum_i h_i$ has been derived in Ref. [361] to be¹

$$\begin{aligned} {}^aP_x = e^{-(ht+xa)} & \left[\delta_{x,0} + (1 - \delta_{x,0})(x-1)! \sum_{n=1}^x \left(\frac{ht}{2}\right)^n \frac{(e^a - 1)^n}{n!(x-n)!(n-1)!} \right. \\ & + \left(\sum_{n=2}^{\infty} \left(\frac{ht}{2}\right)^n \sum_{m=1}^{n-1} [m!(n-m)!(m-1)!(n-m-1)!]^{-1} \right. \\ & \left. \left. \times \sum_{k=k_0}^{\infty} \frac{e^{-2ka}(k-1)!(k+x-1)!}{(k-m)!(k+x-n+m)!} \right) \right] \quad (\text{B.8}) \end{aligned}$$

where k_0 equals the greater of $(n - m - x)$ and m . When $a \rightarrow \infty$, the displacement distribution corresponds to the result of a NN random walk: ${}^aP_x = {}^1P_x$ [see Eqs. (B.4c) and (B.4d)].

¹The only articles apart from Ref. [361] that state the formula derived by Cowan report an incorrect version [329, 330].

APPENDIX C

Nucleation and growth of a new CAMP member

This chapter describes studies and experiments which are only remotely related to the STM work that makes the major part of this work. Moreover, most of the work was not performed at the physics institute and is published already in paper [X].

Introduction

The traditional pre-cloning era production of a new member of the Center for Atomic-scale Materials Physics (CAMP) is described in detail. The successful nucleation of a new CAMP member is confirmed and the growth process up to week 12 is demonstrated for the first time by ultrasound scanning microscopy (USM). The experiments have clearly been stimulated by the movement of the research areas towards “bio-stuff”.

Experimental Results

The nucleation of Schunack Jr. started around July 1, 2000 at a temperature of 37.2 °C and the growth proceeded in liquid around 37.6 °C. All the time, Schunack Jr. was permanently connected to the specially designed, size-adjustable “sample holder”, J. Schunack. This avoided damages and transfer problems. All kinds of essential nutrition were constantly dosed by means of the “sample holder”.



Figure C.1: First experimental real space ultrasound scanning imaging with sub-meter resolution of Schunack Jr. ($\approx 12 \times 9 \text{ cm}^2$ of the inner frame). The image was taken at room temperature and atmospheric pressure.

The first real space ultrasound scanning imaging of Schunack Jr. is shown in Fig. C.1, confirming the nucleation. Due to the sub-meter resolution of the ultrasonic device, the head is clearly revealed in the center of the image. It measures 22 mm in diameter. One of the arms is attached to the back which is pointing to the bottom-left corner. Occasionally, the second arm and even two legs (spacer groups designed for separating the torso from mother earth) can be seen¹. Notwithstanding, imaging of Schunack Jr. at room temperature is not easy due to his rapid movements that are sometimes faster than the time-scale of USM imaging.

New USM studies in week 19 after the nucleation confirmed that Schunack Jr. been grown noticeably (no picture). The date of birth was scheduled for March 21, 2001. For reasons not understood yet, he was delayed and finally born on March 30, 2001. At that time the permanent connection to the sample holder was interrupted which did not prevent him from growing exceedingly fast. This and many more details can be found on the homepage of Schunack Jr., who from now on is called Jonas². A recent photograph is shown in Fig. C.2

Outlook

There are great future prospects for the presented experiment so far. The experiment is expected to be reproducible and we plan to confirm this some time in the

¹J. Schunack, M. Schunack, and *not* F. Besenbacher, to be published.

²<http://www.ifa.au.dk/~schunack/jonasmain.htm>



Figure C.2: Jonas at the age of 8 months, performing solid state experiments. The image was obtained with a visible, light digital camera.

future.

Acknowledgements

We acknowledge C. Sardeli from Randers Centralsygehus³ for technical support and fruitful discussions in interpreting the USM images as well as financial support from the EU network “Bottom-up-Nanomachines”.

³<http://www.aaa.dk/rc/1/1geninf.htm>

Bibliography

- [1] *Molecular materials make their mark*, special issue in Phys. World **12**, 25 (1999).
- [2] *Nanotech*, special issue of Sci. Am. **285** (2001).
- [3] V. Balzani, A. Credi, F. M. Raymo, and J. F. Stoddart, Angew. Chem. Int. Ed. **39**, 3349 (2000).
- [4] G. E. Moore, Electronics **38**, 114 (1965).
- [5] The semiconductor industries association, *The international technology roadmap for semiconductors* (<http://public.itrs.net>, 2001).
- [6] *The future of microelectronics*, special issue in Nature **406**, 1021 (2000).
- [7] M. Schulz, Nature **399**, 729 (1999).
- [8] D. A. Muller, T. Sorsch, S. Moccio, F. H. Baumann, K. Evans-Lutterodt, and G. Timp, Nature **399**, 758 (1999).
- [9] Y. Huang, X. Duan, Q. Wei, and C. M. Lieber, Science **291**, 630 (2001).
- [10] Y. Huang, X. Duan, Y. Cui, L. J. Lauhon, K.-H. Kim, and C. M. Lieber, Science **294**, 1313 (2001).
- [11] V. Derycke, R. Martel, J. Appenzeller, and Ph. Avouris, Nano Lett. **1**, 453 (2001).
- [12] A. Bachtold, P. Hadley, T. Nakanishi, and C. Dekker, Science **294**, 1317 (2001).
- [13] R. F. Service, Science **294**, 2442 (2001).
- [14] A. Aviram and M. A. Ratner, Chem. Phys. Lett. **29**, 277 (1974).
- [15] M. A. Reed and J. M. Tour, Sci. Am. **282**, 68 (2000).

- [16] M. A. Reed, C. Zhou, C. J. Muller, T. P. Burgin, and J. M. Tour, *Science* **278**, 252 (1997).
- [17] C. Joachim, J. K. Gimzewski, and A. Aviram, *Nature* **408**, 541 (2000).
- [18] X. D. Cui, A. Primak, X. Zarate, J. Tomfohr, O. F. Sankey, A. L. Moore, T. A. Moore, D. Gust, G. Harris, and S. M. Lindsay, *Science* **294**, 571 (2001).
- [19] C. Joachim and J. K. Gimzewski, *Chem. Phys. Lett.* **265**, 353 (1997).
- [20] S. J. Tans, R. M. Verschueren, and C. Dekker, *Nature* **393**, 49 (1998).
- [21] R. Martel, T. Schmidt, H. R. Shea, T. Hertel, and P. Avouris, *Appl. Phys. Lett.* **73**, 2447 (1998).
- [22] C. P. Collier, G. Mattersteig, E. W. Wong, Y. Luo, K. Beverly, J. Sampaio, F. M. Raymo, J. F. Stoddart, and J. R. Heath, *Science* **289**, 1172 (2000).
- [23] C. Dekker, *Phys. Today* **52**, 22 (1999).
- [24] *Carbon nanotubes*, edited by M. S. Dresselhaus, G. Dresselhaus, and Ph. Avouris (Springer, Berlin, 2000).
- [25] P. L. McEuen, *Phys. World* **13**, 31 (2000).
- [26] D. M. Eigler and E. K. Schweizer, *Nature* **344**, 524 (1990).
- [27] J. A. Stroscio and D. M. Eigler, *Science* **254**, 1319 (1991).
- [28] P. Avouris, *Acc. Chem. Res.* **28**, 95 (1995).
- [29] G. Meyer, L. Bartels, S. Zöphel, E. Henze, and K. H. Rieder, *Phys. Rev. Lett.* **78**, 1512 (1997).
- [30] L. Bartels, G. Meyer, and K.-H. Rieder, *Appl. Phys. Lett.* **71**, 213 (1997).
- [31] R. M. Nyffenegger and R. M. Penner, *Chem. Rev.* **97**, 1195 (1997).
- [32] S.-W. Hla, L. Bartels, G. Meyer, and K. H. Rieder, *Phys. Rev. Lett.* **85**, 2777 (2000).
- [33] R. Feynman, *Sci. Eng.* **23**, 22 (1960).
- [34] U. Durig, G. Cross, M. Despont, U. Drechsler, W. Haberle, M. I. Lutwyche, H. Rothuizen, R. Stutz, R. Widmer, P. Vettiger, G. K. Binnig, W. P. King, and K. E. Goodson, *Trib. Lett.* **9**, 25 (2000).
- [35] G. M. Whitesides, J. P. Mathias, and C. T. Seto, *Science* **254**, 1312 (1991).
- [36] J. Seto, N. Asai, I. Fujiwara, T. Ishibashi, T. Kamei, and S. Tamura, *Thin Solid Films* **273**, 97 (1996).

- [37] J.-P. Sauvage, *Acc. Chem. Res.* **31**, 611 (1996).
- [38] C. P. Collier, E. W. Wong, M. Belohradský, F. M. Raymo, J. F. Stoddart, P. J. Kuekes, R. S. Williams, and J. R. Heath, *Science* **285**, 391 (1999).
- [39] C. S. Lent, *Science* **288**, 1597 (2000).
- [40] M. O. Lorenzo, C. J. Baddeley, C. Muryn, and R. Raval, *Nature* **404**, 376 (2000).
- [41] C. A. Mirkin, S. Hong, and L. Demers, *Chem. Phys. Chem.* **2**, 37 (2001).
- [42] Y. Xia and G. Whitesides, *Angew. Chem. Int. Ed.* **37**, 550 (1998).
- [43] T. Sano, H. Fujii, Y. Nishio, Y. Hamada, H. Takahashi, and K. Shibata, *Synthetic Metals* **91**, 27 (1997).
- [44] L. Schmidt-Mende, A. Fechtenkötter, K. Müllen, E. Moons, R. H. Friend, and J. D. MacKenzie, *Science* **293**, 1119 (2001).
- [45] C. D. Dimitrakopoulos and P. R. L. Malenfant, *Adv. Mater.* **14**, 99 (2002).
- [46] A. Leson and H. Hilgers, *Physik. Bl.* **55**, 63 (1999).
- [47] D. H. Kim, J. K. Kim, and P. Hwang, *Thin Solid Films* **360**, 187 (2000).
- [48] H. J. Gao, K. Sohlberg, Z. Q. Chen, S. M. Hou, L. P. Ma, X. W. Fang, S. J. Pang, and S. J. Pennycook, *Phys. Rev. Lett.* **84**, 1780 (2000).
- [49] A. N. Shipway, E. Katz, and I. Willner, *Chem. Phys. Chem.* **1**, 18 (2000).
- [50] B. Kasemo and J. Gold, *Adv. Dent. Res.* **13**, 8 (1999).
- [51] C. A. Mitchell, L. Yu, and M. D. Ward, *J. Am. Chem. Soc.* **123**, 10830 (2001).
- [52] C. Mainka, P. S. Bagus, A. Schertel, T. Strunskus, M. Grunze, and Ch. Wöll, *Surf. Sci.* **341**, L1055 (1995).
- [53] K. Weiss, S. Gebert, M. Wühn, H. Wadepohl, and Ch. Wöll, *J. Vac. Sci. Technol. A* **16**, 1017 (1998).
- [54] F. S. Thomas, N. S. Chen, L. P. Ford, and R. I. Masel, *Surf. Sci.* **486**, 1 (2001).
- [55] S. Lukas, S. Vollmer, G. Witte, and Ch. Wöll, *J. Chem. Phys.* **114**, 10123 (2001).
- [56] Q. Chen, D. J. Frankel, and N. V. Richardson, *J. Chem. Phys.* **116**, 460 (2002).
- [57] Q. Chen, D. J. Frankel, and N. V. Richardson, *Surf. Sci.* **497**, 37 (2002).
- [58] S. Lukas, G. Witte, and Ch. Wöll, *Phys. Rev. Lett.* **88**, 028301 (2002).
- [59] S. R. Forrest, *Chem. Rev.* **97**, 1793 (1997).

- [60] F. J. Meyer zu Heringsdorf, M. C. Reuter, and R. M. Tromp, *Nature* **412**, 517 (2001).
- [61] J. K. Gimzewski, E. Stoll, and R. R. Schlittler, *Surf. Sci.* **181**, 267 (1987).
- [62] H. Ohtani, R. J. Wilson, S. Chiang, and C. M. Mate, *Phys. Rev. Lett.* **60**, 2398 (1988).
- [63] T. Sleator and R. Tycko, *Phys. Rev. Lett.* **60**, 1418 (1988).
- [64] P. H. Lippel, R. J. Wilson, M. D. Miller, Ch. Wöll, and S. Chiang, *Phys. Rev. Lett.* **62**, 171 (1989).
- [65] T. A. Jung, R. R. Schlittler, J. K. Gimzewski, H. Tang, and C. Joachim, *Science* **271**, 181 (1996).
- [66] T. A. Jung, R. R. Schlittler, and J. K. Gimzewski, *Nature* **386**, 696 (1997).
- [67] J. K. Gimzewski, C. Joachim, R. R. Schlittler, V. Langlais, H. Tang, and I. Johansen, *Science* **281**, 531 (1998).
- [68] Z. J. Donhauser, B. A. Mantooth, K. F. Kelly, L. A. Bumm, J. D. Monnell, J. J. Stapleton, D. W. Price Jr., A. M. Rawlett, D. L. Allara, J. M. Tour, and P. S. Weiss, *Science* **292**, 2303 (2001).
- [69] S. Datta, W. Tian, S. Hong, R. Reifenberger, J. I. Henderson, and C. P. Kubiak, *Phys. Rev. Lett.* **79**, 2530 (1997).
- [70] J. K. Gimzewski and C. Joachim, *Science* **283**, 1683 (1999).
- [71] S. M. Driver and D. P. Woodruff, *Langmuir* **16**, 6693 (2000).
- [72] J. K. Gimzewski, S. Modesti, and R. R. Schlittler, *Phys. Rev. Lett.* **72**, 1036 (1994).
- [73] M. Pedio, R. Felici, X. Torrelles, P. Rudolf, M. Capozzi, J. Rius, and S. Ferrer, *Phys. Rev. Lett.* **85**, 1040 (2000).
- [74] J. Weckesser, C. Cepek, R. Fasel, J. V. Barth, F. Baumberger, T. Greber, and K. Kern, *J. Chem. Phys.* **115**, 9001 (2001).
- [75] Y. Okawa and M. Aono, *Nature* **409**, 683 (2001).
- [76] Y. Okawa and M. Aono, *J. Phys. Chem.* **115**, 2317 (2001).
- [77] M. Furukawa, H. Tanaka, K. Sugiura, Y. Sakata, and T. Kawai, *Surf. Sci.* **445**, L58 (2000).
- [78] J. V. Barth, J. Weckesser, C. Cai, P. Günther, L. Bürgi, O. Jeandupeux, and K. Kern, *Angew. Chem. Int. Ed.* **39**, 1230 (2000).

- [79] M. Böhringer, K. Morgenstern, W.-D. Schneider, M. Wühn, Ch. Wöll, and R. Berndt, *Surf. Sci.* **444**, 199 (2000).
- [80] T. Yokoyama, S. Yokoyama, T. Kamikado, Y. Okuno, and S. Mashiko, *Nature* **413**, 619 (2001).
- [81] A. K. Boal, F. Ilhan, J. E. DeRouchey, T. Thurn-Albrecht, T. P. Russell, and V. M. Rotello, *Nature* **404**, 746 (2000).
- [82] O. Marchenko and J. Cousty, *Phys. Rev. Lett.* **84**, 5363 (2000).
- [83] M. Ø. Pedersen, P. W. Murray, E. Lægsgaard, I. Stensgaard, and F. Besenbacher, *Surf. Sci.* **389**, 300 (1997).
- [84] G. L. Kellogg, *Surf. Sci. Rep.* **21**, 1 (1994).
- [85] R. Gomer, *Rep. Prog. Phys.* **53**, 917 (1990).
- [86] J. V. Barth, *Surf. Sci. Rep.* **40**, 75 (2000).
- [87] S. Renisch, R. Schuster, J. Wintterlin, and G. Ertl, *Phys. Rev. Lett.* **82**, 3839 (1999).
- [88] L. Österlund, M. Ø. Pedersen, I. Stensgaard, E. Lægsgaard, and F. Besenbacher, *Phys. Rev. Lett.* **83**, 4812 (1999).
- [89] J. D. Wrigley, M. E. Twigg, and G. Ehrlich, *J. Chem. Phys.* **93**, 2885 (1990).
- [90] D. C. Senft and G. Ehrlich, *Phys. Rev. Lett.* **74**, 294 (1995).
- [91] T. R. Linderoth, S. Horch, E. Lægsgaard, I. Stensgaard, and F. Besenbacher, *Phys. Rev. Lett.* **78**, 4978 (1997).
- [92] J. Weckesser, J. V. Barth, and K. Kern, *J. Chem. Phys.* **110**, 5351 (1999).
- [93] J. Weckesser, J. V. Barth, and K. Kern, *Phys. Rev. B* **64**, R161403 (2001).
- [94] S. Berner, M. Brunner, L. Ramoino, H. Suzuki, H. J. Güntherodt, and T. A. Jung, *Chem. Phys. Lett.* **348**, 175 (2001).
- [95] B. Kahr and R. W. Gurney, *Chem. Rev.* **101**, 893 (2001).
- [96] *Chiral reactions in heterogeneous catalysis*, edited by G. Jannes and V. Dubois (Plenum Press, New York, 1995).
- [97] A. Baiker and H. U. Blaser, in *Enantioselective catalysts and reactions*, Vol. 5 of *Handbook of heterogeneous catalysis*, edited by G. Ertl, H. Knözinger, and J. Weitkamp (Wiley VCH, Weinheim, 1997), p. 2422.
- [98] M. von Arx, T. Mallat, and A. Baiker, *Topics in Catalysis* **19**, 75 (2002).
- [99] G. Binnig, H. Rohrer, C. Gerber, and E. Weibel, *Phys. Rev. Lett.* **49**, 57 (1982).

- [100] F. Besenbacher, E. Lægsgaard, K. Mortensen, U. Nielsen, and I. Stensgaard, *Rev. Sci. Instrum.* **59**, 1035 (1988).
- [101] B. J. McIntyre, M. Salmeron, and G. A. Somorjai, *Rev. Sci. Instrum.* **64**, 687 (1993).
- [102] R. Schuster, V. Kirchner, X. H. Xia, A. M. Bittner, and G. Ertl, *Phys. Rev. Lett.* **80**, 5599 (1998).
- [103] J. A. Jensen, K. B. Rider, Y. Chen, M. Salmeron, and G. A. Somorjai, *J. Vac. Sci. Technol. B* **17**, 1080 (1999).
- [104] F. Besenbacher, *Rep. Prog. Phys.* **59**, 1737 (1996).
- [105] J. H. Ferris, J. G. Kushmerick, J. A. Johnson, M. G. Y. Youngquist, R. B. Kessinger, H. F. Kingsbury, and P. S. Weiss, *Rev. Sci. Instrum.* **69**, 2691 (1998).
- [106] M. Kugler, Ch. Renner, O. Fischer, V. Mikheev, and G. Batey, *Rev. Sci. Instrum.* **71**, 1475 (2000).
- [107] S. Horch, P. Zeppenfeld, R. David, and G. Comsa, *Rev. Sci. Instrum.* **65**, 3204 (1994).
- [108] G. Meyer, *Rev. Sci. Instrum.* **67**, 2960 (1996).
- [109] S. Behler, M. K. Rose, J. C. Dunphy, D. F. Ogletree, M. Salmeron, and C. Chapelier, *Rev. Sci. Instrum.* **68**, 2479 (1997).
- [110] B. C. Stipe, M. A. Rezaei, and W. Ho, *Rev. Sci. Instrum.* **70**, 137 (1999).
- [111] B. C. Stipe, M. A. Rezaei, and W. Ho, *Science* **280**, 1732 (1998).
- [112] B. C. Stipe, M. A. Rezaei, and W. Ho, *Phys. Rev. Lett.* **82**, 1724 (1999).
- [113] L. Petersen, Ph.D. thesis, University of Aarhus, 1999.
- [114] G. Binnig and D. P. E. Smith, *Rev. Sci. Instrum.* **57**, 1688 (1986).
- [115] R. M. Feenstra and M. A. Lutz, *J. Vac. Sci. Technol. B* **9**, 716 (1991).
- [116] K. J. Ito, Y. Uehara, S. Ushioda, and K. Ito, *Rev. Sci. Instrum.* **71**, 420 (2000).
- [117] K. Morgenstern, G. Rosenfeld, E. Lægsgaard, F. Besenbacher, and G. Comsa, *Phys. Rev. Lett.* **80**, 556 (1998).
- [118] C. J. Chen, *Introduction to Scanning Tunneling Microscopy* (Oxford University Press, New York, 1993).
- [119] *Scanning Tunneling Microscopy III*, Vol. 29 of *Springer series in surface science*, 2nd ed., edited by R. Wiesendanger and H. J. Güntherodt (Springer, Berlin, 1996).

- [120] D. Drakova, Rep. Prog. Phys. **64**, 205 (2001).
- [121] J. Bardeen, Phys. Rev. Lett. **6**, 57 (1961).
- [122] L. D. Landau and L. M. Lifshitz, *Quantum mechanics*, 3rd ed. (Pergamon Press, Oxford, 1977).
- [123] J. Tersoff and D. R. Hamann, Phys. Rev. Lett. **50**, 1998 (1983).
- [124] J. Tersoff and D. R. Hamann, Phys. Rev. B **31**, 805 (1985).
- [125] J. Wintterlin, R. Schuster, and G. Ertl, Phys. Rev. Lett. **77**, 123 (1996).
- [126] T. Zambelli, J. V. Barth, J. Wintterlin, and G. Ertl, Nature **390**, 495 (1997).
- [127] M. Ø. Pedersen, L. Österlund, J. J. Mortensen, M. Mavrikakis, L. B. Hansen, I. Stensgaard, E. Lægsgaard, J. K. Nørskov, and F. Besenbacher, Phys. Rev. Lett. **84**, 4898 (2000).
- [128] G. Meyer, B. Neu, and K. H. Rieder, Appl. Phys. A **60**, 343 (1995).
- [129] S. Zöphel, J. Repp, G. Meyer, and K. H. Rieder, Chem. Phys. Lett. **310**, 145 (1999).
- [130] B. I. Lundqvist, O. Gunnarsson, H. Hjelmberg, and J. K. Nørskov, Surf. Sci. **89**, 196 (1979).
- [131] B. Hammer and J. K. Nørskov, in *Chemisorption and reactivity on supported clusters and thin films*, Vol. 331 of *NATO ASI series E*, edited by R. M. Lambert and G. Pacchioni (Kluwer Academic Publishers, Amsterdam, 1997), p. 285.
- [132] B. Hammer and J. K. Nørskov, Adv. Catal. **45**, 71 (2000).
- [133] P. W. Anderson, Phys. Rev. **124**, 41 (1961).
- [134] D. M. Newns, Phys. Rev. **178**, 1123 (1969).
- [135] N. D. Lang, Phys. Rev. Lett. **55**, 230 (1985).
- [136] N. D. Lang, Phys. Rev. Lett. **56**, 1164 (1986).
- [137] P. Sautet, Surf. Sci. **374**, 406 (1997).
- [138] I. S. Tilinin, M. K. Rose, J. C. Dunphy, M. Salmeron, and M. A. Van Hove, Surf. Sci. **418**, 511 (1998).
- [139] P. Sautet and C. Joachim, Phys. Rev. B **38**, 12238 (1988).
- [140] P. S. Weiss and D. M. Eigler, Phys. Rev. Lett. **71**, 3139 (1993).
- [141] P. Sautet and M.-L. Bocquet, Phys. Rev. B **53**, 4910 (1996).
- [142] P. Sautet, Chem. Rev. **97**, 1097 (1997).

- [143] F. Moresco, G. Meyer, K.-H. Rieder, H. Tang, A. Gourdon, and C. Joachim, *Phys. Rev. Lett.* **86**, 672 (2001).
- [144] F. Moresco, G. Meyer, K.-H. Rieder, H. Tang, A. Gourdon, and C. Joachim, *Phys. Rev. Lett.* **87**, 088302 (2001).
- [145] T. Zambelli, H. Tang, J. Lagoute, S. Gauthier, A. Gourdon, and C. Joachim, *Chem. Phys. Lett.* **348**, 1 (2001).
- [146] T. Nishino, P. Bühlmann, T. Ito, and Y. Umezawa, *Surf. Sci.* **490**, L579 (2001).
- [147] R. Berndt, J. K. Gimzewski, and R. R. Schlittler, *Surf. Sci.* **310**, 85 (1994).
- [148] C. J. Chen, *J. Vac. Sci. Technol. A* **12**, 2193 (1994).
- [149] J. I. Pascual, J. Gómez-Herrero, C. Rogero, A. M. Baró, D. Sánchez-Portal, E. Artacho, P. Ordejón, and J. M. Soler, *Surf. Sci.* **321**, 78 (2000).
- [150] N. D. Lang, *Phys. Rev. Lett.* **58**, 45 (1987).
- [151] M. A. Dubson and J. S. Hwang, *Rev. Sci. Instrum.* **63**, 3643 (1992).
- [152] G. Pietzsch, A. Kubetzka, D. Haude, M. Bode, and R. Wiesendanger, *Rev. Sci. Instrum.* **71**, 424 (2000).
- [153] Y. Kondo, E. T. Foley, T. Amakusa, N. Shibata, S. Chiba, M. Iwatsuki, and H. Tokumoto, *Rev. Sci. Instrum.* **72**, 2613 (2001).
- [154] G. Binnig and H. Rohrer, *Surf. Sci.* **126**, 236 (1983).
- [155] X. Chen, E. R. Frank, and R. J. Hamers, *Rev. Sci. Instrum.* **65**, 3373 (1994).
- [156] M. Bott, T. Michely, and G. Comsa, *Rev. Sci. Instrum.* **66**, 4135 (1995).
- [157] W. W. Crew and R. J. Madix, *Rev. Sci. Instrum.* **66**, 4552 (1995).
- [158] H. Zhang, U. Memmert, R. Houbertz, and U. Hartmann, *Rev. Sci. Instrum.* **72**, 2613 (2001).
- [159] R. David, K. Kern, P. Zeppenfeld, and G. Comsa, *Rev. Sci. Instrum.* **57**, 2771 (1986).
- [160] F. Pobell, *Matter and methods at low temperatures*, 2nd ed. (Springer, Berlin, 1996).
- [161] *American Institute of Physics Handbook*, edited by D. E. Gray (McGraw-Hill, New York, 1972).
- [162] G. K. White, *Experimental techniques in low-temperature physics*, 3rd ed. (Clarendon, Oxford, 1979).

- [163] *Handbook of chemistry and physics*, 79th ed., edited by D. R. Lide (CRC, New York, 1998).
- [164] R. Berman, *Thermal conduction in solids* (Clarendon, Oxford, 1976).
- [165] H.-P. Rust, M. Doering, J. I. Pascual, T. P. Pearl, and P. S. Weiss, *Rev. Sci. Instrum.* **72**, 4393 (2001).
- [166] L. Petersen, B. Schaefer, E. Lægsgaard, I. Stensgaard, and F. Besenbacher, *Surf. Sci.* **457**, 319 (2000).
- [167] N. W. Ashcroft and N. D. Mermin, *Solid state physics* (Harcourt Brace College, New York, 1988).
- [168] R. H. Tredgold, *Order in Thin Organic Films* (Cambridge University Press, Cambridge, 1994).
- [169] M. Knudsen, *Ann. d. Phys.* **48**, 1113 (1915).
- [170] M. Knudsen, *Kinetic theory of gases* (Methuen, London, 1952).
- [171] M. Ohring, *The material science of thin films* (Academic Press, Boston, 1991), Chap. 3.3.
- [172] W. C. Zeise, *Pogg. Ann.* **9**, 632 (1827).
- [173] *Chemistry of the elements*, edited by N. N. Greenwood and A. Earnshaw (Pergamon, Oxford, 1984).
- [174] T. J. Kealy and P. L. Pauson, *Nature* **168**, 1039 (1951).
- [175] S. A. Miller, J. A. Tebboth, and J. F. Tremaine, *J. Chem. Soc.* 632 (1952).
- [176] G. Wilkinson, M. Rosenblum, M. C. Whiting, and R. B. Woodward, *J. Am. Chem. Soc.* **74**, 2125 (1952).
- [177] E. O. Fischer and W. Pfab, *Z. Naturforsch. B* **7**, 377 (1952).
- [178] M. J. S. Dewar, *J. Am. Chem. Soc.* **74**, 3341 (1952).
- [179] J. Chatt and L. A. Duncanson, *J. Chem. Soc.* 2939 (1953).
- [180] R. Hoffmann, *Solids and surfaces* (VCH, Weinheim, 1988).
- [181] J.-Y. Saillard and R. Hoffmann, *J. Am. Chem. Soc.* **106**, 2006 (1984).
- [182] D. M. P. Mingos, *J. Organomet. Chem.* **635**, 1 (2001).
- [183] D. M. P. Mingos, *Adv. Organomet. Chem.* **15**, 1 (1977).
- [184] G. J. Kubas, R. R. Ryan, B. I. Swason, P. J. Vergamini, and H. J. Wasserman, *J. Am. Chem. Soc.* **106**, 451 (1984).

- [185] G. J. Kubas, *Acc. Chem. Res.* **21**, 120 (1988).
- [186] G. J. Kubas, *J. Organomet. Chem.* **635**, 37 (2001).
- [187] G. Blyholder, *J. Phys. Chem.* **68**, 2772 (1964).
- [188] B. Hammer, Y. Morikawa, and J. K. Nørskov, *Phys. Rev. Lett.* **76**, 2141 (1996).
- [189] J. A. Appelbaum and D. R. Hamann, *Solid State Commun.* **27**, 881 (1978).
- [190] J. Gaudioso and W. Ho, *J. Am. Chem. Soc.* **123**, 10095 (2001).
- [191] P. W. Atkins, *Physical chemistry*, 2nd ed. (Oxford University Press, Oxford, 1984).
- [192] A. Zangwill, *Physics at surfaces* (Cambridge University Press, Cambridge, 1988).
- [193] K. Christmann, in *Surface physical chemistry*, Vol. 1 of *Topics in physical chemistry*, edited by H. Baumgärtel, E. U. Franck, and W. Grünbein (Springer, New York, 1991).
- [194] G. E. Poirier, *J. Vac. Sci. Technol. B* **14**, 1453 (1996).
- [195] S. Haq and F. M. Leibsle, *Surf. Sci.* **355**, L345 (1996).
- [196] X. Zhao, Z. Gai, R. G. Zhao, W. S. Yang, and T. Sakurai, *Surf. Sci.* **424**, L347 (1999).
- [197] T. Schmitz-Hubsch, T. Fritz, R. Staub, A. Back, N. R. Armstrong, and K. Leo, *Surf. Sci.* **437**, 163 (1999).
- [198] E. I. Altman and R. J. Colton, *Surf. Sci.* **279**, 49 (1992).
- [199] J. K. Gimzewski, S. Modesti, C. Gerber, and R. R. Schlittler, *Chem. Phys. Lett.* **213**, 401 (1993).
- [200] A. J. Maxwell, P. A. Brühwiler, S. Andersson, D. Arvanitis, B. Hernnäs, O. Karis, D. C. Mancini, N. Märtensson, S. M. Gray, M. K.-J. Johansson, and L. S. O. Johansson, *Phys. Rev. B* **52**, R5546 (1996).
- [201] P. W. Murray, M. Ø. Pedersen, E. Lægsgaard, I. Stensgaard, and F. Besenbacher, *Phys. Rev. B* **55**, 9360 (1997).
- [202] J. K. Gimzewski, T. A. Jung, M. T. Cuberes, and R. R. Schlittler, *Surf. Sci.* **386**, 101 (1997).
- [203] Q. Chen, D. J. Frankel, and N. V. Richardson, *Langmuir* **17**, 8276 (2001).
- [204] S. Modesti, J. K. Gimzewski, and R. R. Schlittler, *Surf. Sci.* **72**, 331 (1995).
- [205] S. Das and A. J. Pal, *Phys. Stat. Sol. A* **185**, 383 (2001).

- [206] J. McMurry, *Fundamentals of organic chemistry*, 2nd ed. (Brooks/Cole, Belmont, 1990), Chap. 5.8.
- [207] D. M. Ho and R. A. Pascal Jr., *Chem. Matt.* **5**, 1358 (1993).
- [208] K. Zimmermann, R. Goddard, C. Krüger, and M. W. Haenel, *Tetrahedron Lett.* **37**, 8371 (1996).
- [209] M. M. Boorum, Y. V. Vasil'ev, T. Drewello, and L. T. Scott, *Science* **294**, 828 (2001).
- [210] L. Barnett, D. M. Ho, K. K. Baldrige, and R. A. Pascal Jr., *Appl. Phys. Lett.* **71**, 213 (1997).
- [211] M. Hesse, H. Meier, and B. Zeeh, *Spektroskopische Methoden in der organischen Chemie*, 4th ed. (Thieme-Verlag, Stuttgart, 1991).
- [212] C. Y. Nakakura, G. Zheng, and E. I. Altman, *Surf. Sci.* **401**, 173 (1998).
- [213] C. Kendrick, A. Kahn, and S. R. Forrest, *Appl. Surf. Sci.* **104/105**, 586 (1996).
- [214] R. Strohmaier, C. Ludwig, J. Petersen, B. Gompf, and W. Eisenmenger, *Surf. Sci.* **351**, 292 (1996).
- [215] J. T. Li, W. D. Schneider, and R. Berndt, *Appl. Phys. A* **66**, S675 (1998).
- [216] M. Böhringer, W.-D. Schneider, and R. Berndt, *Surf. Sci.* **408**, 72 (1998).
- [217] L. Bartels, G. Meyer, and K.-H. Rieder, *Phys. Rev. Lett.* **79**, 697 (1997).
- [218] S. Horch, H. T. Lorensen, S. Helveg, E. Lægsgaard, I. Stensgaard, K. W. Jacobsen, J. K. Nørskov, and F. Besenbacher, *Nature* **398**, 134 (1999).
- [219] J. C. Dunphy, P. Sautet, D. F. Ogletree, O. Dabbousi, and M. B. Salmeron, *Phys. Rev. B* **47**, 2320 (1993).
- [220] I.-W. Lyo and P. Avouris, *Science* **253**, 173 (1991).
- [221] D. M. Eigler, C. P. Lutz, and W. E. Rudge, *Nature* **352**, 600 (1991).
- [222] U. Dürig, O. Züger, and D. W. Pohl, *Phys. Rev. Lett.* **65**, 349 (1990).
- [223] P. Stoltze, *J. Phys.: Condens. Matter* **6**, 9495 (1994).
- [224] O. B. Christensen and K. W. Jacobsen, *Phys. Rev. B* **45**, 6893 (1992).
- [225] J. K. Nørskov, K. W. Jacobsen, P. Stoltze, and L. B. Hansen, *Surf. Sci.* **283**, 277 (1993).
- [226] H. D. Gesser, N. R. Hunter, and C. B. Prakash, *Chem. Rev.* **85**, 235 (1985).
- [227] J. H. Lunsford, *Angew. Chem. Int. Ed.* **34**, 970 (1995).

- [228] *Challenges in alkane activation and selective oxidation*, special issue of *Catalysis Today* **71** (2001).
- [229] R. H. Crabtree, *Chem. Rev.* **85**, 245 (1985).
- [230] M. Munakata, L. P. Wu, G. L. Ning, T. Kuroda-Sowa, M. Maekawa, Y. Suenaga, and N. Maeno, *J. Am. Chem. Soc.* **121**, 4968 (1999).
- [231] J. J. Schneider, D. Spikermann, T. Labahn, J. Magull, M. Fontani, F. Laschi, and P. Zanello, *Chem. Eur. J.* **6**, 3686 (2000).
- [232] J. J. Schneider, D. Spikermann, D. Bläser, R. Boese, P. Rademacher, T. Labahn, J. Magull, C. Janiak, N. Seidel, and K. Jacob, *Chem. Eur. J.* **6**, 3686 (2000).
- [233] R. L. Schwoebel, *J. Appl. Phys.* **40**, 614 (1966).
- [234] G. Ehrlich and F. G. Hudda, *J. Chem. Phys.* **44**, 1050 (1966).
- [235] R. A. Alberty and R. J. Silbey, *Physical Chemistry* (Wiley & Sons, New York, 1992).
- [236] F. Stevens, D. J. Dyer, and D. M. Walba, *Angew. Chem. Int. Ed.* **35**, 900 (1996).
- [237] G. P. Lopinski, D. J. Moffatt, D. D. M. Wayner, and R. A. Wolkow, *Nature* **392**, 909 (1998).
- [238] Q. Chen, C. W. Lee, D. J. Frankel, and N. V. Richardson, *Phys. Chem. Comm.* **9** (1999).
- [239] F. C. De Feyter, P. C. M. Grim, M. Rücker, P. Vanoppen, C. Meiners, M. Siefert, S. Valiyaveetil, K. Müllen, and F. C. De Schryver, *Angew. Chem. Int. Ed.* **37**, 1223 (1998).
- [240] M. Böhlinger, K. Morgenstern, W.-D. Schneider, and R. Berndt, *Angew. Chem. Int. Ed.* **38**, 821 (1999).
- [241] J. Weckesser, A. De Vita, J. V. Barth, C. Cai, and K. Kern, *Phys. Rev. Lett.* **87**, 096101 (2001).
- [242] A. Ahmadi, G. Attard, J. Feliu, and A. Rodes, *Langmuir* **15**, 2420 (1999).
- [243] C. F. McFadden, P. S. Cremer, and A. J. Gellman, *Langmuir* **12**, 2483 (1996).
- [244] D. S. Sholl, *Langmuir* **14**, 862 (1998).
- [245] T. D. Power and D. S. Sholl, *J. Vac. Sci. Technol. A* **17**, 1700 (1999).
- [246] G. Attard, A. Ahmadi, J. Feliu, A. Rodes, E. Herrero, S. Blais, and G. Jerkiewicz, *Phys. Chem. B* **103**, 1381 (1999).
- [247] A. J. Gellman, J. D. Horvath, and M. T. Buelow, *J. Mol. Catal. A* **167**, 3 (2001).

- [248] J. D. Horvath and A. J. Gellman, *J. Am. Chem. Soc.* **123**, 7953 (2001).
- [249] D. S. Sholl, A. Asthagiri, and T. D. Power, *J. Phys. Chem. B* **105**, 4771 (2001).
- [250] R. S. Cahn, C. Ingold, and V. Prelog, *Angew. Chem. Int. Ed.* **5**, 385 (1966).
- [251] V. Prelog and G. Helmchen, *Angew. Chem.* **94**, 614 (1982).
- [252] G. M. Schwab and L. Rudolph, *Naturwiss.* **20**, 363 (1932).
- [253] G. M. Schwab, F. Rost, and L. Rudolph, *Kolloid-Zeitschrift* **68**, 157 (1934).
- [254] K.-H. Ernst, M. Böhringer, C. F. McFadden, P. Hug, U. Müller, and U. Ellerbeck, *Nanotechnology* **10**, 355 (1999).
- [255] X. Zhao, R. G. Zhao, and W. S. Yang, *Langmuir* **16**, 9812 (2000).
- [256] X. Zhao, *J. Am. Chem. Soc.* **122**, 12584 (2000).
- [257] H. U. Blaser, *Tetrahedron: Asymmetry* **2**, 843 (1991).
- [258] L. Hecht and L. Barron, *Chem. Phys. Lett.* **225**, 525 (1994).
- [259] C. A. Orme, A. Noy, A. Wierzbicki, M. T. McBride, M. Grantham, H. H. Teng, P. M. Dove, and J. J. DeYoreo, *Nature* **411**, 775 (2001).
- [260] M. Doering, H.-P. Rust, B. G. Briner, and A. M. Bradshaw, *Surf. Sci.* **410**, L736 (1998).
- [261] R. H. Martin, *Angew. Chem. Int. Ed.* **13**, 649 (1974).
- [262] V. J. Langlais, R. R. Schlittler, H. Tang, A. Gourdon, C. Joachim, and J. K. Gimzewski, *Phys. Rev. Lett.* **83**, 2809 (1999).
- [263] S. Tsuzuki, K. Honda, T. Uchimarui, M. Mikami, and K. Tanabe, *J. Am. Chem. Soc.* **124**, 106 (2002).
- [264] J. Kuntze and R. Berndt, personal communication.
- [265] P. Sautet and C. Joachim, *Chem. Phys. Lett.* **185**, 23 (1991).
- [266] J. Frohn, M. Giesen, M. Poensgen, J. F. Wolf, and H. Ibach, *Phys. Rev. Lett.* **67**, 3543 (1991).
- [267] K. W. Hipps, *Science* **294**, 536 (2001).
- [268] M. Volmer and I. Estermann, *Z. Physik* **7**, 13 (1921).
- [269] J. M. Blakely, *Prog. Mater. Sci.* **10**, 395 (1963).
- [270] J. L. Brand, M. V. Arena, A. A. Deckert, and S. M. George, *J. Chem. Phys.* **92**, 5136 (1990).

- [271] J. A. Venables, G. D. T. Spiller, and M. Hanbücken, *Rep. Prog. Phys.* **47**, 399 (1984).
- [272] H. Brune, *Surf. Sci. Rep.* **31**, 121 (1998).
- [273] G. Ehrlich and F. G. Hudda, *J. Chem. Phys.* **44**, 1039 (1966).
- [274] G. Binnig, H. Fuchs, and E. Stoll, *Surf. Sci.* **169**, L295 (1986).
- [275] Y. W. Mo, *Phys. Rev. Lett.* **71**, 2923 (1993).
- [276] T. Zambelli, J. Trost, J. Wintterlin, and G. Ertl, *Phys. Rev. Lett.* **76**, 795 (1996).
- [277] S. C. Wang and G. Ehrlich, *Surf. Sci.* **206**, 451 (1988).
- [278] G. Ehrlich, *Surf. Sci.* **246**, 1 (1991).
- [279] G. Ehrlich, *Surf. Sci.* **299/300**, 628 (1994).
- [280] E. Ganz, S. K. Theiss, I.-S. Hwang, and J. Golovchenko, *Phys. Rev. Lett.* **68**, 1567 (1992).
- [281] B. S. Swartzentruber, *Phys. Rev. Lett.* **76**, 459 (1996).
- [282] J. M. Gómez-Rodríguez, J. J. Sáenz, and A. M. Baró, *Phys. Rev. Lett.* **76**, 799 (1996).
- [283] T. R. Linderoth, S. Horch, L. Petesen, S. Helveg, E. Lægsgaard, I. Stensgaard, and F. Besenbacher, *Phys. Rev. Lett.* **82**, 1494 (1999).
- [284] R. van Gastel, E. Somfai, W. van Saarloos, and J. W. M. Frenken, *Nature* **408**, 665 (2000).
- [285] R. van Gastel, E. Somfai, S. B. van Albada, W. van Saarloos, and J. W. M. Frenken, *Phys. Rev. Lett.* **86**, 1562 (2001).
- [286] M. L. Grant, B. S. Swartzentruber, N. C. Bartelt, and J. B. Hannon, *Phys. Rev. Lett.* **86**, 4588 (2001).
- [287] S. C. Wang, J. D. Wrigley, and G. Ehrlich, *J. Chem. Phys.* **91**, 5087 (1989).
- [288] I.-S. Hwang, R.-L. Lo, and T. T. Tsong, *Phys. Rev. Lett.* **78**, 4797 (1997).
- [289] B. G. Briner, M. Doering, H. P. Rust, and A. M. Bradshaw, *Science* **178**, 257 (1997).
- [290] J. V. Barth, T. Zambelli, J. Wintterlin, R. Schuster, and G. Ertl, *Phys. Rev. B* **55**, 12902 (1997).
- [291] For a recent overview see J. V. Barth, *Surf. Sci. Rep.* **40**, 75 (2000).
- [292] J. Yoshinobu, H. Tanaka, T. Kawai, and M. Kawai, *Phys. Rev. B* **53**, 7492 (1996).

- [293] S. Ichihara, J. Yoshinobu, H. Ogasawara, M. Nantoh, M. Kawai, and K. Domen, *J. Electron Spectrosc. Rel. Phenom.* **88-91**, 1003 (1998).
- [294] J. C. Dunphy, M. Rose, S. Behler, D. F. Ogletree, M. B. Salmeron, and P. Sautet, *Phys. Rev. B* **57**, 12705 (1998).
- [295] L. J. Lauhon and W. Ho, *J. Chem. Phys.* **111**, 5633 (1999).
- [296] K. D. Dobbs and D. J. Doren, *J. Chem. Phys.* **97**, 3722 (1992).
- [297] D. Huang, Y. Chen, and K. A. Fichthorn, *J. Chem. Phys.* **101**, 11021 (1994).
- [298] J. S. Raut and K. A. Fichthorn, *J. Chem. Phys.* **108**, 1626 (1998).
- [299] Ph. Ebert, M. G. Lagally, and K. Urban, *Phys. Rev. Lett.* **70**, 1437 (1993).
- [300] M. Bott, M. Hohage, M. Morgenstern, T. Michely, and G. Comsa, *Phys. Rev. Lett.* **76**, 1304 (1996).
- [301] J. T. Li, R. Berndt, and W. D. Schneider, *Phys. Rev. Lett.* **76**, 1888 (1996).
- [302] M. R. Sørensen, K. W. Jacobsen, and H. Jónsson, *Phys. Rev. Lett.* **77**, 5067 (1996).
- [303] U. Kürpick and T. S. Rahman, *Phys. Rev. Lett.* **83**, 2765 (1999).
- [304] W. A. Hofer, A. J. Fisher, R. A. Wolkow, and P. Grütter, *Phys. Rev. Lett.* **87**, 236104 (2001).
- [305] P. Hänggi, P. Talkner, and M. Borkovec, *Rev. Mod. Phys.* **62**, 251 (1990).
- [306] S. J. Lombardo and A. T. Bell, *Surf. Sci. Rep.* **13**, 1 (1991).
- [307] T. Ala-Nissila, R. Ferrando, and S. C. Ying, to appear in: *Advances in Physics*.
- [308] M. N. Barber and B. W. Ninham, *Random and restricted walks: theory and applications* (Gordon and Breach, New York, 1970).
- [309] G. H. Weiss and R. J. Rubin, *Adv. Chem. Phys.* **52**, 363 (1983).
- [310] K. Lakatos-Lindenberg and K. E. Shuler, *J. Math. Phys.* **12**, 633 (1971).
- [311] D. R. Cox and P. A. W. Lewis, *The statistical analysis of series of events* (Methuen, London, 1966).
- [312] S. Chandrasekhar, *Rev. Mod. Phys.* **15**, 1 (1943).
- [313] R. Ferrando, R. Spadacini, G. E. Tommei, and G. Caratti, *Surf. Sci.* **311**, 411 (1994).
- [314] F. Reif, *Fundamentals of statistical and thermal physics* (McGraw-Hill, London, 1985).

- [315] S. Arrhenius, *Z. Phys. Chem.* **4**, 226 (1889).
- [316] A. F. Voter and J. D. Doll, *J. Chem. Phys.* **82**, 80 (1985).
- [317] E. Pollak, J. Bader, B. J. Berne, and P. Talkner, *Phys. Rev. Lett.* **70**, 3299 (1993).
- [318] Y. Georgievskii and E. Pollak, *Phys. Rev. E* **49**, 5098 (1994).
- [319] Y. Georgievskii, M. A. Kozhushner, and E. Pollak, *J. Chem. Phys.* **102**, 6908 (1995).
- [320] Y. Georgievskii and E. Pollak, *Surf. Sci.* **355**, L366 (1996).
- [321] R. Ferrando, R. Spadacini, and G. E. Tommei, *Phys. Rev. E* **48**, 2437 (1993).
- [322] K. J. Laidler, *Chemical kinetics*, 2nd ed. (Harper and Row, New York, 1987).
- [323] H. Eyring, *J. Chem. Phys.* **3**, 107 (1935).
- [324] J. D. Doll and A. F. Voter, *Ann. Rev. Phys. Chem.* **38**, 413 (1987).
- [325] H. A. Kramers, *Physica* **7**, 284 (1940).
- [326] V. I. Mel'nikov, *Phys. Rep.* **209**, 1 (1991).
- [327] J. J. M. Beenakker and S. Yu. Krylov, *Surf. Sci.* **411**, L816 (1998).
- [328] E. Hershkovitz, P. Talkner, E. Pollak, and Y. Geogievskii, *Surf. Sci.* **421**, 73 (1999).
- [329] T. T. Tsong, *Prog. Surf. Sci.* **10**, 165 (1980).
- [330] T. T. Tsong, *Rep. Prog. Phys.* **51**, 759 (1988).
- [331] J. Jacobsen, K. W. Jacobsen, and J. P. Sethna, *Phys. Rev. Lett.* **79**, 2843 (1997).
- [332] D. P. Landau and K. Binder, *A guide to Monte Carlo simulations in statistical physics* (Cambridge University Press, Cambridge, 2000).
- [333] *Monte Carlo method in statistical physics*, Vol. 7 of *Topics in current physics*, 2nd ed., edited by K. Binder (Springer, Berlin, 1986).
- [334] *Applications of the Monte Carlo method in statistical physics*, Vol. 36 of *Topics in current physics*, 2nd ed., edited by K. Binder (Springer, Berlin, 1987).
- [335] K. A. Fichtorn and W. H. Weinberg, *J. Chem. Phys.* **95**, 1090 (1991).
- [336] T. R. Linderoth, Ph.D. thesis, University of Aarhus, 1997.
- [337] U. Kürpick, A. Kara, and T. S. Rahman, *Phys. Rev. Lett.* **78**, 1086 (1996).
- [338] U. Kürpick and T. S. Rahman, *Surf. Sci.* **383**, 137 (1997).

- [339] U. Kürpick, Phys. Rev. B **64**, 075418 (2001).
- [340] G. H. Vineyard, J. Phys. Chem. Solids **3**, 121 (1957).
- [341] J. C. Hamilton, M. R. Sørensen, and A. F. Voter, Phys. Rev. B **61**, R5125 (2000).
- [342] S. C. Wang, U. Kürpick, and G. Ehrlich, Phys. Rev. Lett. **81**, 4923 (1998).
- [343] W. Meyer and H. Neldel, Z. Tech. Phys. **12**, 588 (1937).
- [344] A. Yelon and B. Movaghar, Phys. Rev. Lett. **65**, 618 (1990).
- [345] A. Yelon, B. Movaghar, and H. M. Branz, Phys. Rev. B **46**, 12244 (1992).
- [346] G. Boisvert, L. J. Lewis, and A. Yelon, Phys. Rev. Lett. **75**, 469 (1995).
- [347] E. Peacock-López and H. Suhl, Phys. Rev. B **26**, 3774 (1982).
- [348] P. Višcor, Phys. Rev. B **65**, 077201 (2002).
- [349] A. Yelon and B. Movaghar, Phys. Rev. B **65**, 077202 (2002).
- [350] C. Ratsch and M. Scheffler, Phys. Rev. B **58**, 13163 (1998).
- [351] J. C. Tully, G. H. Gilmer, and M. Shugard, J. Chem. Phys. **71**, 1630 (1979).
- [352] D. A. Reed and G. Ehrlich, Surf. Sci. **120**, 179 (1982).
- [353] J. W. M. Frenken, B. J. Hinch, J. P. Toennies, and Ch. Wöll, Phys. Rev. B **41**, 938 (1990).
- [354] V. P. Zhdanov, Surf. Sci. **214**, 289 (1989).
- [355] K. D. Dobbs and D. J. Doren, J. Chem. Phys. **99**, 10041 (1993).
- [356] F. Montalenti and R. Ferrando, Phys. Rev. B **58**, 3617 (1998).
- [357] H. T. Lorenzen, J. K. Nørskov, and K. W. Jacobsen, Phys. Rev. B **60**, R5149 (1999).
- [358] F. A. Carey and R. J. Sundberg, *Advanced organic chemistry*, 3rd ed. (Plenum Press, New York, 1990).
- [359] R. A. Sheldon, *Chirotechnology*, 3rd ed. (Marcel Dekker, New York, 1993).
- [360] M. Abramowitz and I. A. Stegun, *Handbook of Mathematical Functions* (Dover Pub., New York, 1972).
- [361] P. Cowan, Ph.D. thesis, Pennsylvania State University, 1977.

Acknowledgements

I am grateful to Flemming Besenbacher, who gave me the opportunity to work in his group. The way he leads the group, not only scientifically but also on a social level, is admirable, and his unstoppable enthusiasm and dynamics were surely an additional motivation during my studies. The support and advice given by him and the two other founders of the scanning tunneling microscopy (STM) group in Aarhus, Ivan Stensgaard and Erik Lægsgaard, is deeply appreciated.

Ivan's chamber was an experimental oasis for refuge after a draining period at the "low-low" chamber. In this connection I would like to thank Lars Petersen, who not only introduced me to the world of STM, but also provided continuous support in fighting "low-low". My thank is to all other members of the STM group in Aarhus for their hospitality; it has been a pleasure to work here.

Special thanks go to Line Kühnle for collaborating on the HtBDC project, Trolle Linderoth for reactivating his Monte Carlo simulations and for what would be called fruitful scientific discussions, and to Federico Rosei for working together on the Lander project. I am very grateful to Jeanette Dandanell, Kim Højrup Hansen, Casper Budtz Jørgensen, Line Kühnle, Trolle Linderoth, Federico Rosei and Peter Thostrup, who carefully read the manuscript.

Also all other people at the Institute of Physics and Astronomy in Aarhus, the technical staff from the mechanical workshop, the electronics department, the library and the printshop, who supported this work in numerous ways, I would like to thank very much.

André Gourdon [Centre d'Elaboration de Matériaux et d'Etudes Structurales (CEMES) - Centre National de la Recherche Scientifique (CNRS), Toulouse, France] and Ib Johannsen (Risø National Laboratories, Risø, Denmark) are acknowledged for providing the molecule samples. Ping Jiang, Christian Joachim and Hao Tang (all CEMES - CNRS, Toulouse, France) are acknowledged for performing the computer simulations of the investigated molecules.

Financial support through the Center for Atomic-scale Materials Physics (CAMP), funded by the Danish National Research Foundation, and an EU grant within the TMR project "Manipulation of Individual Atoms and Molecules" is acknowledged.

I would like to express my gratitude to everybody, who contributed in making my stay in Denmark a pleasure. Special thanks go to Tine Andersen, Kim Højrup Hansen, Rune Hildebrandt, Casper Budtz Jørgensen, Ida Wendt Larsen, Chris Sardeli, Christian Schultz, Lars and Malin Österlund and of course my wife Julia. Let's not forget about the Carlsberg brewery which finally found out how to brew a decent "Weissbier"!

Ein besonderer Dank geht an meine Freunde in Deutschland, die mir trotz ihrer Ferne Nähe bewiesen haben; ein extra Dankeschön an Till Osthövener, David Schagen und Pia Schmidt. Meiner Familie ist für ihre fortdauernde Unterstützung und Mühe nicht genug zu danken. Vielen Dank meiner Schwester Ina sowie meinen Eltern. Julia hätte sicher viel mehr Aufmerksamkeit und Zeit gebührt als ich oftmals aufbringen konnte. Unser Sohn Jonas wusste mich mit seiner Quirlichkeit und seinem Temperament nicht nur tagsüber zu unterhalten, danke auch dafür.

Last but not least: Gud være lovet — jeg lærte at tale dansk ...